

UNIVERSITY OF SÃO PAULO
SÃO CARLOS INSTITUTE OF CHEMISTRY

Amanda Hikari Imamura

Improved biosensors towards accessible health care diagnostics

São Carlos

2022

UNIVERSITY OF SÃO PAULO
SÃO CARLOS INSTITUTE OF CHEMISTRY

Amanda Hikari Imamura

Improved biosensors towards accessible health care diagnostics

*Dissertation presented at São Carlos
Institute of Chemistry / University of São
Paulo to obtain the Doctor of Philosophy
degree in Chemistry.*

*Area of concentration: Analytical and
Inorganic Chemistry*

Academic advisor: Prof. Emanuel Carrilho

Exemplar revisado

O exemplar original encontra-se em
acervo reservado na Biblioteca do IQSC-USP

São Carlos

2022

Autorizo a reprodução e divulgação total ou parcial deste trabalho, por qualquer meio convencional ou eletrônico para fins de estudo e pesquisa, desde que citada a fonte.

Assinatura:

Data:

Ficha Catalográfica elaborada pela Seção de Referência e Atendimento ao Usuário do SBI/IQSC

Imamura, Amanda

Improved biosensors towards accessible health care diagnostics / Amanda Imamura. — São Carlos, 2022.
212 f.

Tese (Doutorado em Química Analítica e Inorgânica) — Instituto de Química de São Carlos / Universidade de São Paulo, 2022.

Edição revisada

Orientador: Prof. Dr. Emanuel Carrilho

1. Biosensor. 2. Diagnostics. 3. Point-of-care. 4. Wearable. 5. Sensor. I.
Título.

Wilneide do C. Marchi Maiorano - CRB: 3978/8



ACKNOWLEDGMENTS

To mom and dad, Claudia and Emerson. Without your love and support, none of this would be possible. Thank you for investing in my education and pushing me to do my best. Thank you for believing I could do more. To my sister, Saory. Thank you for cheering for me in every life stage. Also, I would like to acknowledge my grandparents, my aunts and uncles, and my cousins.

To Henrique, who supported me in the final years of my Ph.D. by taking care of me while I was stressed out with experiments and writing. Thank you for lifting my life up.

To Dr. Emanuel Carrilho for your guidance, patience, and support. Thank you for always helping me see the light in dead-end experiments, for letting me explore many paths along with the research, and for encouraging me in my academic endeavors. Your creative mind has always inspired me to look at everything from a different perspective.

To Dr. Michelle Khine for accepting me at the Khine Lab and for the opportunity of working with you. I'm inspired by your strength and passion for transforming the struggles as a daughter and mom into outstanding advances in science. You are an inspiration for all women in science.

To all members of BioMicS lab. To the former members for welcoming me so well and teaching me the ways around the lab, and the new members for bringing new experiences and enriching our group. Amanda, Ana Júlia, Bia, Bruno, Cleyton, Cláudia, Desiree, Eduardo, Elsa, Fabi, Jéssica Albuquerque, Jéssica Feitor, Ju Alberice, Ju Borba, Segato, Laís, Larissa, Letícia Marques, Letícia Jordão, Lucas, Luciana, Ma, Mariana, Manoel, Tatiana, Vinícius, and Weliton.

To the Khine Lab, especially to those who worked closely with me: Darwin, Heather, Josh, Julia, Julien, Michael (and Diane), Sophia, Thao, and Yongxiao. Also, special thanks for the best roommates: Aleida, Irma, and Genesis. Thank you for showing me the way around and taking me on many adventures. You are my American family.

To all the postdocs who helped me closely during graduate school: Dr. Thiago Segato, Dr. Livia Sgobbi, and Dr. Lais Brazaca. Without your extra guidance, this dissertation would not be possible.

To the colleagues who assisted my research: Prof. Dr. Ronaldo Censi Faria and Dr. Wilson T. da Fonseca for fabricating the electrodes; Nathalia Oezau Gomes for fabricating the electrodes; Bruno Bassi Millan Torres for the profilometry analysis; Paulo Augusto Raymundo Pereira for lending the potentiostat.

To IQSC/USP for the support and the professors who taught me so much during my 10 years at the institute. Special thanks to Prof. Dr. Sergio Machado for extra orientation on electrochemistry; Prof. Dr. Álvaro José dos Santos Neto for teaching me the fundamentals of research at my early years as undergraduate research fellow; Prof. Dr. Elisabete Frollini and technician Luiz Antonio Ramos for the DMA analysis; Prof. Dr. Frank Crespilho and Dr. Ayaz Hassan for the micro-FTIR analysis; technicians Marcio de Paula for the MEV analysis and Aldimar for the FTIR analysis.

To FAPESP for the financial support through the grant 2017/05362-9 and 2018/19749-5, and to CNPQ (grant: 130494/2016-0). This study was also financed in part by the Coordenação de Aperfeiçoamento de Pessoal de Nível Superior – Brasil (CAPES) – Finance Code 001.

Saving lives starts with bringing everyone in.

Melinda Gates

RESUMO

Diagnósticos no ponto de atendimento são centrados no paciente para diminuir a dispersão do processo em localizações diferentes (hospitais, clínicas e consultórios médicos). Biossensores são comumente integrados a sistemas miniaturizados para oferecer diagnósticos mais acessíveis com resultados mais rápidos no ponto de atendimento. A miniaturização, no entanto, ainda apresenta desafios, os quais foram discutidos nesta tese. No Capítulo II, otimizou-se a imobilização de biomoléculas sobre o papel por meio da oxidação das fibras de celulose com NaIO_4 . A oxidação foi caracterizada extensivamente visto que as propriedades físico-químicas do papel foram alteradas ao longo do processo. O papel oxidado por fim foi utilizado para determinar a quantidade de proteína em urina, detectando precocemente casos de microalbuminúria. O Capítulo III descreve um método alternativo de fabricação de dispositivos microfluídicos vestíveis usando-se o brinquedo *Shrinky-Dinks* (SD). O dispositivo vestível foi integrado a ensaios colorimétricos de glicose e lactato em suor. Apesar do biossensor não apresentar detectabilidade e sensibilidade adequada para detectar os biomarcadores, o dispositivo microfluídico foi capaz de coletar continuamente o suor sem perturbar o usuário. O Capítulo IV descreve a fabricação de eletrodos altamente sensíveis e flexíveis pela mesma premissa do *Shrinky-Dink*. Os eletrodos enrugados quantificaram glicose na faixa de $0,1 \mu\text{mol L}^{-1}$ a $0,1 \text{mmol L}^{-1}$ em pH fisiológico, demonstrando sensibilidade e detectabilidade na detecção de glicose em suor. Por fim, o Capítulo V descreve dois biossensores eletroquímicos como diagnóstico rápido e barato para COVID-19. Ambos os biossensores são portáteis e foram capazes de detectar a proteína S do vírus SARS-CoV-2 in microlitros de saliva sem a necessidade de reagentes químicos específicos. Espera-se que com os avanços descritos na tese no campo da imobilização, microfabricação e detecção contribuam no desenvolvimento de biossensores modernos para que no futuro diagnósticos mais acessíveis estejam disponíveis no mercado.

ABSTRACT

Point-of-care (POC) testing provides diagnostic tools centered on the patient rather than dispersed in different locations (hospitals, clinics, doctor's offices). POC biosensors are often integrated into miniaturized systems and consist of portable and cheaper devices with fast output than conventional clinical analysis. However, significant challenges still exist in the miniaturization field, addressed in this dissertation. In Chapter II, the immobilization of biomolecules on paper was optimized by oxidating the cellulose with NaIO_4 . The oxidation was extensively characterized since it affected the physicochemical properties of the paper. Moreover, the oxidized paper was applied to quantify protein in urine, detecting early cases of microalbuminuria. Chapter III describes an alternative fabrication method for wearable microfluidic devices using the toy Shrinky-Dinks (SD). As a proof-of-concept, a wearable colorimetric device for glucose and lactate was demonstrated. Although the assays lacked detectability and sensitivity to detect glucose and lactate in sweat, the SD-based microfluidic channels demonstrated the capability of continuously collecting sweat without disturbing the user. Chapter IV describes a sensitive and stretchable electrode fabricated by the same premise of SD wearable devices. The stretchable wrinkled electrodes quantified glucose at a concentration range from $0.1 \mu\text{mol L}^{-1}$ to 0.1mmol L^{-1} in physiological pH, demonstrating the applicability for sensing in sweat. Finally, Chapter V describes two electrochemical biosensors for faster and more accessible diagnosis tools for widespread testing for COVID-19. Although they present different approaches, both biosensors were portable and detected the S protein of SARS-CoV-2 in microliters of saliva without requiring chemical supplies. The improvements described in this dissertation on immobilization, fabrication process, and detection will hopefully contribute to further works on the development of biosensors to finally reach commercial ends and broaden access to health care.

LIST OF FIGURES

- Figure I.1 - (A) Confirmed cases of infected by COVID-19 across the world according to WHO on Jan 15th 2022. (B) Cumulative confirmed cases and deaths in Brazil according to WHO on Jan 15th 2022. 36
- Figure I.2 - Fundamentals of a chemical sensor with a receptor, which recognize the analyte, and a transducer, which convert the chemical information into a measurable signal. 39
- Figure I.3 - Commonly used bioreceptor in a biosensor: aptamer, DNA, enzyme, antibody and cell. Representation out of scale. 42
- Figure I.4 - Enzyme structure and the interaction with substrate: (i) Interaction between the enzyme and its substrate, forming the enzyme-substrate complex; (ii) Catalysis of the substrate to products, forming the enzyme-product complex; (iii) Release of the products and regeneration of the enzyme for new cycle. Types of enzymatic inhibition: (B) Competitive, (C) non-competitive, and (D) uncompetitive inhibitor. 44
- Figure I.5 - (A) Antibody structure: Fc domain, Fab domain and antigen binding site. (B) Difference of monoclonal and polyclonal antibodies interaction with antigen... 46
- Figure I.6 - Lateral flow assay for detection of COVID-19 human IgG and IgM. (A) Scheme of the detection device. (B) Illustration of the results of the test: negative, IgM positive, IgG positive, and IgM and IgG Positive..... 47
- Figure I.7 - Definition of limit of detection (LOD) and limit of quantification (LOQ). The curves represent the Gaussian distribution of errors. 50
- Figure I.8 - Timeline of pregnancy test. From: (A) Ancient pregnancy test, which involved urinating on grain seeds; (B) Animal-based tests, known as A-Z test, in which the urine was injected into an animal; Start of antibody-based techniques with (C) Hemagglutination inhibition test; (D) First at-home pregnancy test; and (E) the first stick test similar to current commercial pregnancy test..... 53
- Figure I.9 - (A) Micropatterning methods on paper. (i) Schematics of a paper-based microfluidic channel with hydrophobic barriers created by (ii) photolithography and (iii) wax printing. An example of a device fabricated by (iv) photolithography and by (v) wax printing. (B) Integration of μ PAD with mobile phone cameras for performing bioassays in remote locations and for exchanging the results of the tests with off-site technicians..... 56
- Figure I.10 - Evolution of glucose sensing: (A) First commercial glucose analyzer based on Clark biosensor by Yellow Springs Instrument Company, (B) hand-held glucose monitor Accu-Chek Advantage by Roche, (C) GlucoWatch by Cygnus Inc operating principles, (D) tooth-mounted glucose sensor, and (E) smart contact lenses for glucose detection in tear. 58

Figure II.1 - Layout and dimensions of the chromatography paper strip to evaluate (A) BSA immobilization and (B) quantify HSA in urine on oxidized paper.	70
Figure II.2 - (A) Oxidation of glucose monomer of the cellulose chain with NaIO ₄ . (B) Reaction between the aldehyde and amine groups, resulting in the Schiff base.	72
Figure II.3 - (A) FTIR-ATR spectra of the native chromatography paper and after 0.5, 1, 2, 4, 8, 12, and 24 h oxidation in 0.5 mol L ⁻¹ NaIO ₄ . (B) Magnification in the range from 2000 to 1500 cm ⁻¹ . Carbonyl stretching band at 1733 cm ⁻¹	72
Figure II.4 - Micro-FTIR spectroscopy of the paper treated for 0.5 h (A, C, E, G) and 2 h (B, D, F, H) recorded with FPA detector from 4000 to 900 cm ⁻¹ at spectral resolution of 4 cm ⁻¹ with 256 spectra co-added. (A), (B) Optical images showing a part of the sample paper, where fibers can be easily seen. The area marked in red was selected for the extraction of the spectra and consequent chemical images. (C), (D) micro-FTIR spectra of the treated paper with the integrated spectral bands highlighted. (E), (F) 2D Chemical images showing the distribution of carbonyl spectral band along the cellulose fibers. (G), (H) 3D chemical images.	73
Figure II.5 - (A) Geometrical area (blue) and volume (red) in function of time. (B) Shrinking of the paper strip after 24 h of oxidation (middle) and micrographs in 500 and 3000 × magnification of the native (left) and the oxidized (right) papers.	74
Figure II.6 - (A) Paper diffractogram with the index peaks of the crystalline planes, and in the insertion, diffractograms of the oxidation progress. (B) Stress-strain curve for paper without (black) and after (red) exposure to NaIO ₄ for 24 h; specimen dimensions: 30 × 3 × 0.18 mm.	75
Figure II.7 - Drops of water on native paper: (A) 1st and (B) 10th frames. Drops of water after 12h oxidation: (C) 1st and (D) 10th frames. Contact angles inserted in the frames.	75
Figure II.8 - (A) Paper chips from native (0 h) and oxidized papers for 0.5, 1.0, 2.0, and 4.0 h after the immobilization with 0.5 μL of BSA at 1.0, 2.0, 4.0, and 8.0 mg mL ⁻¹ solutions. (B) Graphical relation between oxidation time, BSA concentration, and the blot length.	77
Figure II.9 - RGB intensity of the blot after immobilization of BSA (A) 1, (B) 2, (C) 4, and (D) 8 mg mL ⁻¹ on the paper without treatment and after 0.5 to 4.0 h of oxidation.	80
Figure II.10 - Blot lengths of 4 and 8 mg mL ⁻¹ of BSA at pH of 3.8, 4.8 and 5.8 performed in the paper chip oxidized for 4 h; error bars indicate one standard deviation from three chips.	81
Figure II.11 - Plot of blot length vs. BSA concentration in paper chip oxidized for 4 h in a phosphate buffer pH 3.8; error bars indicate one standard deviation from five chips.	82

Figure II.12 - (A) Paper chips oxidized for 4 h after the immobilization of 0.5 μL of HSA 0, 0.1, 0.5, 1.0, 1.5, 2.0, 3.0, 5.0, and 10.0 mg mL^{-1} in urine pool. (B) Blot length vs. HSA concentration in urine pool; error bars indicate the standard deviation from 5 chips.	84
Figure II.13 - (A) Absorbance at 595 nm vs. HSA concentration in urine pool. Error bars indicate the standard deviation from three measurements. (B) Absorbance from Bradford method and blot length from paper chip method plotted against HSA concentration in urine. (C) Correlation between signals obtained from Bradford and paper chip methods. Error bars in x-axis and y-axis represent, respectively, the standard deviations of three absorbance measurement and from five chips.	84
Figure III.1 - Fabrication steps of (A) Shrinky-Dinks (SD) molds and (B) PDMS microfluidic devices with the SD molds.....	95
Figure III.2 – (A) Dimensions of the PDMS microfluidic channels for in-vitro assay. (B) Assembled microfluidic device.....	97
Figure III.3 - (A) Design of the wearable microfluidic device with the dimensions. (B) Layers of the wearable device on top of the skin. (C) Transversal view of the wearable microfluidic device.	98
Figure III.4 - Microfluidic channels fabricated with SD-based molds. (A) Vertical cut of PDMS channel sealed with thin layer of PDMS. (B) Microfluidic channel depth and width in function of printing layers. Error bars indicate the standard deviation for three samples.	99
Figure III.5 - One electron oxidation process of TMB to a cation radical and subsequent formation of charge-transfer complex in the presence of H_2O_2 and HRP.	101
Figure III.6 - Chitosan chemical structure.....	102
Figure III.7 - Chitosan effect on glucose colorimetric assay for the channels (A) red, (B) green, and (C) blue. Tested conditions: (i) without chitosan, (ii) with acetic acid, (iii) with 1 μL of chitosan, (iv) with 2 μL of chitosan, and (v) with 3 μL of chitosan. Error bars represent the standard deviation for three samples.....	102
Figure III.8 - Concentration curve of glucose in PBS from 0 to 1 mmol L^{-1} for (A) red, (B) green, and (C) blue channels. Linear fit represented by the dotted line from 0 to 0.5 mmol L^{-1} and parameters inserted in the graphs. Error bars represent the standard deviation for three measurements.....	103
Figure III.9 - Lactate concentration curve from 0 to 60 mmol L^{-1} in (A) red, (B) green, and (C) blue channels and from 0 to 1 mmol L^{-1} in (D) red, (E) green, and (F) blue channels. Linear fits are represented as dotted line and parameters are inserted in the graphs. Error bars represent the standard deviation for three measurements.	104

- Figure III.10 - Kinetics of a competitive inhibitor. (A) Reaction of the enzyme with the substrate and a competitive inhibitor. (B) A typical graph of the competitive inhibitor effect on the kinetics of the enzyme. (C) Double-reciprocal graph of the enzymatic kinetics without and with inhibitor. Intercept on the vertical and horizontal axis represent, reciprocally, the $1V_{max}$ and the $1KM$ 105
- Figure III.11 - Chemical structures of L-lactate (A) and LOx inhibitors: (B) 2-hydroxybutyrate, (C) D-Lactate, (D) Oxalate, and (E) Glycolate. The KM and Ki are displayed as well..... 106
- Figure III.12 - (A) Effect of glycolate (Gly) on LOx kinetics. (B) Linearized Lineweaver-Burk plot. (C) Lactate concentration curve from 10 to 75 mmol L⁻¹ in the presence of 400 mmol L⁻¹ of glycolate. Linear fit for the concentration curve is represented by dotted line and its parameters are insert in the graph. Error bars represent the standard deviation from three measurements. 107
- Figure III.13 - (A) Frames of the paper disk in the microfluidic chamber wetting with glucose 1 mmol L⁻¹ followed by PBS under a flow rate of 5 μL min⁻¹. Normalized R values along time when pumping (B) glucose 1 mmol L⁻¹ followed by (C) PBS. (D) Frames of the paper disk in the microfluidic channel wetting with PBS followed by glucose 1 mmol L⁻¹ under a flow rate of 5 μL min⁻¹. Normalized R values along time when pumping (E) PBS followed by (F) glucose 1 mmol L⁻¹. Normalization was calculated regarding to the first point (0 s). Error bars represent the standard deviation from 3 measurements. 108
- Figure III.14 - Simple schematics of solution path line through the chamber with the (A) dry and (B) wet paper disk. The blue circles represent the solution particles, the red arrows represent the velocity vector of the particles, and the yellow arrow represents the capillarity from the paper..... 109
- Figure III.15 - Color development along time for flowing 1 mmol L⁻¹ of glucose in (A) native paper and (B) oxidized paper. Error bars represent the standard deviation for three measurements..... 110
- Figure III.16 - Glucose colorimetric assay in microfluidic chamber. (A) Paper disks after flowing glucose from 0 to 1 mmol L⁻¹. Concentration curve of glucose at same concentration range in (B) red, (C) green, and (D) blue channels. Linear fits are represented as dotted line and the parameters are inserted in the graphs. Error bars represent the standard deviation for three measurements. 110
- Figure III.17 - Color progression for lactate 50 mmol L⁻¹ in R channel over time for (A) native and (B) oxidized paper with and without chitosan. Error bars represent the standard deviation for three measurements..... 111

Figure III.18 - Lactate colorimetric assay in microfluidic chamber. (A) Paper disks after flowing lactate from 0 to 75 mmol L ⁻¹ . Concentration curve of lactate at same concentration range in (B) red, (C) green, and (D) blue channels. Linear fits are represented as dotted line and the parameters are inserted in the graphs. Error bars represent the standard deviation for three measurements.	112
Figure III.19 - Sweat flowing in the wearable device. (A) Images of the wearable devices during 30 min of indoor biking. (B) Sequential frames from left to right of the chamber at 10 min illustrating the capillary force from the paper disk pulling the sweat.	113
Figure III.20 - On-body measurement for (A) glucose and (B) lactate before and after 30 min of exercise.	114
Figure III.21 - Wearable device for lactate measurement during outdoor biking. Photos of the wearable device at the forearm at the (A) beginning of the test and (B) after 20 km of biking.	115
Figure IV.1 - Photo of the gold electrodes, from left to right: Unshrunk electrode, shrunk electrode on PO, and shrunk electrode on elastomer substrate.	126
Figure IV.2 - Current density voltammograms of unshrunk, shrunk, and transferred electrodes in (a) H ₂ SO ₄ and (b) [Fe(CN) ₆] ^{3-/4-} . (c) Shrinking factor and signal enhancement for shrunk and transferred gold electrode expressed as ratios. Error bars represent the standard deviation from three measurements.	127
Figure IV.3 - Schematics of the electrochemical reactions at wrinkled gold surface. (A) Gold oxidation nonlimited by diffusion. (B) [Fe(CN) ₆] ^{3-/4-} diffusion-limited reaction.	129
Figure IV.4 - Stretching of the electrode. (A) Photo of electrode transferred to elastomer substrate. SEM of the unstretched electrode at (B) 1.1 and (C) 12.9 k × magnification. (D) Transferred electrode being stretched. SEM of the stretched transferred electrode at (E) 1.1 and (F) 12.9 k× magnification.	130
Figure IV.5 - (A) Schematics of the crack formation on the transferred gold electrode with strain. (B) Normalized resistance response with 200% strain across 10 cycles.	130
Figure IV.6 - Cyclic voltammograms of transferred gold electrode stretched up to 210% of its length in (A) H ₂ SO ₄ and (B) [Fe(CN) ₆] ^{3-/4-} . (C) Signal increase measured as peak height before and after stretch in H ₂ SO ₄ and [Fe(CN) ₆] ^{3-/4-}	131
Figure IV.7 - Cyclic voltammograms of transferred gold electrodes in (A) H ₂ SO ₄ and (B) [Fe(CN) ₆] ^{3-/4-} before and after stretching to 210% of its length and relaxing overnight. (C) Signal increase measured after relaxing the electrodes overnight in H ₂ SO ₄ and [Fe(CN) ₆] ^{3-/4-}	132
Figure IV.8 - (A) Cyclic voltammograms of stretchable electrode in phosphate buffer (black), and 5 mmol L ⁻¹ glucose (red). (B) Close-up view from 0 to 0.4 V.	133

Figure IV.9 - Mechanism of glucose oxidation at gold surface. (A) Adsorption of glucose at the gold surface by dehydrogenation. (B) Direct oxidation to gluconate. (C) Oxidation to glucolactone then conversion to gluconate.....	133
Figure IV.10 - (A) Amperometry detection of glucose from 1×10^{-3} to 1 mmol L^{-1} in PBS using unstrained electrode. (B) Linear correlation of current values with glucose concentration in unstrained electrode ($R^2 = 0.9972$). (C) Amperometry detection of glucose from 1×10^{-1} to 1 mmol L^{-1} in PBS using pre-strained electrode. (D) Linear correlation of current values with glucose concentration in pre-strained electrode ($R^2 = 0.9969$).....	134
Figure V.1 - SARS-CoV-2 structure and main components: (A) Envelope protein, (B) membrane protein, (C) spike protein, (D) nucleocapsid protein, and (E) lipid membrane.....	146
Figure V.2 - Fabrication processes of the (A) minicells and (B) SPEs.....	149
Figure V.3 - (A) SPE before and after electrodeposition of gold for 9, 30, and 90 s. (B) Elemental mapping of SPE after electrodeposition of gold for 9 s. Pink and yellow shades represent carbon and gold, respectively. SEM images of (C) bare SPE and modified with gold electrodeposited for (D) 9 s, (E) 30 s, and (F) 90 s.	150
Figure V.4 - Electrochemical characterization of the SPE (black) modified with gold electrodeposited for 9s (red), 30s (blue), and 90s (yellow). (A) CVs in H_2SO_4 at 100 mV s^{-1} . Insert shows a zoomed view of the CV of SPE. (B) Nyquist plots in $[\text{Fe}(\text{CN})_6]^{4-/3-}$ from 10 kHz to 10 mHz. (C) CVs in $[\text{Fe}(\text{CN})_6]^{4-/3-}$ at 100 mV s^{-1}	151
Figure V.5 - Peak currents and peak current densities of redox probe methylene blue in commercial disk and SD wrinkled electrodes with same geometric areas.	151
Figure V.6 - Functionalization of the SPE. (A) Steps of the modifications on the SPE: (i) Bare Au; (ii) MAA; (iii) EDC-NHS; (iv) Ab; (v) BSA; (vi) S protein. (B) Nyquist plots of the SPE after each functionalization step. Fluorescence images of the electrode with (C) MAA/EDC-NHS/Ab, and (D) after incubation with fluorescein-labeled protein S from SARS-CoV. Amplification $20 \times$	153
Figure V.7 - Calibration curves of S protein and BSA for different Au deposition times: 9 (A), 30 (B), and 90 s (C). S protein and BSA were incubated for 30 min prior to EIS measurements. (D) Sensitivities for S protein and BSA for each Au deposition condition. (E) R_{CT} signals from SARS-CoV, SARS-CoV-2, and BSA at $10^{-9} \text{ mol L}^{-1}$ in PBS.....	154
Figure V.8 - Application of the proposed immunosensor in biological samples. (A) Nyquist plots after incubation of S protein from SARS-CoV from 10^{-11} to $10^{-7} \text{ mol L}^{-1}$ in saliva samples. (B) Calibration curves for S protein from SARS-CoV and BSA in saliva. (C) Nyquist plot for detection of inactivated SARS-CoV-2 viruses in saliva. The inset shows the R_{CT} obtained for negative (in the absence of the virus) and positive (in the presence of 10^6 PFU mL^{-1} of the virus) samples.	155

- Figure V.9 - Simple schematic of binding-induced conformational change of an aptamer and the effect on the current. Binding to a target leads to a (A) decrease or (B) increase in electron transfer rate and consequently, on current. 156
- Figure V.10 - Response of commercial disk gold electrodes functionalized with the aptamer upon addition of S1 protein. (A) SWVs upon addition of S1 protein at 10 Hz. (B) Titration curves at different frequencies. Error bars represent the standard error from three electrodes..... 157
- Figure V.11 - Titration curve of S1 protein performed at 10 Hz in 10% saliva. Error bars represent standard error of the mean among five SD wrinkled mini cells..... 158

LIST OF TABLES

Table II.1 - Main effect of BSA concentration. Pink-shaded area highlights the statistically significant variance of data.....	78
Table II.2 - Main effect of time of oxidation. Pink-shaded area highlights the statistically significant variance of data.....	78
Table II.3 - Simple effect of oxidation time for BSA concentration of 1 mg mL ⁻¹	78
Table II.4 - Simple effect of time oxidation for BSA concentration of 2 mg mL ⁻¹ . Pink-shaded area highlights the statistically significant variance of data.	79
Table II.5 - Simple effect of Time oxidation for BSA concentration of 4 mg mL ⁻¹ . Pink-shaded area highlights the statistically significant variance of data.	79
Table II.6 - Simple effect of Time oxidation for BSA concentration of 8 mg mL ⁻¹ . Pink-shaded area highlights the statistically significant variance of data.	79
Table II.7 - Summary of the figures of merit from the Bradford method (reference) and the paper chip method.	85
Table III.1 - Relation between RGB channel, observed, and complementary colors.	98
Table IV.1 - Charge and surface area of shrunk and transferred gold electrodes.	128
Table IV.2 - Sheet resistance of transferred gold electrode before straining, at 100% strain, and after relaxation.	131
Table IV.3 - Summary of published flexible enzymatic and non-enzymatic glucose sensors.	135
Table V.1 - Summary of peer-reviewed published works on antigen-based POC diagnosis for COVID-19.	143

ABBREVIATION AND ACRONYMS LIST

A-Z test	Aschheim-Zondek test
Ab	Antibody
ACE2	Angiotensin converting enzyme 2
Ag/AgCl	Silver/silver chloride
ATR	Attenuated Total Reflectance
Au	Gold
AuNP	Gold nanoparticle
BSA	Bovine Serum Albumin
<i>c</i>	Specific charge equivalent
CBD	Cellulose Binding Domain
CM	Culture Medium
CNT	Carbon Nanotube
CO₂	Carbon dioxide
COVID-19	Coronavirus disease of 2019
CTM	Clinical Transport Medium
CV	Cyclic Voltammetry
DI water	Distilled water
DIC	Digital Image Colorimetry
DMA	Dynamic Mechanical Analysis
EAB	Electrochemical Aptamer-Based
EASA	Electrochemically Active Surface Area
EDC	1-ethyl-3-(3-dimethylamino-propyl) carbodiimide
EIS	Electrochemical Impedance Spectroscopy
ePAD	Electrochemical paper-based analytical device
Fab	Fragment antigen-binding
FAD⁺/FADH₂	Flavin adenine dinucleotide in oxidized and reduced forms
Fc	Fragment crystallizable region
FDA	Food and Drug Administration
[Fe(CN)₆]^{3-/4-}	Ferro and ferricyanide
FET	Field-Effect Transistor
FMN/FMNH₂	Flavin-mononucleotide in oxidized and reduced forms
FTIR	Fourier Transform Infrared

GOx	Glucose oxidase
H₂O₂	Hydrogen Peroxide
H₂SO₄	Sulfuric Acid
hCG	Human Chorionic Gonadotropin
HIV	Human Immunodeficiency Virus
HRP	Horseradish Peroxidase
HSA	Human Serum Albumin
HSL	Hue, Saturation, and Lightness
HSV	Hue, Saturation, and Value
HSB	Hue, Saturation, and Brightness
IgG	Immunoglobulin G
IgM	Immunoglobulin M
IUPAC	International Union of Pure and Applied Chemistry
K_D	Dissociation constant of the receptor on Hill-Langmuir isotherm
K_M	Michaelis-Menten constant
LFA	Lateral Flow Assay
LH	Luteinizing Hormone
LOD	Limit of Detection
LOQ	Limit of Quantification
LOx	Lactate Oxidase
MAA	Mercaptoacetic Acid
MB	Methylene Blue
MCH	Mercaptohexanol
MERS-CoV	Middle East Respiratory Syndrome-Related Coronavirus
mM	Milimolar
MPTMS	3-(mercaptopropyl)trimethoxysilane
n	Hill Coefficient on Hill-Langmuir Isotherm
N protein	Nucleocapsid Protein
NHS	N-Hydroxysuccinimide
NSS	Nasopharyngeal Swab Specimen
PBS	Phosphate Buffer Saline
PCR	Polymerase Chain Reaction
PDMS	Poly(dimethylsiloxane)

PET	Polyethylene Terephthalate
PFU	Plaque Forming Units
PMMA	Poly(methyl methacrylate)
PO	Polyolefin
POC	Point-of-Care
POCT	Point-of-Care Testing
PS	Polystyrene
<i>Q</i>	Charge
REASSURED	Real-time, Affordable, Sensitive, Specific, User-friendly, Robust and Rapid, Equipment-free, and Deliverable
RBD	Receptor-Binding Domain
R_{CT}	Resistance to Charge Transfer
RGB	Red, Green, and Blue
RSD	Relative Standard Deviation
RT-PCR	Reverse-Transcriptase-Based Polymerase Chain Reaction
S protein	Spike Protein
SARS-CoV	Severe Acute Respiratory Syndrome Coronavirus
SARS-CoV-2	Severe Acute Respiratory Syndrome Coronavirus 2
SD	Shrinky-Dink
SELEX	Systematic Evolution of Ligands by EXponential enrichment
SEM	Scanning Electron Microscope
SNR	Signal-to-Noise Ratio
SPE	Screen-Printed Electrode
SWCNT	Single-Walled Carbon Nanotube
[<i>T</i>]	Concentration of the target on Hill-Langmuir isotherm
TMB	3,3',5,5'-tetramethylbenzidine
VLP	Virus Like Particle
V_{max}	Maximum Rate
VTM	Virus Transportation Medium
WHO	World Health Organization
WSe₂	Tungsten Diselenide
μPAD	Microfluidic Paper-Based Analytical Devices
θ	Target-bound fraction of the receptor on Hill-Langmuir isotherm

TABLE OF CONTENTS

CHAPTER I

Chemical sensors and biosensors in health care	33
I.1. INTRODUCTION.....	35
I.2. CHEMICAL SENSORS AND BIOSENSORS.....	39
I.3. POINT-OF-CARE TESTING AND MINIATURIZATION.....	52
I.4. WEARABLE DEVICES	56
I.5. CHALLENGES IN THE FIELD OF MINIATURIZATION AND PORTABLE BIOSENSING DEVICES.....	59
I.6. REFERENCES	60

CHAPTER II

Oxidative treatment on chromatography paper for bioreceptor immobilization in analytical device	65
II.1. INTRODUCTION.....	67
II.2. AIMS	68
II.3. MATERIALS & METHODS.....	69
II.4. RESULTS & DISCUSSION	71
II.5. CONCLUSION	85
II.6. REFERENCES	86

CHAPTER III

Shrinky-Dinks for fabrication of wearable microfluidic devices for sweat glucose and lactate sensing	89
III.1. INTRODUCTION.....	91
III.2. AIMS	94
III.3. MATERIALS & METHODS.....	94
III.4. RESULTS & DISCUSSION	99
III.5. CONCLUSION	115

III.6. REFERENCES	117
-------------------------	-----

CHAPTER IV

Electrochemical characterization of wrinkled electrodes and its application for glucose sensing.....	121
---	------------

IV.1. INTRODUCTION.....	123
-------------------------	-----

IV.2. AIMS	124
------------------	-----

IV.3. MATERIALS & METHODS.....	124
--------------------------------	-----

IV.4. RESULTS & DISCUSSION	126
----------------------------------	-----

IV.5. CONCLUSION	137
------------------------	-----

IV.6. REFERENCES.....	138
-----------------------	-----

CHAPTER V

Electrochemical sensing devices for diagnosing COVID-19 in saliva samples.....	141
---	------------

V.1. INTRODUCTION.....	143
------------------------	-----

V.2. AIMS	147
-----------------	-----

V.3. MAIN DIFFERENCES	148
-----------------------------	-----

V.4. CONCLUSION	158
-----------------------	-----

V.5. REFERENCES.....	160
----------------------	-----

FINAL REMARKS AND PERSPECTIVES	163
---	------------

CURRICULUM VITAE	167
-------------------------------	------------

ANNEX 1.....	171
---------------------	------------

ANNEX 2.....	181
---------------------	------------

ANNEX 3.....	189
---------------------	------------

ANNEX 4.....	201
---------------------	------------

PRESENTATION

This dissertation describes the work and results obtained in 6 years financially supported by CNPQ (130494/2016-0) from 2016 to 2017, and FAPESP (2017/05362-9 and 2018/19749-5) from 2017 to 2021. The financed project aimed the detection of cortisol in a wearable and paper-based microanalytical device integrated with contactless conductometric detection. Although the initial goal was not accomplished, the research resulted in two published manuscripts as first author from the advances achieved over the years as well as two manuscripts related to COVID-19 research as second author in the last couple years. The dissertation is divided into five chapters, with introduction and four chapters based on the manuscripts, and with a closing with final remarks and perspectives.

Chapter 1 is an introduction revisiting the historical context on the development of sensors and the contribution of Analytical Chemistry. It states the importance of low-cost and portable diagnostic technologies, describes the fundamentals of sensors and biosensors, and finally, the actuation of microfluidic in the miniaturization of sensing devices.

Chapter 2 investigates the oxidation of cellulose to functionalize biomolecules on paper-based sensing devices. Later, the oxidized paper quantified protein in urine. The results obtained in this work were published on *Microchimica Acta*, paper attached in *ANNEX 1* (DOI: [10.1007/s00604-020-04250-6](https://doi.org/10.1007/s00604-020-04250-6)).

Chapter 3 describes the colorimetric detection of glucose and lactate in sweat by wearable devices fabricated using the toy Shrinky-Dinks.

Chapter 4 describes the electrochemical characterization of the wrinkled electrode fabricated with Shrinky-Dinks. The work was conducted during a research internship abroad at Khine Lab (University of California, Irvine). The wrinkled electrodes were also applied for glucose sensing. The results were published on *Advanced Materials Technology* manuscript attached in *ANNEX 2* (DOI: [10.1002/admt.201900843](https://doi.org/10.1002/admt.201900843)).

Chapter 5 highlights two works developed during the COVID-19 pandemic for the detection of SARS-CoV-2. One of the works, in collaboration with the Khine Lab, exploits high-sensitive wrinkled electrodes for the detection of the S protein using an aptamer (published at *Analytical Methods*, attached at *ANNEX 3* - DOI: [10.1039/D1AY00041A](https://doi.org/10.1039/D1AY00041A)). The second work was developed at BioMicS lab in collaboration with other researchers and was based on gold-modified screen-printed electrode as immunosensor for S protein and inactivates virus. The results were published on *Analytical and Bioanalytical Chemistry*, manuscript attached in *ANNEX 4* (DOI: [10.1007/s00216-022-03956-1](https://doi.org/10.1007/s00216-022-03956-1)).

CHAPTER I

Chemical sensors and biosensors in health care

I.1. INTRODUCTION

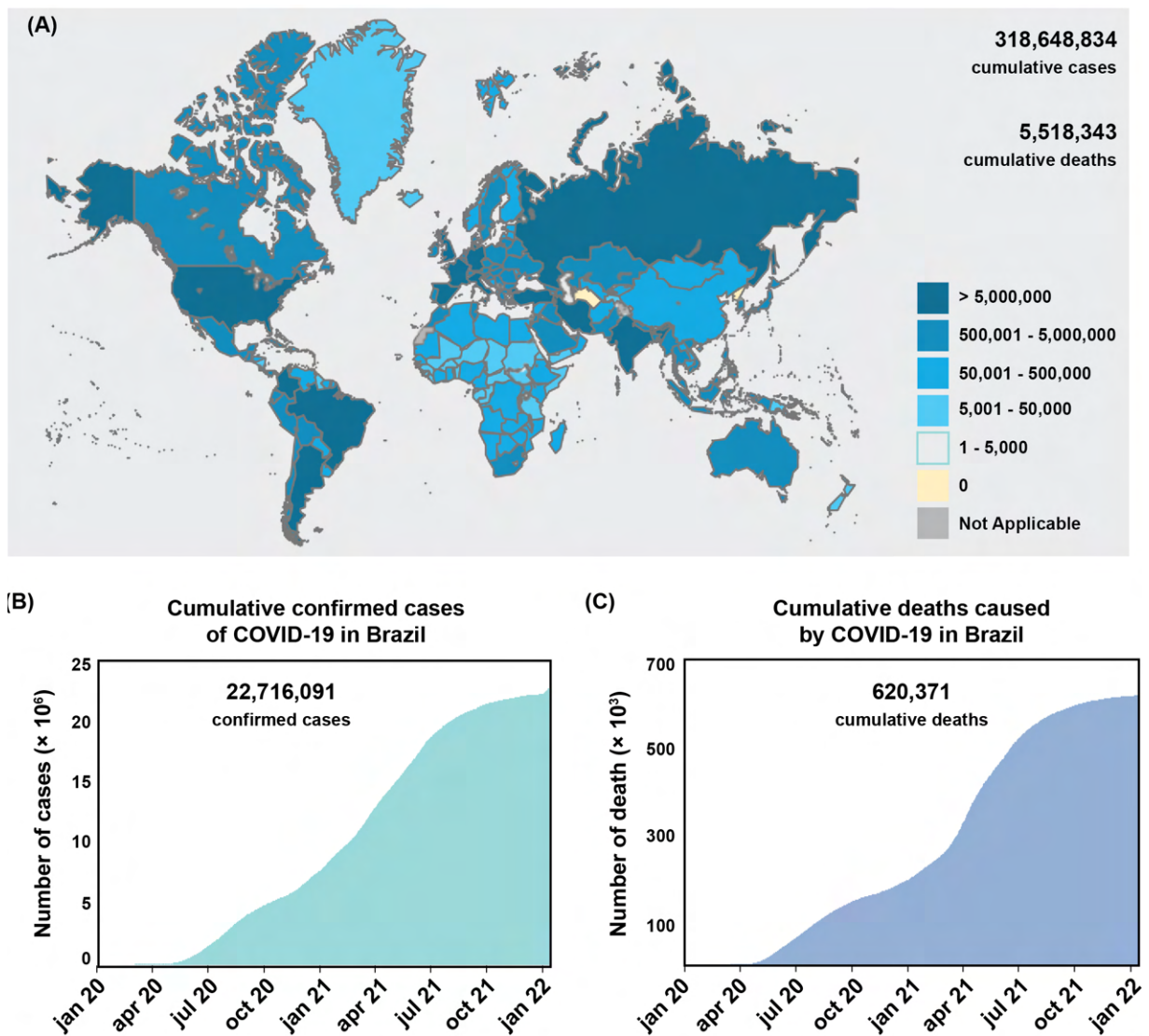
The diagnosis of a disease is the first step in the health care system to assess the adequate treatment, reduce the disease dissemination, and minimize the costs and resources in inefficient treatments. Although medicine technology has advanced with more specific diagnosis and efficient treatments for several diseases, only a small part of the worldwide population is benefited. Countries in development sometimes lack on minimum resources, such as electricity, and health care professionals to run clinical laboratories. Moreover, the low income of the population discourages the diagnosis step since most of the medical treatments can be expensive and sometimes not even available in these regions.

Conventionally, the diagnosis is performed by a health professional, who evaluates the symptoms and interpret the results from clinical analysis. With the development of point-of-care (POC) testing, the approach for health care has been shifting from a fragmented diagnosis taking places in different locations (hospitals, clinics, doctor's offices) to a more centralized system focused on the patient. POC testing consists of medical tests that can be performed at or near the patient care. The POC testing devices are characterized by the portability, fast output, and lower cost compared to conventional clinical analysis. Some of the commercially successful POC devices are glucose meter and pregnancy test, which will be further discussed in this *Chapter*.

The importance of the development of the tests centralized in the patients with fast diagnosis has never been so evident as during the current pandemic. The year of 2020 was struck by the COVID-19, an infectious disease caused by the severe acute respiratory syndrome coronavirus 2 (SARS-CoV-2). Despite the lower fatality rate compared to other respiratory diseases, such as caused by SARS-CoV or Middle East respiratory syndrome-related coronavirus (MERS-CoV),¹ the number of people infected by SARS-CoV-2 increased exponentially since its first appearance in the Chinese city of Wuhan in December of 2019. According to the World Health Organization (WHO), the virus spread to 215 countries with more than 318 million cases and 5 million deaths by Jan 15th 2022, as shown in the map provided by WHO in Figure I.1A.² Given the rapid spread of the virus and consequently the high number of confirmed cases, COVID-19 was described as a pandemic by WHO in March 2020.³ In Brazil, there are more than 22 millions confirmed cases (Figure I.1B) and 620 thousands of deaths (Figure I.1C) since the first confirmed case in February 26th 2020.² The infection rate by the SARS-CoV-2 concerned the health agencies around the world since the

health care systems could hardly assist the elevated number of infected people, which unfortunately was the case in many countries.

Figure I.1 - (A) Confirmed cases of infected by COVID-19 across the world according to WHO on Jan 15th 2022. (B) Cumulative confirmed cases and deaths in Brazil according to WHO on Jan15th 2022.



Source: Data from WHO. Accessed in Jan 15th 2022.²

The main symptoms of COVID-19 can be similar to a common flu, including cough and fever, and in severe cases, respiratory issues with difficulty in breathing.¹ However, the infection by SARS-CoV-2 can be asymptomatic. Some studies indicated that more than half of the people that tested positive for the SARS-CoV-2 were asymptomatic, but still carried a high viral load even before the development of the symptoms, differently from infections caused by SARS-CoV.⁴ Due to the silence transmission of the virus by asymptomatic patient, symptom-

based screening failed to detect a high proportion of the infected cases and COVID-19 spread unnoticedly. The number of confirmed cases and deaths provided by WHO is underestimated since many asymptomatic people were not tested for COVID-19.

The screening of COVID-19 has been based on the Polymerase Chain Reaction (PCR) testing, which is considered the gold standard for diagnosing infectious agent. Once the genetic sequence of the infectious agent is elucidated, primers (an essential component for the functioning of the PCR) can be produced for the PCR tests. The first quantitative reverse-transcriptase-based PCR (RT-PCR) tests for SARS-CoV-2 were designed and distributed in January 2020 by the WHO. RT-PCR protocols are complex and expensive, mainly suited to centralized diagnostic laboratories. The test takes 4 to 6 h for the results, but due to logistical requirement to ship the samples, the turnaround time can be up to 24 h. In Brazil, less than 150,000 tests for COVID-19 were performed by April 2020, which, considering the population of 210 million people, represents the proportion of 0.63 (or 63 tests per 100,000 inhabitants).⁵ By the time, other countries performed more tests, such as Argentina (0.76), Chile (6.43), United States (12.08), Germany (23.64), Iceland (127.58).⁶ The bottleneck to perform the tests by the health care system in many countries, including Brazil, is attributed to the lack of resources such as clinical laboratories, equipment, and specialized professionals. In Brazil, the clinical laboratories were oversaturated with samples to be tested for COVID-19 and the results could take up to weeks to be delivered during the highest infection peaks. Unfortunately, large part of the Brazilian population was unaware if they carried the virus and many deaths could not be confirmed if they were related to SARS-CoV-2.⁵

Some countries and regions that limited the impact of the sudden new respiratory disease were Singapore, Taiwan and Hong Kong. Despite their proximity to China, these regions have managed to hold the infection and fatalities under control by learning from the previous coronavirus (SARS-CoV) outbreak in 2003. The rapid response for the imminent outbreak of the new coronavirus prevented the exponential growth in the number of infected people and deaths. These regions quickly deployed several actions to fight against the spread of SARS-CoV-2, such as strict quarantine in suspect cases and widespread testing combined with digital surveillance to trace individual's movement.⁷ Symptomatic people were quickly tested for the disease then socially isolated, and by contact tracing, the health agencies were able to test possible new sources of transmission including the asymptomatic people. Although these regions are comparably smaller in area and population, which facilitate the management of a pandemic, it demonstrates the positive impact of widespread diagnosing in the fight against COVID-19.

In countries in development, the widespread testing would be facilitated with the employment of POC tests, which would take some of the workload off the clinical laboratories and more people could be tested for the disease. When coupled with digital surveillance, the density of the cases can be mapped and preventive campaigns and assistance can be better addressed. Some of the home-testing POC for COVID-19 consist of immunoassay, which is detailed under the chemical aspect further in this *Chapter*. Immunoassays are based on the antibody-antigen recognition and can either detect the pathogen or the antibodies produced by the patient's immune system (IgG, IgM, IgA, etc). Immunoassays are easier to use compared to PCR and deliver the results in 20-60 minutes, however they are less accurate.⁷ The first immunoassays for COVID-19 were based on the detection of IgG and IgM, therefore they only provided historic information about the viral exposure. If the patient has already been exposed to the virus, meaning that their immune system previously produced the antibodies against the SARS-CoV-2, the result will be positive regardless of the infection status at the moment of the test. Also, IgM and IgG take respectively from 3 to 6 days and up to 8 days to be produced, therefore initial state of the infection cannot be detected with this device. Later, immunoassays for antigen detection were developed, in which the virus itself is detected by the antibodies on the device. For the antigen detection, the immunoassays provided fast results at lower costs in comparison to PCR. However, immunoassays are typically less sensitive, not being able to detect low viral loads in infected patients. Although immunoassays are easily mass produced, there are still some concerns on the recognition elements applied in these tests because of the inherent variability of antibody response.

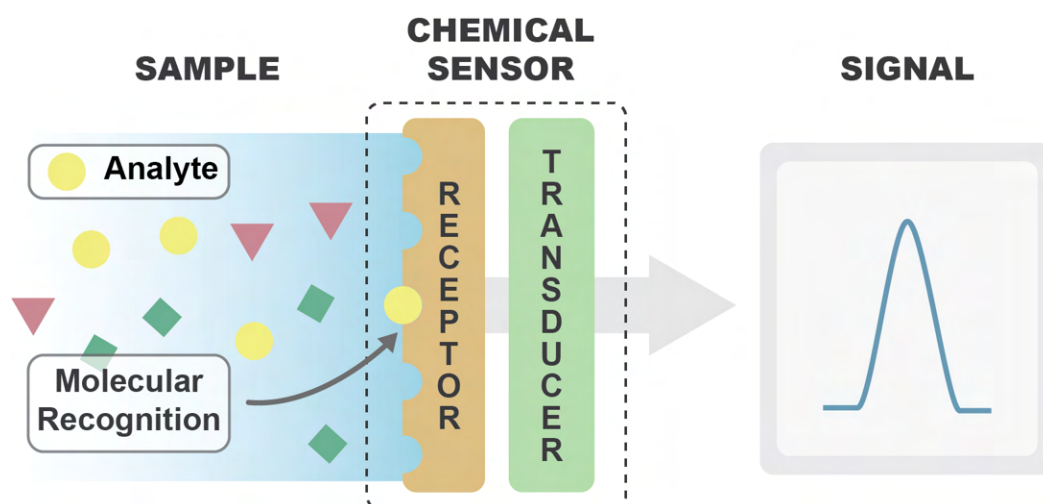
It is evident that, with a widespread testing, the fight against COVID-19 would be more efficient since large part of the transmission of the virus is carried by asymptomatic people. Unfortunately, the PCR was not ideal to restrain the spread of the disease in many countries, especially for those under development, like Brazil, at the beginning of the pandemic. Alongside with the production of vaccines, more efficient and faster diagnosis for the COVID-19 were heavily developed by several biotechnology companies and research centers, which helped to restrain the pandemic.⁷ Science progressed fast and the scientific community profusely investigated the new coronavirus, publishing new findings on daily basis, which contributed to fight COVID-19. The fast response of the scientific community on investigating the new coronavirus and on developing new technologies has contributed to fight COVID-19, proving that investments in science and technology are crucial to critical events.

I.2. CHEMICAL SENSORS AND BIOSENSORS

I.2.1. Chemical sensors

Chemical sensors are defined as devices that acquire analytical signal from a sample by analyzing the chemical information originated from a physical property of the system or a chemical (or biochemical) reaction of the analyte.⁸ The chemical sensor is constituted by two parts: the receptor and the transducer, as illustrated in Figure I.2. The receptor component is responsible for recognizing the analyte and transforming the chemical information into a form of energy analyzed by the transducer. Then the transducer transforms the energy carrying the chemical information into a useful analytical signal.⁸⁻¹⁰

Figure I.2 - Fundamentals of a chemical sensor with a receptor, which recognize the analyte, and a transducer, which convert the chemical information into a measurable signal.



Source: Own authorship.

The transduction techniques can be mainly divided in chemical and physical transduction. Chemical transduction relies on the change in the chemical composition, such as the concentration of the analyte or of the product that forms after the recognition process. If the analyte or its products are not detectable, signaling labels can be used. Label is a simple molecule or a nanostructure that can be detected in function of the analyte concentration. In a physical transduction, the signal is based on a specific physical property of the sensing element that is affected by its interaction with the analyte. Changes in mass, dielectric properties or electrical resistivity can be measured and correlated to the concentration of the analyte. Physical transductions are as a rule label-free methods.⁹

The operating principles of a transducer can be classified as:

- a) *Optical* sensors transform the change of optical property into a useful signal, such as absorbance, reflectance, luminescence, fluorescence, refractive index, or light scattering. The optical transduction can be achieved by the interaction of the receptor with the analyte or by the label species.^{8,9}
- b) *Electrochemical* sensors are based on transport, distribution, and reactivity (electron transfer reactions) of the analytes at the solution-electrode interface. In a potentiometric transduction, the potential of an indicator electrode is measured against a reference electrode. In an amperometry detection, the current generated by the interaction of the analyte with the electrode is measured. Transducers based on electrochemical impedance measures the opposition to the flow of an alternating current through the electrochemical cell and provides information about the physicochemical processes of the analyte interacting with the receptor.^{8,9}
- c) *Electrical* sensors measure the change in the electrical properties cause by the interaction of the analyte without any occurrence of an electrochemical process. The interaction of the analyte with the receptor can affect the electrical resistivity or the dielectric constant, known as resistive and capacitive transduction respectively.^{8,9}
- d) *Mass sensitive* sensors are known for applying mass crystal microbalance, which is based on a vibrating piezoelectric crystal. The accumulation of the analyte on the support material (receptor) causes a change in the mass, affecting the vibration frequency measured by the transducer.^{8,9}
- e) *Magnetic* sensors are commonly used for oxygen monitors by analyzing the paramagnetic properties of a gas.^{8,9}
- f) *Thermometric* sensors are based on the thermal effect of the recognition process of the analyte by the receptor, resulting in a change of temperature. The recognition process can be a specific chemical reaction such as enzymatic reaction or adsorption.^{8,9}

Concerning the reception process, there are several methods of recognition of the analyte by the receptor. The extension of this interaction is defined by the affinity of the receptor for the analyte. Higher affinity is preferred to guarantee the recognition process of the analyte in a complex sample. Another important characteristic of the recognition process is the selectivity of the receptor, which is the ability of the sensor to respond preferentially to the analyte over other species that may be present in the sample acting as an interferent.⁹

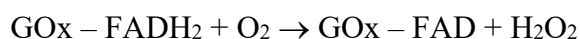
The mechanism of recognition of the analyte by the receptor may be based upon different principles: physical, chemical, and biochemical. In the physical recognition, there is not a chemical reaction. It is based on the measurements of physical properties of the analyte, such as absorbance, conductivity, refractive index, temperature, or mass change. The chemical receptor recognizes the analyte through a chemical reaction that results in the analytical signal. Best known chemical sensor is the pHmeter, firstly designed by Dr. A. O. Beckman in 1934.¹¹ The pH measurement is based on a glass electrode (receptor), which is selective to hydrogen ions. The difference in the concentration of the hydrogen ions between the test solution and the solution inside the glass electrode translate to a potential difference (potentiometric transduction), which is measured by a voltmeter.¹² Sensors with physical and chemical recognition processes usually lack on selectivity of chemical species, which are required in clinical analysis. The use of biochemical recognition on sensors improves the specificity of the detection method due to the high affinity interactions encountered in biological and biochemical processes. Sensors that utilize biochemical recognition (bioreceptor) are known as biosensors.

I.2.2. Biosensors

Biosensors are sensors with a biochemical receptor, also known as bioreceptor. The bioreceptor recognizes the analyte through a biochemical process that results in the analytical signal. The field of biosensors was founded by Leland C. Clark Jr, considered as the “Father of Biosensor”.¹³ The first biosensor was reported by him and Lyons in 1962 for glucose measurement.¹⁴ The glucose biosensor evolved from Clark’s previous work on oxygen electrode, which was calibrated by adding glucose and the enzyme glucose oxidase (GOx) to deoxygenate the test solutions.¹³ Glucose oxidase requires the flavin adenine dinucleotide (FAD), a redox cofactor, to oxidize the glucose to glucolactone, as the reaction below:¹⁵



Subsequently, the cofactor regenerates to the former oxidation state by reacting with oxygen (O₂) present in the enzyme environment and producing hydrogen peroxide (H₂O₂):¹⁵



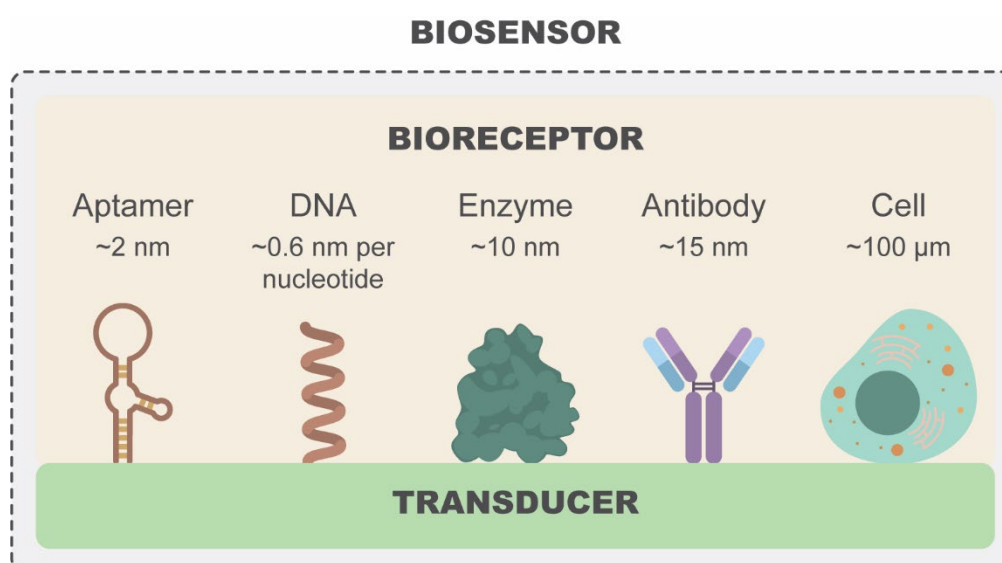
Eventually Clark realized that the calibration procedure could also work to detect glucose itself. He developed the first prototype by immobilizing the enzyme on his oxygen electrode and monitored the oxygen signal. The decrease in the signal was proportional to the increase of glucose concentration in the solution. Further glucose sensors were developed to monitor the oxidation of peroxide instead of oxygen consumption (more details on glucose

sensor in the next section).^{14,15} With the development of electronics and miniaturization (discussed in *CHAPTER III* and *CHAPTER IV*), hand-held glucose meters for self-monitoring of blood glucose have been substituted by wearable devices for continuous glucose monitoring and without the need of puncture.

I.2.2.1. Biosensing elements

In a biosensor, the bioreceptor carries a specific group reaction or binds to a particular group of compounds through biochemical processes. The bioreceptor can be attached near to or onto the transducer surface by several approaches depending on the nature of the bioreceptor and the analyte to be detected, and on the surface chemistry. The immobilization of bioreceptors can be achieved by different mechanisms: adsorption, physical entrapment, covalent coupling and bioaffinity.¹⁶ The immobilization mechanism will be discussed in more details in *CHAPTER II* more specifically on paper substrate. The bioreceptor are classified in catalytic and affinity types. Catalytic biochemical reactions are mediated by enzyme, as described for the glucose biosensor, microbes, organelles, cells, or tissues. Affinity bioreceptors include antibodies, receptors, and nucleic acids.^{9,17,18} The characteristics, as well as the advantages and disadvantages, of the most used bioreceptors, illustrated in Figure I.3, are described as follows.

Figure I.3 - Commonly used bioreceptor in a biosensor: aptamer, DNA, enzyme, antibody and cell. Representation out of scale.



Source: Own authorship.

Recognition by enzymes

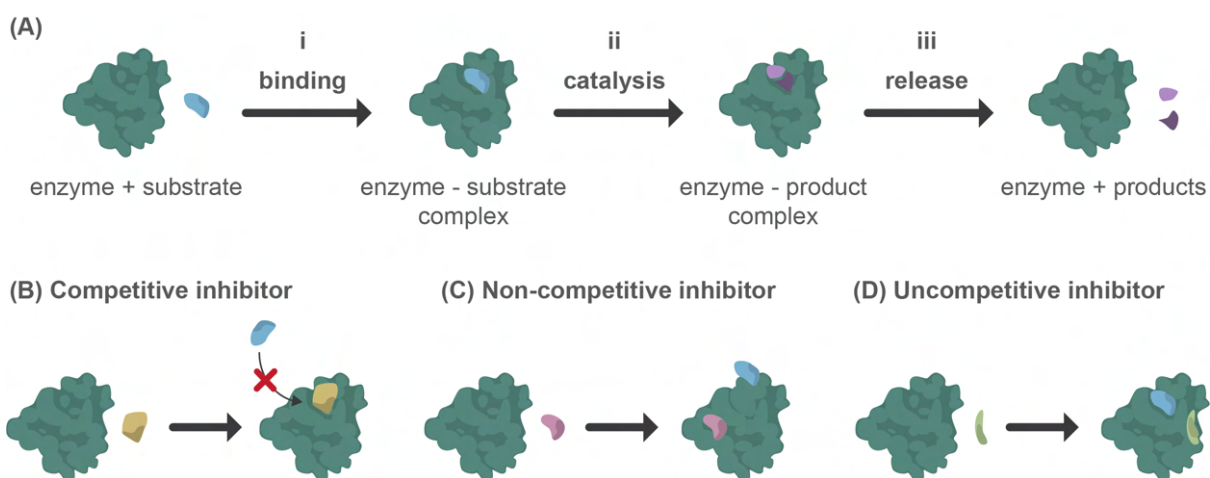
Enzyme-based sensors have been widely developed and commercially applied for medical applications. The most successful commercial enzymatic biosensor is the glucose biosensor, firstly introduced in the market in 1973 by Yellow Springs Instrument based on Clark's first glucose biosensor.^{15,19} Glucose is an important health biomarker specially for those diagnosed with diabetes, which is a metabolic disorder.¹⁹ According to the WHO, diabetes is one of the leading causes of death in the world and about 422 million people worldwide have this endocrine disease.²⁰ Assessment of the glucose level is an important tool for the management and therapy of the disease, which is achieved by the glucose biosensors. The glucose biosensor accounted for approximately 85% of the world market for biosensors in 2004, which had been estimated to be around \$5 billion USD.¹⁹

Enzymes are proteins that function as catalysts in biochemical reactions with selectivity. The enzymatic recognition of a compound (enzyme substrate) is a dynamic process involving three steps, as shown in Figure I.4.⁹ Considering the glucose oxidase as an example, the first step consists of the binding of the glucose (substrate) on the active site of the glucose oxidase (enzyme) to form a substrate-enzyme complex. Then, the substrate undergoes a chemical reaction catalyzed by the enzyme with contribution of other species such as cofactors and accompanied by the consumption or generation of compounds like O₂, CO₂, H₂O₂, NH₃, and H⁺.^{9,21} In this example, the chemical reaction is the oxidation of the glucose to glucoactone by the GOx assisted by the cofactor FAD⁺ with consumption of O₂ and production of H₂O₂. Finally, the product (glucoactone) is released by the enzyme and the enzyme returns to its initial state, ready to catalyze the next substrate.⁹ Besides GOx, commonly used enzymes as recognition element in a biosensor are horseradish peroxidase and alkaline phosphatase.²¹

The enzymes activity is susceptible of inhibition by the bonding of small molecules and ions. Irreversible inhibitor slowly dissociates from the enzyme because it binds strongly covalently or non-covalently to the enzyme. Reversible inhibitor, on the other hand, dissociates quickly from the enzyme due to weaker binding strength. Competitive inhibitors present a chemical structure similar to the substrate and bind to the enzyme's active site, blocking the substrate (Figure I.4B). This kind of inhibition slows the kinetics by reducing the available enzymes to catalyze the substrate. The competitive inhibitor effect is annulated by a large amount of substrate; in this case, the substrate can successfully compete for the active sites. Unlike the competitive inhibitors, non-competitive inhibitors bind to a different site of the enzyme (Figure I.4C). This inhibitor decreases the number of functional enzymes, slowing the

kinetics. Finally, the uncompetitive inhibitor only binds to the enzyme-substrate complex (Figure I.4D). In fact, the binding site of the uncompetitive inhibitor is created after the substrate binds to the enzyme. The complex enzyme-substrate-inhibitor is incapable to proceed the catalysis reaction on the substrate.²² Inhibitors can be applied in enzymatic assays to modulate the kinetics for sensing applications, as will be shown in *CHAPTER III*.

Figure I.4 - Enzyme structure and the interaction with substrate: (i) Interaction between the enzyme and its substrate, forming the enzyme-substrate complex; (ii) Catalysis of the substrate to products, forming the enzyme-product complex; (iii) Release of the products and regeneration of the enzyme for new cycle. Types of enzymatic inhibition: (B) Competitive, (C) non-competitive, and (D) uncompetitive inhibitor.



Source: Own authorship.

The main advantage of the enzyme-based recognition in a biosensor is the continuous measurement since the enzyme remains unaltered after the reaction with its substrate. The isolation and purification of enzymes are simple and, with genetic engineering, the binding sites can be modified to be applied for a wide range of analytes. However, enzyme activity is highly dependent on the pH, ionic strength and temperature of its environment, which can limit its application.^{17,21}

Recognition by microbes, organelles, cells and tissues

Instead of using isolated enzymes, whole biological materials such as microbes, organelles, cells and tissues can be incorporated in the sensor as biosensing element. Using whole biological structures are easier and cheaper than the enzymes since the purification step is not necessary, and the enzymes perform better in their natural environment, which can result in higher efficient.⁹ However, these complex structures are still sensitive to their environment, and harsh physical and chemical conditions should be avoided as well. Due to its sensitivity to the

surrounding environment, cells have been used to monitor treatment effects of drugs and to detect global parameter like stress conditions, toxicity, and organic derivatives.¹⁷ The complex structure found in microbes, organelles, cells and tissues results in a broader and convoluted response, hard to discriminate individual effect from different chemical stimuli of the environment. Therefore, specificity is hard to be achieved with this recognition process.

Recognition by antibodies

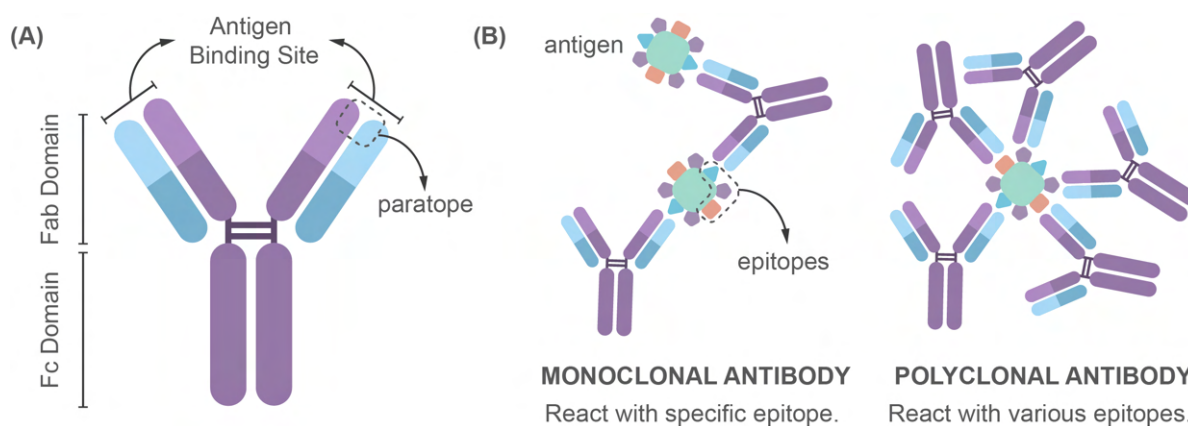
Antibodies are glycoproteins found in plasma and other extracellular fluids that are used by the immune system to neutralize and/or eliminate molecules and organisms, called antigen.²³ Because of the high affinity and specificity of the complex antibody-antigen, antibodies have been widely applied in diagnostic assays and as therapeutic reagents. Antibodies are produced for medical and research application by stimulating the immune system of animals, usually mice, rabbits, sheep and goats. The B-lymphocytes respond to the antigenic stimulation and secrete antibodies with specific binding domains for the antigen. Then the antibodies are extracted from the blood.^{9,17}

The antibodies are often illustrated as a Y-shaped molecule (Figure I.5). The two arms of the antibody contain the antigen-binding domains (Fab), which recognize the antigen, and the base (Fc), which is responsible for modulating other biological functions of the cell. For research and medical application, the antigen interaction draws most of the interest. Each Fab contains a region, known as paratope, that specifically binds to one particular region of the antigen, known as epitope. The paratope from the antibody and epitope from the antigen present complementary shapes and chemical reactivities to form the association complex with high specificity.⁹ The recognition of an antigen epitope by the paratope of an antibody occurs through affinity interactions, which involve multiple non-covalent bonds, such as ionic bond, hydrogen bond, and van der Waals interaction.

Antibodies are classified as polyclonal and monoclonal, depending on the response of multiple or a single clone lymphocyte.²³ Because an antigen can present numerous epitopes, several lymphocytes can recognize each one of epitopes and produces a polyclonal antibody response. Therefore, polyclonal antibodies are heterogeneous and can differ among immunized animals with different response over time. Meanwhile, monoclonal antibodies are produced by a single lymphocyte clone, resulting in a homogenous and consistent antibody.²³ However, the specificity of monoclonal antibody limit their use since a small structural change of the epitope can affect the performance of the antibody in recognizing the antigen. Also, monoclonal antibodies are more sensitive to pH and salt concentration. Monoclonal antibodies are useful in

evaluating changes in the molecular conformation, protein-protein interactions, and in identifying single member of protein families.²³ Polyclonal antibodies frequently have better specificity than monoclonal antibodies because they can recognize more epitopes, and are frequently used in quantitative and qualitative assays. Biosensors with antibodies are known as immunosensors and apply the highly selective antigen-antibody reaction for the recognition.²¹

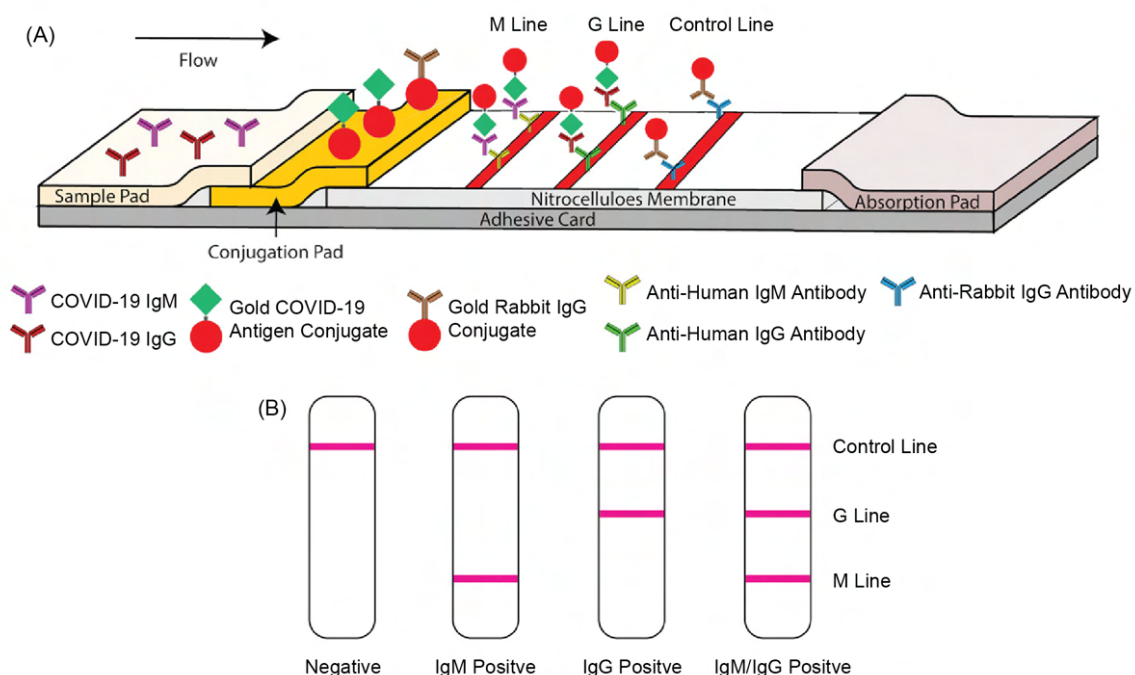
Figure I.5 - (A) Antibody structure: Fc domain, Fab domain and antigen binding site. (B) Difference of monoclonal and polyclonal antibodies interaction with antigen.



Source: Own authorship.

Immunoreactions are widely applied for infectious disease diagnosis, such as for human immunodeficiency virus (HIV) and most recently for SARS-CoV-2.^{9,24,25} The diagnosis of an infection is usually based on the detection of antibodies produced in the human body to fight against the virus. After the infection by SARS-CoV-2, the immune system produces the antibodies at detectable levels after 3 to 6 days for IgM and 8 days for IgG. The immunosensor is based on lateral flow assay (LFA) technology employing two antibodies. These antibodies are against the human IgG and IgM (anti-human IgG and anti-human IgM antibodies) and are immobilized on a nitrocellulose strip in two testing lines, as shown in Figure I.6. A recombinant protein of the SARS-CoV-2 was labeled with gold nanoparticles and deposited upstream the test lines. With the application of the blood or serum infected by the virus, the IgG and IgM interact with its antigen recombinant protein, forming a labeled complex. The complex flows through the strip by capillary action. When reach the test lines, the IgG and IgM now in the form of labeled complex interact with the immobilized anti-human antibodies and are captured in the strip, resulting in a red line.²⁵

Figure I.6 - Lateral flow assay for detection of COVID-19 human IgG and IgM. (A) Scheme of the detection device. (B) Illustration of the results of the test: negative, IgM positive, IgG positive, and IgM and IgG Positive.



Source: Reprinted with permission from Li *et al.* Journal of Medical Virology, 92, 9, 1518-1524 © 2020 The Authors. Journal of Medical Virology Published by Wiley Periodicals, Inc. DOI:10.1002/jmv.25727.²⁵

Another commercial immunoassay is home pregnancy testing. Pregnancy tests are also based on lateral flow technology employing two antibodies specific for human chorionic gonadotrophin (hCG), a hormone which concentration rises rapidly days after the conception. One of the antibodies is immobilized on a nitrocellulose test strip (test line). The second antibody is labeled with colored marker, usually gold or latex nanoparticles, and it is placed freely upstream of the test line. When a positive sample (urine) is applied on the strip, the hCG reacts with the labeled antibody and the formed complex flows by capillary action along the strip. When it reaches the testing zone, the complex is captured by the immobilized antibody on the strip by the reaction with its antigen, resulting in a colored line on the strip.²⁶

Despite the success of several immunoreaction-based devices, there are some limitations for antibody-based sensors. As for enzymes, the binding strength of an antibody is strongly affected by pH, ionic concentration and temperature. The typical high affinity of antibody toward its antigen results in highly specific detection, however it can also result in irreversible interaction, which translates to a one-measurement sensor.¹⁷

Recognition by nucleic acids

Nucleic acids are composed by four nucleobases namely adenine (A), cytosine (C), guanine (G) and thymine (T) for DNA, and uracil (U) replacing thymine for RNA. The nucleobases interact specifically with each other by hydrogen bonds forming distinct pairs: G-C, A-T or A-U. Through this pairing, two nucleic acid strands associate with each other forming the double-strand complex in a process called hybridization.⁹ A sensor with a short nucleic acid sequence as receptor is known as genosensor and it detects the complementary sequence by the hybridization process. The complexed strands can be denatured to reverse binding and regenerated to be reused.²¹ Genosensors are applied in clinical diagnosis to detect genetic anomalies and diagnose pathogen microorganisms, however, their limitation relies on the small DNA amount in samples. These sensors usually require an amplification step beforehand such as polymerase chain reaction (PCR) to achieve a readable amount of the target nucleic acid sequence.

Recognition by aptamers

Aptamers are synthetic nucleic acid molecules engineered through a process known as SELEX (Systematic Evolution of Ligands by EXponential enrichment).^{27,28} In this process, aptamers can be designed to associate with a variety of target molecules, from small molecules hard to be recognized by antibodies to full microorganisms such as a virus.²⁹ Unlike the genosensors, the biosensors with aptamers recognize the target molecule through affinity reactions rather than hybridization. The single stranded DNA or RNA sequence folds into a variety of secondary structural elements, and its conformational shape functions as a pocket to bind the target molecule. Since they are composed of nucleotides, aptamers can be regenerated to the unbound state by denaturation induced by heat or light, allowing the reuse of the biosensor if desired. Aptamers are often compared to antibodies due to the similar affinity mechanisms and high specificity for their targets. However, aptamers productions are significantly easier and cheaper than the production of antibodies.²⁹ Also, aptamers are 10 to 100 times smaller (usually from 20 to 60 nucleotides) than antibodies therefore can be more densely immobilized on the substrate, enhancing the binding sites for the target molecule.²⁷ Compared to immunosensors, aptamer-based sensors are recent and there is limited knowledge on the structural and biochemical mechanism of the aptamer-target interaction.^{28,29}

I.2.3. Characteristics of a biosensor and analytical figures of merit

In analytical chemistry, method validation is crucial to prove that the results obtained by the analytical procedure is statistically close to the real value from the target analyte. As an analytical device, sensors and biosensors performance can be evaluated by parameters used to characterize an analytical method. Main analytical parameters are given by the analytical calibration relationship between the analyte concentration (x) and the analytical signals (y):

$$y = a + b x \quad \text{Eq I-1}$$

where a is the intercept and b is the slope.

Sensitivity

Sensitivity is defined as the slope (b) of the analytical calibration curve. A sensitive biosensor gives a large change in the signal with small change in the analyte concentration, *i.e.*, large slope.³⁰

Detection and Quantification Capabilities

Limit of detection (LOD) has been calculated in different ways in literature, but the general concept is defined as the lowest concentration of the analyte that can be statistically distinguished from the absence of the substance (blank).^{9,30} The recommended calculation of LOD by IUPAC is based on the statistical theory of hypothesis testing.³⁰⁻³² According to the IUPAC, the smallest measure y_L that can be determined with reasonable certainty is given by the equation:

$$y_L = y_b + k S_b \quad \text{Eq I-2}$$

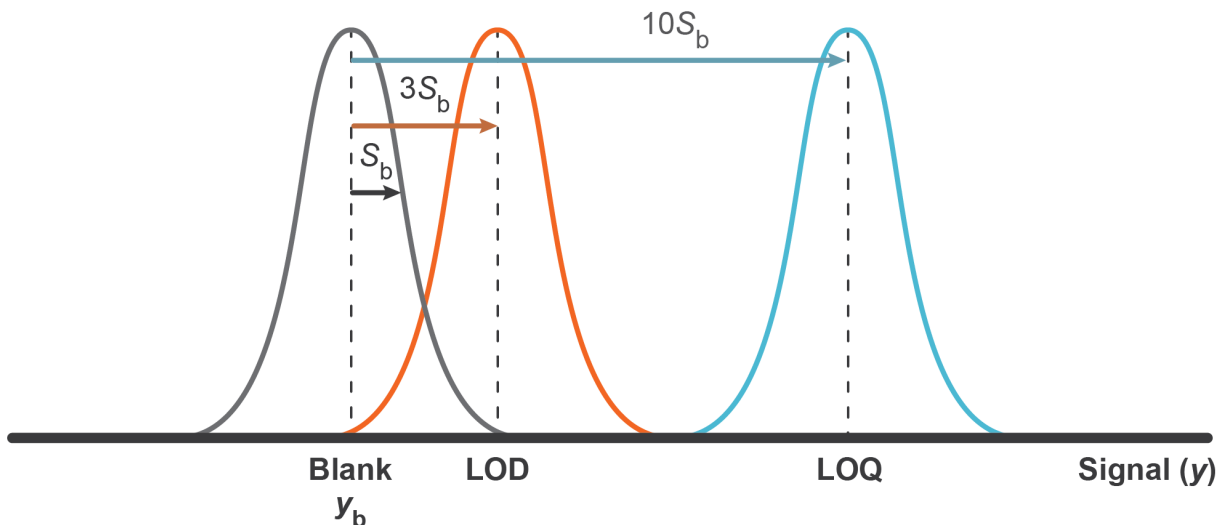
where y_b is the mean of blank measurements, S_b is the standard deviation of the blank measurements, and k is a numerical factor chosen according to the confidence level desired.³¹ The recommended value for k is 3 for LOD, which implies that there is less than 5% of probability of a signal being higher than $3S_b$, as illustrated in Figure I.7.^{9,32} LOD is a function of y_L according to the analytical calibration relationship:

$$y_L = b \text{ LOD} + y_b \Rightarrow \text{LOD} = (y_L - y_b)/b \quad \text{Eq I-3}$$

Because the measurements of the blank do not always equal to zero, the signal must be corrected for the background ($y_L - y_b$). The LOD then can be calculated as:

$$\text{LOD} = 3 S_b / b \quad \text{Eq I-4}$$

Figure I.7 - Definition of limit of detection (LOD) and limit of quantification (LOQ). The curves represent the Gaussian distribution of errors.



Source: Own authorship.

As demonstrated by the equation, the LOD depends on the blank response and its standard deviation, which represents the noise of the system. By the Eq I – 4, a low LOD is obtained when the blank response and the noise are very low. But in practice, the detectability also relies on the ability of the sensor to detect the target analyte. Blank fluctuations, which may arise from the transduction and electronic components of the system, deteriorate the detectability of the sensor.⁹ If the LOD of a method is poor, there is a possibility of the sensor reporting the absence of the analyte when it is in fact present in the sample. These false-negative results may have an impact on decision making ability in health care area. A more reliable analytical result can be obtained by limit of quantification (LOQ), which corresponds to a signal that differs from the blank average by $10S_b$ ($k = 10$).⁹ At this range, the analyte signal is not interfered by the blank fluctuations, as illustrated in Figure I.7. The LOQ can be calculated as:

$$LOQ = 10 S_b / b \quad Eq I-5$$

Although the IUPAC method is widely applied due to its statistical simplicity, the resulting LOD can be too small to be detected by the calibration curve since, in this calculation, it depends on the standard deviation of the blank measurements, which often are very low.³³ Miller and Miller statistical calculation can provide more accurate LOD than the IUPAC.³⁴ The equation is similar to the Eq I – 2. y_b can be replaced by the intercept of the calibration curve (a), S_b by the random errors in y -direction, calculated as:

$$S_{y/x} = \sqrt{\sum_i (y_i - \hat{y}_i)^2 / n - 2} \quad \text{Eq I-6}$$

where y_i is the analytical signal for each concentration x , \hat{y}_i is the fitted y -value calculated by the linear regression, and n is the number of the points in the calibration curve. The analytical signal from the LOD based on Miller and Miller statistical approach is calculated as:

$$y_{LOD} = a + 3 S_{y/x} \quad \text{Eq I-7}$$

Finally, the LOD is determined by the linear regression of the calibration curve. In this approach, the LOD is independent of the blank measurements since $S_{y/x}$ is obtained directly from the analytical calibration curve.

Selectivity and Specificity

Selectivity is the ability of the biosensor to detect a specific target in a sample containing other molecules. Selectivity is a broad definition for the interaction between the analyte and the receptor. The ultimate selectivity is denominated as specificity, which is typically used for a particular pair of receptor and analyte that interact with each other with high affinity. If another component of the sample interferes in the signal of the analyte by interacting with the bioreceptor, it is known as specific interference. Concomitant effects on other parts of the biosensor are known as nonspecific interference.⁹ Selectivity can be calculated as the ratio of the slopes of the calibration curves of the target analyte and a particular interference.³⁰ A selective sensor detects the analyte with a signal that can be significantly differentiate from the signal resulted by the interference.

The application of biochemical recognition processes enhanced the selectivity of the sensors. An appropriate bioreceptor should be chosen for improved selectivity of the biosensor. Poor selectivity in health care biosensors may result in false-positive measurements, which could potentially jeopardize patients' lives.

Repeatability and reproducibility (reliability)

For a same sample condition, the sensor needs to deliver results that closely agree between successive measurements carried out in the same (repeatability) or different (reproducibility) conditions related to operation, apparatus, laboratories and intervals of time analysis.³⁰ Poor repeatability arises from unwanted modification in the sensing properties during extended exposure to the sample or repeated measurements, resulting in the drift of the calibration parameters. The susceptibility of a sensor to ambient disturbances is defined as stability.³⁵ For commercialization, high reproducibility of the sensors is required since the

performance should not fluctuate significantly in different environment. However, optimal conditions such as storage and working temperature should be stated especially for biosensors and if followed, they should be reproducible.

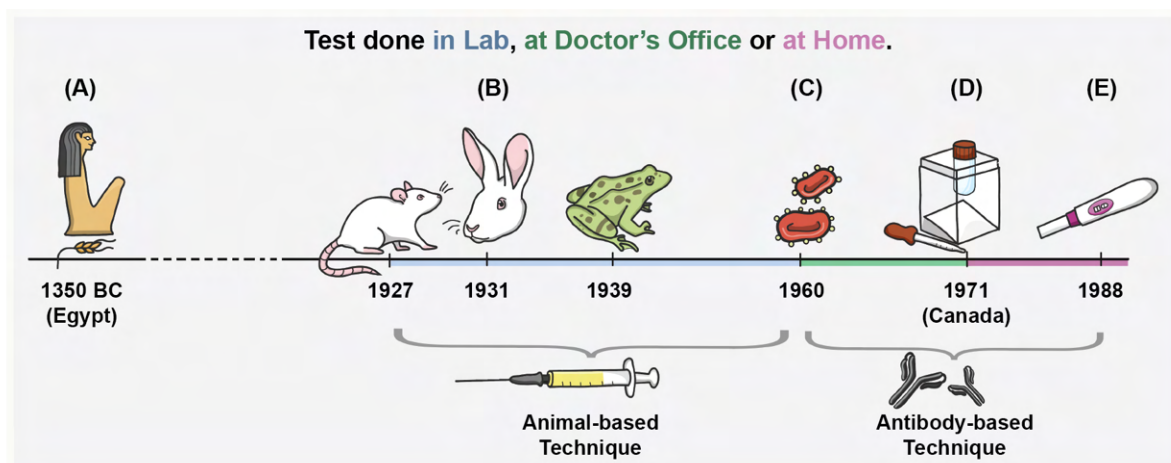
I.3. POINT-OF-CARE TESTING AND MINIATURIZATION

As stated before, laboratory test results are pivotal to critical care decisions. Unlike conventional clinical analysis, point-of-care testing (POCT) offers a rapid turnaround time with fewer processing steps. It eliminates the need for transporting the specimens, avoiding sample degradation and sources of errors caused by pre-analytic (sample preparation and pipetting) and post-analytic procedures. It also minimizes multiple persons handling the sample, with ready-to-use reagents like in disposable cassettes or unit-use devices. Therefore, the diagnosis can be operated outside of a central laboratory and without medical technical qualification.^{36,37} Because of these advantages, POCTs have many applications within the hospital settings, like in intensive care units, operating and recovering rooms, delivery room and neonatal ward, and outside the hospital settings, for example, in sports medicine, outpatient care, home care, forensic drug screening, patient self-monitoring, and by emergency physicians in a military setting or disaster control.³⁷

The first generation of POCT relied on the detection of biomarkers that occur at high levels in biological fluids and with easy detection mechanism based on simple biochemical reactions.³⁸ One of the well-known first-generation POC is the home pregnancy test, which was firstly introduced in the US market in 1977 (Figure I.8).³⁹ The first home pregnancy test consisted of a nine-step procedure executed in a kit similar to a chemistry setup with a test-tube, two droppers, and a plastic tube-holder with a mirror to reveal the results from the bottom of the tube.³⁹ Despite the complex procedure for women without laboratory training, the home testing allowed women for the first time to knowledge the pregnancy in the privacy of their bathroom without the need of visiting a doctor's office. Previously, pregnancy was identified by many procedures dating from the ancient Egyptian Age, when women urinated on barley or wheat seeds, and their sprouting was confirmed as a positive case.³⁹ Since then, it was known that the urine properties are different during the pregnancy, which in early 1920 was attributed to the presence of hormones, more specifically to the human chorionic gonadotropin (hCG) hormone.⁴⁰ The first large scale laboratory testing for pregnancy, known as the Aschheim-Zondek reaction (A-Z test), was introduced in the 1920s and it was based in the women's urine as well.⁴¹ In the A-Z test, the urine was injected into sexually immature female animals (mice,

rabbits, or toads), and in the case of pregnancy, the animals' ovaries would grow and produce eggs.⁴¹

Figure I.8 - Timeline of pregnancy test. From: (A) Ancient pregnancy test, which involved urinating on grain seeds; (B) Animal-based tests, known as A-Z test, in which the urine was injected into an animal; Start of antibody-based techniques with (C) Hemagglutination inhibition test; (D) First at-home pregnancy test; and (E) the first stick test similar to current commercial pregnancy test.



Source: Reprinted with permission of SITN Boston. *Pee is for Pregnant: The history and science of urine-based pregnancy tests*. Available at: <https://sitn.hms.harvard.edu/flash/2018/pee-pregnant-history-science-urine-based-pregnancy-tests/#>.

With the development of polyclonal antibodies in 1960, the first immunoassay for pregnancy testing was introduced and animal sacrifices were no longer required.⁴⁰ Compared to bioassays, the immunoassays are more cost-effective and deliver results in a couple of hours. However, the immunoassay, which was based on a hemagglutination inhibition test, was still primarily performed in the doctor's office, where the woman's urine was sampled and tested in a tube.³⁹ Subsequently, with efforts from pharmaceutical companies, the laboratory setup was transferred into the first usable, portable test for home use. In addition to the laborious protocol, the first home pregnancy test resulted in many false-positives because it utilized polyclonal antibody, which was not specific enough to the hCG. The polyclonal antibody also recognized the luteinizing hormone (LH), which is naturally present in the urine during the ovulation phase. Since the proteins hCG and LH have identical alpha subunits, the polyclonal antibody is not capable to distinguish the hormones, resulting in many false-positives.⁴² In 1973, the biologic specificity of hCG was found in the beta subunit of the protein.⁴² With the discovery of monoclonal antibodies in 1975,⁴³ these findings led to the development of the immunoassays technology still used in the current commercial pregnancy test strips, firstly introduced in 1988.²⁶ The test only requires one step, which is peeing in the stick, and it is extremely accurate.

Modern women can confirm pregnancy at the early stages even before noticing physical changes in their body, like weight gain or abdominal movements, as it was done back in the 1950s. The home pregnancy testing, though not even half-century old, not only symbolizes the progress in the field of POC testing but also allowed women to assume control of knowledge that had been previously in the hands of doctors. Later on, other diagnostic tools were introduced in the market such as blood-sugar testing for diabetes, workplace drug testing, highway blood-alcohol testing, malaria, and HIV testing.

POC diagnostic testing plays an important role in the control of the spread of infectious diseases, especially in low- and middle-income countries. For instance, Zambia is one of the countries with the highest incidences of HIV infection but with only three PCR equipment to diagnose the disease in children.⁴⁴ As consequence, the treatment for the patient is often delayed with poor follow-up and adherence to appropriate therapy, contributing to transmission and mortality increased rates. With the development and application of HIV POC testing, there was an increase in the volume of HIV tests and it has a positive effect on programs to prevent HIV transmission.⁴⁴ However, these POC testing needs to meet the quality assurance to deliver trustable results. Concerning the quality assurance issue, the World Health Organization established the REASSURED criteria, a guideline which the testing is required to attend to. The REASSURED criteria are an acronym for Real-time, Affordable, Sensitive, Specific, User-friendly, Robust and Rapid, Equipment-free, and Deliverable to those who need them.⁴⁵

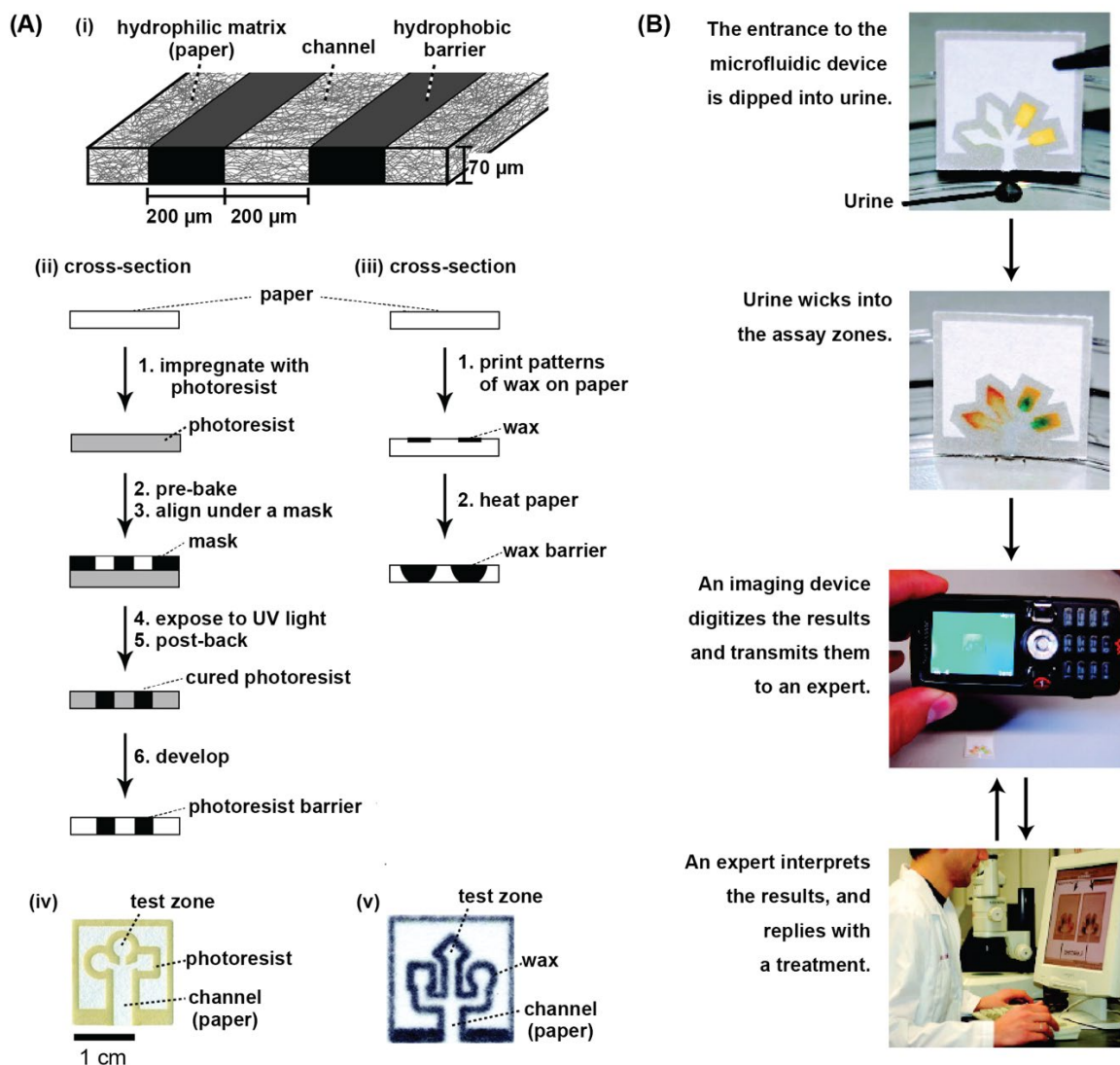
In order to improve the performance and reliability of the POC testing, the sensors have been integrated into microfluidics systems. The more complex systems integrated with microelectronics gave rise to the second generation of POC testing, which can detect less accessible biomarkers, such as nucleic acids and cell-surface markers. Microfluidics started with the concept of manipulating small sample volumes and reagents within a chip.⁴⁶ Microfluidic technology has been developed under the expectation to revolutionize the health care industry by providing simple, inexpensive, effective, and ubiquitous miniaturized diagnostic devices. Although the field has been continuously progressing, significant challenges still exist, and many microfluidic devices cannot reach out of the laboratories and launch to the practical settings. An example is the miniaturization of PCR methods into centrifugal microchips to diagnose infectious diseases. The detection of the pathogen's nucleic acids involves several steps from lysing the pathogen to expose the genetic material, separating the nucleic acid strands from other biological components, amplifying the genetic material, and reading out the answer. Despite the high sensitivity of the method, in practice these on-chip processes are not possible without the support of a bulky and external centrifugal force source

(such as CD player or a rotational support) and optical detectors for signal measurements. Many published microfluidic chips face the same challenges of relying on external components, such as pumps, switches for fluid actuation and detectors for signal reading.

Paper microfluidics is a good example of novel low-cost fluidic manipulation. Pioneered by Whitesides groups at Harvard University, the paper-based microfluidic devices, also known as μ PAD, does not require an external pumping system since the flow is driven by capillary forces. Also, paper is a lightweight, biocompatible low-cost material that can be easily modified for different applications. The first μ PAD introduced by Whitesides group in 2007 consisted of microchannels patterned with photoresist onto chromatography paper.⁴⁷ Another way of patterning the paper is by wax printing, which dispenses the use of organic solvents as for the photolithography.^{48,49} The areas with photoresist or printed with wax are hydrophobic which provides spatial control of the fluids within the area delimited by the lines and walls of the photoresists or wax (Figure I.9). There are several other approaches to micropattern the paper such as by inkjet printing, laser cutting, polydimethyl-siloxane (PDMS) printing, hot embossing, hydrophobic silanization, among others.⁵⁰ The μ PADs were proven to analyze a variety of biomarkers in blood, urine, saliva, tear, and sweat samples. Integrated with mobile phone camera for optical transduction, the μ PADs enabled the first signs of telemedicine for diagnostic testing (Figure I.9B).⁵¹ Telemedicine provides in site diagnostic tests in remote locations and shares the results of the assay with the physicians without their presence at the site of the test.

As technology advances, the future of POC testing will allow the detection of multiple targets (multiplexing), gathering more information about the body. Correlating each physiological and chemical parameter could give a better and deeper understanding of the patient's health condition. The future of POC testing is trending to increasingly smaller devices with simple operation and instrument-free, enabling reliable self-testing, but still connected to the clinics and health care professionals through the internet of things.

Figure I.9 - (A) Micropatterning methods on paper. (i) Schematics of a paper-based microfluidic channel with hydrophobic barriers created by (ii) photolithography and (iii) wax printing. An example of a device fabricated by (iv) photolithography and by (v) wax printing. (B) Integration of μ PAD with mobile phone cameras for performing bioassays in remote locations and for exchanging the results of the tests with off-site technicians.



Source: (A) Reprinted with permission from Martinez *et al.* Anal. Chem. 2010, 82, 1, 3–10 © 2009 American Chemical Society. DOI: 10.1021/ac9013989.⁴⁸ (B) Reprinted with permission from Martinez *et al.* Anal. Chem. 2008, 80, 10, 3699–3707 © 2008, American Chemical Society. DOI: 10.1021/ac800112r.⁵¹

I.4. WEARABLE DEVICES

With the advance of smartphones and other mobile devices technology, wearable devices emerged as a new concept for health care sensors. Wearable devices are characterized as sensors mounted onto to the user's skin on which they detect body signals, analyze, and transmit the information without restricting the user's motion. These devices promote real-time

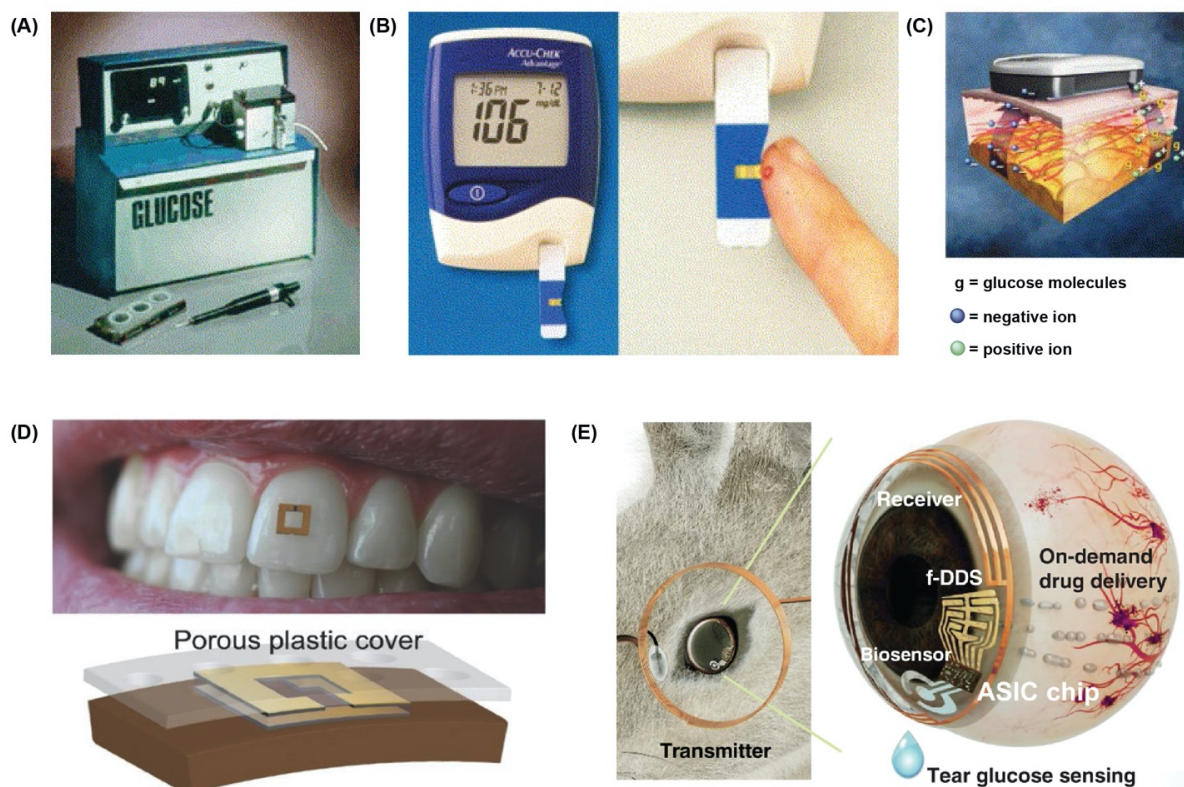
measurement of the signals originated from the body without the need of bulky equipment nor sampling or storage of samples for the results, empowering individual health care.

Early wearable devices focused on mobility, such as steps, burned calories, and walking distance, which are helpful for tracking physical activity performance.⁵² With advances in the field, wearable devices has been proven to monitor vital signs such as heart rate, oxygen levels, temperature, and blood pressure. Motion-based and physical wearable sensors have been commercialized for a while and are heavily used by consumers. However, only few chemical wearable sensors are available on the market since chemicals parameters are relatively more difficult to detect.⁵³ Chemical wearable devices focused on the analysis of body fluids that can be sampled by minimally invasive way such as sweat, saliva, tear, and interstitial fluid. Commonly analyzed biomarkers by wearable devices are metabolites such as glucose, lactate, urea, ethanol, and cortisol, along with other electrolytes such as sodium, potassium, chloride, and ammonium. Trace elements, such as zinc and copper, can also be detected as well.

Technology for detecting glucose has been evolving since first commercial glucose biosensor by Yellow Springs Instrument Company in 1973 (Figure I.10A). With advance in electronic miniaturization, as discussed earlier, the biosensor was miniaturized to a hand-held instrument for home monitoring of glucose (Figure I.10B). Since the detection of glucose was extensively exploited over the decades, glucose wearable devices are so far the most developed and available on the market. The first “real-time” continuous glucose monitoring was launched in 2002 by Cygnus as GlucoWatch (Figure I.10C).⁵⁴ The device was worn as a wristwatch and utilized two gel pads on the skin for the reverse iontophoresis. A cycle of DC potential was applied on the electrodes and stimulated the extraction of the interstitial fluid, in which glucose levels were measured by the enzymatic reaction with glucose oxidase firstly described by Clark. Although the innovative and impressive approach, the GlucoWatch failed commercially. The device required constant calibration with traditional finger-prick methods, failed in readings in the presence of sweat, and caused tingling sensation or skin damage after multiple hours of use.⁵⁴ Since then many improvements were achieved for wearable glucose sensors and some of the wearable glucose devices are already approved by the FDA. Other biomarkers have also been detected by wearable technology.

Glucose was also measured as a food intake parameter by a tooth-mounted device (Figure I.10D).⁵⁵ For this sensor, a conformal radiofrequency sensor was integrated to a permeable hydrogel membrane capable of responding to changes in temperature, pH, and glucose concentration. The sensor can be sensitized to others fluid properties (salinity and alcohol content for example) by functionalizing the biopolymer films or hydrogels.

Figure I.10 - Evolution of glucose sensing: (A) First commercial glucose analyzer based on Clark biosensor by Yellow Springs Instrument Company, (B) hand-held glucose monitor Accu-Chek Advantage by Roche, (C) GlucoWatch by Cygnus Inc operating principles, (D) tooth-mounted glucose sensor, and (E) smart contact lenses for glucose detection in tear.



Source: (A - C) Reprinted with permission from Newman *et al.* Biosens. Bioelectron., 2005, 20, 2435-2453 © 2004 Elsevier B. V. DOI: 10.1016/j.bios.2004.11.012.¹⁹ (D) Reproduced with permission from Tseng *et al.* Adv. Mater, 2018, 30, 1703257 © 2018 WILEY-VCH Verlag GmbH & Co. KGaA, Weinheim. DOI: 10.1002/adma.201703257.⁵⁵ (E) Reproduced with permission from Keum *et al.* Science Advances, 2020, 6, eaba3252 © 2020 The Authors, some rights reserved; exclusive licensee American Association for the Advancement of Science. DOI: 10.1126/sciadv.aba3252.⁵⁶

Glucose levels have been tracked in other fluids like tear by smart contact lenses as shown in Figure I.10E.⁵⁷ Although promising, these devices are not commercially available yet since there is a need to establish correlation of glucose levels in tear and blood. Recently, it has been demonstrated the integration of wireless smart contact lenses for diabetes diagnostic and therapy. The smart contact lenses developed by Do Hee *et al.* not only continually monitor glucose levels in tear but also control drug delivery for treating diabetes retinopathy.⁵⁶ Although only tested in rabbits, this study shows a promising and feasible future for wearable devices, which will be integrated with personalized drug therapy.

I.5. CHALLENGES IN THE FIELD OF MINIATURIZATION AND PORTABLE BIOSENSING DEVICES

Despite the advance in the field, only a few miniaturized and portable biosensors are available in the market as point-of-care tests or continuous sensing devices. Some of the technological gaps in the biosensing field can be found in the analytical procedure, power supply if needed, materials, data acquisition, integration, and interface of many components required for the functioning of the device.⁵⁴ For the portability and easy use for people without any laboratory training, these devices must control the sample introduction and preparation, flow rate, mixing of reagents, reaction time, separation of possible interferents and provide effective and easy to read measurement capability.⁵⁸

Regarding the chemical aspect, the miniaturization of biosensors is challenging because of the small sample volumes of complex biological fluids with femtomolar to millimolar concentrations of the analytes.⁵⁸ Although non-invasive biological fluids, such as tear, saliva, and sweat, have been exploited as sample sources, they are not as reliable as blood, and there is still a need to establish a correlation of the analyte levels between fluids.⁵⁴ Furthermore, the concentrations of the analytes are often diluted in non-invasive biological fluids, demanding higher sensitivity and detectability of the biosensor. The issue can be addressed by coupling a preconcentration technique prior to the analysis or by improving the signal-to-noise ratio of the device. Another challenge in the biosensing field is the selectivity often impaired by the biofluid complex matrix.

In this dissertation, some of these challenges under the chemical scope are addressed by improving bioreceptor immobilization (*CHAPTER II*), device wearability (*CHAPTER III*), and sensitivity (*CHAPTER IV*). Furthermore, in *CHAPTER V*, it is demonstrated the adaptability of the sensing technology for a current global concern: detecting SARS-CoV-2.

I.6. REFERENCES

1. GUAN, W.; NI, Z.; HU, Y.; LIANG, W.; OU, C.; HE, J.; LIU, L.; SHAN, H.; LEI, C.; HUI, D. S. C.; DU, B.; LI, L.; ZENG, G.; YUEN, K.-Y.; CHEN, R.; TANG, C.; WANG, T.; CHEN, P.; XIANG, J.; LI, S.; WANG, J.; LIANG, Z.; PENG, Y.; WEI, L.; LIU, Y.; HU, Y.; PENG, P.; WANG, J.; LIU, J.; CHEN, Z.; LI, G.; ZHENG, Z.; QIU, S.; LUO, J.; YE, C.; ZHU, S.; ZHONG, N. Clinical characteristics of coronavirus disease 2019 in China. **New England Journal of Medicine**, Waltham, v. 382, p. 1708–1720, 2020. DOI:10.1056/NEJMoa2002032.
2. WORLD HEALTH ORGANIZATION. **Who covid-19 dashboard**. Geneva: World Health Organization, 2020. Disponível em: <https://covid19.who.int>. Acesso em: 15 Jan. 2022.
3. WORLD HEALTH ORGANIZATION / EUROPE. **Who announces covid-19 outbreak a pandemic**. Copenhagen: WHO Regional Office for Europe, 2020. Disponível em: <https://www.euro.who.int/en/health-topics/health-emergencies/coronavirus-covid-19/news/news/2020/3/who-announces-covid-19-outbreak-a-pandemic>. Acesso em: 05 abr. 2020.
4. ARONS, M. M.; HATFIELD, K. M.; REDDY, S. C.; KIMBALL, A.; JAMES, A.; JACOBS, J. R.; TAYLOR, J.; SPICER, K.; BARDOSSY, A. C.; OAKLEY, L. P.; TANWAR, S.; DYAL, J. W.; HARNEY, J.; CHISTY, Z.; BELL, J. M.; METHNER, M.; PAUL, P.; CARLSON, C. M.; MCLAUGHLIN, H. P.; THORNBURG, N.; TONG, S.; TAMIN, A.; TAO, Y.; UEHARA, A.; HARCOURT, J.; CLARK, S.; BROSTROM-SMITH, C.; PAGE, L. C.; KAY, M.; LEWIS, J.; MONTGOMERY, P.; STONE, N. D.; CLARK, T. A.; HONEIN, M. A.; DUCHIN, J. S.; JERNIGAN, J. A. Presymptomatic SARS-CoV-2 infections and transmission in a skilled nursing facility. **New England Journal of Medicine**, Waltham, v. 382, p. 2081-2090, 2020. DOI: 10.1056/NEJMoa2008457.
5. MAGENTA, M. Mortes, testes e contágio: como o Brasil se compara a outros países na pandemia de coronavírus. **BBC News Brasil**, Londres. Disponível em: <https://www.bbc.com/portuguese/brasil-52509734>. Acesso em: 05 maio 2020.
6. RITCHIE, H.; MATHIEU, E.; RODÉS-GUIRAO, L.; APPEL, C.; GIATTINO, C.; ORTIZ-OSPINA, E.; HASELL, J.; MACDONALD, B.; BELTEKIAN, D.; ROSER, M. Coronavirus (COVID-19) testing. **Our World in Data**, Oxford. Disponível em: <https://ourworldindata.org/coronavirus-testing>. Acesso em: 05 maio 2020.
7. SHERIDAN, C. Fast, portable tests come online to curb coronavirus pandemic. **Nature Biotechnology**, Berlin, v. 38, p. 515 – 518, 2020. DOI: 10.1038/d41587-020-00010-2.
8. HULANICKI, A.; GLAB, S.; INGMAN, F. Chemical sensors: definitions and classification. **Pure and Applied Chemistry**, Berlin, v. 63, p. 1247–1250, 1991. DOI: 10.1351/pac199163091247.
9. BANICA, F. G. **Chemical sensors and biosensors: fundamentals and applications**. New York: John Wiley, 2012.
10. EGGINS, B. R. **Chemical sensors and biosensors**. New York: John Wiley, 2008.

11. TARBELL, D. S.; TARBELL, A. T. The development of the pH meter. **Journal of Chemical Education**, Washington, v. 57, p. 133, 1980. DOI: 10.1021/ed057p133.
12. KARASTOGIANNI, S.; GIROUSI, S.; SOTIROPOULOS, S. pH: principles and measurement. *In: Encyclopaedia of food and health*. Amsterdam: Elsevier, 2016. p. 333–338.
13. HEINEMAN, W. R.; JENSEN, W. B. LELAND C. CLARK JR. 1918–2005. **Biosensors and Bioelectronics**, Oxford, v. 21, p. 1403–1404, 2006. DOI: 10.1016/j.bios.2005.12.005.
14. CLARK, L. C.; LYONS, C. Electrode systems for continuous monitoring in cardiovascular surgery. **Annals of the New York Academy of Sciences**, Hoboken, v. 102, p. 29–45, 1962. DOI: 10.1111/j.1749-6632.1962.tb13623.x.
15. YOO, E.-H.; LEE, S.-Y. Glucose biosensors: an overview of use in clinical practice. **Sensors**, Basel, v. 10, p. 4558–4576, 2010. DOI: 10.3390/s100504558.
16. NICU, L.; LEIČHLÉ, T. Biosensors and tools for surface functionalization from the macro- to the nanoscale: the way forward. **Journal of Applied Physics**, Melville, v. 104, p. 111101, 2008. DOI: 10.1063/1.2973147.
17. HASAN, A.; NURUNNABI, M.; MORSHED, M.; PAUL, A.; POLINI, A.; KUILA, T.; AL HARIRI, M.; LEE, Y.; JAFFA, A. A. Recent advances in application of biosensors in tissue engineering. **BioMed Research International**, London, v. 2014, p. e307519, 2014. DOI: 10.1155/2014/307519.
18. IUPAC. Biosensor. *In: Compendium of Chemical Terminology*. 2 ed. Oxford: Blackwell Scientific, 1997. DOI: 10.1351/goldbook.B00663. Disponível em: <https://goldbook.iupac.org/terms/view/B00663>. Acesso em: 16 abr. 2020.
19. NEWMAN, J. D.; TURNER, A. P. F. Home blood glucose biosensors: a commercial perspective. **Biosensors and Bioelectronics**, Oxford, v. 20, p. 2435–2453, 2005. DOI: 10.1016/j.bios.2004.11.012.
20. WORLD HEALTH ORGANIZATION. **Global report on diabetes**. Geneva: World Health Organization, 2016. Disponível em: https://apps.who.int/iris/bitstream/handle/10665/204871/9789241565257_eng.pdf;jsessionid=1F9BB7E89ECD35D5574259BDAA3BF273?sequence=1. Acesso em: 21 abr. 2020.
21. PATEL, S.; NANDA, R.; SAHOO, S.; MOHAPATRA, E. Biosensors in health care: the milestones achieved in their development towards lab-on-chip-analysis. **Biochemistry Research International**, London, v. 2016, 2016. DOI: 10.1155/2016/3130469.
22. STRYER, L. **Biochemistry**. 9 ed. New York: W. H. Freeman, 2019. 1296p.
23. LIPMAN, N. S.; JACKSON, L. R.; TRUDEL, L. J.; WEIS-GARCIA, F. Monoclonal versus polyclonal antibodies: distinguishing characteristics, applications, and information resources. **ILAR Journal**, Oxford, v. 46, p. 258–268, 2005. DOI: 10.1093/ilar.46.3.258.

24. GUILLON, G.; YEARWOOD, G.; SNIPES, C.; BOSCHI, D.; REED, M. R. Human anti-HIV IgM detection by the OraQuick Advance® rapid HIV 1/2 antibody test. **PeerJ**, Corte Madera, v. 6, p. e4430, 2018. DOI: 10.7717/peerj.4430.
25. LI, Z.; YI, Y.; LUO, X.; XIONG, N.; LIU, Y.; LI, S.; SUN, R.; WANG, Y.; HU, B.; CHEN, W.; ZHANG, Y.; WANG, J.; HUANG, B.; LIN, Y.; YANG, J.; CAI, W.; WANG, X.; CHENG, J.; CHEN, Z.; SUN, K.; PAN, W.; ZHAN, Z.; CHEN, L.; YE, F. Development and clinical application of a rapid IgM-IgG combined antibody test for SARS-CoV-2 infection diagnosis. **Journal of Medical Virology**, Hoboken, v. 92, p. 1518 – 1524. DOI: 10.1002/jmv.25727.
26. TIPLADY, S. Lateral flow and consumer diagnostics. *In: The Immunoassay Handbook*. Amsterdam: Elsevier, 2013. p. 533–536.
27. LAKHIN, A. V.; TARANTUL, V. Z.; GENING, L. V. Aptamers: problems, solutions and prospects. **Acta Naturae**, Moscow, v. 5, p. 34–43, 2013. PMCID: PMC3890987.
28. SONG, S.; WANG, L.; LI, J.; FAN, C.; ZHAO, J. Aptamer-based biosensors. **TrAC - Trends in Analytical Chemistry**, Oxford, v. 27, p. 108–117, 2008. DOI: 10.1016/j.trac.2007.12.004.
29. BINNING, J. M.; LEUNG, D. W.; AMARASINGHE, G. Aptamers in virology: recent advances and challenges. **Frontiers in Microbiology**, Lausanne, v. 3, 2012. DOI: 10.3389/fmicb.2012.00029.
30. JUSTINO, C. I. L.; ROCHA-SANTOS, T. A.; DUARTE, A. C.; ROCHA-SANTOS, T. A. Review of analytical figures of merit of sensors and biosensors in clinical applications. **TrAC - Trends in Analytical Chemistry**, Oxford, v. 29, p. 1172–1183, 2010. DOI: 10.1016/j.trac.2010.07.008.
31. IUPAC. Limit of detection. *In: Compendium of Chemical Terminology*. 2^{ed}. Oxford: Blackwell, 1997. DOI: 10.1351/goldbook.L03540. Disponível em: <https://goldbook.iupac.org/terms/view/L03540>. Acesso em: 16 abr. 2020.
32. LONG, G. L.; WINEFORDNER, J. D. Limit of detection a closer look at the IUPAC definition. **Analytical Chemistry**, Washington, v. 55, p. 712A-724A, 1983. DOI: 10.1021/ac00258a724.
33. SILVA, O. B. DA; MACHADO, S. A. S. Evaluation of the detection and quantification limits in electroanalysis using two popular methods: application in the case study of paraquat determination. **Analytical Methods**, Cambridge, v. 4, p. 2348–2354, 2012. DOI: 10.1039/C2AY25111F.
34. MILLER, J. N.; MILLER, J. C. **Statistics and chemometrics for analytical chemistry**. Hoboken: Pearson Prentice Hall, 2005. 268p.
35. BHALLA, N.; JOLLY, P.; FORMISANO, N.; ESTRELA, P. Introduction to biosensors. **Essays in Biochemistry**, London, v. 60, p. 1–8, 2016. DOI: 10.1042/EBC20150001.

36. LOUIE, R. F.; TANG, Z.; SHELBY, D. G.; KOST, G. J. Point-of-care testing: millennium technology for critical care. **Laboratory Medicine**, Oxford, v. 31, p. 402–408, 2000. DOI: 10.1309/0Y5F-B7NP-5Y67-GW7T.
37. LUPPA, P.; JUNKER, R. **Point-of-care testing: principles and clinical applications**. Berlin: Springer, 2018.
38. JANI, I. V.; PETER, T. F. How point-of-care testing could drive innovation in global health. **New England Journal of Medicine**, Waltham, v. 368, p. 2319–2324, 2013. DOI: 10.1056/NEJMs1214197.
39. LEAVITT, S. A. A private little revolution: the home pregnancy test in American culture. **Bulletin of the History of Medicine**, Baltimore, v. 80, p. 317–345, 2006. DOI: 10.1353/bhm.2006.0064.
40. COLE, L. A. New discoveries on the biology and detection of human chorionic gonadotropin. **Reproductive Biology and Endocrinology**, London, v. 7, p. 8, 2009. DOI: 10.1186/1477-7827-7-8.
41. OLSZYNKO-GRYN, J. The demand for pregnancy testing: the Aschheim–Zondek reaction, diagnostic versatility, and laboratory services in 1930s Britain. **Studies in History and Philosophy of Biological and Biomedical Sciences**, Amsterdam, v. 47, p. 233–247, 2014. DOI: 10.1016/j.shpsc.2013.12.002.
42. VAITUKAITIS, J. L.; BRAUNSTEIN, G. D.; ROSS, G. T. A radioimmunoassay which specifically measures human chorionic gonadotropin in the presence of human luteinizing hormone. **American Journal of Obstetrics and Gynecology**, New York, v. 113, p. 751–758, 1972. DOI: 10.1016/0002-9378(72)90553-4.
43. KÖHLER, G.; MILSTEIN, C. Continuous cultures of fused cells secreting antibody of predefined specificity. **Nature**, Berlin, v. 256, p. 495–497, 1975. DOI: 10.1038/256495a0.
44. WORLD HEALTH ORGANIZATION. **Low-cost tools for diagnosing and monitoring HIV infection in low-resource settings**. Geneva: World Health Organization, 2012. Disponível em: <https://www.who.int/bulletin/volumes/90/12/12-102780/en/>. Acesso em: 01 jun. 2020.
45. PEELING, R. W.; HOLMES, K. K.; MABEY, D.; RONALD, A. Rapid tests for sexually transmitted infections (STIs): the way forward. **Sexually Transmitted Infections**, London, v. 82, p. v1–v6, 2006. DOI: 10.1136/sti.2006.024265.
46. MAO, X.; JUN HUANG, T. Microfluidic diagnostics for the developing world. **Lab on a Chip**, Cambridge, v. 12, p. 1412–1416, 2012. DOI: 10.1039/C2LC90022J.
47. MARTINEZ, A. W.; PHILLIPS, S. T.; BUTTE, M. J.; WHITESIDES, G. M. Patterned paper as a platform for inexpensive, low-volume, portable bioassays. **Angewandte Chemie**, Weinheim, v. 119, p. 1340–1342, 2007. DOI: 10.1002/ange.200603817.

48. MARTINEZ, A. W.; PHILLIPS, S. T.; WHITESIDES, G. M.; CARRILHO, E. Diagnostics for the developing world: microfluidic paper-based analytical devices. **Analytical Chemistry**, Washington, v. 82, p. 3–10, 2010. DOI: 10.1021/ac9013989.
49. CARRILHO, E.; MARTINEZ, A. W.; WHITESIDES, G. M. Understanding wax printing: a simple micropatterning process for paper-based microfluidics. **Analytical Chemistry**, Washington, v. 81, p. 7091–7095, 2009. DOI: 10.1021/ac901071p.
50. SINGH, A. T.; LANTIGUA, D.; MEKA, A.; TAING, S.; PANDHER, M.; CAMCI-UNAL, G. Paper-based sensors: emerging themes and applications. **Sensors**, Basel, v. 18, p. 2838, 2018. DOI: 10.3390/s18092838.
51. MARTINEZ, A. W.; PHILLIPS, S. T.; CARRILHO, E.; THOMAS, S. W.; SINDI, H.; WHITESIDES, G. M. Simple telemedicine for developing regions: camera phones and paper-based microfluidic devices for real-time, off-site diagnosis. **Analytical Chemistry**, Washington, v. 80, p. 3699–3707, 2008. DOI: 10.1021/ac800112r.
52. KIM, J.; CAMPBELL, A. S.; DE ÁVILA, B. E. F.; WANG, J. Wearable biosensors for healthcare monitoring. **Nature Biotechnology**, Berlin, v. 37, p. 389–406, 2019. DOI: 10.1038/s41587-019-0045-y.
53. LI, G.; WEN, D. Wearable biochemical sensors for human health monitoring: sensing materials and manufacturing technologies. **Journal of Materials Chemistry B**, Cambridge, v. 8, p. 3423–3436, 2020. DOI: 10.1039/C9TB02474C.
54. HEIKENFELD, J.; JAJACK, A.; ROGERS, J.; GUTRUF, P.; TIAN, L.; PAN, T.; LI, R.; KHINE, M.; KIM, J.; WANG, J.; KIM, J. Wearable sensors: modalities, challenges, and prospects. **Lab on a Chip**, Cambridge, v. 18, p. 217–248, 2018. DOI: 10.1039/C7LC00914C.
55. TSENG, P.; NAPIER, B.; GARBARINI, L.; KAPLAN, D. L.; OMENETTO, F. G. Functional, RF-trilayer sensors for tooth-mounted, wireless monitoring of the oral cavity and food consumption. **Advanced Materials**, Weinheim, v. 30, p. 1703257, 2018. DOI: 10.1002/adma.201703257.
56. KEUM, D. H.; KIM, S.-K.; KOO, J.; LEE, G.-H.; JEON, C.; MOK, J. W.; MUN, B. H.; LEE, K. J.; KAMRANI, E.; JOO, C.-K.; SHIN, S.; SIM, J.-Y.; MYUNG, D.; YUN, S. H.; BAO, Z.; HAHN, S. K. Wireless smart contact lens for diabetic diagnosis and therapy. **Science Advances**, Washington, v. 6, p. eaba3252, 2020. DOI: 10.1126/sciadv.aba3252.
57. FARANDOS, N. M.; YETISEN, A. K.; MONTEIRO, M. J.; LOWE, C. R.; YUN, S. H. Contact lens sensors in ocular diagnostics. **Advanced Healthcare Materials**, Hoboken, v. 4, p. 792–810, 2015. DOI: 10.1002/adhm.201400504.
58. GUBALA, V.; HARRIS, L. F.; RICCO, A. J.; TAN, M. X.; WILLIAMS, D. E. Point of care diagnostics: status and future. **Analytical Chemistry**, Washington, v. 84, p. 487–515, 2012. DOI: 10.1021/ac2030199.

CHAPTER II

Oxidative treatment on chromatography paper for bioreceptor immobilization in analytical device

II.1. INTRODUCTION

Paper has been used for analytical purposes since the 1850s firstly for urine test strips, then for chromatography, electrophoresis and pH measurements.¹⁻³ Paper was mainly utilized as strip in which the sample (aqueous solution) wicked along its length and reacted with any chemicals previously deposited in the substrate, such as in lateral flow assays. In 2007, Whitesides's group developed the first microfluidic paper-based analytical devices (μ PADs), which consisted of patterning hydrophobic walls in the paper to manipulate the flow of the sample within the device without external pumping.⁴ Since then, paper has been majorly adopted as substrate for microfluidic analytical platforms.

The development of a biosensor requires the immobilization of the bioreceptor onto the device substrate. This is a crucial step since the molecular recognition of the analyte plays an important role on the final performance of the biosensor. The rate of false-positives is strictly related to the specific recognition of the analyte. Other parameters such as stability, robustness, repeatability and reproducibility are affected by the attachment of the bioreceptor near to or onto the transducer surface since it dictates the stability, attachment, conformation, activity and orientation of the biomolecule. Therefore, it is important to properly evaluate the immobilization of the biomolecule into the analytical device.

The first paper-based biosensor was reported in 1957 for the detection of glucose in urine by impregnating paper strip with glucose oxidase, peroxidase, and orthodoline.⁵ In this work, the enzymes were merely adsorbed in the fibers of the paper. Physical adsorption is a straightforward approach of immobilizing molecules onto the paper. However, due to the weak interactions of van der Waals forces, hydrogen bonding, hydrophobic interactions, and electrostatic forces, the biomolecule is easily washed off the substrate. In fact, many biomolecules desorb from the papers, for example for antibodies the loss is around 40%.⁶ Moreover, the biomolecule is hardly anchored in an oriented way, which affects its ability of recognizing and interacting with the target analyte and results in biosensors with poor sensitivity and reproducibility. Despite that, because of its simplicity, physical adsorption has been reported in many works in the literature for the immobilization of enzymes,^{4,7,8} DNA,⁸ antibodies,⁹ and aptamers^{9,10}.

Biochemical coupling or bioaffinity attachment explores specific biochemical interactions to immobilize biomolecules on paper, for example protein/ligand (streptavidin/biotin), protein/antibody (protein G/human IgG) or metal ion/chelator (Ni^{+2} /His-tag).¹¹ This approach requires the modification of both biomolecule and paper, one of the

binding parts is attached onto the substrate and the other is conjugated or genetically expressed in the biomolecule. By strategically modifying the biomolecule, preferably far from its active site, bioaffinity attachment ensures controlled orientation of the biomolecules and guarantees the retention of the biological activity. To avoid the modification of the cellulose with one of the binding parts, a special protein domain, the cellulose binding domain (CBD), was introduced by genetic engineering. CBDs are naturally found in enzymes that degrades cellulose.¹² Biomolecules can be genetically fused with CBDs and spontaneously bind to cellulose. Although bioaffinity attachment is noncovalent, it is still a strong and specific, allowing for robust biosensors. However, the modifications required for this technique are expensive and time-consuming.¹³

Another approach consists on chemically bonding the biomolecules with the paper through covalent bonds.¹⁴ Chemical coupling results in a uniform and stable adhesion of the biomolecules on the surface of the paper. However, cellulose carries few functional groups for the chemical coupling. Since the hydroxyl groups are negligibly reactive, activation of the cellulose is required to promote a covalent immobilization on the paper.^{14,15} Cellulose are susceptible to oxidation in the presence of different chemicals such as nitrogen oxides, alkali metal nitrites and nitrates, permanganates, peroxides, nitroxyl radicals, and periodate.¹⁶ Periodate (IO_4^-) oxidizes selectively the vicinal hydroxyl groups to aldehyde groups, which are more reactive. The aldehyde group can react with amine groups from biomolecules, forming an imide bond and covalently attaching it to the paper.

Despite the oxidative treatment with IO_4^- is widely described in the literature, the literature lacks on characterization and standardization of this process. Therefore, this chapter describe an in-depth characterization of the physicochemical properties of a chromatography paper after the oxidation with periodate and its performance on protein immobilization.

II.2. AIMS

Oxidize Whatman chromatography paper with sodium periodate (NaIO_4) and characterize the physicochemical properties of the oxidized paper. Evaluate the oxidized paper as substrate for covalent immobilization of proteins. Finally, apply the oxidized paper for protein quantification in urine.

II.3. MATERIALS & METHODS

II.3.1. Oxidation of chromatography paper with sodium periodate

Whatman chromatography paper (CHR #1) was submerged into 25 mL of supersaturated NaIO₄ solution at 0.5 mol L⁻¹ for 30 min, 1, 2, 4, 8, 12 and 24 h. Less concentrated solutions of NaIO₄ were not evaluated since longer oxidation time would be required to achieved same oxidation efficiency. During the oxidation, the solution with the paper was kept away from the light. After the established time, the paper was washed abundantly with distilled water and then left to dry in the desiccator overnight.

II.3.2. Characterization of oxidized paper

Once the paper strips were dried, the dimensions of the oxidized papers were measured with a digital caliper Mituoyo ABSOLUTE Super Caliper SERIES 500.

The functional groups of the native and oxidized paper were analyzed by infrared spectroscopy PerkinElmer Spectrum Frontier with universal attenuated total reflection (ATR) accessory (diamond/ZnSe crystal). Spectra were recorded between 4000 and 600 cm⁻¹ by accumulation of 32 scans with a resolution of 4 cm⁻¹. The distribution of functional groups along the cellulose fibers was also evaluated by Micro-FTIR Spectroscopy using an FTIR spectrometer (Vertex 70v) coupled with an FTIR microscope Hyperion 3000 (Bruker). The measurements were done in the transmittance mode with spectral resolution of 4 cm⁻¹ and 256 scans in the mid infrared spectral range (4000 – 600 cm⁻¹). The FTIR microscope was equipped with cooled liquid N₂, a 64 x 64 elements focal plane array detector. Each element of the focal plane array worked as an individual detector, measuring 4096 spectra from the probed sample area in a single detection with a spatial resolution of approximately 2.5 μm. The 2D and 3D chemical images were acquired by integrating the area under the peak corresponding to a specific vibrational mode in the FTIR spectrum. All the FTIR spectra are the difference spectra where the absorption signals corresponding to the background were subtracted from those of the samples.

The surface of the native paper and oxidized for 24h were visualized by scanning electron microscopy (SEM; Zeiss LEO-440). Before the analysis, the samples were sputtered with gold.

The crystallinities of native and oxidized cellulose were evaluated by an X-ray diffractor (Model D8 Advance, Bruker). The diffractograms were obtained in the range from 5 to 60 degrees with step of 0.02 degree and 0.5 s as irradiation time.

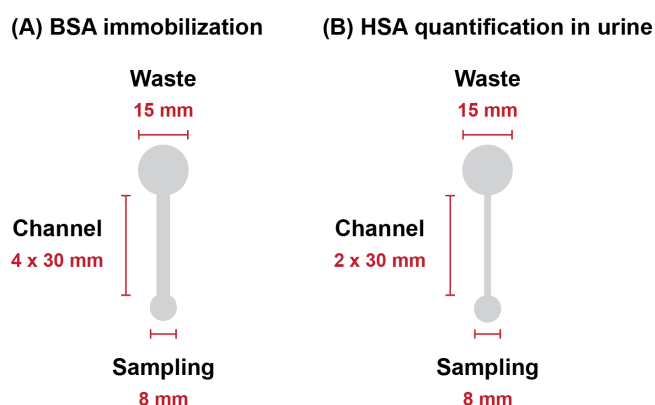
The contact angle of the paper before and after 12h of oxidative treatment were measured by a goniometer (KSV CAM 200) equipped with CAM 2008 software.

Dynamic mechanical analysis (DMA; TA instruments Q800) using the tension film clamps characterized the native and 24h-oxidized papers. For this analysis, the native paper was cut in the dimensions of 30 × 3 mm and 54.5 × 1.76 mm. The larger specimen was oxidized for 24 h, as described in the protocol above. After the oxidation, the specimen shrunk to the same dimension of the smaller native paper.

II.3.3. Evaluation of the oxidized paper on protein immobilization

The oxidized paper was evaluated as a substrate to covalently immobilize proteins. Bovine serum albumin (BSA) was chosen as a proof of concept for immobilization since it is a widely used protein in the bioanalytical field. The BSA immobilization was only evaluated on the paper oxidized for 0.5, 1, 2 and 4 h since longer oxidation caused significant change in the physicochemical properties of the paper as further discussed. The paper was laser cut in the design shown in Figure II.1A. The evaluated BSA concentrations were 1, 2, 4 and 8 mg mL⁻¹ in phosphate buffer at pH 4.8.

Figure II.1 - Layout and dimensions of the chromatography paper strip to evaluate (A) BSA immobilization and (B) quantify HSA in urine on oxidized paper.



Source: Own Authorship.

For the immobilization assay, 0.5 μ L of BSA solution was applied at 0.5 cm above the absorption circle (diameter = 8 mm). For the percolation step, the paper strip was stood up with the absorption circle immersed in a phosphate buffer to allow the solution to percolate through

the channel (length = 30 mm) until it reached to the end of the waste circle (diameter = 15 mm), around 20 min. In this step, the pH of the percolation solution was evaluated at BSA pI \pm 1 (3.8, 4.8, and 5.8). The temperature was set at 24 °C and the humidity was controlled with room air conditioner. After the percolation step, the paper strip was quickly immersed in a 0.1% (m/v) Ponceau in 10% (v/v) acetic acid solution. The paper strip was washed 3 times with 10 mL of 10% (v/v) acetic acid solution and then dried in an oven at 80 °C with an absorbent paper on it. The dried paper strip was scanned in a digital scanner and then analyzed on ImageJ® software, by which the lengths of the blot and the color intensity were measured.

II.3.4. Quantification of proteins in human urine

Chromatography paper was cut as shown with a narrower channel of 2 mm (Figure II.1B). The paper chips were oxidized for 4 h, as described previously. Firstly, to evaluate the correlation between blot length and protein concentration, BSA solutions from 1 to 8 mg mL⁻¹ were applied on the paper chip and the immobilization protocol described above was applied.

The oxidized paper chips were evaluated as a platform to detect protein in urine in order to demonstrate the versatility of oxidized paper. For this study, a urine pool was spiked with human serum albumin (HSA) for a final concentration of 10 mg mL⁻¹. The concentrated HSA solution was diluted in urine pool to concentrations of 0.1, 0.5, 1.0, 1.5, 2.0, 3.0, and 5.0 mg mL⁻¹. 0.5 μ L of the HSA sample was spot in the oxidized paper chip and the protocol for BSA immobilization described above was applied.

The HSA samples were analyzed by Bradford method, which is considered as a reference method to quantify proteins. 2 μ L of the urine sample were mixed with 200 μ L of Bradford reagent and 798 μ L of water. The mix reacted for 20 min before the measurement on ThermoFisher NanoDrop 2000c spectrophotometer at 595 nm in a quartz cuvette of 10 mm wide.

II.4. RESULTS & DISCUSSION

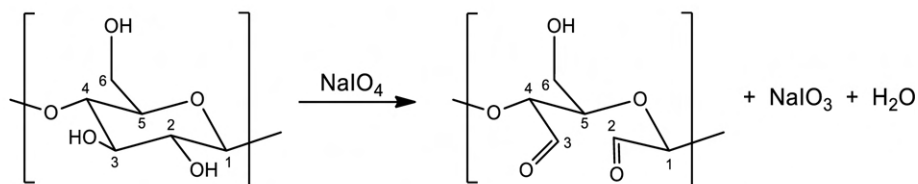
II.4.1. Chromatography paper oxidation with NaIO₄

Cellulose is a natural polymer with linear chains of D-glucose units. Periodate selectively oxidizes vicinal hydroxyl groups on carbon C2 and C3 of the glucose to aldehyde groups, as shown in Figure II.2A.¹⁷ The aldehyde groups are more reactive than the hydroxyl groups and react with amine groups from the protein, resulting in the imide bond (Schiff base), shown in Figure II.2B. The presence of the carbonyl group on the oxidized samples were

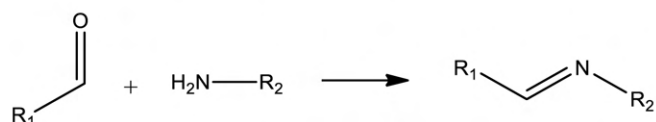
evaluated by FTIR-ATR. The C=O stretching band at 1733 cm^{-1} appears and intensifies over the oxidation time, as shown in Figure II.3. It is also possible to visualize the decrease in the O–H stretching band at 3333 cm^{-1} after the oxidation with the IO_4^- .

Figure II.2 - (A) Oxidation of glucose monomer of the cellulose chain with NaIO_4 . (B) Reaction between the aldehyde and amine groups, resulting in the Schiff base.

(A) Glucose monomer oxidation with NaIO_4

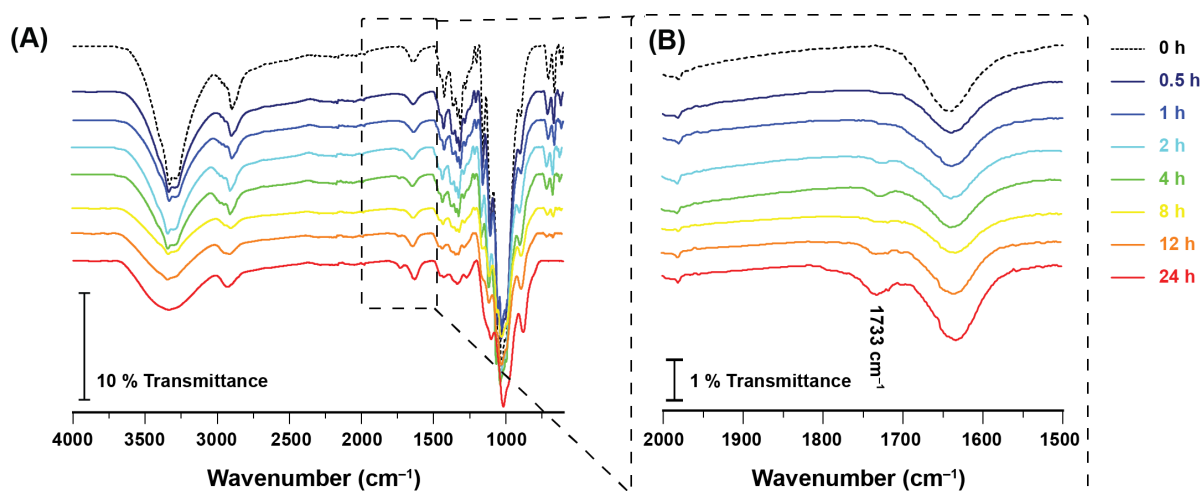


(B) Condensation reaction of carbonyl and amine



Source: Own Authorship.

Figure II.3 - (A) FTIR-ATR spectra of the native chromatography paper and after 0.5, 1, 2, 4, 8, 12, and 24 h oxidation in $0.5\text{ mol L}^{-1}\text{ NaIO}_4$. (B) Magnification in the range from 2000 to 1500 cm^{-1} . Carbonyl stretching band at 1733 cm^{-1} .

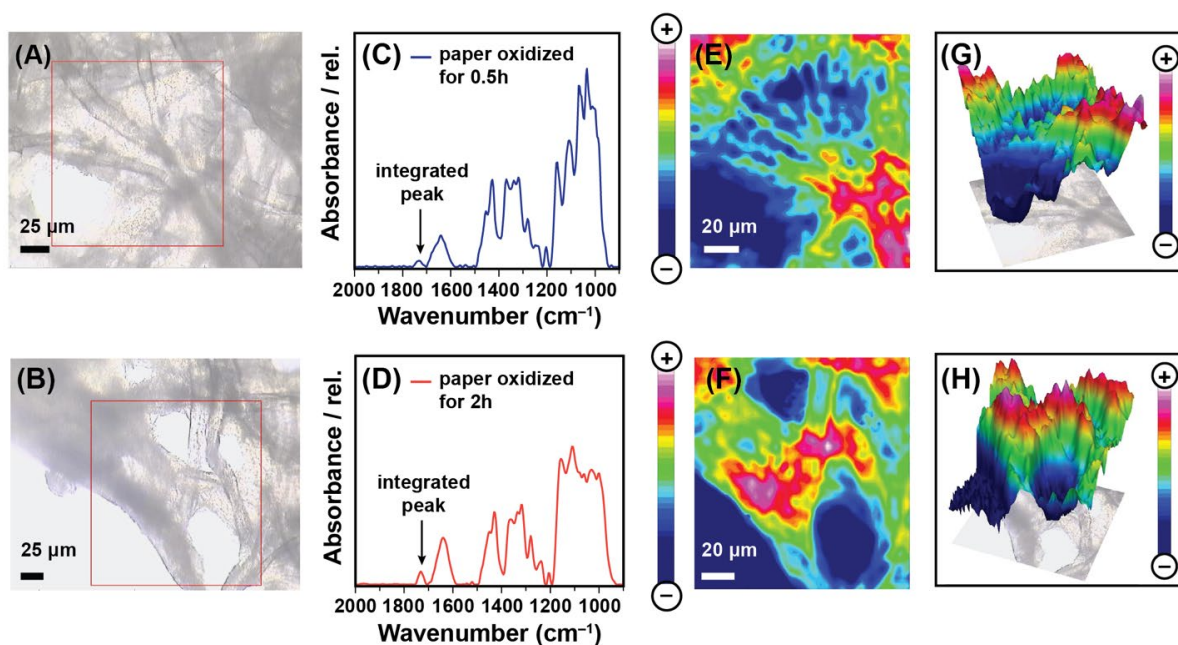


Source: Adapted by permission from Imamura *et al.* *Microchim Acta*, 2020, 187: 272 © 2020 Springer Nature Customer Service Gmb DOI: 10.1007/s00604-020-04250-6.

The oxidized paper for 0.5 and 2 h were analyzed by micro-FTIR. Samples 2D and 3D images of the chemical distribution of carbonyl groups were obtained, as illustrated in Figure II.4. Firstly, the micrographs of the oxidized paper for 0.5 and 2 h were acquired, Figure II.4A and B respectively. Infrared spectra were collected within the delineated area on the micrograph, resulting in several individual FTIR as shown in Figure II.4C and D. In these spectra, the

carbonyl stretching band at 1733 cm^{-1} can be observed. The area under this band was integrated for all FTIR spectra collected, from which the 2D and 3D chemical images were reconstructed (Figure II.4E-H). In these chemical images, the distribution of the carbonyl group along the cellulose fibers can be visualized. Because of the absence of the carbonyl groups on the native paper, the chemical images with the distribution of the C=O bond were not reconstructed. The blue regions represent the absence of the carbonyl group, which correspond to the pore areas in the micrograph. The red regions illustrate the aldehyde groups in the cellulose fibers and its distribution is not homogenous at this magnification. There is no significant difference in the distribution of aldehyde group in the samples oxidized for 0.5 and 2 h. This is further evidenced on the BSA immobilization assay (see Section II.4.2).

Figure II.4 - Micro-FTIR spectroscopy of the paper treated for 0.5 h (A, C, E, G) and 2 h (B, D, F, H) recorded with FPA detector from 4000 to 900 cm^{-1} at spectral resolution of 4 cm^{-1} with 256 spectra co-added. (A), (B) Optical images showing a part of the sample paper, where fibers can be easily seen. The area marked in red was selected for the extraction of the spectra and consequent chemical images. (C), (D) micro-FTIR spectra of the treated paper with the integrated spectral bands highlighted. (E), (F) 2D Chemical images showing the distribution of carbonyl spectral band along the cellulose fibers. (G), (H) 3D chemical images.

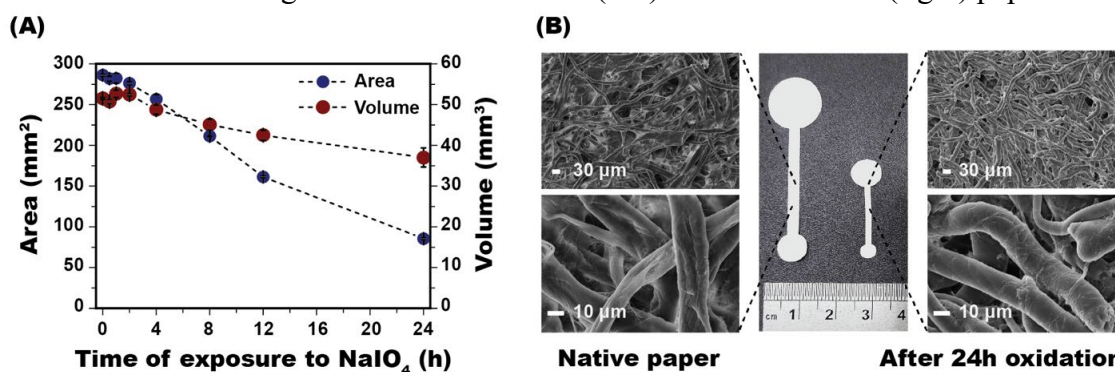


Source: Adapted by permission from Imamura *et al.* *Microchim Acta*, 2020, 187: 272 © 2020 Springer Nature Customer Service Gmb DOI: 10.1007/s00604-020-04250-6.

The oxidation results in the cleavage of the D-glucose rings, as illustrated in Figure II.2A, which can modify the physicochemical properties of the chromatography paper. In fact, the paper shrunk after long hours of oxidation, as also described by Strong *et al.*¹⁸ The area

decreased significantly after 2 h of oxidation (Figure II.5A). Simultaneously, the thickness of the paper increased 2.4-fold from 0.18 to 0.43 mm. Since the decrease in area is more noticeable than the increase in thickness, the volume of the paper strips reduced over the oxidation time. The decrease in the volume of the paper can worsen the device capacity of carrying chemicals and diminish the performance of the paper as a substrate for analytical devices. It is important to state that there is no evidence of mass loss after the oxidation, which indicated that the shrinking is due to the reducing of the pore size. The micrography in Figure II.5B illustrate the cellulose fiber closer to each other after 24 h of oxidation, leading to a lower porosity.

Figure II.5 - (A) Geometrical area (blue) and volume (red) in function of time. (B) Shrinking of the paper strip after 24 h of oxidation (middle) and micrographs in 500 and 3000 \times magnification of the native (left) and the oxidized (right) papers.

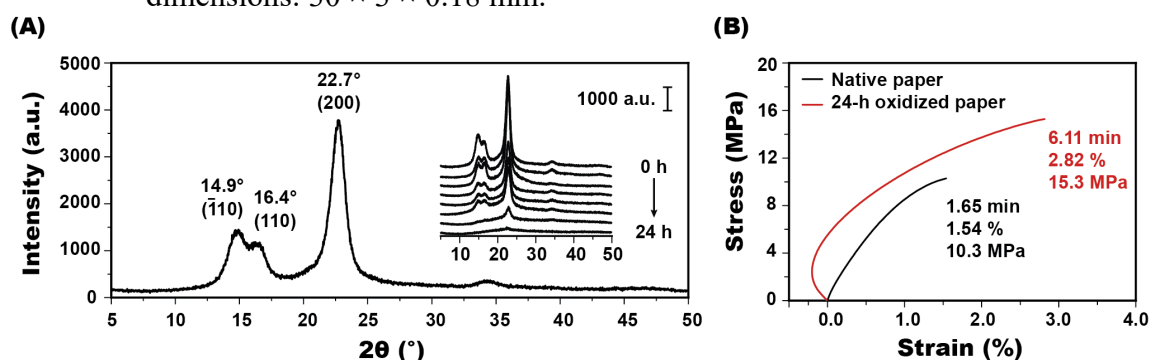


Source: Adapted by permission from Imamura *et al.* *Microchim Acta*, 2020, 187: 272 © 2020 Springer Nature Customer Service Gmb DOI: 10.1007/s00604-020-04250-6.

Each glucose unit has three hydroxyl groups, which form intra- and interchain hydrogen bonds. These bonds are responsible for the linear structure of the cellulose chains and for the physical properties of this polysaccharide. The alignment of the chains arranges the crystallographic planes ($1\bar{1}0$), (110) e (200),¹⁹ shown in Figure II.6A. Because the oxidation by periodate resulted in the conversion of two hydroxyl groups to two aldehyde groups (Figure II.2A), the cellulose chains disarranged. In addition, the opening of the glucose ring disarranged the linear chains. This effect was observed in the diffractograms in the insert of Figure II.6A. There is a decrease of the peak intensity along the oxidation time, implying the loss of cellulose crystallinity. The disarrangement of the chains entailed the changes in the physico-chemical properties of the cellulose, such as an increased rigidity after long exposure to periodate. The mechanical properties of the 24h oxidized cellulose was evaluated by a tensile test. The strain vs. stress profile of the oxidized paper was unique, with a region of negative strain (Figure II.6B) even stressing the specimen. After the oxidation, the oxidized specimen was not fully straight, which under the application of the initial pressure curled back, representing the

negative strain. Even with the negative strain region, the oxidized paper required higher pressure (15.3 MPa) to rupture the strip with the same dimensions of the native paper (10.3 MPa). This implied an increase in the stiffness of the paper after prolonged oxidation treatment which can be explained by the higher density of cellulose fiber on the oxidized paper.

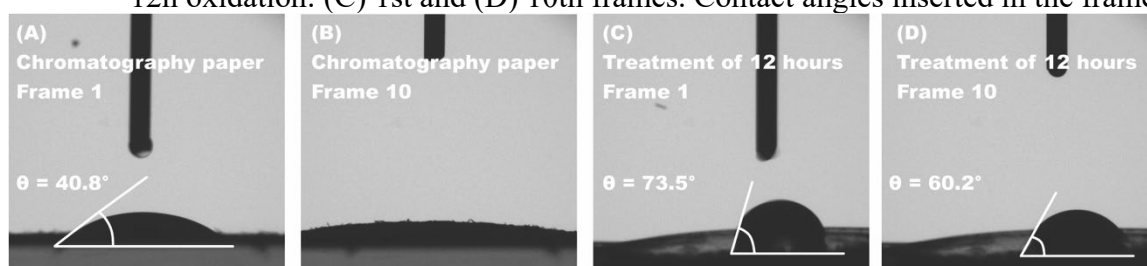
Figure II.6 - (A) Paper diffractogram with the index peaks of the crystalline planes, and in the insertion, diffractograms of the oxidation progress. (B) Stress-strain curve for paper without (black) and after (red) exposure to NaIO_4 for 24 h; specimen dimensions: $30 \times 3 \times 0.18$ mm.



Source: Adapted by permission from Imamura *et al.* *Microchim Acta*, 2020, 187: 272 © 2020 Springer Nature Customer Service Gmb DOI: 10.1007/s00604-020-04250-6.

The oxidation of the paper by NaIO_4 also altered its capillarity. The capillarity of water in paper occurs through the hydrogen bonds between the water molecules and the glucose hydroxyl groups. Figure II.7 illustrates the oxidation effect on the contact angle of a drop of water on paper. On the native paper, the contact angle is 40.8° (Figure II.7A) and the water quickly absorbed by the paper (Figure II.7B). The contact angle increased to 73.5° when the drop of water contacted the paper oxidized for 12h (Figure II.7C) and remained on the paper until 10th frame with a contact angle of 60.2° (Figure II.7D). The excessive oxidation hindered the capillarity since the hydroxyl groups were converted to aldehyde groups, resulting in the loss of hydrogen bond sites and decreased polarity.

Figure II.7 - Drops of water on native paper: (A) 1st and (B) 10th frames. Drops of water after 12h oxidation: (C) 1st and (D) 10th frames. Contact angles inserted in the frames.



Source: Adapted by permission from Imamura *et al.* *Microchim Acta*, 2020, 187: 272 © 2020 Springer Nature Customer Service Gmb DOI: 10.1007/s00604-020-04250-6.

II.4.2. BSA immobilization on oxidized paper

II.4.2.1. Influence of the oxidation time on protein immobilization

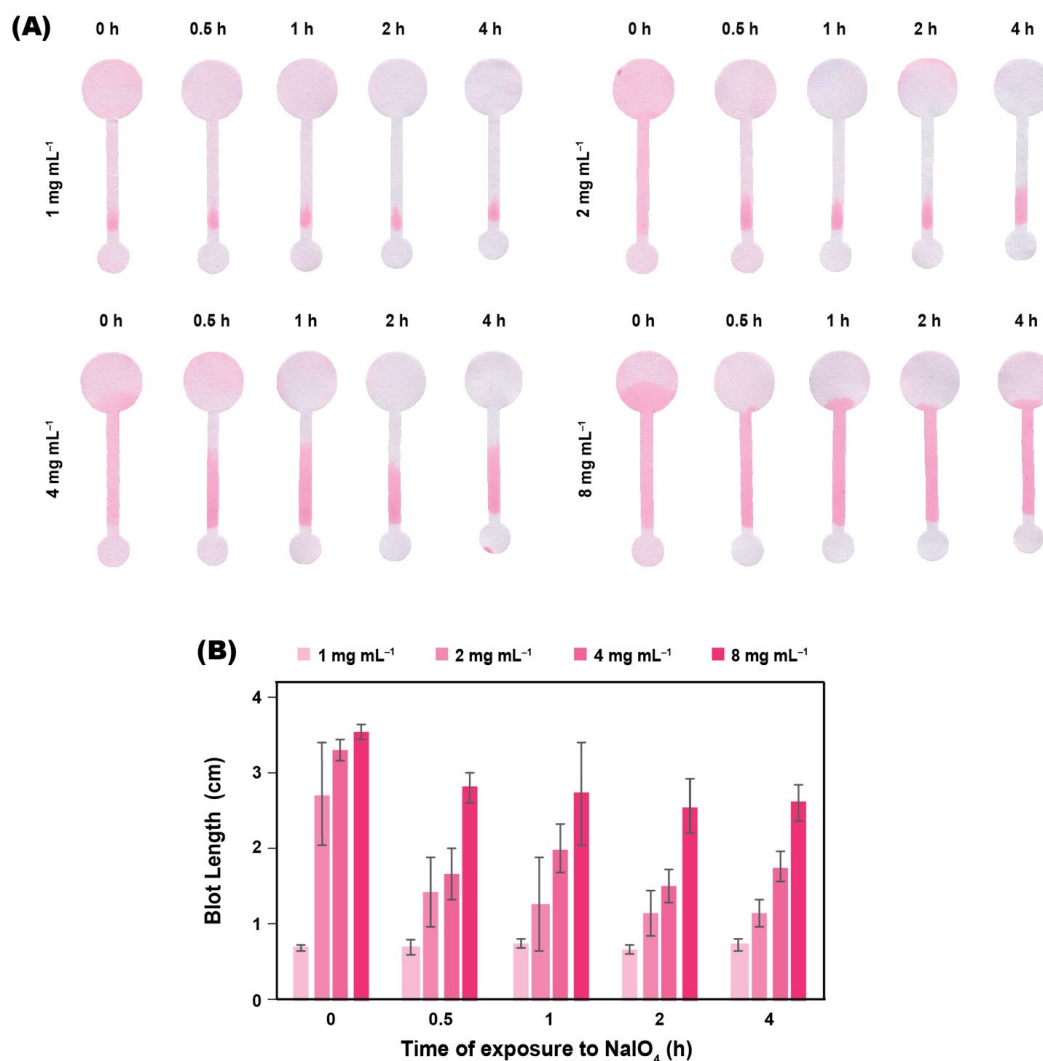
On the oxidized paper, there are aldehyde groups with which the protein can covalently bind through their amine groups, forming a Schiff base (imide bond), as shown in Figure II.2B. With the application of BSA on the oxidized paper, the protein covalently linked to the paper at the application spot area. In this method, it did not require a rigid time control after spotting the protein in the paper as in many typical adsorption protocols, in which the incubation time usually takes at least 30 min.²⁰ The percolation of buffer solution carried away any excess of unbound protein through the channel until finding a free binding site of the oxidized paper. The time required for the buffer to percolate the channel and reach to the end of the saturation circle was close to 20 min for all oxidized paper chips, demonstrating that the capillarity has not changed significantly in samples oxidized up to 4 h. Evaporation rate was not quantified, though room temperature and humidity were controlled by a room air conditioner. To visualize the immobilized protein on paper, Ponceau dye was applied. This dye is characterized by three sulfonic acid groups negatively charged, which interact with the positively charged amine groups from proteins. Once electrostatically attached to the protein, the dye defined with red color the region where the proteins are immobilized. Figure II.8A illustrates the paper strips after the application of BSA in different concentrations and staining with the Ponceau dye. The lengths of the blots were measured by ImageJ® and they were illustrated in Figure II.8B. The length data was analyzed by ANOVA and Tukey test.

For all samples of paper including non-oxidized and oxidized for 0.5, 1, 2 and 4 h, there is an increase in the blot length with increase on BSA concentration. Due to the minimal change in area and volume of the paper chips oxidized for 0.5 - 4h (Figure II.5A), the blot length is correlated to the amount of protein. The correlation with protein mass and blot length was confirmed by comparing between BSA concentrations, in which the variance of data is significantly and statistically different (Table II.1).

Comparing within the same BSA concentration, the blot lengths of any oxidized paper were shorter than the native paper ones (Figure II.8B), which was statistically proven as shown in Table II.1. With the oxidation of the cellulose, there was a reduced displacement of the protein through the channel during the percolation step because of the improved immobilization of the protein on paper. However, increasing the oxidation time did not improve the immobilization since there is no statistically significant difference between the blot lengths, proven by ANOVA and Tukey's tests. (Table II.2). Therefore, the oxidation of chromatography

paper with periodate for 0.5 h suffices to promote the immobilization of any concentration of BSA.

Figure II.8 - (A) Paper chips from native (0 h) and oxidized papers for 0.5, 1.0, 2.0, and 4.0 h after the immobilization with 0.5 μL of BSA at 1.0, 2.0, 4.0, and 8.0 mg mL^{-1} solutions. (B) Graphical relation between oxidation time, BSA concentration, and the blot length.



Source: Adapted by permission from Imamura *et al.* *Microchim Acta*, 2020, 187: 272 © 2020 Springer Nature Customer Service Gmb DOI: 10.1007/s00604-020-04250-6.

The effect of oxidation time was also analyzed for each BSA concentration (Table II.3 - Table II.6). For BSA concentrations of 2, 4 and 8 mg mL^{-1} (Table II.4 - Table II.6), the native paper statistically differed from the oxidized papers on the immobilization of protein, in agreement with the main effect (Table II.2).

Table II.1 - Main effect of BSA concentration. Pink-shaded area highlights the statistically significant variance of data.

Tukey's multiple comparison test	Mean Difference	95% Confidence Interval of difference	Significant?	Summary	Adjusted P Value
1 mg mL ⁻¹ vs. 2 mg mL ⁻¹	-0.8300	-1.132 to -0.5279	Yes	****	<0.0001
1 mg mL ⁻¹ vs. 4 mg mL ⁻¹	-1.283	-1.585 to -0.9813	Yes	****	<0.0001
1 mg mL ⁻¹ vs. 8 mg mL ⁻¹	-2.130	-2.432 to -1.828	Yes	****	<0.0001
2 mg mL ⁻¹ vs. 4 mg mL ⁻¹	-0.4534	-0.7555 to -0.513	Yes	**	0.0014
2 mg mL ⁻¹ vs. 8 mg mL ⁻¹	-1.300	-1.602 to -0.9980	Yes	****	<0.0001
4 mg mL ⁻¹ vs. 8 mg mL ⁻¹	-0.8467	-1.149 to -0.5446	Yes	****	<0.0001

Source: Reprinted with permission from Imamura *et al.* *Microchim Acta*, 2020, 187: 272 © 2020 Springer Nature Customer Service Gmb DOI: 10.1007/s00604-020-04250-6.

Table II.2 - Main effect of time of oxidation. Pink-shaded area highlights the statistically significant variance of data.

Tukey's multiple comparison test	Mean Difference	95% Confidence Interval of difference	Significant?	Summary	Adjusted P Value
0 h vs. 0.5 h	0.9691	0.6092 to 1.329	Yes	****	<0.0001
0 h vs. 1 h	0.8494	0.4895 to 1.209	Yes	****	<0.0001
0 h vs. 2 h	1.100	0.7400 to 1.460	Yes	****	<0.0001
0 h vs. 4 h	0.9965	0.6366 to 1.356	Yes	****	<0.0001
0.5 h vs. 1 h	-0.1197	-0.4795 to 0.2402	No	ns	0.8755
0.5 h vs. 2 h	0.1308	-0.2290 to 0.4907	No	ns	0.8360
0.5 h vs. 4 h	0.02742	-0.3325 to 0.3873	No	ns	0.9995
1 h vs. 2 h	0.2505	-0.1094 to 0.6104	No	ns	0.2902
1 h vs. 4 h	0.1471	-0.2128 to 0.5070	No	ns	0.7696
2 h vs. 4 h	-0.1034	-0.4633 to 0.2565	No	ns	0.9227

Source: Reprinted with permission from Imamura *et al.* *Microchim Acta*, 2020, 187: 272 © 2020 Springer Nature Customer Service Gmb DOI: 10.1007/s00604-020-04250-6.

Table II.3 - Simple effect of oxidation time for BSA concentration of 1 mg mL⁻¹.

Tukey's multiple comparisons test	Mean Difference	95% Confidence Interval of difference	Significant?	Summary	Adjusted P Value
0 vs. 0.5	-0.01367	-0.7334 to 0.7061	No	ns	>0.9999
0 vs. 1	-0.06633	-0.7861 to 0.6534	No	ns	0.9989
0 vs. 2	0.01900	-0.7008 to 0.7388	No	ns	>0.9999
0 vs. 4	-0.03800	-0.7578 to 0.6818	No	ns	0.9999
0.5 vs. 1	-0.05267	-0.7724 to 0.6671	No	ns	0.9996
0.5 vs. 2	0.03267	-0.6871 to 0.7524	No	ns	>0.9999
0.5 vs. 4	-0.02433	-0.7441 to 0.6954	No	ns	>0.9999
1 vs. 2	0.08533	-0.6344 to 0.8051	No	ns	0.9971
1 vs. 4	0.02833	-0.6914 to 0.7481	No	ns	>0.9999
2 vs. 4	-0.05700	-0.7768 to 0.6628	No	ns	0.9994

Source: Reprinted with permission from Imamura *et al.* *Microchim Acta*, 2020, 187: 272 © 2020 Springer Nature Customer Service Gmb DOI: 10.1007/s00604-020-04250-6.

Table II.4 - Simple effect of time oxidation for BSA concentration of 2 mg mL⁻¹. Pink-shaded area highlights the statistically significant variance of data.

Tukey's multiple comparisons test	Mean Difference	95% Confidence Interval of difference	Significant?	Summary	Adjusted P Value
0 vs. 0.5	1.279	0.5596 to 1.999	Yes	****	<0.0001
0 vs. 1	1.453	0.7336 to 2.173	Yes	****	<0.0001
0 vs. 2	1.558	0.8386 to 2.278	Yes	****	<0.0001
0 vs. 4	1.570	0.8502 to 2.290	Yes	****	<0.0001
0.5 vs. 1	0.1740	-0.5458 to 0.8938	No	ns	0.9574
0.5 vs. 2	0.2790	-0.4408 to 0.9988	No	ns	0.8018
0.5 vs. 4	0.2907	-0.4291 to 1.010	No	ns	0.7772
1 vs. 2	0.1050	-0.6148 to 0.8248	No	ns	0.9934
1 vs. 4	0.1167	-0.6031 to 0.8364	No	ns	0.9902
2 vs. 4	0.01167	-0.7081 to 0.7314	No	ns	>0.9999

Source: Reprinted with permission from Imamura *et al.* *Microchim Acta*, 2020, 187: 272 © 2020 Springer Nature Customer Service Gmb DOI: 10.1007/s00604-020-04250-6.

Table II.5 - Simple effect of Time oxidation for BSA concentration of 4 mg mL⁻¹. Pink-shaded area highlights the statistically significant variance of data.

Tukey's multiple comparisons test	Mean Difference	95% Confidence Interval of difference	Significant?	Summary	Adjusted P Value
0 vs. 0.5	1.881	1.161 to 2.600	Yes	****	<0.0001
0 vs. 1	1.205	0.4849 to 1.924	Yes	***	0.0002
0 vs. 2	1.837	1.117 to 2.557	Yes	****	<0.0001
0 vs. 4	1.527	0.8069 to 2.246	Yes	****	<0.0001
0.5 vs. 1	-0.6760	-1.396 to 0.04376	No	ns	0.0746
0.5 vs. 2	-0.04367	-0.7634 to 0.6761	No	ns	0.9998
0.5 vs. 4	-0.3540	-1.074 to 0.3658	No	ns	0.6283
1 vs. 2	0.6323	-0.08743 to 1.352	No	ns	0.1088
1 vs. 4	0.3220	-0.3978 to 1.042	No	ns	0.7061
2 vs. 4	-0.3103	-1.030 to 0.4094	No	ns	0.7333

Source: Reprinted with permission from Imamura *et al.* *Microchim Acta*, 2020, 187: 272 © 2020 Springer Nature Customer Service Gmb DOI: 10.1007/s00604-020-04250-6.

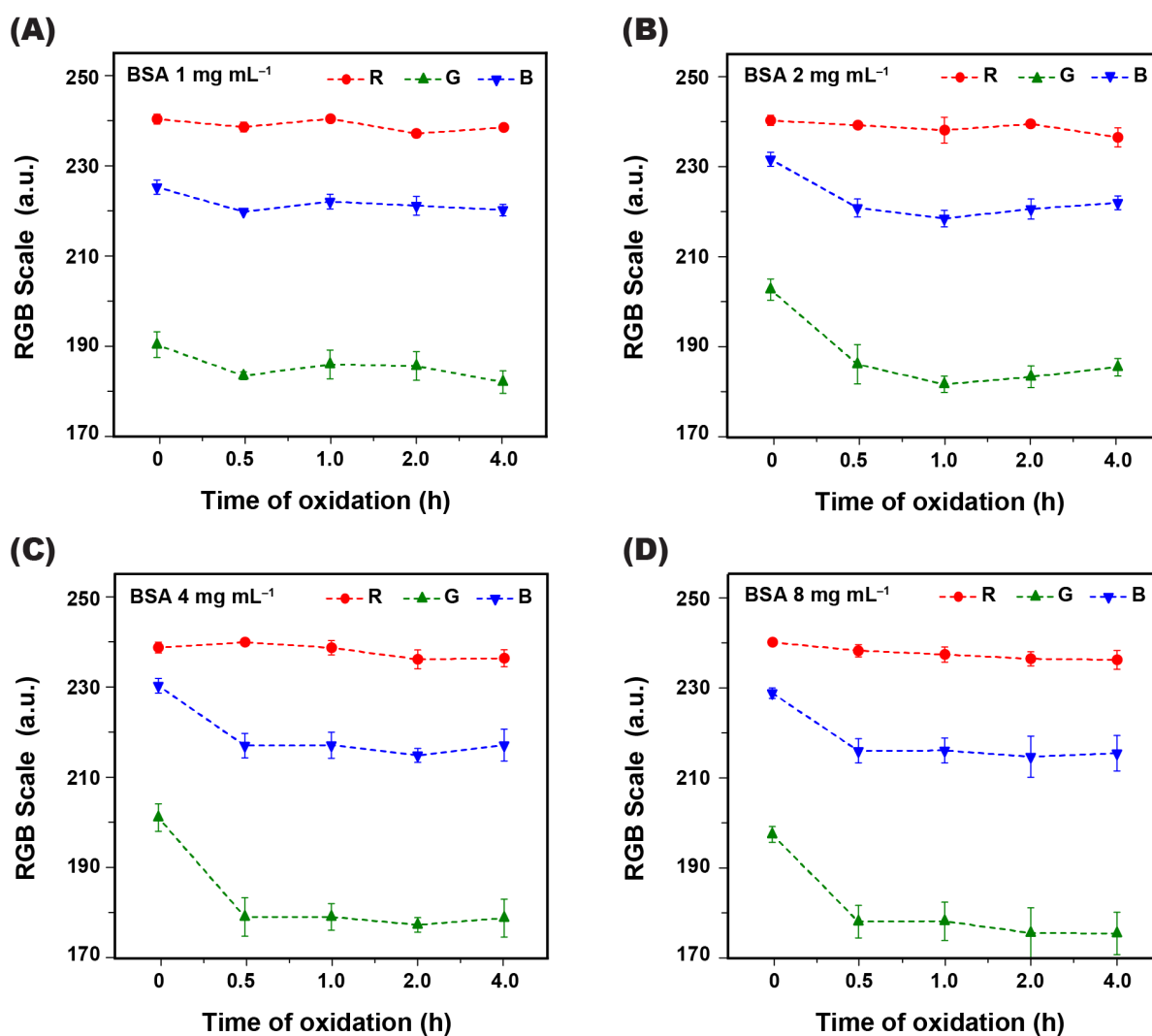
Table II.6 - Simple effect of Time oxidation for BSA concentration of 8 mg mL⁻¹. Pink-shaded area highlights the statistically significant variance of data.

Tukey's multiple comparisons test	Mean Difference	95% Confidence Interval of difference	Significant?	Summary	Adjusted P Value
0 vs. 0.5	0.7300	0.01024 to 1.450	Yes	*	0.0454
0 vs. 1	0.8060	0.08624 to 1.526	Yes	*	0.0215
0 vs. 2	0.9853	0.2656 to 1.705	Yes	**	0.0030
0 vs. 4	0.9273	0.2076 to 1.647	Yes	**	0.0059
0.5 vs. 1	0.07600	-0.6438 to 0.7958	No	ns	0.9981
0.5 vs. 2	0.2553	-0.4644 to 0.9751	No	ns	0.8478
0.5 vs. 4	0.1973	-0.5224 to 0.9171	No	ns	0.9340
1 vs. 2	0.1793	-0.5404 to 0.8991	No	ns	0.9526
1 vs. 4	0.1213	-0.5984 to 0.8411	No	ns	0.9886
2 vs. 4	-0.05800	-0.7778 to 0.6618	No	ns	0.9994

Source: Reprinted with permission from Imamura *et al.* *Microchim Acta*, 2020, 187: 272 © 2020 Springer Nature Customer Service Gmb DOI: 10.1007/s00604-020-04250-6.

For 1 mg mL^{-1} of BSA, there was no statistically significant difference between blot lengths from native and oxidized samples, as shown by the error bars in Figure II.8B and confirmed by ANOVA and Tukey's tests (Table II.3). This can be explained by the small amount of protein used for the immobilization. For low concentration of protein, the paper chip required higher sensitivity to distinguish the blots from different concentrations and oxidation time. The sensitivity to detect protein in the range of low concentration can be improved by narrowing the channel width, as it was done to detect human serum albumin in urine (further described in the *Section II.4.3*). However, the color intensity for the non-treated paper is faded when compared with oxidized samples, including for the low BSA concentration of 1 mg mL^{-1} , as illustrated in Figure II.9.

Figure II.9 - RGB intensity of the blot after immobilization of BSA (A) 1, (B) 2, (C) 4, and (D) 8 mg mL^{-1} on the paper without treatment and after 0.5 to 4.0 h of oxidation.



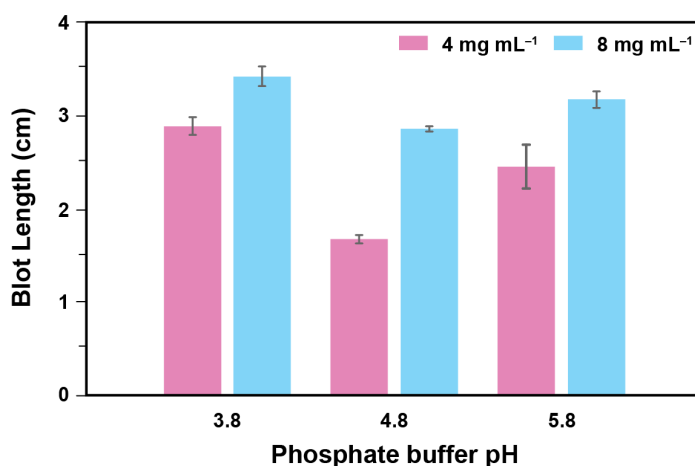
Source: Adapted by permission from Imamura *et al.* *Microchim Acta*, 2020, 187: 272 © 2020 Springer Nature Customer Service Gmb DOI: 10.1007/s00604-020-04250-6.

Because the Ponceau dye attached to the protein, the color intensity in Figure II.9 is related to the amount of protein immobilized in the application spot. Despite the blot lengths could not be distinguished at 1 mg mL^{-1} , there was a decrease of the green channel in the RGB scale after the oxidation. This trend was also observed for higher BSA concentration but with more noticeable effect. Therefore, the oxidation of paper with NaIO_4 improve the immobilization of proteins. However, it is important to state that the results may change with the type of the paper, the oxidant agent and protein evaluated.

II.4.2.2. Influence of the percolation solution pH on protein immobilization

The pH of the protein solution was evaluated for the immobilization of BSA at 4 and 8 mg mL^{-1} . The evaluated pHs consisted of isoelectric point of the protein (4.8), and 1 pH unit around the pI (3.8 and 5.8). The blot lengths are shorter at pI of the protein for both concentrations (Figure II.10). This result agrees with the work of McCann *et al.* in which the adsorption of BSA on chromatography paper 3 MM was studied.²⁰ At pH different than the pI, the proteins are positively ($\text{pH} < \text{pI}$) or negatively ($\text{pH} > \text{pI}$) charged and they repel each other electrostatically. When the protein attached to a binding site on the paper, the electrostatic repulsion forces the remaining proteins to flow through the channel to find a new binding spot, which resulted in an enlarged blot and in a distribution similar to a monolayer. When the pH of the buffer was at pI, the proteins aggregates and linked to binding sites next to each other, resulting in the stacking and formation of multilayers of proteins.

Figure II.10 - Blot lengths of 4 and 8 mg mL^{-1} of BSA at pH of 3.8, 4.8 and 5.8 performed in the paper chip oxidized for 4 h; error bars indicate one standard deviation from three chips.



Source: Adapted by permission from Imamura *et al.* *Microchim Acta*, 2020, 187: 272 © 2020 Springer Nature Customer Service Gmb DOI: 10.1007/s00604-020-04250-6.

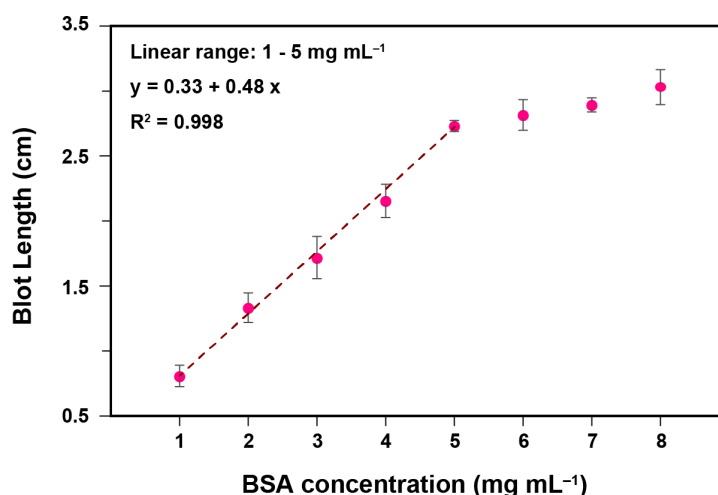
II.4.3. Quantification of protein in urine

II.4.3.1. Blot length and protein concentration correlation

As previously discussed, the oxidation for 0.5 h was enough to improve the immobilization of protein on chromatography paper. The oxidation protocol can be used to enhance the performance of paper-based analytical devices as a biosensor. However, the oxidation of the paper for 4 h exhibited lower variation of the blot lengths (Figure II.8B), which can be explained by a more homogenous oxidation of the cellulose promoted by prolonged exposition to NaIO_4 . Therefore, the paper oxidized by 4 h was evaluated as a sensing platform.

BSA at 1 to 8 mg mL^{-1} were spotted in the paper chip oxidized for 4h and the resulting blot lengths were plotted against concentration. Two distinct correlation regions are observed in the plot of Figure II.11. The first region consisted in a linear correlation ($R^2 = 0.998$), comprising the BSA concentrations from 1 to 5 mg mL^{-1} . The concentration range from 5 to 8 mg mL^{-1} could not be linearly correlated with the blot length since it spread to the saturation circle. To extend the linearity of the device, paper chips with longer channels can be fabricated.

Figure II.11 - Plot of blot length vs. BSA concentration in paper chip oxidized for 4 h in a phosphate buffer pH 3.8; error bars indicate one standard deviation from five chips.



Source: Adapted by permission from Imamura *et al.* *Microchim Acta*, 2020, 187: 272 © 2020 Springer Nature Customer Service Gmb DOI: 10.1007/s00604-020-04250-6.

II.4.3.2. Quantification of HSA in urine

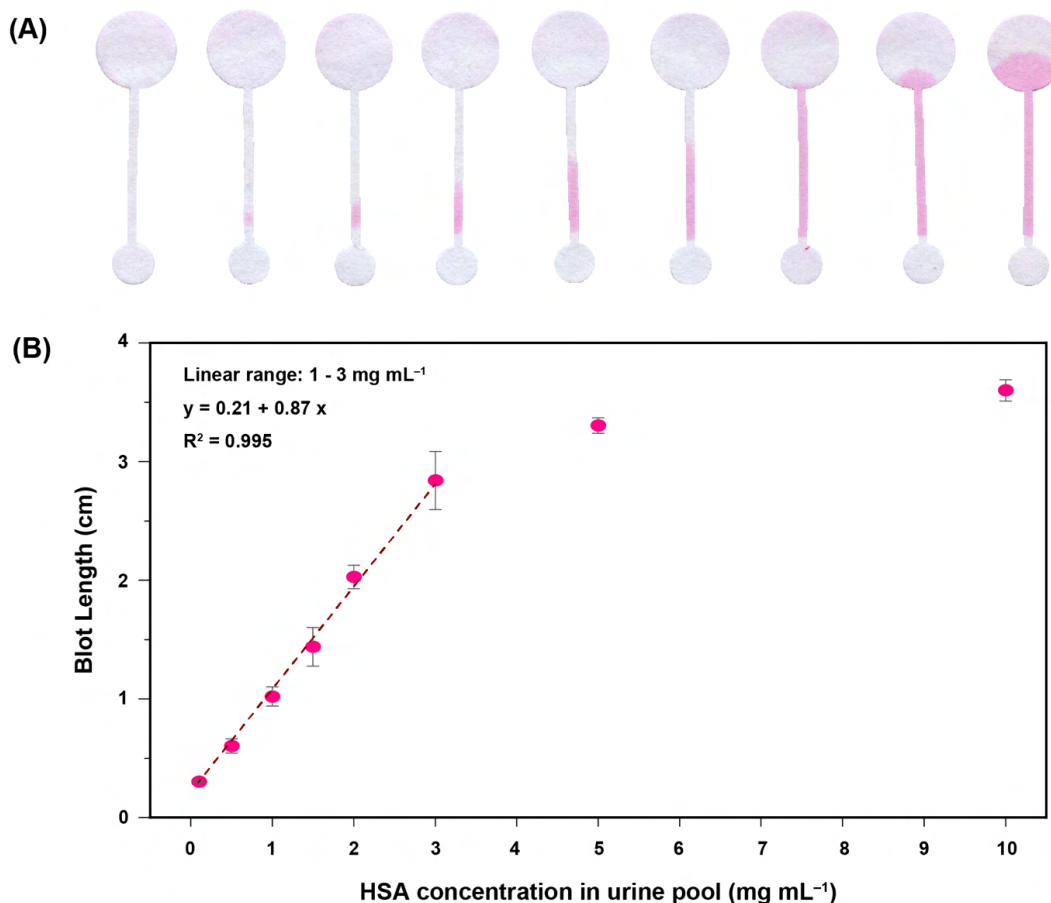
The paper oxidized for 4h was tested as a sensing device for quantification of total protein in human urine. From healthy individuals, the level of protein in urine is less than 30 mg per day for a daily volume from 1 to 3 L.²¹ Microalbuminuria is characterized by a protein

concentration ranging from 0.01 to 0.3 mg mL⁻¹ and proteinuria by concentrations above 0.3 mg mL⁻¹.²²

The urine pool was tested to check the initial concentration of proteins, which was below the detectability of the sensor. Thus, the urine pool was spiked with HSA reaching a concentration range from 0.1 to 10 mg mL⁻¹ to simulate proteinuria samples and then tested in the oxidized paper chip since no color was revealed in the paper chip for smaller concentrations (Figure II.12A). The blot lengths were plotted against HSA concentrations, as shown in Figure II.12B, and two regions of correlations were observed. The first region comprising from 0.1 to 3 mg mL⁻¹ is a linear correlation ($R^2 = 0.995$) representing the blots confined in the channel area of the paper chip. At concentrations higher than 3 mg mL⁻¹, the blot reached the waste circle area and the lateral spreading of the protein attenuated the length-increasing rate, which translated to the loss of linearity in the analytical curve. As stated before, increasing the channel length would increase the linear range of the protein quantification. However, if a real urine sample was tested in this paper chip design and resulted in a blot that reached the drain pad (therefore, protein concentration above 3 mg mL⁻¹), the subject would be under a severe proteinuria case.

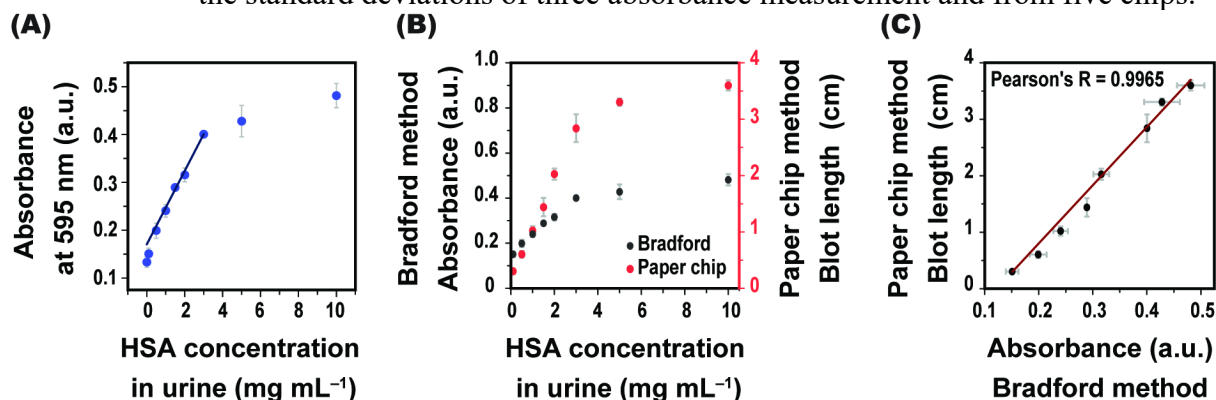
Bradford method was also performed to quantify proteins in the urine samples for analytical comparisons. The Bradford reagent reacts with the protein through its peptide bonds, resulting in a colorimetric response that can be measured by UV/Vis spectroscopy at 595 nm and its absorbance correlated to the protein concentration. The absorbance at 595 nm was plotted against HSA concentration as shown in Figure II.13A. The linear range for HSA detection in urine composed from 0.1 to 3 mg mL⁻¹ ($R^2 = 0.995$), as for the paper chip. The Bradford method presented a lower limit of quantification of 0.02 mg mL⁻¹ calculated according to IUPAC definition (Eq I – 5). For the paper chip, however, it was not possible to calculate the LOQ using the IUPAC definition since the blank measurements in this method does not result in any blot to measure its length. Therefore, the LOQ was defined as the lowest protein concentration that resulted in a blot in the paper chip channel, in this case 0.1 mg mL⁻¹. Although the Bradford method offered lower LOQ, the paper chip method is a low-cost sensing platform which does not require a spectrophotometer or large amount of Bradford reagent. The paper chip method also presented a higher sensitivity, as can be visualized by the larger changes in signal with increasing concentration of protein (Figure II.13B). Furthermore, the paper chips method correlated with the Bradford method (Figure II.13C). Table II.7 summarizes the figure of merit from both methods.

Figure II.12 - (A) Paper chips oxidized for 4 h after the immobilization of 0.5 μL of HSA 0, 0.1, 0.5, 1.0, 1.5, 2.0, 3.0, 5.0, and 10.0 mg mL^{-1} in urine pool. (B) Blot length vs. HSA concentration in urine pool; error bars indicate the standard deviation from 5 chips.



Source: Adapted by permission from Imamura *et al.* *Microchim Acta*, 2020, 187: 272 © 2020 Springer Nature Customer Service Gmb DOI: 10.1007/s00604-020-04250-6.

Figure II.13 - (A) Absorbance at 595 nm vs. HSA concentration in urine pool. Error bars indicate the standard deviation from three measurements. (B) Absorbance from Bradford method and blot length from paper chip method plotted against HSA concentration in urine. (C) Correlation between signals obtained from Bradford and paper chip methods. Error bars in x-axis and y-axis represent, respectively, the standard deviations of three absorbance measurement and from five chips.



Source: Adapted by permission from Imamura *et al.* *Microchim Acta*, 2020, 187: 272 © 2020 Springer Nature Customer Service Gmb DOI: 10.1007/s00604-020-04250-6.

Table II.7 - Summary of the figures of merit from the Bradford method (reference) and the paper chip method.

	Linear range (mg mL ⁻¹)	Sensitivity	Limit of quantification (mg mL ⁻¹)
Bradford method	0.1 to 3.0	0.0767 ua mg mL ⁻¹	0.02
Paper device	0.1 to 3.0	0.8666 cm mg mL ⁻¹	0.10

Source: Reprinted by permission from Imamura *et al.* *Microchim Acta*, 2020, 187: 272 © 2020 Springer Nature Customer Service Gmb DOI: 10.1007/s00604-020-04250-6.

A commercial urine test strip is available for a semi-quantitative analysis of protein. The protein level is given by a color scale corresponding a set of concentrations of 0.3, 1.0, 3.0, and 20 mg mL⁻¹. Any concentration smaller than 0.3 mg mL⁻¹ results in a color less intense than the scale and is considered as trace level of protein. The commercially available urine test strip is not sensitive enough to distinguish healthy levels of protein from microalbuminuria (0.01 to 0.3 mg mL⁻¹), which is a clinical marker of early diabetic nephropathy and concomitant cardiovascular disease.⁶⁴ The paper chip method could detect protein three times lower than the commercial strip, perceiving early symptoms of health problems.

II.5. CONCLUSION

Immobilization of proteins on paper is an important step for a fabrication of a biosensing devices in both lateral flow and flow-through assays. The immobilization of protein on paper was improved by oxidizing the chromatography paper for 0.5 h with NaIO₄ 0.5 M. The covalent bonding of protein on paper promotes the fabrication of more reproducible μ PADs as well as makes them more resistant to variabilities from handling. However, the oxidation process modified drastically the physical properties of the paper. The longer exposure of the cellulose in NaIO₄ resulted in a reduction of capillarity, loss of crystallinity and shrinkage of the substrate. Therefore, the oxidation process must be controlled and well-characterized.

The oxidized paper was applied as a low-cost platform to quantify protein in urine without the need of any instrument. The alternative method correlated really well with a standard method to quantify proteins and presented higher sensitivity. Although there is already a commercial urine dipstick for protein screening, the paper chips arise as quantitative determination of total protein and it even perceived cases of microalbuminuria. The protein quantification by this method still requires multiple steps, which can be further optimized for practical purposes. Moreover, this method allows the detection of any protein non-specifically and can be adjusted for several applications.

II.6. REFERENCES

1. HU, J.; WANG, S.; WANG, L.; LI, F.; PINGGUAN-MURPHY, B.; LU, T. J.; XU, F. Advances in paper-based point-of-care diagnostics. **Biosensors and Bioelectronics**, Oxford, v. 54, p. 585–597, 2014. DOI: 10.1016/j.bios.2013.10.075.
2. NANTHASURASAK, P.; CABOT, J. M.; SEE, H. H.; GUIJT, R. M.; BREADMORE, M. C. Electrophoretic separations on paper: past, present, and future- a review. **Analytica chimica acta**, Amsterdam, v. 985, p. 7–23, 2017. DOI: 10.1016/j.aca.2017.06.015.
3. FOSTER, L. S.; GRUNTFEST, I. J. Demonstration experiments using universal indicators. **Journal of Chemical Education**, Washington, v. 14, p. 274, 1937. DOI: 10.1021/ed014p274.
4. MARTINEZ, A. W.; PHILLIPS, S. T.; BUTTE, M. J.; WHITESIDES, G. M. Patterned paper as a platform for inexpensive, low-volume, portable bioassays. **Angewandte Chemie**, Weinheim, v. 119, p. 1340–1342, 2007. DOI: 10.1002/ange.200603817.
5. FREE, A. H.; ADAMS, E. C.; KERCHER, M. L.; FREE, H. M.; COOK, M. H. Simple specific test for urine glucose. **Clinical Chemistry**, Cary, v. 3, p. 163–168, 1957. DOI: 10.1093/clinchem/3.3.163.
6. JARUJAMRUS, P.; TIAN, J.; LI, X.; SIRIPINYANOND, A.; SHIOWATANA, J.; SHEN, W. Mechanisms of red blood cells agglutination in antibody-treated paper. **Analyst**, Cambridge, v. 137, p. 2205–2210, 2012. DOI: 10.1039/C2AN15798E.
7. ABE, K.; SUZUKI, K.; CITTERIO, D. Inkjet-printed microfluidic multianalyte chemical sensing paper. **Analytical Chemistry**, Washington, v. 80, p. 6928–6934, 2008. DOI: 10.1021/ac800604v.
8. HALDER, E.; CHATTORAJ, D. K.; DAS, K. P. Adsorption of biopolymers at hydrophilic cellulose–water interface. **Biopolymers**, Hoboken, v. 77, p. 286–295, 2005. DOI: 10.1002/bip.20232.
9. SU, S.; ALI, MD. M.; FILIPE, C. D. M.; LI, Y.; PELTON, R. Microgel-based inks for paper-supported biosensing applications. **Biomacromolecules**, Washington, v. 9, p. 935–941, 2008. DOI: 10.1021/bm7013608.
10. SU, S.; NUTIU, R.; FILIPE, C. D. M.; LI, Y.; PELTON, R. Adsorption and covalent coupling of ATP-binding DNA aptamers onto cellulose. **Langmuir**, Washington, v. 23, p. 1300–1302, 2007. DOI: 10.1021/la060961c.
11. CREDOU, J.; BERTHELOT, T. Cellulose: from biocompatible to bioactive material. **Journal of Materials Chemistry B**, Cambridge, v. 2, p. 4767–4788, 2014. DOI: 10.1039/C4TB00431K.
12. LEVY, I.; SHOSEYOV, O. Cellulose-binding domains: biotechnological applications. **Biotechnology Advances**, Oxford, v. 20, p. 191–213, 2002. DOI: 10.1016/S0734-9750(02)00006-X.

13. SASSOLAS, A.; BLUM, L. J.; LECA-BOUVIER, B. D. Immobilization strategies to develop enzymatic biosensors. **Biotechnology Advances**, Oxford, v. 30, p. 489–511, 2012. DOI: 10.1016/j.biotechadv.2011.09.003.
14. KONG, F.; HU, Y. F. Biomolecule immobilization techniques for bioactive paper fabrication. **Analytical and Bioanalytical Chemistry**, Heidelberg, v. 403, p. 7–13, 2012. DOI: 10.1007/s00216-012-5821-1.
15. KIM, D.; HERR, A. E. Protein immobilization techniques for microfluidic assays. **Biomicrofluidics**, Melville, v. 7, p. 041501, 2013. DOI: 10.1063/1.4816934.
16. COSERI, S.; BILIUTA, G.; SIMIONESCU, B. C.; STANA-KLEINSCHEK, K.; RIBITISCH, V.; HARABAGIU, V. Oxidized cellulose: survey of the most recent achievements. **Carbohydrate Polymers**, Oxford, v. 93, p. 207–215, 2013. DOI: 10.1016/j.carbpol.2012.03.086.
17. KIM, U.-J.; KUGA, S.; WADA, M.; OKANO, T.; KONDO, T. Periodate oxidation of crystalline cellulose. **Biomacromolecules**, Washington, v. 1, p. 488–492, 2000. DOI: 10.1021/bm0000337.
18. STRONG, E. B.; KIRSCHBAUM, C. W.; MARTINEZ, A. W.; MARTINEZ, N. W. Paper miniaturization via periodate oxidation of cellulose. **Cellulose**, Dordrecht, v. 25, p. 3211–3217, 2018. DOI: 10.1007/s10570-018-1805-4.
19. PARK, S.; BAKER, J. O.; HIMMEL, M. E.; PARILLA, P. A.; JOHNSON, D. K. Cellulose crystallinity index: measurement techniques and their impact on interpreting cellulase performance. **Biotechnology for Biofuels**, London, v. 3, p. 10, 2010. DOI: 10.1186/1754-6834-3-10.
20. MCCANN, L.; BENAVIDEZ, T. E.; HOLTSCRAW, S.; GARCIA, C. D. Addressing the distribution of proteins spotted on μ PADs. **The Analyst**, Cambridge, v. 142, p. 3899–3905, 2017. DOI: 10.1039/C7AN00849J.
21. JULIAN, B. A.; SUZUKI, H.; SUZUKI, Y.; TOMINO, Y.; SPASOVSKI, G.; NOVAK, J. Sources of urinary proteins and their analysis by urinary proteomics for the detection of biomarkers of disease. **Proteomics Clinical applications**, Weinheim, v. 3, p. 1029–1043, 2009. DOI: 10.1002/prca.200800243.
22. BARRATT, J.; TOPHAM, P. Urine proteomics: the present and future of measuring urinary protein components in disease. **Canadian Medical Association Journal**, Ontario, v. 177, p. 361–368, 2007. DOI: 10.1503/cmaj.061590.

CHAPTER III

***Shrinky-Dinks* for fabrication of wearable microfluidic devices for sweat glucose and lactate sensing**

III.1. INTRODUCTION

Athletes are continually seeking new technologies to enhance their performance and improve their safety to gain competitive advantages on the field. Time-motion analysis, such as video recording and computer digitalization, was commonly utilized in sports science. However, these procedures are laborious to acquire data, and they were incapable of retrieving key metrics to the current physiological state of the athletes.^{1,2} With the advance of wearable technologies, important physiological and biochemical parameters can be acquired in real-time, quantifying the athlete's health and performance. In sports medicine, saliva and sweat from eccrine glands are commonly analyzed since they are easily accessed without interrupting the athlete during activities.² To analyze saliva during a physical activity, a mouthguard device is required, limiting the applicability depending on the sport (*e.g.*, swimming). Moreover, the modified mouthguards described in the literature could not continuously measure biomarkers in saliva.² On the other hand, sweat can be sourced continuously and non-invasively. The eccrine glands are easily accessed in the body, and the wearable devices can be placed in many regions, such as the forearm, back, fingers, wrist, forehead, among other parts of the body. The sweat is rich in biomarkers important for sports medicine: glucose, lactate, orexin-A, cortisol, some ions (Na^+ , Cl^- , K^+ , NH_4^+), and pH.² Glucose is a known biomarker for diabetes, and in sports medicine, it can control the fatigue levels in the athlete. Lactate is also an important biomarker that indicates body fatigue and can indicate body exertion and exercise intensity since it is produced during anaerobic activity without sufficient oxygen.² By monitoring these biomarkers in sweat, it is possible to track the biochemical fatigue of the body, intervene early if necessary to prevent injuries, and maximize performance.¹ Wearable devices are ideal for tracking individual parameters in athletes and enables personalized sports medicine.

Microfluidic wearable technology is defined as the application of microfluidics into wearable devices.³ As microfluidics, by definition, manipulates a minute volume of samples in a confined space, they have been widely applied to develop wearable devices to retrieve the signals originated by the body at the chemical level. The precise handling of samples combined with the small volume required for the analyses enabled microfluidics to extract information from samples with limited volumes, such as sweat. Furthermore, microfluidic devices are ideal for attaching to the body without causing discomfort since they are miniaturized and lightweight. Besides appropriate size and weight, the wearability of a device depends on properly mounting onto the skin, which consists of irregular, curvilinear, and contoured surfaces. Moreover, the skin is highly deformable and viscoelastic.³ Therefore, the materials employed for wearable

microfluidic devices are often soft, flexible, and stretchable. Commonly used materials as a substrate consist of fabric, polymer, and silicone rubber, which present low elastic modulus. These materials minimize the slipping of the device from the skin since they can easily deform under slight pressure without detachment or fracture.⁴

Polydimethylsiloxane (PDMS) is a silicon-based polymer commonly used for soft lithography. Besides the excellent flexibility and stretchability, PDMS is biocompatible and optically transparent.⁵ Furthermore, chemical modifications on PDMS are extensively reported in the literature for altering hydrophobicity, immobilizing biomolecules, and covalently bonding onto other substrates without the need for adhesive.⁶ There are several prototyping techniques for fabricating PDMS-based microfluidic devices. They can be classified as photolithography, print-and-peel, which uses printers to make the molds, and scaffolding, which commonly employ 3D printers.⁶ Photolithography is the gold standard for the fabrication of PDMS-based microfluidic networks. This technique is based on silicon molds fabricated by photolithography and deep reactive ion etching that defines the geometry of the channels, valves, and reservoirs. The uncured PDMS is cast onto the silicon mold and is peeled off after the curing process. Photolithography based on silicon molds produces high resolution and accurate microfluidic networks at the sub-micrometer scale. Although this technique is still the most applied for the fabrication of PDMS-based microfluidic devices, it is a laborious and time-intensive (up to 24 h) manufacturing process, requiring specialized equipment and laboratory conditions, such as cleanroom.⁵ In contrast, the print-and-peel techniques rapidly prototype the molds at a low cost outside the cleanroom. The molds can be printed onto a transparency film using a laser-jet printer. The final PDMS device presented channels widths of 60 μm and depth of 10 μm .⁷ Although the technique is straightforward, the molds are not reusable due to their degradation after casting. Besides, the channels' low aspect ratio (depth/width) increases the resistance of the solution to flow in the channels and restricts the fluidic manipulation. Channels with a higher aspect ratio were achieved by Grimes *et al.* by replacing the transparency films with the toy Shrinky-Dinks (SD), on which the microfluidic networks were printed.⁸ SD consists of a thermoplastic sheet, such as polystyrene (PS), that shrinks upon heating. The drawn or printed features on the plastic shrunk dimensionally with the thermoplastic film by 63% from the original size. In addition, there was an increase in the height of the features by over 500%. The shrunk thermoplastic was used as the mold for PDMS, resulting in channels as thin as 65 μm and down to 80 μm depth.⁸ The SD molds are reusable, like the silicon wafers, and present inherent rounded channels, which are difficult to make by typical photolithography.

The microfluidic devices fabricated by SD molds were tested as gradient generators and for the flowing of mammalian cells.⁸

Textile or fabric-based microfluidic devices are an extension of the microfluidic paper-based analytical devices (μ PAD). μ PADs have been exploited for wearable applications since the paper is lightweight and cheap with slight flexibility. The capillarity from the cellulose fibers promotes the flowing of the sweat into the device, enabling sample collection. There are several microfabrication techniques on paper described in the literature, as well as chemical modifications for a variety of detection strategies. However, paper is fragile, which can be easily torn apart, especially when it is wet. Besides, papers do not often conformally mount onto the skin. Fabric-based microfluidic devices also exploit the fibers' capillarity for sample collection with additional resistance to tear and conformal mounting on skin.

μ PADs are often coupled with colorimetric transduction because it is simple and does not require external equipment. A sample-to-answer system can be simply developed for wearable devices with colorimetric assay without a power supply for electronics components required for data acquisition and transfer systems. However, colorimetric detection assessed by the human eye is susceptible to variability from user interpretations, suffering from person-to-person perceptual differences which can cause inaccurate results.⁹ To mitigate the subjective analysis on colorimetric detection, the assay can be coupled with an image acquisition system, such as a scanner or cellphone, and an image processing tool. In a digitalized image, the colors information is converted into a numeric matrix of binary digits (0 or 1) that form a checkered structure, known as a matrix of points. Each point is equivalent to a pixel of the image. The colorimetric analysis of digitalized images by image processing software, such as Adobe Photoshop, Image J, and MATLAB, is known as digital image colorimetry (DIC).

In DIC, common color spaces, also known as color models, are RGB and HSV (or HSB, HSL). RGB is a color model system composed of the primary colors Red, Blue, and Green. The model is based on the linear combination of the primary colors to generate the remaining colors. The intensity of each color ranges from 0 to 255 or 0 to 1 in normalized values. Since the black color is the absence of any color, it is represented as [0 0 0], and white as [1 1 1] or [255 255 255].⁹ HSV model defines color space in terms of three components: hue, saturation, and brightness. The hue component is represented by a circle with the color types ranging from 0° to 360°. For example, red, yellow, green, and cyan are represented as 0°, 60°, 120°, and 180° respectively. Saturation is the intensity of color, and brightness (or value) is the brightness of the color, both ranging from 0 to 100%.¹⁰ For monotonal and colorless-to-colored responses, it is indicated to report the intensity as one or more components of RGB and as saturation channel

of HSV color space. Meanwhile, for bitonal transition, the hue channel of HSV is more indicative of distinguishing bitonal transitions.⁹ Other color models, such as L*a*b and Y'UV, are often applied in DIC for image segmentation and masking.⁹

In this Chapter, we integrated paper-based colorimetric assay into a soft microfluidic device fabricated with SD molds for sweat sampling and spot analysis of glucose and lactate for physical activities.

III.2. AIMS

Fabrication of soft microfluidics with SD molds and evaluation of the wearability. Optimize the colorimetric detection of glucose and lactate on paper-based platforms. Integrate the SD-based microfluidics with the μ PAD for glucose and lactate.

III.3. MATERIALS & METHODS

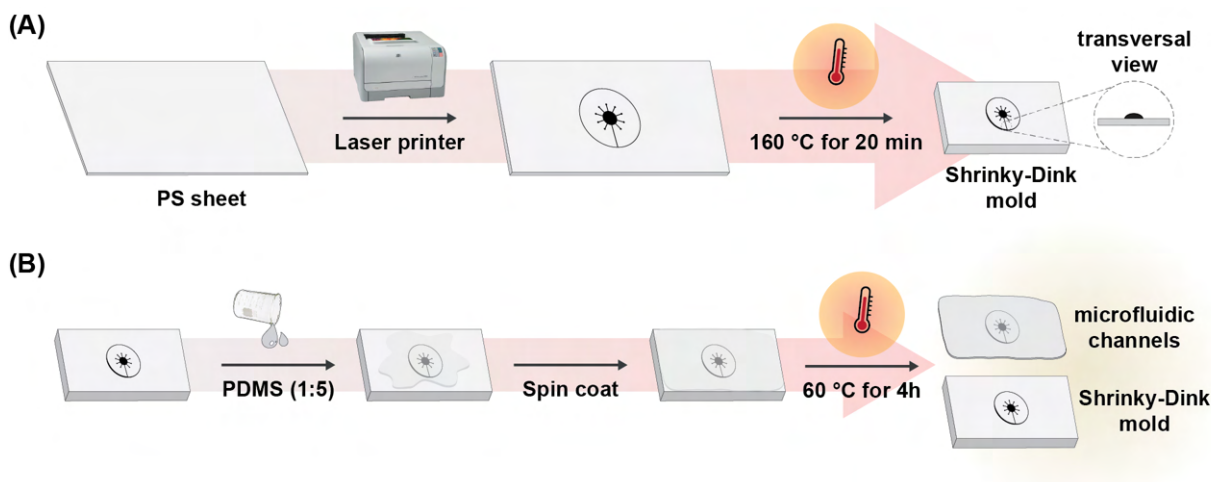
III.3.1. Fabrication of microfluidic channel by Shrinky-Dinks

SD-based mold was used to fabricate soft microfluidic channels for wearable devices. For the fabrication of the molds, the microfluidic design was drawn in AutoCAD software upscaled by 2.6 times the desired final size. The pattern was printed with a laser printer (model HP CP1215) on the highest quality printing mode (photography printing) on prestressed polystyrene (PS) sheet up to 5 times to optimize the microfluidic channel height. The PS sheet with the printed tonner was heated up in an oven for 20 min at 160 °C for the shrinking. (Figure III.1A). Before taking the PS piece out of the oven, a Teflon weight with a flat surface was placed on top to flatten the shrunk PS, which can curl during the shrinking process.

For the *in vitro* studies, an acrylic wall was glued with epoxy glue around the embossing to function as a container to hold the uncured PDMS and control the thickness of the final microfluidic device. Around 2 g of uncured PDMS (ratio of 1:5) was deposited onto the mold and degassed for 10 min before curing at 60 °C for 4 h.

Since the on-body studies required a thinner PDMS layer for a conformal adhesion on the skin, there was no need for the acrylic wall. However, the uncured PDMS (1:5) was deposited on the mold and spun coat at 100 rpm for 10 s to guarantee a uniform film. The PDMS was also degassed for 10 min then cured at 60 °C for 4 h (Figure III.1B).

Figure III.1 - Fabrication steps of (A) Shrinky-Dinks (SD) molds and (B) PDMS microfluidic devices with the SD molds.



Source: Own authorship.

Once cured, the PDMS was lifted off the mold with a scalpel. A punch with 2 mm of diameter was used to create the holes required for the connections with the syringe pump. To seal the channels, the patterned PDMS was covered with double-sided polystyrene adhesive (thickness of 0.3 mm) or with a thin layer of flat PDMS (1:10) that was prior activated with O₂ plasma for 5 min. The resulting microfluidic channels were characterized by stylus profilometry.

III.3.2. Functionalization of the paper

Chromatography paper was cut in small disks of 3 mm of diameter in a laser cutter and washed abundantly with distilled water prior to use. For the oxidation, the paper disks were soaked in NaIO₄ 0.5 mol L⁻¹ solution in DI water for 30 min, as previously described in *CHAPTER II*.

III.3.2.1. Enzymatic assays on paper for glucose

The colorimetric assay for glucose consisted of a couple of enzymes, glucose oxidase (GOx) and horseradish peroxidase (HRP), and a color indicator, 3,3',5,5'-tetramethylbenzidine (TMB).

The oxidized and native paper disks were modified with 1 or 2 μL of low-weight chitosan solution (15 mmol L⁻¹ in acetic acid) to improve the sensitivity of the color change. After the application, the paper disks were dried at room temperature for 30 min. Then 1 μL of a solution containing both enzymes, GOx at 120 U mL⁻¹ and HRP at 30 U mL⁻¹ in phosphate

buffer (0.01 mol L⁻¹, pH 7.4), was dropped on the paper. After 20 min drying at room temperature, 1 μL of TMB 15 mmol L⁻¹ in methanol was added to the paper. The paper was dried for another 10 min prior to use.

For the static setup, 3 μL of glucose solutions ranging from 0.1 to 1 mmol L⁻¹ in PBS (0.01 mol L⁻¹, pH 7.4) was added in each paper disk.

III.3.2.2. Enzymatic assays on paper for lactate

Lactate oxidase (LOx) was combined with HRP and TMB to detect lactate, similarly to glucose enzymatic assay. The oxidized and native paper disks were modified with 1 μL of a solution with both enzymes (LOx at 40 U mL⁻¹ and HRP 30 U mL⁻¹) and dried for 30 min. Then 1 μL of TMB 15 mmol L⁻¹ in methanol was added, and the papers were allowed to dry for 10 min before lactate solution application.

Glycolate was chosen to inhibit the LOx kinetics and improve the concentration range of the assay. Glycolate solution was prepared by dissolving glycolic acid and neutralizing the pH to 7.0 with NaOH solution. The glycolic solution was then diluted in water to reach final concentrations of 200 and 400 mmol L⁻¹. For the enzymatic inhibition tests, 1 μL of glycolate solution was dropped on the paper disks 15 min prior to the addition of the enzymes. For the tests with chitosan, the inhibitor was added after chitosan modification, which was similar to the glucose assay. For static setup, 3 μL of lactate solutions in PBS was added in each paper disk.

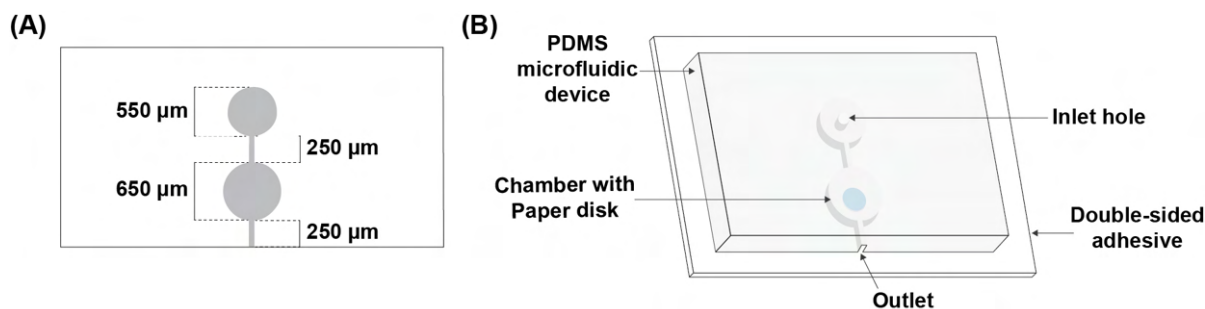
For the kinetics study of the inhibition test, the R channel values were plotted over time for every concentration of lactate, obtaining a horizontal asymptote profile. The reaction rate was extracted from the plot by calculating the slope of the linear descending region from the R values vs. time plot. For the Lineweaver-Burk plot, the inverses of the lactate concentration (x-axis) and the reaction rate were plotted (y-axis).

III.3.3. Colorimetric enzymatic assays in in-vitro microfluidic device

A microfluidic device similar to the wearable patch was fabricated to emulate the colorimetric assay in wearable devices. The device consisted of two channels connected diametrically to a chamber where the functionalized paper was placed, as illustrated in Figure III.2. One of the channels was also attached to an inlet hole through which the syringe pump

was connected. In all setups, the flow rate was fixed at $5 \mu\text{L min}^{-1}$ to mimic the highest flow rate in the relevant physiological range (1 to $5 \mu\text{L min}^{-1}$).^{11,12}

Figure III.2 - (A) Dimensions of the PDMS microfluidic channels for in-vitro assay. (B) Assembled microfluidic device.



Source: Own authorship.

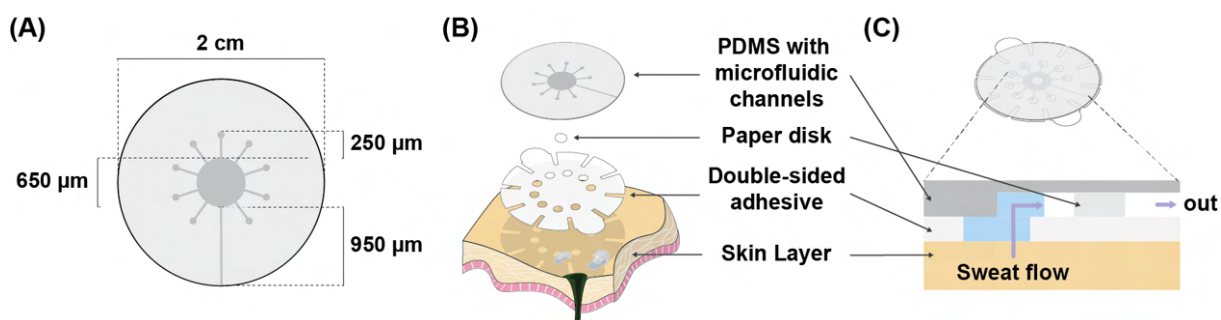
Two sets of systems were evaluated. One of them consisted of pumping a solution of 1 mmol L^{-1} of glucose in PBS for 5 min, followed by pumping only PBS for another 5 min, to evaluate the washing off the color on the paper. The second setup consisted of the inverse order of solutions, *i.e.*, pumping first the PBS then the glucose solution, to evaluate the washing off the reagents from the paper disks. Both native and oxidized papers functionalized with the enzymes and the dye were assessed.

III.3.4. On-body measurement of glucose and lactate in sweat

For the on-body assay, the SD-based device consisted of nine inlet holes connected through channels of $250 \mu\text{m}$ to a central chamber ($d = 650 \mu\text{m}$) where the functionalized paper was placed, as illustrated in Figure III.3A. The chamber was also connected with an outlet channel to prevent back-pressure and allow the constant flow of sweat into the chamber. The pattern was sealed with double-sided polystyrene adhesive that was previously cut by a laser cut in the layout as shown in Figure III.3B. The cuts along the circumference of the adhesive were created to improve the conformal attachment onto the skin. Figure III.3C illustrates the transversal view of the wearable device and the sweat flow through the microfluidic channel.

For the on-body measurement, the SD-based wearable device was placed on the subject's back or arms previously cleansed with alcohol. The subject then exercised for 30 min on a stand-bike or outdoor bike to provide sweat for the analysis.

Figure III.3 - (A) Design of the wearable microfluidic device with the dimensions. (B) Layers of the wearable device on top of the skin. (C) Transversal view of the wearable microfluidic device.



Source: Own authorship.

III.3.5. Color Analysis

For the analysis of the colorimetric assay, a cellphone was used to record the color progression. The information was extracted as frames for every one second of the recording. The frames were later analyzed by a MATLAB algorithm developed by the author, consisting of the following steps:

- i. Identify the paper disks in the frames;
- ii. Find the pixels that compose the paper disk, *i.e.*, that are arranged within a circle with a diameter that fits the paper disk;
- iii. Analyze the color distribution in RGB values for each pixel within the circle;
- iv. Calculate the average of each color space (red, blue, and green), taking all the pixels within the circle.

The RGB was chosen as the color model since the assay consisted of a color transition from colorless to blue. It is important to state that the observed color is represented by the model as its complementary color, as shown in Table III.1.¹³ Therefore, the colorimetric assays in this work had the most pronounced change in the red channel.

Table III.1 - Relation between RGB channel, observed, and complementary colors.

Channel color	Observed color	Complementary color
R	Blue	Orange
G	Red	Green
B	Yellow	Purple

Source: Adapted from Benedetti *et al.*¹³

This procedure was repeated for all paper disks in every assay. The averages and the standard deviations were calculated by the final RGB values from each paper disk. In a kinetic

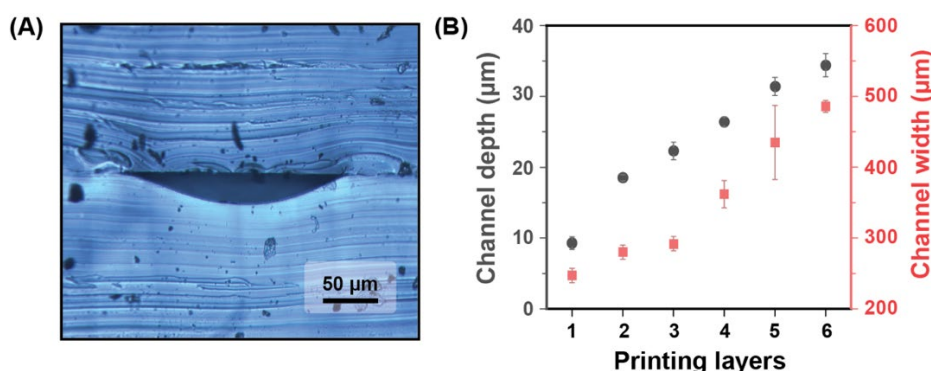
study, the same paper disk was analyzed over predefined time stamps (10 s interval up to 2 min, 30 s interval up to 5 min, and 1 min interval up to 10 or 15 min). For the concentration curves, the paper disks were analyzed after a time determined in the kinetics study (when the color reaches the saturation).

III.4. RESULTS & DISCUSSION

III.4.1. Characterization of the microfluidic channels with Shrinky-Dinks mold

The prestressed plastic shrinks upon heating it above its glass transition temperature (100 °C). Along with the shrinkage of the thermoplastic, the heating process also induces the diminishing of the pattern of materials deposited on its surfaces, such as thin metal films or printed layers of toner. As shrinkage occurs dimensionally, the height increases. Since the toner melts at temperatures above 100 °C, the stress on the supporting thermoplastic forces its structure to shrink along into a solid embossing. As previously showed by Grimes *et al.*,⁸ the shrunk toner presented rounded corners, which resulted in rounded PDMS microfluidic channels, as can be observed in Figure III.4A.

Figure III.4 - Microfluidic channels fabricated with SD-based molds. (A) Vertical cut of PDMS channel sealed with thin layer of PDMS. (B) Microfluidic channel depth and width in function of printing layers. Error bars indicate the standard deviation for three samples.



Source: Own authorship.

The depth of the PDMS channels is regulated by the height of the toner on the mold, which can be adjusted by the number of printing layers. As shown in Figure III.4B, the channel depth increased with printing layers, reaching up to 34.4 μm for 6 layers of printed toner. The nominal width of the channel, *i.e.*, adjusted in the drawing software, was 352.8 μm. The final PDMS channel presented a width of 247 ± 10 μm for 1 printing layer, corresponding to 30% of

the nominal width. The decrease in width resulted from the pattern's shrinkage during the mold fabrication process. However, after four layers of printed toner, the channels broadened above the nominal width, resulting in $362 \pm 19 \mu\text{m}$ of width. This can be explained by the spreading of toner during the heating process since it presents in its melted state. Furthermore, the alignment of the printed design for consecutive printings becomes troublesome, which can also result in the broader channels as well as difficulties in achieving reproducible channels. Considering the difficulties on aligning several printing layers and the required minimum depth for a functional microfluidic channel, the following experiments were performed in microfluidic channels fabricated with Shrinky-Dink molds with four printed layers.

The fabrication of the SD molds is straightforward and requires simple equipment, a laser printer and an oven, allowing the microfluidics fabrication in low-resource laboratories. The channels resulting from these molds presented depth and width with low standard deviation for a few printing layers. More importantly, the molds are reusable, avoiding time and resource waste. This technique is adaptable for many applications, and its limitation relies on the printers' resolutions.

The PDMS channels cast by Shrinky-Dink molds with four toner layers presented a final depth of $26.4 \pm 0.67 \mu\text{m}$. For the on-body and in-vitro devices, the length of the channels was 2.5 mm, measured with a caliper. The calculated volume of the channels was 23.9 nL. For the chambers, the calculated volume was 87.6 nL, considering a diameter of 6.5 mm also measured with the caliper. The large diameter combined with the thin layer of PDMS resulted in the collapse of the chamber due to the lack of structural support in the center of the chamber, obstructing the flow.⁶ However, placing the paper disk ($d = 3 \text{ mm}$) in the middle of the chamber prevented the collapsing and carried the reagents necessary for the colorimetric assay.

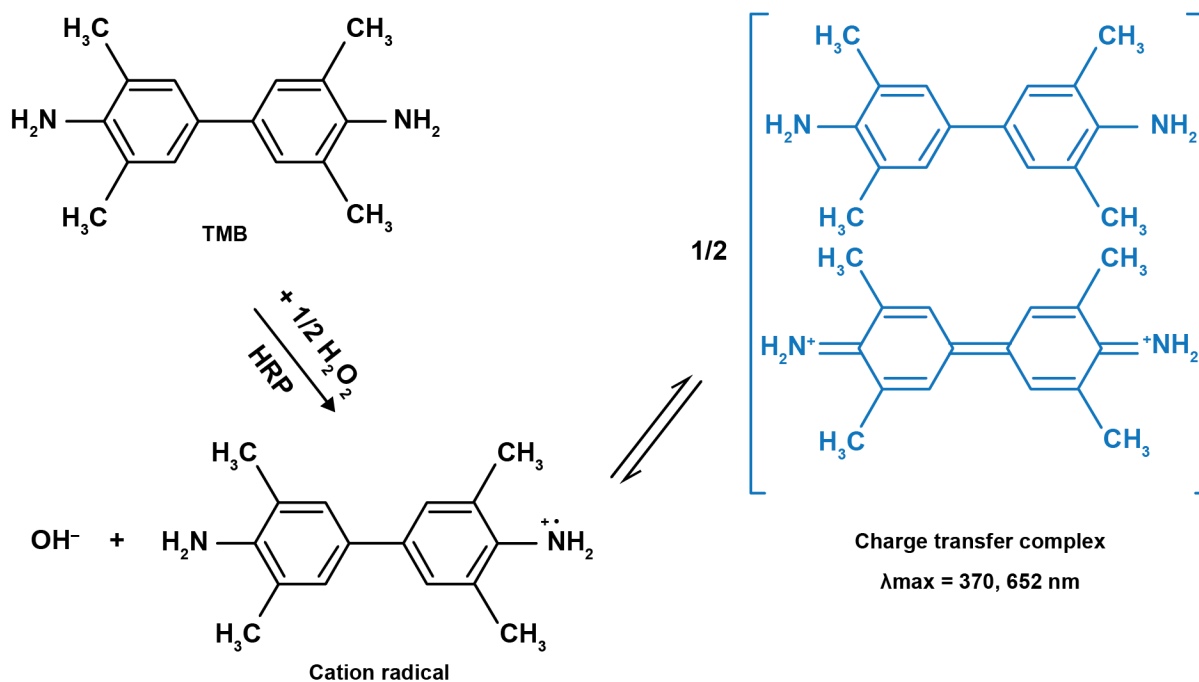
Both wearable and in-vitro devices were reusable after the colorimetric assay. The PDMS piece was detached from the double-sided adhesive with isopropanol. The adhesive and the paper disks were discarded after the assay. Before new usage, the PDMS piece was abundantly washed in DI water and sonicated in isopropanol to remove any interferents trapped in the structure. Moreover, the PDMS stands high temperature, such as in an autoclave, and deeper cleaning of the channels can be performed if necessary.

III.4.2. Optimization of enzymatic colorimetric assay

III.4.2.1. Effect of chitosan on glucose enzymatic assay

As briefly discussed in *CHAPTER I*, the first enzymatic sensor and many following biosensors for glucose are based on its oxidation by the GOx. The peroxide resulting from the oxidation of glucose is consumed by the HRP, which oxidizes the colorless TMB to a cation radical, forming a charge-transfer complex with maximum absorbance at 370 and 650 nm (Figure III.5). TMB can oxidize once more to form a second oxidized product with maximum absorbance at 420 nm, which is only stable in acidic conditions.¹⁴ Although this strategy of applying GOx, HRP, and a chromogenic reagent is largely described in the literature, only a few works achieved enough sensitivity to detect glucose at a lower range of concentrations found in sweat (from 0.01 to 1.11 mmol L⁻¹ according to Lee *et al.*¹⁵ or 0.02 to 0.6 mmol L⁻¹ according to Nery *et al.*¹⁶).

Figure III.5 - One electron oxidation process of TMB to a cation radical and subsequent formation of charge-transfer complex in the presence of H₂O₂ and HRP.

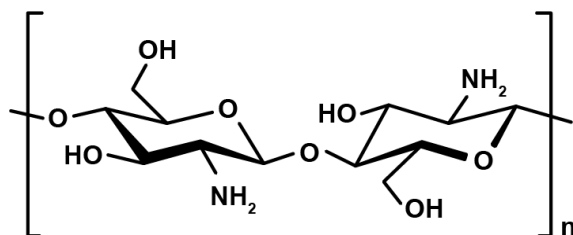


Source: Adapted from Josephy *et al.*¹⁴

Chitosan is a biopolymer with a backbone similar to cellulose but with amine groups, that protonate at pH lower than 6.2 (Figure III.6). Moreover, this biopolymer is biodegradable, biocompatible, and biofunctional. It has been widely applied in the biosensing field as an immobilization support of biomolecules.¹⁷ Chitosan-modified paper-based devices have

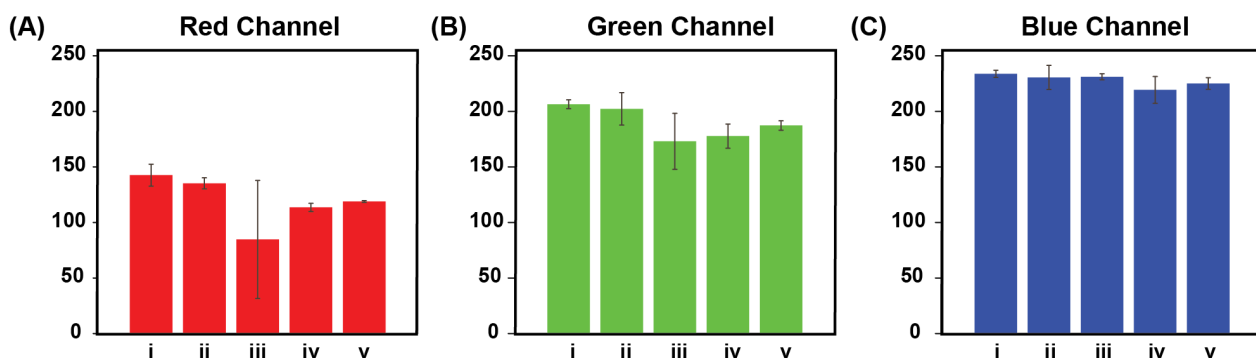
improved the sensitivity of colorimetric enzymatic assays for glucose and uric acid.¹⁸ Figure III.7 illustrates the effect of chitosan on glucose colorimetric assay, which resulted in a more intense blue color, represented in the graph by lowering the values of red channels. Chitosan improves the color uniformity and intensity by providing solid support for the enzymes to be adsorbed and ensuring a more effective reactive area.¹⁸

Figure III.6 - Chitosan chemical structure.



Source: Adapted from Koev *et al.*¹⁷

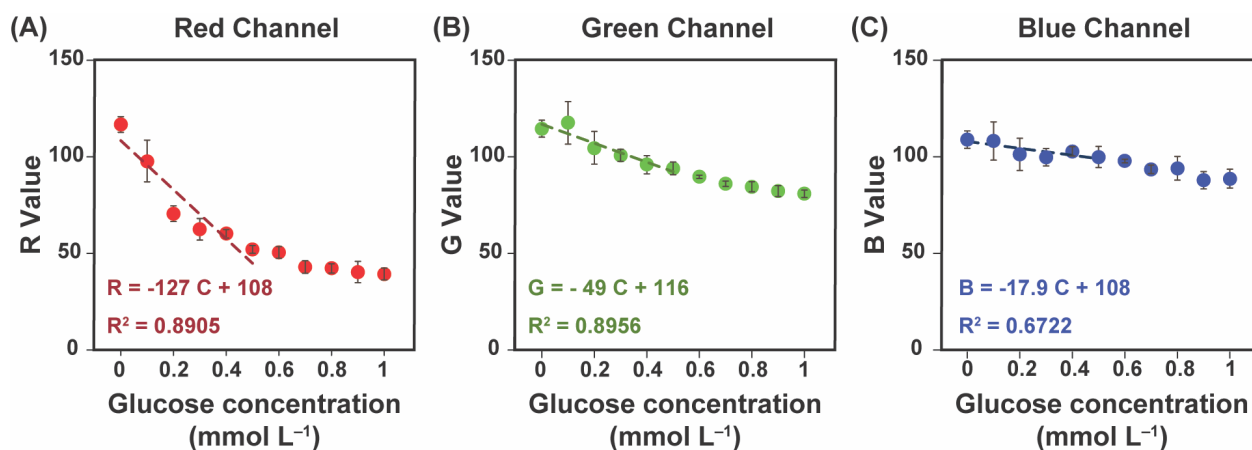
Figure III.7 - Chitosan effect on glucose colorimetric assay for the channels (A) red, (B) green, and (C) blue. Tested conditions: (i) without chitosan, (ii) with acetic acid, (iii) with 1 μL of chitosan, (iv) with 2 μL of chitosan, and (v) with 3 μL of chitosan. Error bars represent the standard deviation for three samples.



Source: Own authorship.

The volume of chitosan deposited on the paper disk influenced on the final color, which can be explained by the distribution of the chitosan through the cellulose fiber. For 1 μL of chitosan, the volume was too small to cover the paper disk in uniformly, which contributed to the significant deviation of color among the replicates. Two and three μL of chitosan showed similar performance. However, due to the faster drying of the chitosan required to continue the next functionalization steps and lower consumption of reagents, two μL of chitosan was applied for the following experiments, including for the concentration curve illustrated in Figure III.8. The glucose concentration curve is shown for each color channel in the concentration range relevant in sweat. The red channel showed the most change in color with increasing glucose concentration. However, the color intensity saturated around 0.5 mmol L^{-1} .

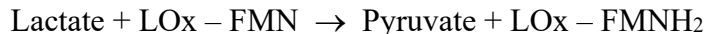
Figure III.8 - Concentration curve of glucose in PBS from 0 to 1 mmol L⁻¹ for (A) red, (B) green, and (C) blue channels. Linear fit represented by the dotted line from 0 to 0.5 mmol L⁻¹ and parameters inserted in the graphs. Error bars represent the standard deviation for three measurements.



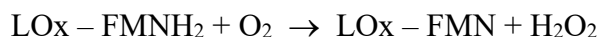
Source: Own authorship.

III.4.2.2. Effect of an inhibitor on lactate enzymatic assay

Lactate is oxidized to pyruvate by the enzyme lactate oxidase (LOx), forming peroxide as a co-product:



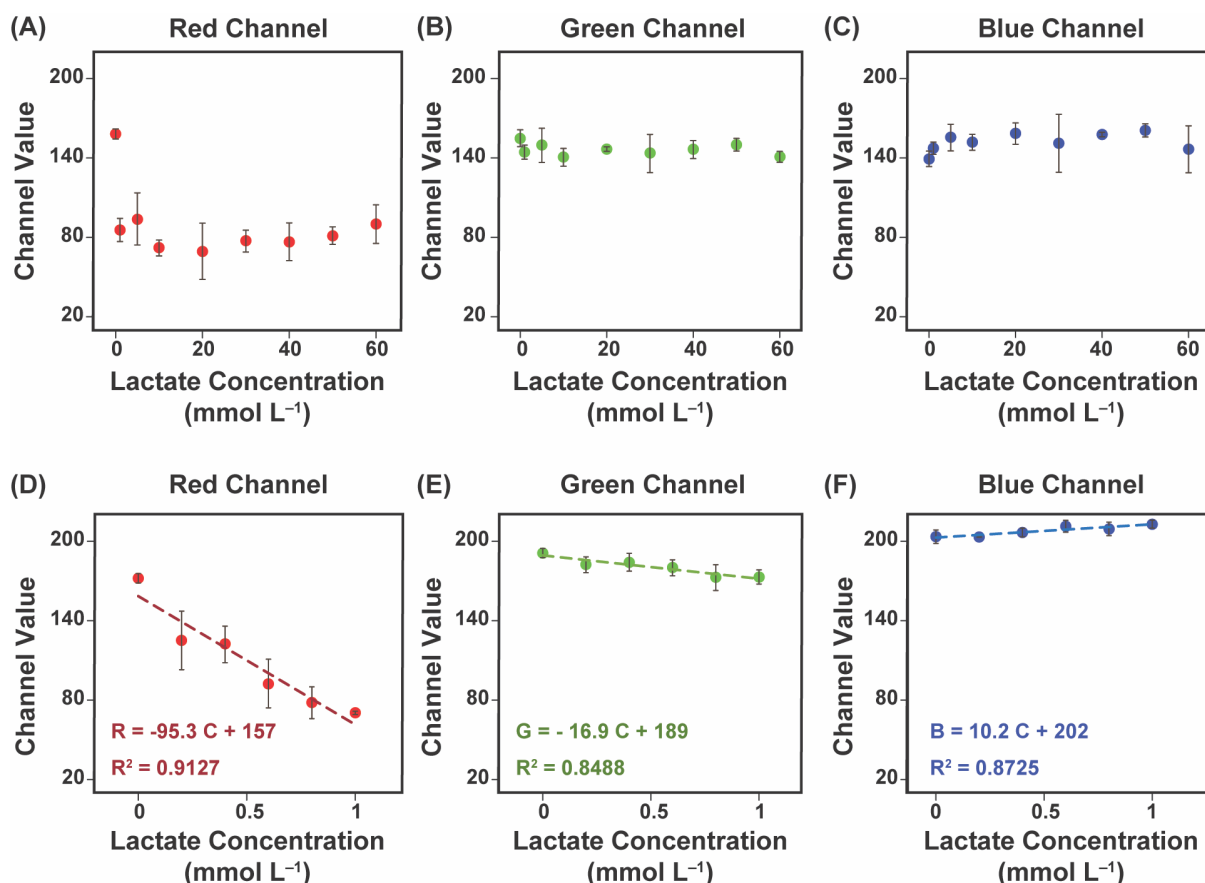
Similarly to GOx, LOx also depends on a redox cofactor, flavin-mononucleotide (FMN), which receives the electrons from the lactate. The FMNH₂ recovers its oxidized states by promoting the reduction of oxygen to peroxide:



The peroxide is then consumed by the HRP and the colorless TMB is oxidized to its blue product, as shown in Figure III.5.

The change in color from TMB was evaluated for lactate in a concentration range typically reported in sweat, from 1 to 60 mmol L⁻¹, as shown in Figure III.9A – C. Even without the addition of chitosan, the response saturated after 1 mmol L for all color channels. The saturation can be explained by the LOx Michaelis-Menten constant (K_M) of 0.43 mmol L⁻¹ for L-lactate. At the K_M , the reaction rate reaches half of the maximum rate (V_{\max}), and the enzyme is saturated by the substrate.¹⁹ A linear range for lactate can be achieved in a concentration range closer to the K_M value, such as from 0 to 1 mmol L⁻¹ in PBS, as illustrated in Figure III.9B – D.

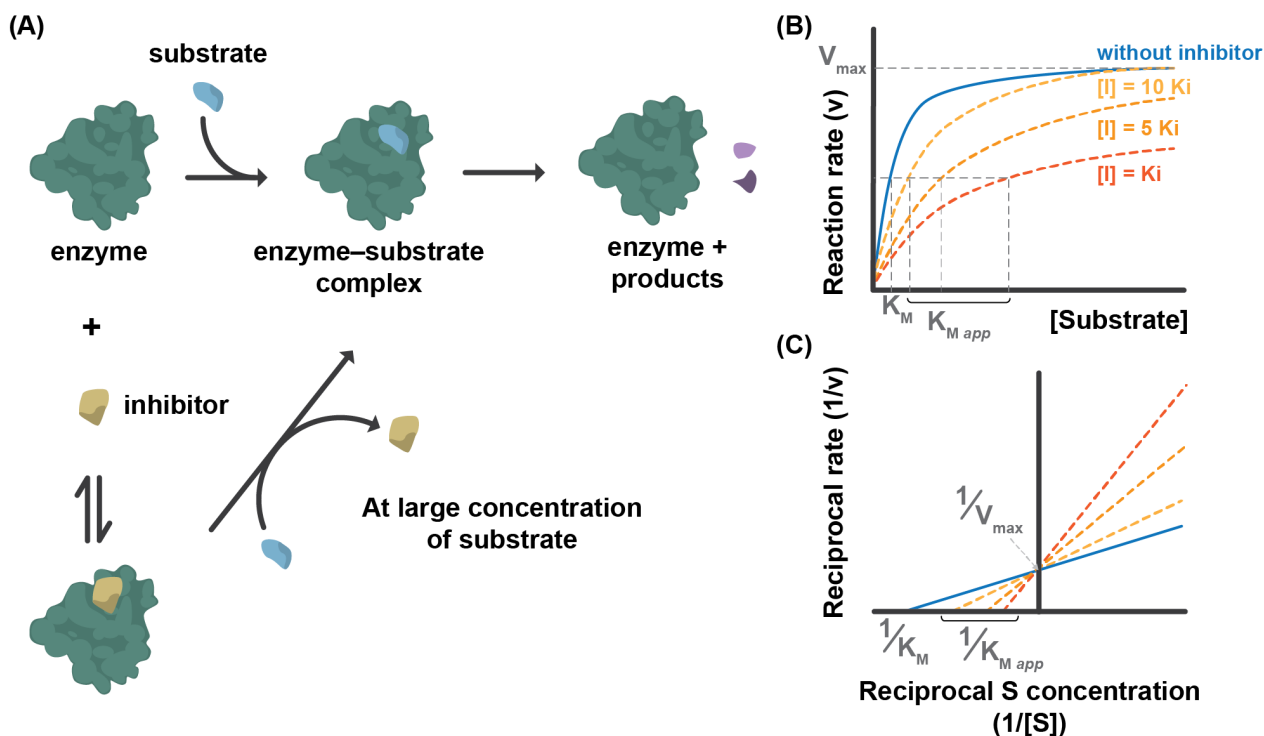
Figure III.9 - Lactate concentration curve from 0 to 60 mmol L⁻¹ in (A) red, (B) green, and (C) blue channels and from 0 to 1 mmol L⁻¹ in (D) red, (E) green, and (F) blue channels. Linear fits are represented as dotted line and parameters are inserted in the graphs. Error bars represent the standard deviation for three measurements.



Source: Own authorship.

One alternative for quantitatively measuring higher concentrations of lactate in sweat is diluting the sample to a final concentration that fits into the linear range. However, sample preparation steps are impractical for wearable devices if *in situ* measurement is desired unless they are integrated into the device. Vaquer *et al.* developed a wearable paper-based device for lactate detection in sweat by modulating the enzyme with an inhibitor.²⁰ Enzymatic kinetic parameters, such as V_{max} and K_M , are modified in the presence of inhibitor, which has different effects in the kinetics depending on the type of inhibition. Among the reversible inhibition types discussed in *CHAPTER I*, competitive inhibitor competes with the substrate to bind at the enzyme's active site, requiring larger amounts of the substrate to achieve the V_{max} (Figure III.10A).

Figure III.10 - Kinetics of a competitive inhibitor. (A) Reaction of the enzyme with the substrate and a competitive inhibitor. (B) A typical graph of the competitive inhibitor effect on the kinetics of the enzyme. (C) Double-reciprocal graph of the enzymatic kinetics without and with inhibitor. Intercept on the vertical and horizontal axis represent, reciprocally, the $1/V_{max}$ and the $1/K_M$.



Source: Adapted from Stryer L.²¹

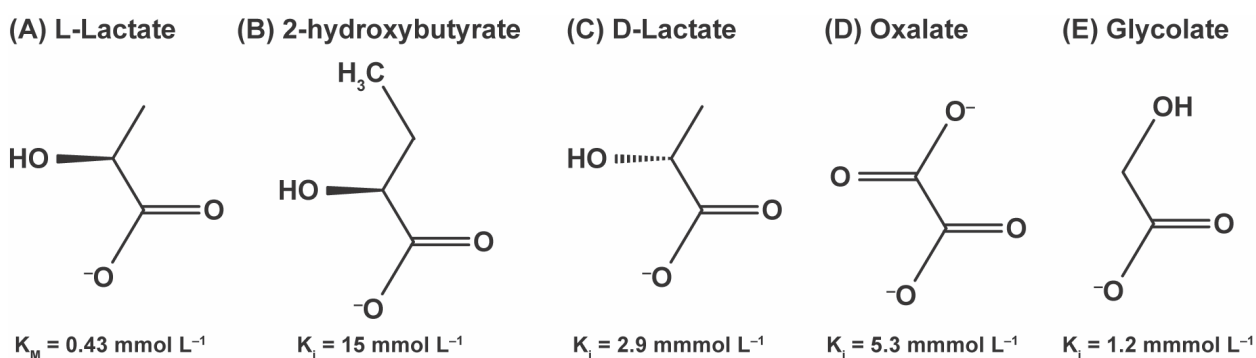
At sufficiently high substrate concentration, the competitive inhibition can be annulled, reaching the V_{max} .²¹ The effect of the competitive inhibitor on the enzymatic kinetics is illustrated in Figure III.10B. In the presence of the competitive inhibitor, more substrate is required for the enzyme to reach the V_{max} . This effect corresponds to an increase of the K_M without altering the V_{max} . The V_{max} can be calculated by an asymptomatic approach or by linearizing the Michaelis-Menten equation:

$$V_0 = V_{max} \cdot \left(\frac{[S]}{[S] + K_M} \right) \Rightarrow \frac{1}{V_0} = \frac{K_M}{V_{max}} \cdot \frac{1}{[S]} + \frac{1}{V_{max}} \quad \text{Eq III-1}$$

The $1/V$ vs. $1/[S]$ graph is known as the Lineweaver-Burk plot or double-reciprocal plot. The vertical and horizontal intercepts correspond to the reciprocal of V_{max} and the reciprocal of K_M , respectively. In the presence of competitive inhibitors, the Lineweaver-Burk plot presents the same y-axis intercept from the plot in the absence of the inhibitor. On the other hand, the x-axis intercept increases in the presence of the inhibitor (Figure III.10C).

Competitive inhibitors present similar chemical structures of the substrate since they occupy the reaction binding site. For lactate, it has demonstrated that D,L-2-hydroxybutyrate, oxalate, D-lactate, and glycolate inhibit the enzyme LOx in a competitive manner, with dissociation constant (K_i) of 15 mmol L^{-1} , 5.3 mmol L^{-1} , 2.9 mmol L^{-1} , and 1.2 mmol L^{-1} , respectively.¹⁹ Chemical structures of the competitive inhibitors are shown in Figure III.11. Strong inhibitor, *i.e.*, small K_i , requires larger amounts of the substrate to surpass the inhibition effect. Therefore, among the competitive inhibitors, glycolate inhibition effect should require a higher lactate concentration for the enzyme to reach saturation. Consequently, the linear range for the enzymatic assay for lactate should confine relevant concentration ranges in sweat.

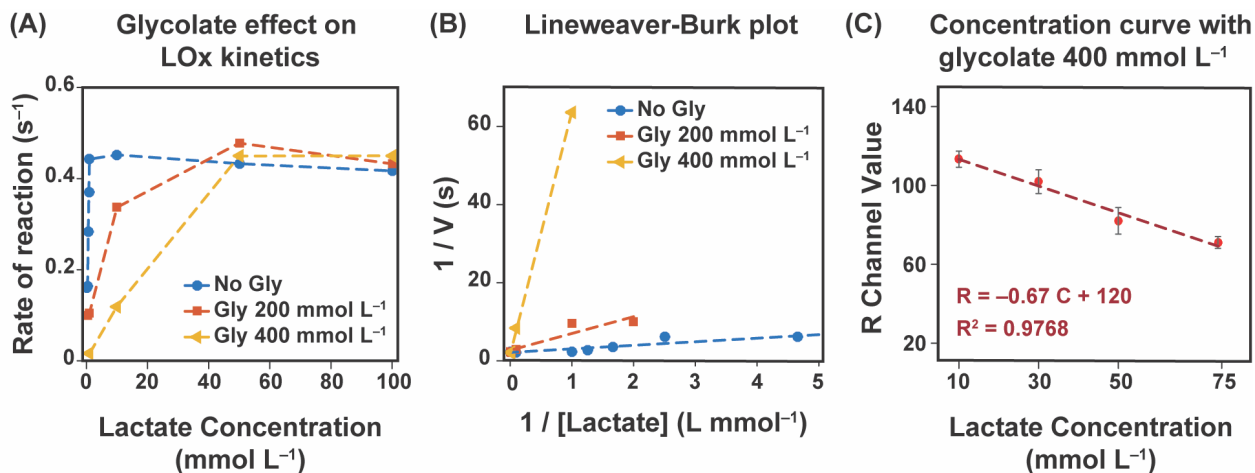
Figure III.11 - Chemical structures of L-lactate (A) and LOx inhibitors: (B) 2-hydroxybutyrate, (C) D-Lactate, (D) Oxalate, and (E) Glycolate. The K_M and K_i are displayed as well.



Source: Adapted from Duncan *et al.*¹⁹

The effect of glycolate on the LOx kinetics is illustrated in Figure III.12. The V_{max} was not altered with the addition of glycolate at two different concentrations. Without the inhibitor, the maximum rate was reached with 1 mmol L^{-1} of lactate. However, in the presence of the inhibitor, the V_{max} was reached after 50 mmol L^{-1} of lactate, increasing the apparent K_M by modulating the enzyme's affinity for its substrate. The inhibitor concentration for the following experiments was set at 400 mmol L^{-1} to detect lactate at higher concentration range in sweat. The resulting concentration curve of lactate was able to linearly distinguish lactate from 10 to 75 mmol L^{-1} in PBS in the R channel.

Figure III.12 - (A) Effect of glycolate (Gly) on LOx kinetics. (B) Linearized Lineweaver-Burk plot. (C) Lactate concentration curve from 10 to 75 mmol L⁻¹ in the presence of 400 mmol L⁻¹ of glycolate. Linear fit for the concentration curve is represented by dotted line and its parameters are insert in the graph. Error bars represent the standard deviation from three measurements.



Source: Own authorship.

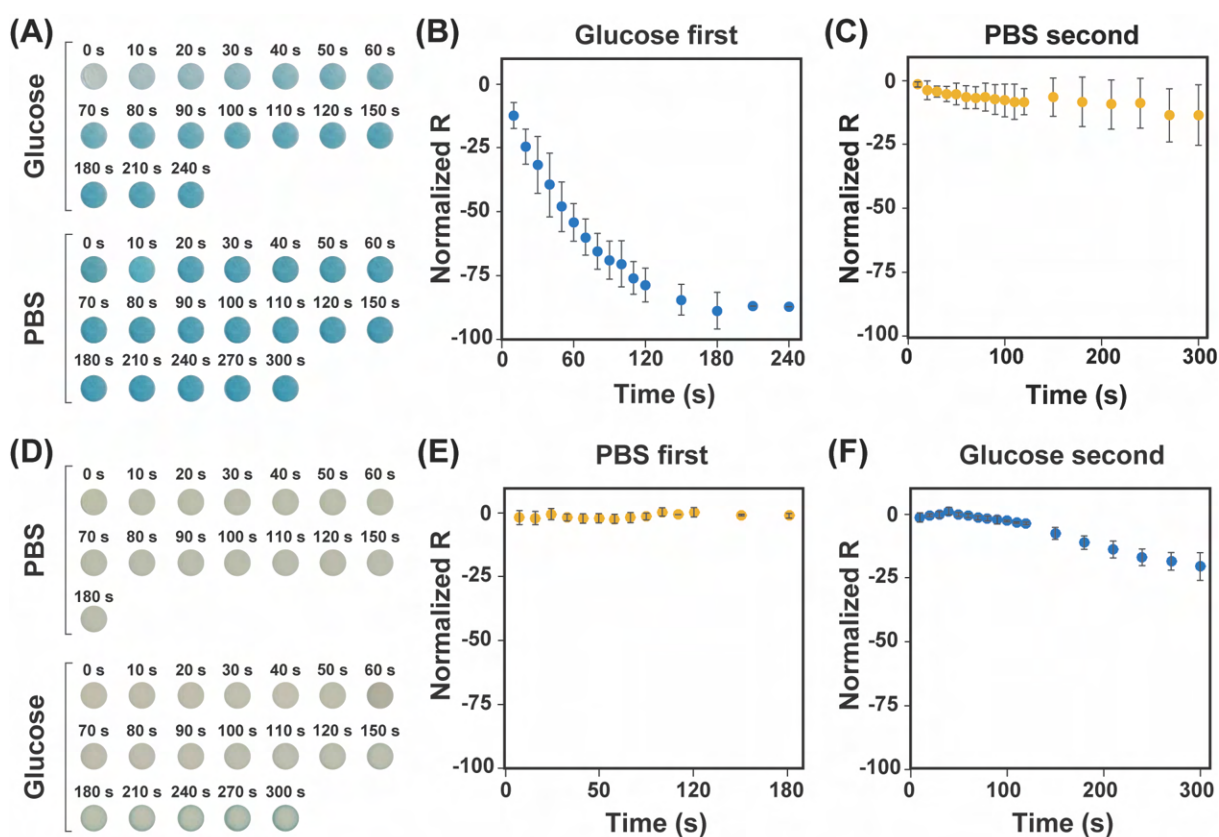
III.4.3. Flow influence on the colorimetric detection

Although the colorimetric assay was optimized for both analytes of interest, it is necessary to evaluate the effect of the flow on the performance of the assays since the sweat rate will influence the final wearable device. The sweat rate was simulated by coupling a syringe pump into the SD-based microfluidic device where the functionalized paper was placed. The flow rate was set at 5 $\mu\text{L min}^{-1}$ to mimic the highest flow rate in the relevant physiological range (1 to 5 $\mu\text{L min}^{-1}$).^{11,12}

In the first setup, 1 mmol L⁻¹ of glucose flowed through the channel. When the solution reached the chamber, the paper rapidly absorbed the solution through capillarity combined with the outside pumping source. After the wetting, the paper developed the blue color from the oxidation of TMB, as observed in Figure III.13A. The color eventually saturated after 3 min, as observed in plateauing of the normalized R values (calculated as the difference from time 0 s) from Figure III.13B. Then, PBS solution was pumped through the chamber to evaluate the stability of the color. The color did not fade with the constant flow of PBS; on the contrary, it turned more intense compared to the first frame from PBS pumping (Figure III.13C). When the inverse order of solution was tested, an interesting effect happened. At first, when the PBS was flowing through the chamber, no color was developed, as expected (Figure III.13D – E). However, with the pumping of glucose, the paper disk did not turn blue immediately after 10 s, as happened for the first setup. In fact, even after 150 s, the blue color did not emerge (Figure

III.13E). However, the edges of the paper disk started to gain a light blue coloration, indicating the oxidation of the chromogenic reagent at the border rather than in the center (Figure III.13D).

Figure III.13 - (A) Frames of the paper disk in the microfluidic chamber wetting with glucose 1 mmol L^{-1} followed by PBS under a flow rate of $5 \mu\text{L min}^{-1}$. Normalized R values along time when pumping (B) glucose 1 mmol L^{-1} followed by (C) PBS. (D) Frames of the paper disk in the microfluidic channel wetting with PBS followed by glucose 1 mmol L^{-1} under a flow rate of $5 \mu\text{L min}^{-1}$. Normalized R values along time when pumping (E) PBS followed by (F) glucose 1 mmol L^{-1} . Normalization was calculated regarding to the first point (0 s). Error bars represent the standard deviation from 3 measurements.

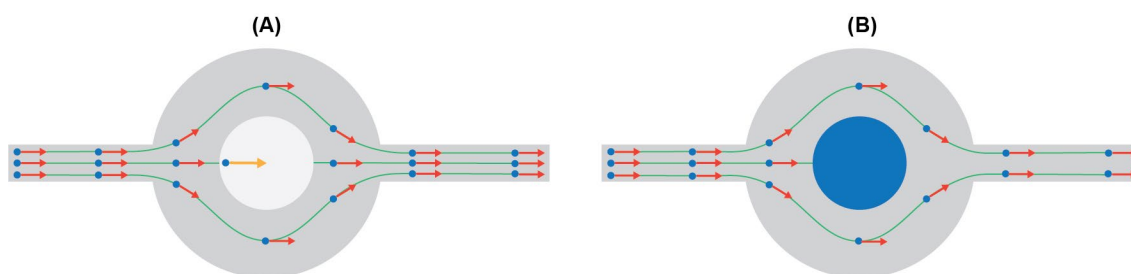


Source: Own authorship.

The border effect can be explained by the preferred path line created by the presence of the paper in the center of the chamber (Figure III.14). For the first solution, the paper is dry; therefore, the capillarity force from the paper helps the solution to wet the fibers (Figure III.14A). However, because the paper is already wet, the cellulose fibers act as a flow resistance for the second solution, which flows around the paper disks rather than in the center (Figure III.14B). For the second system, glucose solution was pumped through the chamber after the passage of PBS. In this case, the color development was observed only at the edge of the paper disk. With sufficient time, the glucose should diffuse through the paper to result in a uniform

blue disk. However, considering a diffusion constant of approximately $7 \times 10^{-6} \text{ cm}^2 \text{ s}^{-1}$ for glucose in water (at $27 \text{ }^\circ\text{C}$)²² and the area of 0.0314 cm^2 for the paper disk, the calculated time for the glucose to diffuse through the paper disk is around 75 min, which is much longer than the performed experiment. Moreover, the ability of glucose to diffuse in porous media, such as paper, is slower than in free solution, requiring even longer time for the entire paper to change the color to blue.

Figure III.14 - Simple schematics of solution path line through the chamber with the (A) dry and (B) wet paper disk. The blue circles represent the solution particles, the red arrows represent the velocity vector of the particles, and the yellow arrow represents the capillarity from the paper.



Source: Own authorship.

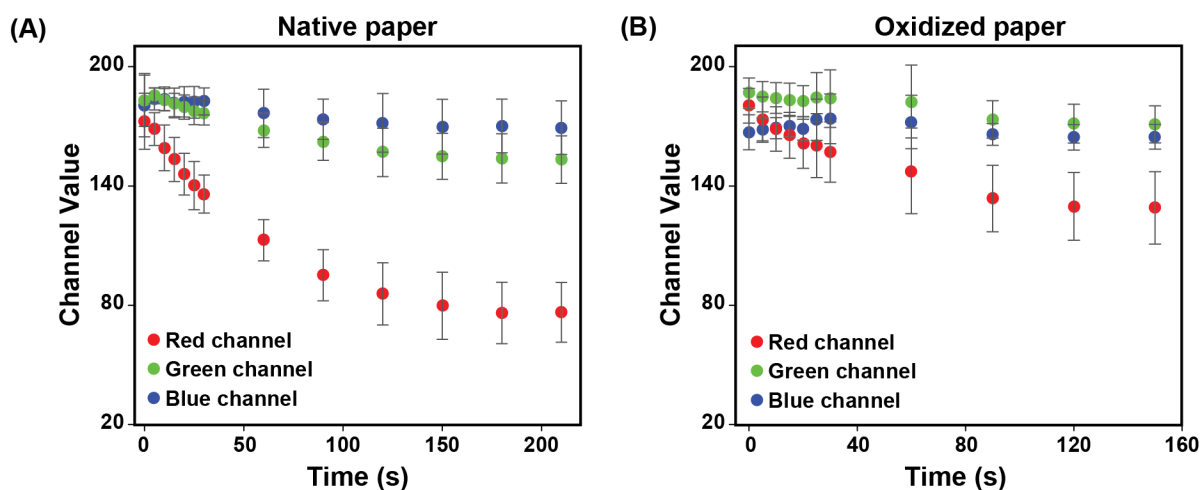
III.4.3.1. Native and oxidated papers for glucose colorimetric assay under flow

The native and oxidized papers were evaluated as substrates for glucose detection under the influence of the flow. Figure III.15 shows the color development on native (Figure III.15A) and oxidized paper (Figure III.15B) along time by flowing glucose 1 mmol L^{-1} . For native paper, the color saturation was reached around 150 s, while in the oxidized paper, the color saturated faster, around 90 s. However, the oxidized paper lacked in color intensity, represented for higher values of RGB. Therefore, the native paper was chosen for the following experiments since the sensitivity gain is more advantageous than fastness in this case. Furthermore, it was shown in the previous section that the reagents were not washed off from the paper even for the native paper, and the color was stable along time.

The concentration curve was performed in the microfluidic chamber with functionalized native paper for glucose at 0 to 1 mmol L^{-1} in PBS. The frames for each concentration are shown in Figure 14A. Among the color channels, the red channel was more sensitive, as expected, for the change in glucose concentration, with a sensitivity of $-102.3 \text{ L mmol}^{-1}$. The linear region was achieved from 0 to 0.8 mmol L^{-1} (equivalent to 14.4 mg dL^{-1}) since the color saturated after that. The limit of detection calculated according to IUPAC was below the linear region of the curve since the standard deviation from the blank measurements was low.

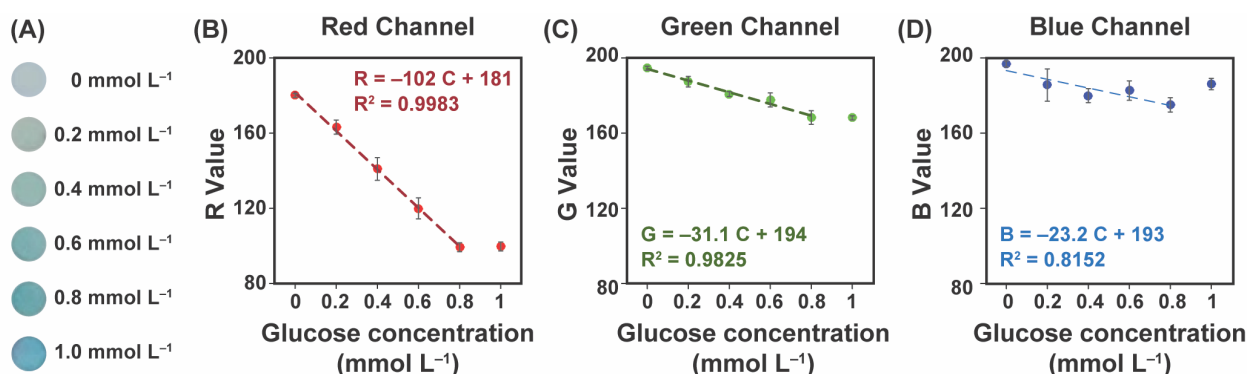
Therefore, Miller and Miller’s statistical approach was applied, resulting in a LOD of 0.05 mmol L⁻¹ and LOQ of 0.15 mmol L⁻¹. The SD-based microfluidic device with the colorimetric biosensors showed good reproducibility of 2.40%, calculated as the RSD from three different microfluidic devices.

Figure III.15 - Color development along time for flowing 1 mmol L⁻¹ of glucose in (A) native paper and (B) oxidized paper. Error bars represent the standard deviation for three measurements.



Source: Own authorship.

Figure III.16 - Glucose colorimetric assay in microfluidic chamber. (A) Paper disks after flowing glucose from 0 to 1 mmol L⁻¹. Concentration curve of glucose at same concentration range in (B) red, (C) green, and (D) blue channels. Linear fits are represented as dotted line and the parameters are inserted in the graphs. Error bars represent the standard deviation for three measurements.



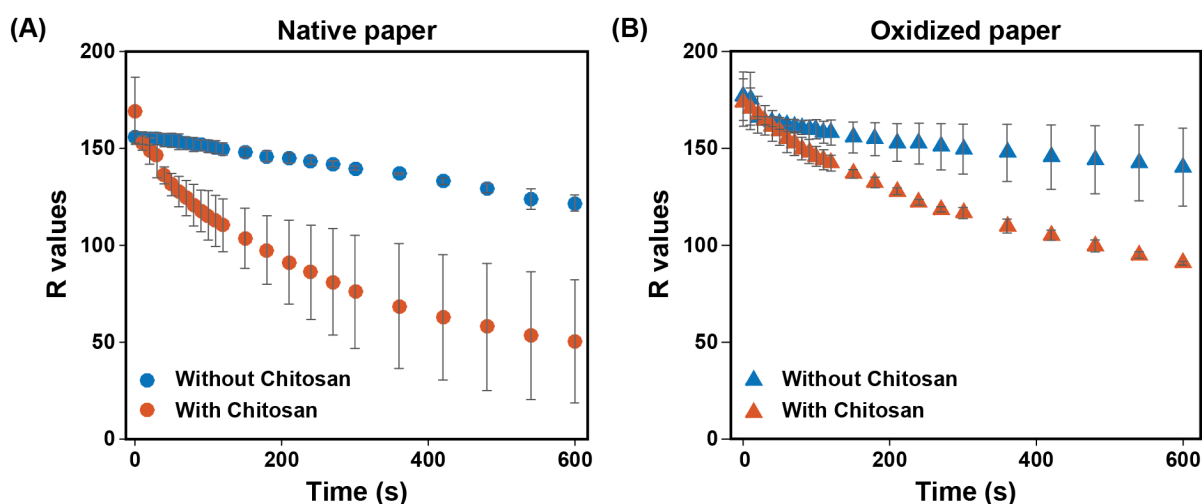
Source: Own authorship.

III.4.3.2. Lactate colorimetric assay under flow

Native paper without chitosan was tested in the microfluidic chamber for the flow influence study by flowing lactate 50 mmol L⁻¹ in PBS (Figure III.17A). Even after 10 min, the

color did not reach saturation differently from the stationary setup. Since chitosan has improved the sensitivity for glucose assay, chitosan was added to the native paper disk for lactate detection. However, the color reached low values of R, implicating the color saturation after 50 mmol L⁻¹ of lactate. Then oxidized paper was tested with and without chitosan (Figure III.17B). Like the native paper, chitosan improved the color intensity and reached color saturation around 5 min (600 s). Therefore, oxidized paper functionalized with chitosan was tested for the lactate concentration curve under the influence of the flow.

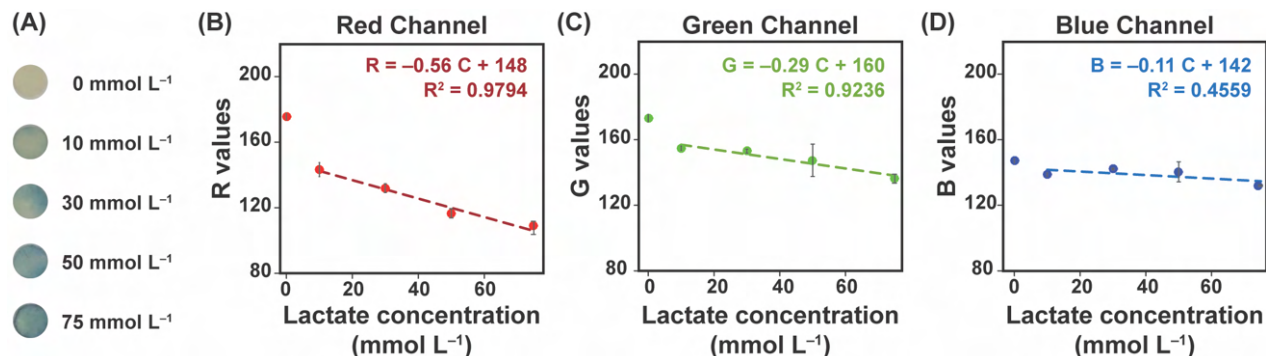
Figure III.17 - Color progression for lactate 50 mmol L⁻¹ in R channel over time for (A) native and (B) oxidized paper with and without chitosan. Error bars represent the standard deviation for three measurements.



Source: Own authorship.

The concentration curve for lactate in the microfluidic device is illustrated in Figure III.18. The red channel showed the best sensitivity from the three colors channels, with -0.563 L mmol⁻¹ from 10 to 75 mmol L⁻¹. It is important to state that from 0 to 10 mmol L⁻¹ of lactate, there is another linear range with higher sensitivity, not evaluated in this work since the relevant range of lactate in sweat is from 5 to 60 mmol L⁻¹.²³ Since the Miller and Miller's statistical approach assumes the linear regression with the blank measurements as the first points, it was not possible to adequately estimate the LOD for this device. For future work, a lower concentration range must be evaluated in a biosensor without the enzymatic inhibitor and integrated into the final wearable device. The sensors showed good reproducibility of 3.69%, calculated as the RSD from three different microfluidic devices.

Figure III.18 - Lactate colorimetric assay in microfluidic chamber. (A) Paper disks after flowing lactate from 0 to 75 mmol L⁻¹. Concentration curve of lactate at same concentration range in (B) red, (C) green, and (D) blue channels. Linear fits are represented as dotted line and the parameters are inserted in the graphs. Error bars represent the standard deviation for three measurements.



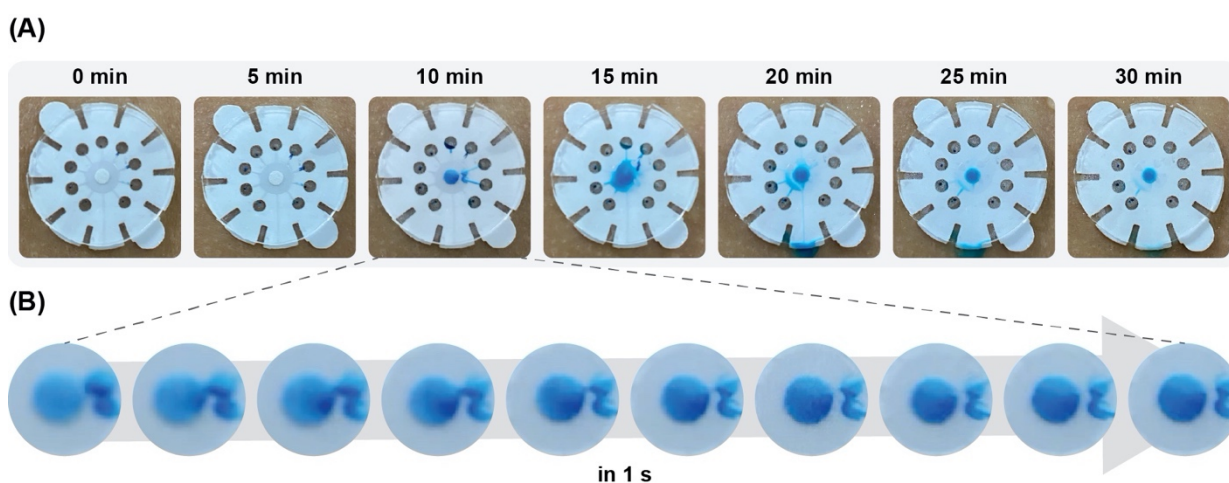
Source: Own authorship.

III.4.4. Sweat analysis by SD-based wearable device

The microfluidic device for on-body measurement was first tested to evaluate the flow of sweat into the chamber. For the test, each inlet hole was stained with blue food dye to visualize the sweat flowing through the channel to the chamber. As shown in Figure III.19A, initially, the inlet holes were saturated with condensate sweat produced during the exercise until sufficient sweat was accumulated in the inlet to push through the channel. In fact, the natural pressure associated with perspiration (approximately 70 kPa) pumps the sample through the channels.⁴ The sweat reached the chamber and the paper disk in less than 10 min of intense indoor biking. Around 10 min (Figure III.19B), it was possible to capture the capillary force from the paper disk pulling the sweat, resulting in a more intense shade of blue. In the following minutes, more sweat was collected by the other inlets, filling the chamber. It was observed that the accumulated sweat in the chamber was not sampled from all nine inlets. For some of the inlets, the sweat did not flow through, which can be explained by the absence of glands to secrete sweat in the inlet area and by the change in the pressure inside the chamber. When the chamber is empty, the pressure pulling the sweat inside the channel is high. However, once the chamber is filled with solution, fresh sweat from other inlets has less volume to occupy; therefore, the pressure pulling new sweat decreases as the chamber is filled. To fully understand the flow in such device and optimize the sweat collection, fluid dynamic simulations will be performed. After 20 min, sweat without the dye started filling the chamber, pushing the previously collected sweat with the dye out of the device through the outlet channel. At 25 min, almost all colored sweat is pumped out of the chamber, and fresh sweat is accumulated,

demonstrating the continuous sampling of sweat. This feature is vital for further wearable devices coupled with continuous detection methods. After 30 min of exercise, the paper disk remained blue since the sample flowed around rather than through the fibers, as explained previously in *Section III.4.3*. Regardless, the wearable device demonstrated efficient sweat sampling during physical activity without detaching from the skin and disturbing the user.

Figure III.19 - Sweat flowing in the wearable device. (A) Images of the wearable devices during 30 min of indoor biking. (B) Sequential frames from left to right of the chamber at 10 min illustrating the capillary force from the paper disk pulling the sweat.



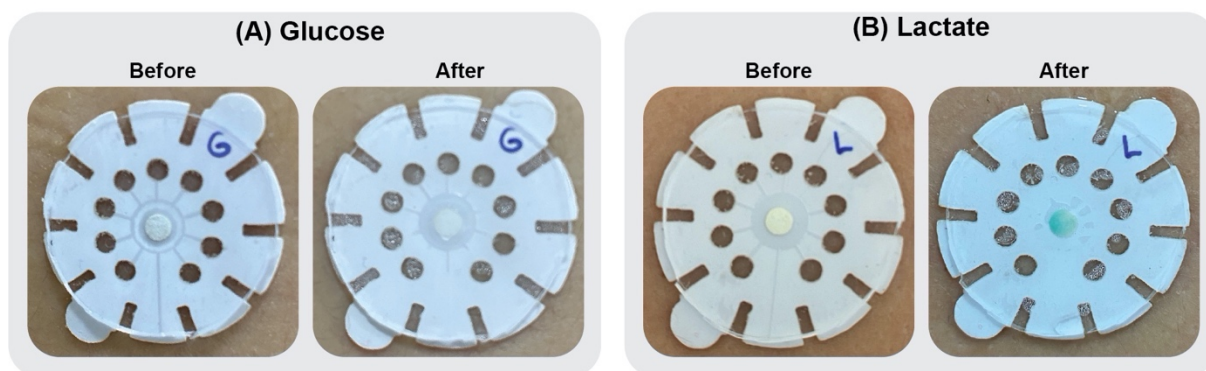
Source: Own authorship.

III.4.4.1. On-body measurement of glucose and lactate

The colorimetric assays for glucose and lactate were tested as a wearable device by coupling with the on-body microfluidic chamber. Within 30 min of indoor biking, the chambers were filled with sweat. For glucose, the paper remained colorless for the on-body measurement during physical activity, as shown in Figure III.20A. The glucose assay was tested multiple times, including after high-calory meals, and the color was not developed. Then sweat samples were collected in a plastic tube after 30 min of exercise. The samples were spiked with glucose to reach a final concentration of 0.2 mmol L^{-1} . The spiked sweat was then applied on a functionalized paper, and the blue color was achieved, proving that the sweat did not interfere in the colorimetric assay. For hypoglycemia and hyperglycemia, respectively, glucose concentration in sweat ranges from $10 \text{ }\mu\text{mol L}^{-1}$ to approximately 1 mmol L^{-1} . Concerning the applicability of the biosensor for long-endurance athletes, glucose is more likely to be found at the lower concentration range. Moreover, the tested subjects were all healthy, and the glucose levels in sampled sweat could be below the LOD for the assay. For detecting glucose at a lower

concentration range, other transduction methods could be integrated into the wearable device, such as electrochemical detections as described in *CHAPTER IV*.

Figure III.20 - On-body measurement for (A) glucose and (B) lactate before and after 30 min of exercise.

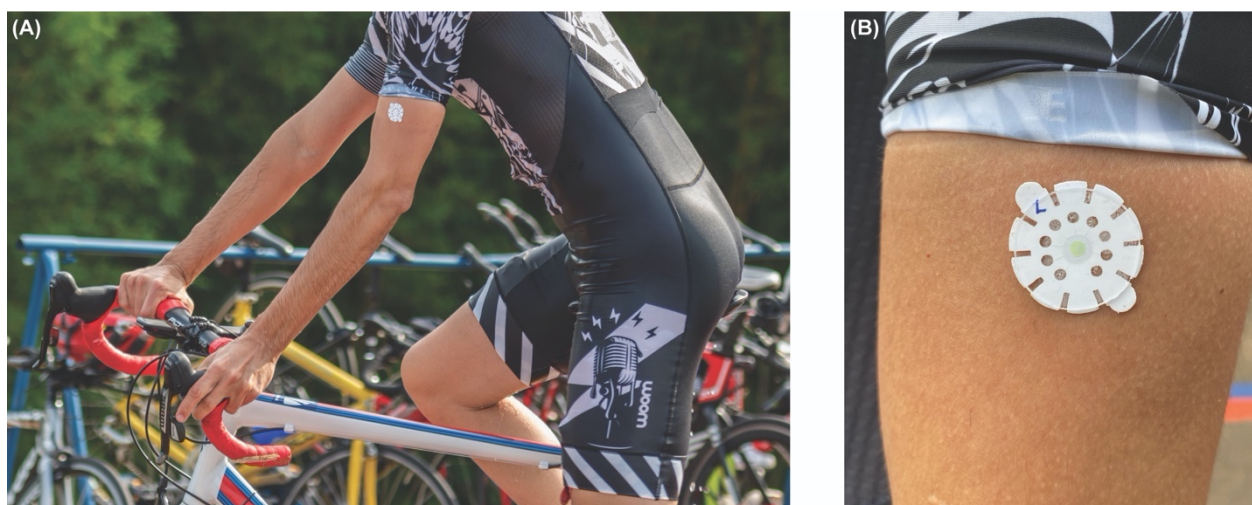


Source: Own authorship.

The lactate assay showed a change in the coloration of the paper disk, as illustrated in Figure 18B. According to the concentration curve on the previous section, the R values extracted from the colored paper disk ($R = 160.9$) fall in the range from 0 to 10 mmol L⁻¹ of lactate, which was not calibrated analytically. Unfortunately, under current conditions, the device could only detect lactate qualitatively. The smaller concentration of lactate found in sweat compared to the literature might be due to the dilution effect of the lactate by the sweat. This effect can be minimized by including a sweat volume measurement to compensate for the dilution. Vaquer *et al.* integrated a lactate colorimetric biosensor with a volumetric sweat sensor. It was shown that the volume of the sweat in the sensor affected the colorimetric response of the lactate sensor. Therefore, the colorimetric output was divided by the sample volume measured in the volumetric sensor to correct the dilution effect.²⁰

The wearable device was also tested outdoors in a triathlon test, as shown in Figure III.21. The device was placed in the forearm before biking (Figure III.21A). After 20 km of outdoor biking, around 40 min, the biosensor indicated the presence of lactate, however their color intensity was below the linear range from the concentration curve (Figure III.21B). Moreover, the exposure of the paper disk to the sunlight might have degraded the reagents, resulting in a yellowish background. In fact, the chromogenic reagent used in the assay, TMB, is light-sensitive. Therefore, for outdoor monitoring of lactate, the device should be placed in regions under the clothing to block direct sunlight.

Figure III.21 - Wearable device for lactate measurement during outdoor biking. Photos of the wearable device at the forearm at the (A) beginning of the test and (B) after 20 km of biking.



Source: Own authorship.

III.5. CONCLUSION

The Shrinky-Dinks-based mold for the fabrication of wearable microfluidics has been demonstrated in this work. The channel's depth is tunable by the amount of toner printed on the thermoplastic sheet, enabling various applications. Furthermore, the shrinking process holds the shape of the printed design, making variable geometries molds for the PDMS casting. The channel presented rounded corners resulting from the melting of the toner during the shrinking process. The difficulty of this fabrication method is aligning the printing layers to achieve higher molds for creating deep PDMS channels. The limitation of this technique lies in the printer configuration. Although it has shown its applicability, the microfluidic devices benefit from a fluid dynamic simulation study, especially for the effect of a porous material in the chamber obstructing the flow.

The microfluidic device is easily coupled with colorimetric assays to detect analytes present in the sweat if there is a specific colorimetric reaction. For glucose and lactate, the detection was based on similar enzymatic reactions, constituted of the oxidase enzyme (glucose oxidase and lactate oxidase) and horseradish peroxidase, coupled with a chromogenic reagent, TMB in this case. For glucose detection, the device did not present enough detectability to sense glucose at concentrations lower than 0.2 mmol L^{-1} found in hypoglycemia cases. For detecting lactate at a relevant concentration in sweat, the assay was modulated by adding a competitive enzymatic inhibitor, glycolate. With the addition of glycolate, the colorimetric assay detected

lactate from 10 to 75 mmol L⁻¹. The wearable device endured intense physical activity for 30 to 40 min and detected lactate under 10 mmol L⁻¹ range. The low concentration of lactate detected might be due to the dilution effect during the sweating, which could be normalized by the sweat volume. Furthermore, for accurate detection of lactate in a low concentration range, a second sensing area without adding the enzymatic inhibitor could be added into the device.

One of the drawbacks of the colorimetric assay is the low sensitivity (narrow range of detected concentration) observed for glucose detection. This wearable microfluidic device can be integrated with the flexible wrinkled electrodes presented in the next *CHAPTER IV*. A PDMS layer with the wrinkled electrodes could be used as the top layer of the device to seal the PDMS microfluidic channels by using O₂ plasma. The final device could also be integrated with wireless data transfer electronics and coupled with a mobile app for real-time measurement of glucose in sweat. Moreover, integrating with an electrical or electrochemical transduction system eliminate chromogenic reagents, commonly light sensitives.

The SD-based wearable devices are lightweight and conformal to the skin, allowing their attachment for long periods without causing any discomfort to the user. The presented final device might not be ready for commercial use yet. However, it demonstrates the potential of wearable devices for individualized analysis of performance in sports. Although the devices were applied to track key biomarkers for physical activity, they can be adapted to analyze the sweat in a diagnosing context to promote personalized medicine. Furthermore, these devices could be applied in many clinical studies to prove the correlation of many analytes between blood and sweat, which is still a concern for the applicability of sweat in clinical diagnostics.

III.6. REFERENCES

1. SESHADRI, D. R.; ROWBOTTOM, J. R.; DRUMMOND, C.; VOOS, J. E.; CRAKER, J. A. A review of wearable technology: moving beyond the hype: from need through sensor implementation. *In: CAIRO INTERNATIONAL BIOMEDICAL ENGINEERING CONFERENCE*, 8., 2016, Cairo. **Resumos [...]**. Cairo: [s. n.] , 2016. p. 52–55.
2. SESHADRI, D. R.; LI, R. T.; VOOS, J. E.; ROWBOTTOM, J. R.; ALFES, C. M.; ZORMAN, C. A.; DRUMMOND, C. K. Wearable sensors for monitoring the physiological and biochemical profile of the athlete. **npj Digital Medicine**, Berlin, v. 2, p. 1–16, 2019. DOI: 10.1038/s41746-019-0150-9.
3. CHUAN YEO, J.; KENRY; TECK LIM, C. Emergence of microfluidic wearable technologies. **Lab on a Chip**, Cambridge, v. 16, p. 4082–4090, 2016. DOI: 10.1039/C6LC00926C.
4. CHEN, G.; ZHENG, J.; LIU, L.; XU, L. Application of microfluidics in wearable devices. **Small Methods**, Weinheim, v. 3, p. 1900688, 2019. DOI: 10.1002/smt.201900688.
5. LI, S.; MA, Z.; CAO, Z.; PAN, L.; SHI, Y. Advanced wearable microfluidic sensors for healthcare monitoring. **Small**, Weinheim, v. 16, p. 1903822, 2020. DOI: 10.1002/sml.201903822.
6. MORBIOLI, G. G.; SPELLER, N. C.; STOCKTON, A. M. A practical guide to rapid-prototyping of PDMS-based microfluidic devices: a tutorial. **Analytica Chimica Acta**, Amsterdam, v. 1135, p. 150–174, 2020. DOI: 10.1016/j.aca.2020.09.013.
7. BAO, N.; ZHANG, Q.; XU, J.-J.; CHEN, H.-Y. Fabrication of poly(dimethylsiloxane) microfluidic system based on masters directly printed with an office laser printer. **Journal of Chromatography A**, Amsterdam, v. 1089, p. 270–275, 2005. DOI: 10.1016/j.chroma.2005.07.001.
8. GRIMES, A.; BRESLAUER, D. N.; LONG, M.; PEGAN, J.; LEE, L. P.; KHINE, M. Shrinky-Dink microfluidics: rapid generation of deep and rounded patterns. **Lab on a Chip**, Cambridge, v. 8, p. 170–172, 2007. DOI: 10.1039/B711622E.
9. WOOLF, M. S.; DIGNAN, L. M.; SCOTT, A. T.; LANDERS, J. P. Digital postprocessing and image segmentation for objective analysis of colorimetric reactions. **Nature Protocols**, Berlin, v. 16, p. 218–238, 2021. DOI: 10.1038/s41596-020-00413-0.
10. FAN, Y.; LI, J.; GUO, Y.; XIE, L.; ZHANG, G. Digital image colorimetry on smartphone for chemical analysis: a review. **Measurement**, Oxford, v. 171, p. 108829, 2021. DOI: 10.1016/j.measurement.2020.108829.
11. BENEDETTI, L. P. S. **Determinação in situ de analitos de interesse alimentício empregando tratamento de imagens digitais de spot tests**. Orientador: Orlando Fatibello Filho. 2013. 78 f. Tese (Mestrado em Química Analítica). Universidade Federal de São Carlos, São Carlos, 2013.

12. JOSEPHY, P. D.; ELING, T.; MASON, R. P. The horseradish peroxidase-catalyzed oxidation of 3,5,3',5'-tetramethylbenzidine. Free radical and charge-transfer complex intermediates. **Journal of Biological Chemistry**, Rockville, v. 257, p. 3669–3675, 1982. DOI: 10.1016/S0021-9258(18)34832-4.
13. LEE, H.; HONG, Y. J.; BAIK, S.; HYEON, T.; KIM, D.-H. Enzyme-based glucose sensor: from invasive to wearable device. **Advanced Healthcare Materials**, Hoboken, v. 7, p. 1701150, 2018. DOI: 10.1002/adhm.201701150.
14. WITKOWSKA NERY, E.; KUNDYS, M.; JELEŃ, P. S.; JÖNSSON-NIEDZIÓŁKA, M. Electrochemical glucose sensing: is there still room for improvement? **Analytical Chemistry**, Washington, v. 88, p. 11271–11282, 2016. DOI: 10.1021/acs.analchem.6b03151.
15. KOEV, S. T.; DYKSTRA, P. H.; LUO, X.; RUBLOFF, G. W.; BENTLEY, W. E.; PAYNE, G. F.; GHODSSI, R. Chitosan: an integrative biomaterial for lab-on-a-chip devices. **Lab on a Chip**, Cambridge, v. 10, p. 3026–3042, 2010. DOI: 10.1039/C0LC00047G.
16. GABRIEL, E. F. M.; GARCIA, P. T.; CARDOSO, T. M. G.; LOPES, F. M.; MARTINS, F. T.; COLTRO, W. K. T. Highly sensitive colorimetric detection of glucose and uric acid in biological fluids using chitosan-modified paper microfluidic devices. **Analyst**, Cambridge, v. 141, p. 4749–4756, 2016. DOI: 10.1039/C6AN00430J.
17. DUNCAN, J. D.; WALLIS, J. O.; AZARI, M. R. Purification and properties of *Aerococcus viridans* lactate oxidase. **Biochemical and Biophysical Research Communications**, San Diego, v. 164, p. 919–926, 1989. DOI: 10.1016/0006-291X(89)91546-5.
18. VAQUER, A.; BARÓN, E.; DE LA RICA, R. Wearable analytical platform with enzyme-modulated dynamic range for the simultaneous colorimetric detection of sweat volume and sweat biomarkers. **ACS Sensors**, Washington, v. 6, p. 130–136, 2021. DOI: 10.1021/acssensors.0c01980.
19. STRYER, L. **Biochemistry**. 9. ed. New York: W.H. Freeman, 2019. 1296p.
20. MATZEU, G. **Development, optimization and applications of screen-printed electrochemical sensors**. 2015. 124 f. Thesis (Doctor of Philosophy degree in Chemistry) – National Centre for Sensor Research, School of Chemical Sciences, Dublin City University, Dublin, 2015.
21. KWON, K.; KIM, J. U.; DENG, Y.; KRISHNAN, S. R.; CHOI, J.; JANG, H.; LEE, K.; SU, C.-J.; YOO, I.; WU, Y.; LIPSCHULTZ, L.; KIM, J.-H.; CHUNG, T. S.; WU, D.; PARK, Y.; KIM, T.; GHAFFARI, R.; LEE, S.; HUANG, Y.; ROGERS, J. A. An on-skin platform for wireless monitoring of flow rate, cumulative loss and temperature of sweat in real time. **Nature Electronics**, Berlin, v. 4, p. 302–312, 2021. DOI: 10.1038/s41928-021-00556-2.
22. SUHAIMI, H.; WANG, S.; DAS, D. B. Glucose diffusivity in cell culture medium. **Chemical Engineering Journal**, Lausanne, v. 269, p. 323–327, 2015. DOI: 10.1016/j.cej.2015.01.130.

23. SONNER, Z.; WILDER, E.; HEIKENFELD, J.; KASTING, G.; BEYETTE, F.; SWAILE, D.; SHERMAN, F.; JOYCE, J.; HAGEN, J.; KELLEY-LOUGHNANE, N.; NAIK, R. The microfluidics of the eccrine sweat gland, including biomarker partitioning, transport, and biosensing implications. **Biomicrofluidics**, Melville, v. 9, p. 031301, 2015.
DOI: 10.1063/1.4921039.

CHAPTER IV

Electrochemical characterization of wrinkled electrodes and its application for glucose sensing

IV.1. INTRODUCTION

Colorimetric assays are widely applied transduction method in biosensors because of its inherent simplicity and potential for instrument free analysis. However, color changes are limited by the background surface and the detection often presents limited dynamic range and low sensitivity.¹ Moreover, colorimetric detection is susceptible to errors from environmental illumination. Electrochemical transduction offers an alternative system providing enhanced sensitivity and detectability. Furthermore, electrochemical detection systems are easily miniaturized, which enables the integration to platforms of low consumption of chemicals and sample, low-cost of fabrication and portable. However, its miniaturization results in the decay of the electrochemical signal since it is proportional to the area of the sensing electrode.² Furthermore, the portable electronics are not as equally robust as traditional systems, which results in higher electromagnetic interference and noise.

A strategy to improve the signal of miniaturized electrochemical system is to enhance the electrochemically active surface area (EASA) of the sensing electrode. There are several methods to deposit and electrodeposit materials that increase the EASA, such as porous carbon-based and metallic nanostructures.^{3,4}

The shrink electrodes are a simple approach to fabricate high EASA electrodes without the need of specific equipment or cleanroom. These electrodes are fabricated by the heat-induced shrinking of a memory-shape polymer (substrate) coated with a thin metallic film (electrode). Because of the stiffness mismatch between the polymer and the metal, the latter deforms during the shrinking process of the polymer when it is heated above its glass transition temperature. The resulting electrodes present a rough surface with micro- and nano-wrinkles created during the shrinking process.^{5,6} The final electrode exhibit a smaller geometric area than the initial area, but with a higher EASA.⁶

The shrink electrodes can be transferred to an elastomer, such as polydimethylsiloxane (PDMS), creating highly flexible and stretchable electrodes. Because of the high conformation to the skin, the flexible electrodes can be applied as wearable devices for sensing of body movements at elbow, fingers and knees.⁷ The shrink electrodes were also applied as respiration and beat-to-beat blood pressure sensors because of the high sensitivity to conformation change of the skin.^{8,9}

Gold shrink electrodes were applied for electrochemical detection in previous works showing an increase in the electrochemical signal. Pegan et. al⁵ achieved 6.6-fold increase in electrochemical signal in sulfuric acid (H₂SO₄) for an electrode with 20-fold reduction in

geometric area. This indicated that only a part of theoretical surface was electrochemically active. Hauke et. al² applied a hydrophilic polymer on the wrinkled electrode to improve the wettability of the surface, increasing the EASA by 2-fold, still not fully accessing the surface area. All the study published before characterized the wrinkled electrodes in H₂SO₄ solution and the stretchable electrodes were not yet characterized.

IV.2. AIMS

Electrochemically characterize gold wrinkled electrode in both non-stretchable and stretchable substrate in H₂SO₄ and ferricyanide/ferrocyanide ([Fe(CN)₆]^{3-/4-}). Apply stretchable gold electrode for detection of glucose as proof-of-concept.

IV.3. MATERIALS & METHODS

IV.3.1. Fabrication of the electrodes

IV.3.1.1. Fabrication of wrinkled electrodes

Polyolefin (PO) is a shape-memory polymer and was used as a shrinking substrate. PO was placed on a silicon wafer for support. A solution of poly(methyl methacrylate) (PMMA) dissolved in toluene was used as a sacrificial layer to further dissolve it in acetone during the transference process (described below). The PMMA was spin coated at 3200 rpm and dried overnight. Masks for the electrode design was laser cut from adhesive and applied on the PMMA film as stencils for the metal deposition. Gold was deposited on the PO/PMMA at a thickness of 80 nm via sputtering (Quorum 150R). The PO/PMMA/Au was removed from the silicon wafer for the thermal-induced shrinking process. The films were shrunk in a convection oven at 140 °C for 13 min.

IV.3.1.2. Transference of the wrinkled electrodes to elastomer

A silicon-based elastomer (commercial name Ecoflex™) was used as a flexible and stretchable substrate. Before the application of the elastomer, the wrinkled gold film was treated for at least 1 hour with 3-(mercaptopropyl)trimethoxysilane (MPTMS) in ethanolic solution to promote the chemical bonding of the gold to the silicon-based polymer. Ecoflex™ was drop casted onto the gold film treated with MPTMS and cured overnight at 60 °C. The transference

of the wrinkled film to the elastomer was completed by dissolving the PMMA between the gold film and the PO in acetone. Once the gold wrinkled films were lifted off from the PO, they were in isopropanol bath for an hour and dried overnight.

IV.3.2. Electrochemical characterization

IV.3.2.1. Electrochemical characterization of unshrunk, shrunk, and stretchable electrodes

Electrochemical measurements were performed on a Reference 600 potentiostat (Gamry Instruments). The unshrunk, shrunk and transferred gold electrodes were used as working electrodes, and commercial silver/silver chloride (Ag/AgCl) as reference, and platinum (Pt) wire as counter electrodes, respectively. Cyclic voltammetry was performed in H₂SO₄ 0.5 M solution from 0 to 1.5 V at 10, 25, 50, 100, 250, 500, and 1000 mV s⁻¹. The same scan rates were applied for measurements in [Fe(CN)₆]^{3-/4-} 5 mmol L⁻¹ solution in 0.05 mol L⁻¹ phosphate buffer saline (PBS) at pH 7.4 from -0.2 to 0.7 V.

IV.3.2.2. Electrochemical characterization of stretchable electrodes under strain

A stretching device was fabricated to control the strain of the stretchable electrodes and maintain them under strain while an electrochemical measurement was performed. Cyclic voltammetry was performed at every 30% strain until it reached 210% of its length. This procedure was repeated in H₂SO₄ and [Fe(CN)₆]^{3-/4-} solutions. The electrodes were allowed to relax overnight before repeating the stretching procedure for the second time on the next day.

IV.3.2.3. Sheet resistance measurement of stretchable electrodes

A *Signatone Pro4 Resistivity Test System* with an SP4 inline probe was used to measure the sheet resistance of stretchable electrodes before, during, and after strain. The stretchable electrodes were firstly measured without any previous strain. Then, the sheet resistance was measured again on the electrodes under 200% strain of its length. The electrodes were stretched up to 210% 10 times and relaxed for 5 min. The sheet resistance was measured again.

IV.3.3. Glucose detection

The stretchable electrodes were evaluated for the detection of glucose, an important biomarker for physiological condition. The potential at which glucose oxidized was measured in 5 mmol L⁻¹ glucose solution in PBS at pH 7.2 by cyclic voltammetry from -1 to 1 V at a scan rate of 20 mV s⁻¹.

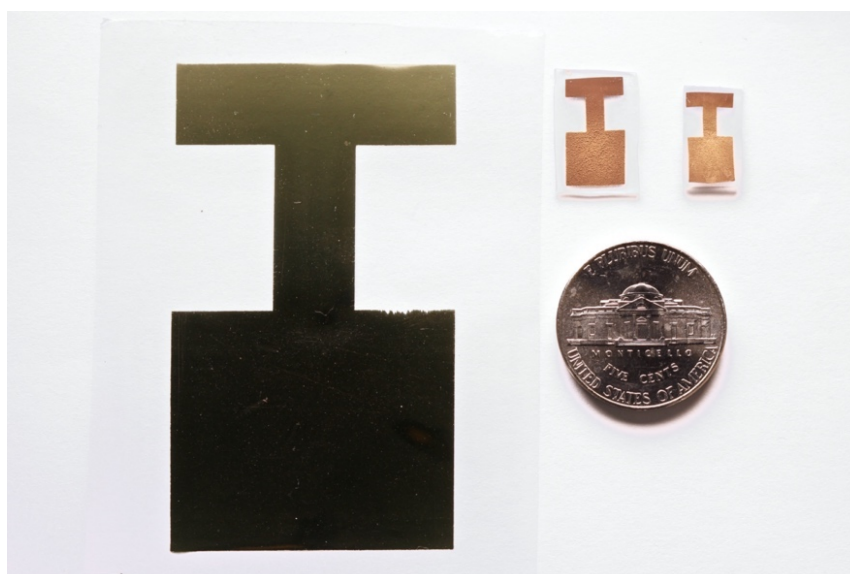
Chronoamperometry was performed at 0.3 V, and glucose was titrated into 20 mL of PBS at pH 7.4 every 30 s. This procedure was repeated for non-strained electrodes (n = 3) and pre-strained electrodes (n = 3). For the pre-strained electrodes, the electrodes were stretched up to 210% of its length 10 times and relaxed overnight.

IV.4. RESULTS & DISCUSSION

IV.4.1. Shrinking of the electrodes

The initial working area of the electrode was 10.5 cm² and, after the thermal-induced shrinking process, the geometric area of shrunk electrode was 0.48 cm² (Figure IV.1). The shrinking factor, defined as the ratio of geometric areas of the unshrunk to the shrunk or transferred electrodes, of the PO is 21.8. The wrinkled film when transferred to the elastomer shrunk once more to the final area of 0.31 cm² due to the lift-off process in acetone, resulting on a shrinking factor of 33.4.

Figure IV.1 - Photo of the gold electrodes, from left to right: Unshrunk electrode, shrunk electrode on PO, and shrunk electrode on elastomer substrate.

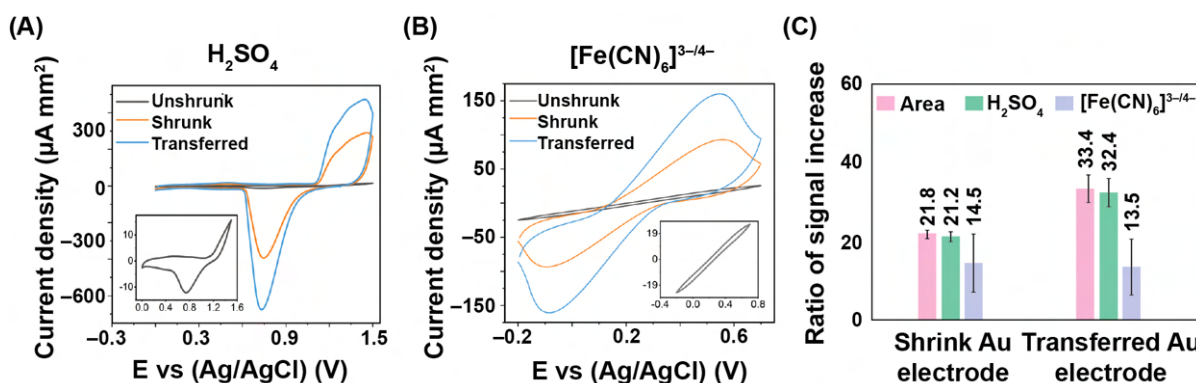


Source: Adapted by permission from Imamura *et al.* Adv. Mater. Technol, 2020, 5, 1900843 © 2020 WILEY-VCH Verlag GmbH & Co. kGaA, Weinheim. DOI: 10.1002/admt.201900843.

IV.4.2. Enhancement of the electrochemical signal

The wrinkles contribute to a high surface area, which correlates to the current. The EASA of the wrinkled electrodes was evaluated by measuring the current via cyclic voltammetry in H_2SO_4 and $[\text{Fe}(\text{CN})_6]^{3-/4-}$ solutions. The current densities of the electrodes were obtained by dividing the raw current by the geometric area (Figure IV.2A and B). The current densities for shrunk and transferred electrodes are larger than for the unshrunk electrode in both solutions. The signal enhancements were calculated as the ratio of the current densities of processed electrodes to unshrunk electrodes. In H_2SO_4 , the shrunk and transferred electrodes obtained a signal enhancement of approximately 21- and 32- fold respectively (Figure IV.2C), an improvement of 2.5-fold over previous work by Hauke *et al.*² Because the wrinkles are naturally hydrophobic due to the air pockets between the wrinkles, there is a surface wettability restriction. The hydrophobicity was overcome by treating the wrinkled film with oxygen plasma, which makes the surface hydrophilic, removing the need of coating polymers as the previous work.

Figure IV.2 - Current density voltammograms of unshrunk, shrunk, and transferred electrodes in (a) H_2SO_4 and (b) $[\text{Fe}(\text{CN})_6]^{3-/4-}$. (c) Shrinking factor and signal enhancement for shrunk and transferred gold electrode expressed as ratios. Error bars represent the standard deviation from three measurements.



Source: Adapted by permission from Imamura *et al.* Adv. Mater. Technol, 2020, 5, 1900843 © 2020 WILEY-VCH Verlag GmbH & Co. kGaA, Weinheim. DOI: 10.1002/admt.201900843.

Several methods can be applied to estimate the surface area of nanostructured electrodes, such as gas sorption, underpotential deposition of metal, capacitance measurement by electrochemical impedance spectroscopy or cyclic voltammetry, and cyclic voltammetry in H_2SO_4 . The latter method was chosen to characterize the wrinkled gold surface of the shrunk and transferred electrodes since it can be easily performed and provides a good estimate of the EASA.^{10,11} This method was reported to provide an estimated surface area that aligns with

underpotential deposition¹² and nitrogen adsorption/desorption isotherms.¹³ Scanlon *et al.* evaluated the EASA of nanoporous gold by several methods and demonstrated that the gold oxide reduction in H₂SO₄ was the most accurate and reliable method when compared to the assessment of monolayers, redox reactions of [Fe(CN)₆]^{3-/4-}, [Ru(NH₃)₆]^{3-/4-} and O₂, and double layer capacitance.¹¹ In H₂SO₄, the cyclic voltammetry measurement enables the oxidation of the gold to gold oxide starting at 1.0 V and the successive reduction of the gold oxide back to gold at 0.7 V on the reverse scan. The charge associated with the reduction of gold oxide at relatively slow scan rate is directly proportional to the surface area by the following relation:

$$\text{EASA} = Q/c \quad \text{Eq IV-1}$$

in which Q is the charge, which is calculated by integrating the area under the reduction peak and c is the specific charge equivalent, which equals to 390 $\mu\text{C cm}^{-2}$ for polycrystalline gold.¹⁴ Table IV.1 shows the calculated values for EASA of shrunk and transferred gold electrodes based on the integrated area under the reduction peak of gold oxide in H₂SO₄ at 100 mV s⁻¹.

Table IV.1 - Charge and surface area of shrunk and transferred gold electrodes.

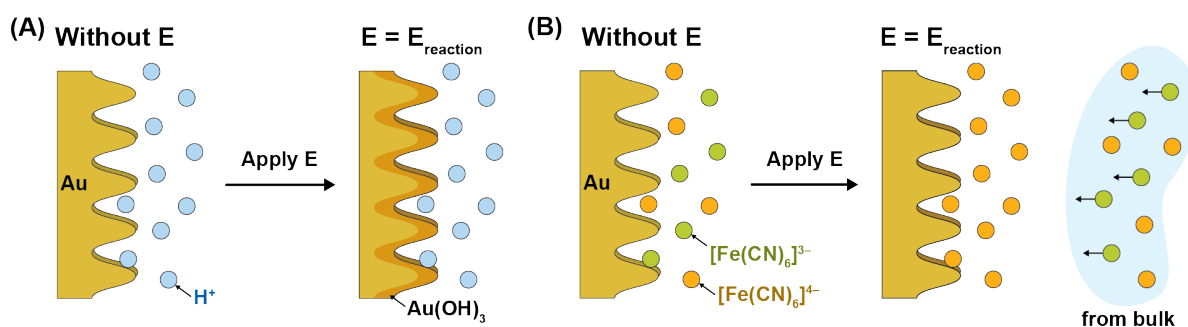
	SHRUNK	TRANSFERRED
Charge (mC)	4.10 ± 0.05	4.31 ± 0.42
EASA (cm ²)	10.5 ± 0.14	11.1 ± 1.09

Source: Reproduced with permission from Imamura *et al.* Adv. Mater. Technol, 2020, 5, 1900843 © 2020 WILEY-VCH Verlag GmbH & Co. kGaA, Weinheim. DOI: 10.1002/admt.201900843.

Despite the limitations of this method to accurately assess surface area due to the possibility of multilayer formation instead of monolayer, this method provides an approximated value of shrunk and transferred surfaces areas with the initial geometric area of the unshrunk electrode (10.5 cm²). Furthermore, the signal enhancement of 21- and 32-fold in H₂SO₄ respectively for shrunk and transferred electrodes matches the shrinking factor. Therefore, we can conclude that the surface area is maintained after shrinking and transferring the thin film and the access to the entire surface area during the electrochemical measurement in H₂SO₄ was preserved. However, the signal enhancements in [Fe(CN)₆]^{3-/4-} solution are approximately 14- and 13-fold for shrunk and transferred electrodes respectively (Figure IV.2C). This indicates that the signal enhancement depends on the solution where the electrochemistry measurement is performed. The lower signal enhancements achieved in this solution can be explained by the diffusion-limited reaction of [Fe(CN)₆]^{3-/4-}, as schematically shown in Figure IV.3. As the

potential is applied, the concentration of $[\text{Fe}(\text{CN})_6]^{3-/4-}$ at the outermost surface of the electrode approaches zero, and a concentration gradient forms in the solution. Diffusion takes place at the surface of the electrodes as the reaction proceeds; however, the diffusion of electroactive species is impeded by the morphology of the wrinkles. A significant portion of the inner surface of the gold wrinkles is therefore not accessed by the $[\text{Fe}(\text{CN})_6]^{3-/4-}$ ions because the time for diffusion deep into the wrinkles is not sufficient, leading to the disagreement between signal enhancement and shrinking factor. Similarly, the electrochemical behavior of nanoporous gold was reported by Scanlon,¹¹ Collinson,¹⁵ and Jia¹⁰ wherein high-surface area, porous electrodes were shown to be biased against redox couples like $[\text{Fe}(\text{CN})_6]^{3-/4-}$.

Figure IV.3 - Schematics of the electrochemical reactions at wrinkled gold surface. (A) Gold oxidation nonlimited by diffusion. (B) $[\text{Fe}(\text{CN})_6]^{3-/4-}$ diffusion-limited reaction.



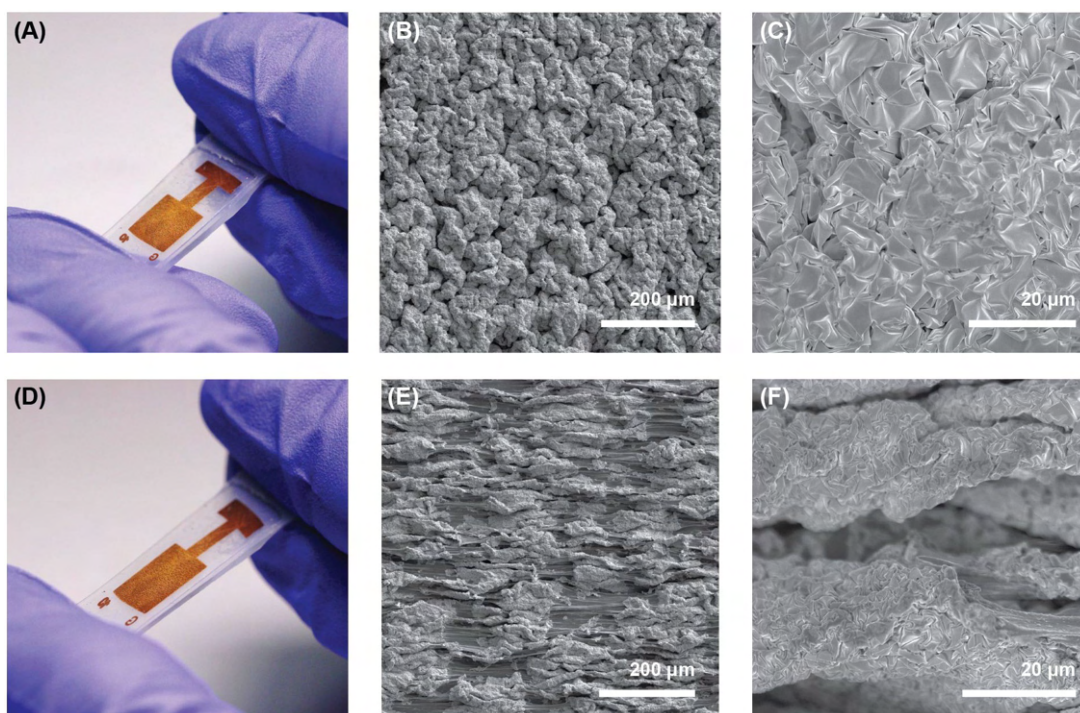
Source: Own authorship.

IV.4.3. Electrochemical signal of electrodes under and after strain

Figure IV.10) application as a wearable device by conforming onto the skin (Figure IV.4). As shown in Figure IV.4B and C, the wrinkled structures are retained during the transference process. The straining of the electrodes results in the stretching and opening of the wrinkled (Figure IV.4E and F). As the electrode is stretched, the neighboring wrinkles are separated from each other and some cracks on the metal film are formed, as illustrated in Figure IV.5A.¹⁶ This phenomenon results in the increase of the electrical resistance of the metal film when the electrode is maintained at the strained state, as can be observed on Figure IV.5B. Subsequently, once the electrode returns to the relaxed state, the electrical resistance decreases since the wrinkles are once again close to each other, shortening the electron pathway. However, the relaxed wrinkled electrode is more resistive after the stretching due to the formed cracks in the film. The sheet resistance values before strain, at 100% strain and after relaxing are shown in Table IV.2. It is important to state that the cracks are continuously introduced to the metal film from handling and natural stress release before the electrode is strained. Stretching the

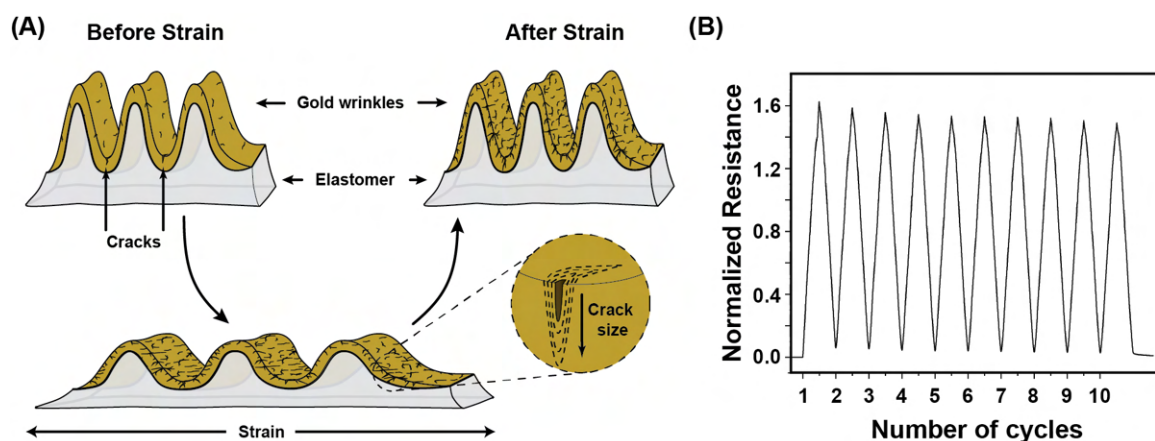
electrodes induces the crack formation, increasing the number and sizes of the cracks (Figure IV.5A). However, stretching the electrode several times eventually stabilizes the wrinkled film since no more cracks are formed and the resistance eventually plateaus, as can be observed in Figure IV.5C.

Figure IV.4 - Stretching of the electrode. (A) Photo of electrode transferred to elastomer substrate. SEM of the unstretched electrode at (B) 1.1 and (C) 12.9 k × magnification. (D) Transferred electrode being stretched. SEM of the stretched transferred electrode at (E) 1.1 and (F) 12.9 k × magnification.



Source: Adapted by permission from Imamura *et al.* Adv. Mater. Technol, 2020, 5, 1900843 © 2020 WILEY-VCH Verlag GmbH & Co. kGaA, Weinheim. DOI: 10.1002/admt.201900843.

Figure IV.5 - (A) Schematics of the crack formation on the transferred gold electrode with strain. (B) Normalized resistance response with 200% strain across 10 cycles.



Source: Adapted by permission from Imamura *et al.* Adv. Mater. Technol, 2020, 5, 1900843 © 2020 WILEY-VCH Verlag GmbH & Co. kGaA, Weinheim. DOI: 10.1002/admt.201900843.

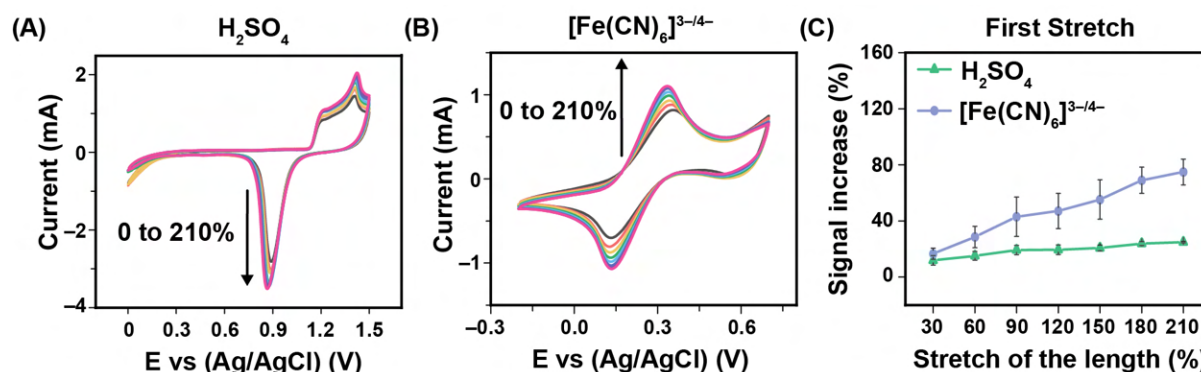
Table IV.2 - Sheet resistance of transferred gold electrode before straining, at 100% strain, and after relaxation.

State of electrode	Sheet Resistance (Ω)
Before strain	2.44 ± 0.08
At 100% strain	4.88 ± 0.50
After relaxation	2.96 ± 0.26

Source: Reproduced with permission from Imamura *et al.* Adv. Mater. Technol, 2020, 5, 1900843 © 2020 WILEY-VCH Verlag GmbH & Co. kGaA, Weinheim. DOI: 10.1002/admt.201900843.

The effect of the strain on the electrochemical signal was evaluated in H_2SO_4 and $[\text{Fe}(\text{CN})_6]^{3-/4-}$ by stretching the electrode up to 210% of its length in increments of 30% (Figure IV.6). Stretching the electrodes resulted in a greater peak height for faradaic current without significant increase in the capacitive current in both solutions. Since the faradaic current scales with the surface area, the increase in signal can be explained by newly exposed surface area due to the crack formation. The increase in the surface area seemed to have a major effect than the increase in resistance with the crack formation.

Figure IV.6 - Cyclic voltammograms of transferred gold electrode stretched up to 210% of its length in (A) H_2SO_4 and (B) $[\text{Fe}(\text{CN})_6]^{3-/4-}$. (C) Signal increase measured as peak height before and after stretch in H_2SO_4 and $[\text{Fe}(\text{CN})_6]^{3-/4-}$.



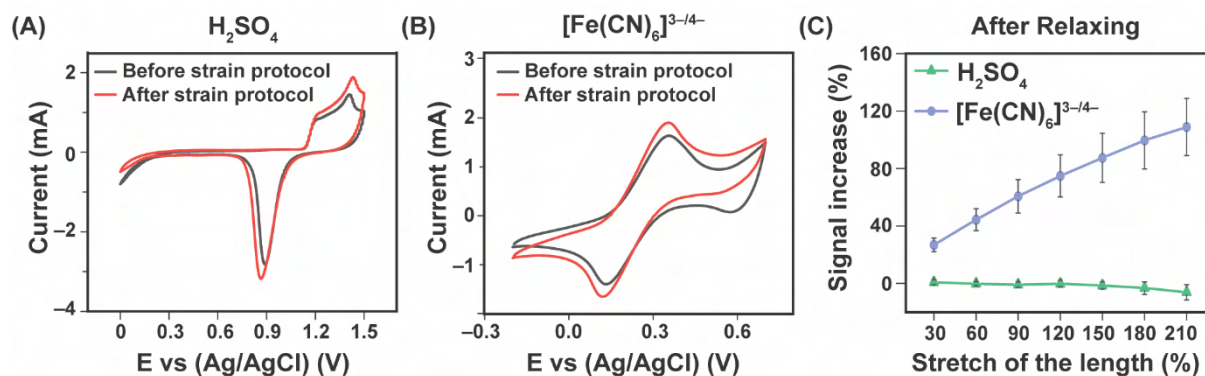
Source: Adapted by permission from Imamura *et al.* Adv. Mater. Technol, 2020, 5, 1900843 © 2020 WILEY-VCH Verlag GmbH & Co. kGaA, Weinheim. DOI: 10.1002/admt.201900843.

The signal increase in Figure IV.6C was calculated as a ratio between the peak current of the electrode stretched at a specific strain and unstrained electrode. It was observed a 20% increase in signal in H_2SO_4 . However in $[\text{Fe}(\text{CN})_6]^{3-/4-}$ a greater increase in signal with strain was achieved. This indicated that crack formation was not the only phenomenon contributing to the 60% signal enhancement in $[\text{Fe}(\text{CN})_6]^{3-/4-}$ solution. Stretching the electrode exposed the wrinkle “pockets”, as shown in the micrograph in Figure IV.4E and F, which were isolated from the solution and thus not accessed by the electroactive species $[\text{Fe}(\text{CN})_6]^{3-/4-}$ due to its

diffusion. This results in less rough surface and the $[\text{Fe}(\text{CN})_6]^{3-/4-}$ ions can more easily access the inner surface area.¹⁵ As the electrode is stretched, the wrinkled electrode behaves more likely to a planar electrode, overcoming the diffusion limitations of the $[\text{Fe}(\text{CN})_6]^{3-/4-}$ reaction. This phenomenon combined with the new surface area exposed by the crack formation explain the 60% increase in signal.

After the first straining protocol, the elastomer of the electrode relaxed overnight and the current was measured again in a relaxed state in H_2SO_4 and $[\text{Fe}(\text{CN})_6]^{3-/4-}$, as shown in the voltammograms in Figure IV.7A and B. It was observed a gain in signal of 16 and 13% in H_2SO_4 and $[\text{Fe}(\text{CN})_6]^{3-/4-}$ respectively when compared to unstrained virgin electrode. The gain in signal is explained by the new surface area created by the cracks formed during the first straining protocol. The same straining protocol was applied once again on the previously stretched electrodes in both solutions. The gain in signal was calculated as a ratio of the peak current at specific strain over the peak current of the pre-stretched electrode in a relaxed state (Figure IV.6C). The current did not increase significantly in H_2SO_4 upon stretch because all the cracks were already formed during the first strain protocol. Conversely, in $[\text{Fe}(\text{CN})_6]^{3-/4-}$, the signal continued to increase upon strain. This demonstrated that the access to the surface area of the wrinkled can be controlled by stretching the electrode to facilitate the diffusion of $[\text{Fe}(\text{CN})_6]^{3-/4-}$ species. Stretching the electrodes prior the electrochemical measurement showed to increase the signal in both solutions due to the crack formation. Therefore, the stretching protocol was used as an electrode preconditioning step to maximize the electrochemical response of the flexible electrodes, which further improved the detection of biomarkers at low concentration.

Figure IV.7 - Cyclic voltammograms of transferred gold electrodes in (A) H_2SO_4 and (B) $[\text{Fe}(\text{CN})_6]^{3-/4-}$ before and after stretching to 210% of its length and relaxing overnight. (C) Signal increase measured after relaxing the electrodes overnight in H_2SO_4 and $[\text{Fe}(\text{CN})_6]^{3-/4-}$.

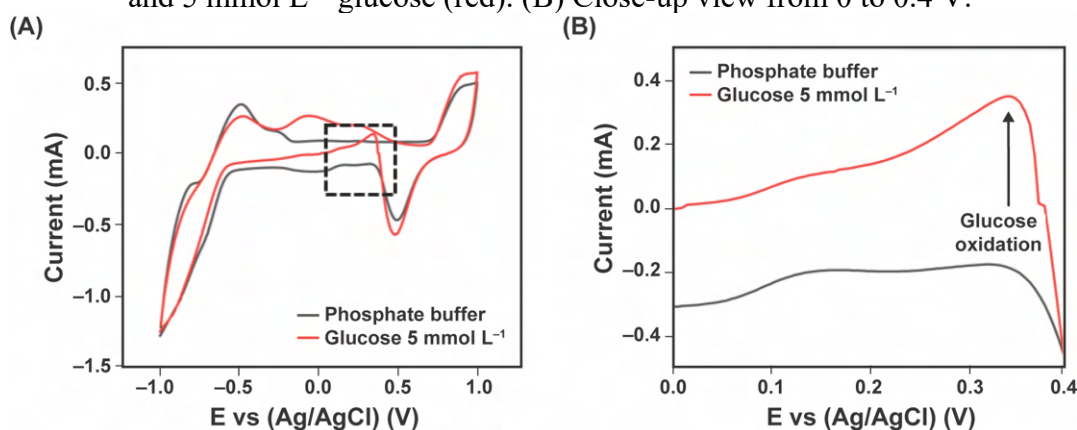


Source: Adapted by permission from Imamura *et al.* Adv. Mater. Technol, 2020, 5, 1900843 © 2020 WILEY-VCH Verlag GmbH & Co. kGaA, Weinheim. DOI: 10.1002/admt.201900843.

IV.4.4. Glucose detection

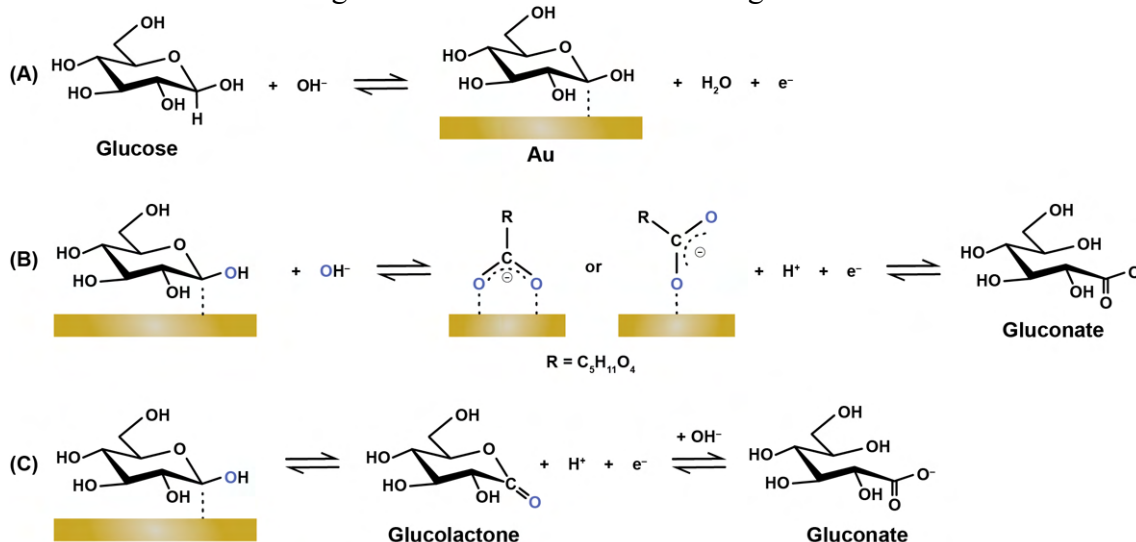
Glucose is an important biomarker for health tracking and its detection is commonly studied and optimized. Therefore, as a proof-of-concept, the detection of glucose with flexible electrodes were evaluated. The gold flexible electrode detected glucose without enzyme at physiological pH at 0.3 V (Figure IV.8). It is hypothesized that glucose oxidizes at this potential through an oxidation mechanism proposed by Pasta *et al.*,¹⁷ summarized in Figure IV.9. First, the glucose adsorbs at the gold surface through dehydrogenation reaction (Figure IV.9A). Then the adsorbed glucose is directly oxidized to gluconate (Figure IV.9B) or it is oxidized to gluconolactone, which reacts with a hydroxide and then converts to gluconate (Figure IV.9C).

Figure IV.8 - (A) Cyclic voltammograms of stretchable electrode in phosphate buffer (black), and 5 mmol L⁻¹ glucose (red). (B) Close-up view from 0 to 0.4 V.



Source: Adapted by permission from Imamura *et al.* Adv. Mater. Technol, 2020, 5, 1900843 © 2020 WILEY-VCH Verlag GmbH & Co. kGaA, Weinheim. DOI: 10.1002/admt.201900843.

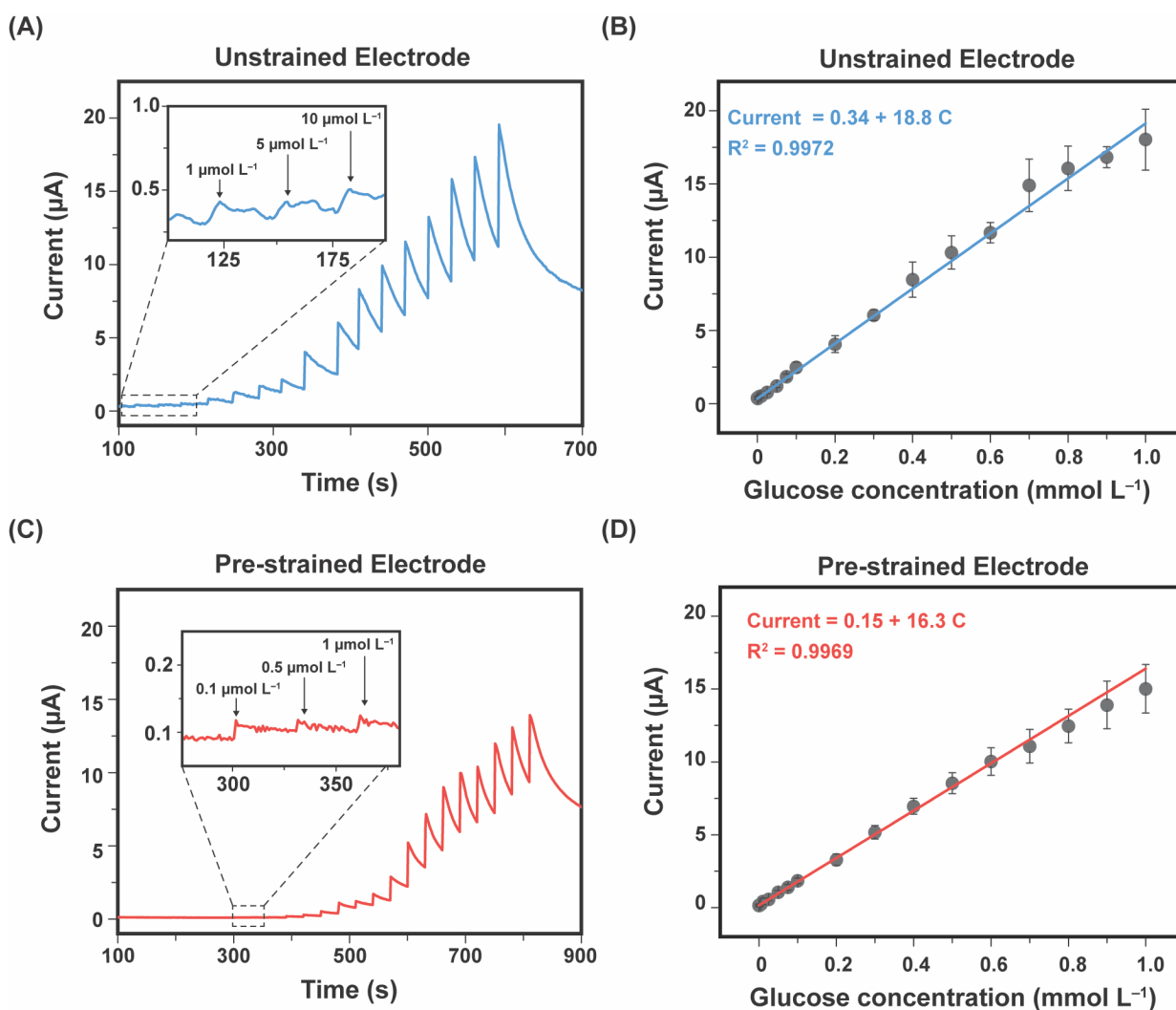
Figure IV.9 - Mechanism of glucose oxidation at gold surface. (A) Adsorption of glucose at the gold surface by dehydrogenation. (B) Direct oxidation to gluconate. (C) Oxidation to gluconolactone then conversion to gluconate.



Source: Adapted from Pasta *et al.*¹⁷

Based on the potential at which glucose oxidation was observed, chronoamperometry was used to measure sequential addition of glucose into phosphate buffer saline solution at pH 7.2 (Figure IV.10). On unstrained flexible electrode, glucose was detected in a concentration range from $1 \mu\text{mol L}^{-1}$ to 1mmol L^{-1} (Figure IV.10A and Figure IV.10B), which is adequate for glucose detection in the sweat of hypoglycemic and hyperglycemic patients ($20 \mu\text{M}$ to 0.6mM).¹⁸ The limit of detection (LOD) was calculated according to IUPAC Eq I – 2. The calculated LOD of glucose on unstrained electrode was $0.27 \mu\text{mol L}^{-1}$.

Figure IV.10 - (A) Amperometry detection of glucose from 1×10^{-3} to 1mmol L^{-1} in PBS using unstrained electrode. (B) Linear correlation of current values with glucose concentration in unstrained electrode ($R^2 = 0.9972$). (C) Amperometry detection of glucose from 1×10^{-1} to 1mmol L^{-1} in PBS using pre-strained electrode. (D) Linear correlation of current values with glucose concentration in pre-strained electrode ($R^2 = 0.9969$).



Source: Adapted by permission from Imamura et al. Adv. Mater. Technol, 2020, 5, 1900843 © 2020 WILEY-VCH Verlag GmbH & Co. kGaA, Weinheim. DOI: 10.1002/admt.201900843.

The glucose detection was also evaluated on flexible electrodes that were previously stretched up to 210% of its length and then relaxed overnight as a preconditioning step (Figure IV.10C and D). The glucose titration was performed on these pre-strained electrodes in relaxed state (without strain) in the next day. Although the sensitivity was slightly lower than for unstrained electrodes, the pre-strained electrodes detected glucose in a broader range of concentration from $0.1 \mu\text{mol L}^{-1}$ to 1mmol L^{-1} with a calculated LOD of 22nmol L^{-1} , an order of magnitude lower than on unstrained electrodes. The lower range of detection of glucose on pre-strained electrode is due to a significant improvement to signal-to-noise ratio (SNR) of an order of magnitude. The improvement in SNR is attributed to the mechanical stabilization of the wrinkled film during the preconditioning step. As stated in *Section IV.4.3*, the strain cycle promotes the crack formation into the film and the electron pathways are stabilized. As well as the electrical resistance eventually plateaus with strain cycle, the noise during the electrochemical measurement is also likely to reduce. Comparatively, the achieved LOD of 22nmol L^{-1} is lower than those reported for flexible electrodes with and without use of enzyme. Table IV.3 compares the figures of merit obtained in this work with other published works on flexible glucose sensors.

Table IV.3 - Summary of published flexible enzymatic and non-enzymatic glucose sensors. (To be continued).

Group	Electrode Material	Linear range [mol L^{-1}]	Sensitivity [$\text{A L mol}^{-1} \text{cm}^{-2}$]	LOD [mol L^{-1}]	Enzyme
This work	Wrinkled Au	$1 \times 10^{-7} - 1 \times 10^{-3}$	0.047	2×10^{-8}	No
Toi <i>et al.</i> ¹⁹	Reduced graphene oxide-polyurethane with Au wrinkles	$1 \times 10^{-6} - 1 \times 10^{-3}$	0.140	5×10^{-7}	No
Chan <i>et al.</i> ²⁰	Wrinkled Au	$1 \times 10^{-3} - 1 \times 10^{-2}$	0.860	9×10^{-4}	No
Sedighi <i>et al.</i> ²¹	NiP _{0.1} -SnO _x /PANI/CuO/cotton	$1 \times 10^{-6} - 1 \times 10^{-3}$	1.625	1.3×10^{-7}	No
		$1 \times 10^{-3} - 1 \times 10^{-2}$	1.325		
Bae <i>et al.</i> ²²	Nanoporous Au	$1 \times 10^{-5} - 1 \times 10^{-3}$	0.2534	nr ^{a)}	No
Yoon <i>et al.</i> ²³	Nanoporous Pt coated with Nafion	$0 - 1.2 \times 10^{-2}$	6.84×10^{-6}	3×10^{-5}	No
Zhai <i>et al.</i> ²⁴	Nanowire Au functionalized (NaOH)	$0 - 8 \times 10^{-4}$	2.37×10^{-2}	1×10^{-5}	Yes
Zhao <i>et al.</i> ²⁵	Au Fiber (PBS)	$0 - 5 \times 10^{-4}$	1.17×10^{-2}	2×10^{-5}	Yes

Table IV.3 - Summary of published flexible enzymatic and non-enzymatic glucose sensors.
(End)

Group	Electrode Material	Linear range [mol L ⁻¹]	Sensitivity [A L mol ⁻¹ cm ⁻²]	LOD [mol L ⁻¹]	Enzyme
Bandodkar <i>et al.</i> ²⁶	Prussian Blue carbon ink	nr ^{a)}	2.3×10^{-2}	3×10^{-6}	Yes
Lee <i>et al.</i> ²⁷	Porous Au with Prussian Blue and Nafion	$1 \times 10^{-5} - 1 \times 10^{-3}$	nr ^{a)}	nr ^{a)}	Yes
Xuan <i>et al.</i> ²⁸	Reduced graphene oxide with Au and Pt alloy nanoparticles	$0 - 2.4 \times 10^{-3}$	4.5×10^{-2}	5×10^{-6}	Yes
Yang <i>et al.</i> ²⁹	Cr/Au/PEDOT:PSS	$3 \times 10^{-8} - 3 \times 10^{-4}$	nr ^{a)}	3×10^{-8}	Yes
Lin <i>et al.</i> ³⁰	Ni/Cu/MWCNT	$2.5 \times 10^{-8} - 8 \times 10^{-4}$	2.633	2.5×10^{-8}	No
		$2 \times 10^{-3} - 8 \times 10^{-3}$	2.437		
Liu <i>et al.</i> ³¹	In ₂ O ₃ nanoribbons on Au	$1 \times 10^{-8} - 1 \times 10^{-3}$	nr ^{a)}	1×10^{-8}	Yes
Pellitero <i>et al.</i> ³²	Graphite modified with Prussian Blue	$1 \times 10^{-4} - 1 \times 10^{-3}$	0.08	1×10^{-6}	Yes

a) nr = Not reported

IV.5. CONCLUSION

High surface area electrodes were fabricated by heat-induced shrinking of a polymer coated with thin metallic film without the need of specific equipment or cleanroom. The shrink electrodes were characterized by the wrinkled structures on the surface, responsible for the high surface area, which was explored for electrochemical measurements. The wrinkled films were transferred into an elastomer substrate to further apply as a wearable sensor.

It was observed an increase in the electrochemical signal of 32- and 13-fold in H_2SO_4 and $[\text{Fe}(\text{CN})_6]^{3-/4-}$ for the transferred films. The initial surface area before the shrinking and transfer was maintained and fully accessed during the electrochemical measurement in H_2SO_4 . However, because $\text{Fe}(\text{CN})_6]^{3-/4-}$ is a diffusion-dependent reaction, the morphology of the wrinkles hinder the diffusion of the electroactive species into the inner surface of the wrinkles. Therefore, it was observed a lower signal increase in $\text{Fe}(\text{CN})_6]^{3-/4-}$ solution. Stretching the electrodes contributed to further increase the electrochemical signal by creating more surface area through cracks formation and by opening the wrinkles allowing the $\text{Fe}(\text{CN})_6]^{3-/4-}$ ions to access the inner surface of the wrinkles. The strain cycle also improved the SNR by stabilizing the wrinkled film. This effect was observed during the measurement of glucose. On pre-strained electrode, the LOD was 22 nmol L^{-1} , an order of magnitude lower than the one calculated for the non-strained electrode. The achieved LOD is among the lowest reported in the literature. Selectivity study must be carried to ensure the detection of glucose in complex matrix such as sweat before its application as wearable sensor. Nevertheless, these findings encourage the application of the flexible wrinkled electrode as an electrochemical sensing surface of important biomarkers in a miniaturized setting, enabling POC applications and individualized monitoring in a form of wearable devices.

IV.6. REFERENCES

1. METTAKOONPITAK, J.; BOEHLE, K.; NANTAPHOL, S.; TEENGAM, P.; ADKINS, J. A.; SRISA-ART, M.; HENRY, C. S. Electrochemistry on paper-based analytical devices: a review. **Electroanalysis**, Weinheim, v. 28, p. 1420–1436, 2016. DOI: 10.1002/elan.201501143.
2. HAUKE, A.; KUMAR, L. S. S.; KIM, M. Y.; PEGAN, J.; KHINE, M.; LI, H.; PLAXCO, K. W.; HEIKENFELD, J. Superwetting and aptamer functionalized shrink-induced high surface area electrochemical sensors. **Biosensors & Bioelectronics**, Oxford, v. 94, p. 438–442, 2017. DOI: 10.1016/j.bios.2017.03.024.
3. KATZ, E.; WILLNER, I.; WANG, J. Electroanalytical and bioelectroanalytical systems based on metal and semiconductor nanoparticles. **Electroanalysis**, Weinheim, v. 16, p. 19–44, 2004. DOI: 10.1002/elan.200302930.
4. SCHRÖPER, F.; BRÜGGEMANN, D.; MOURZINA, Y.; WOLFRUM, B.; OFFENHÄUSSER, A.; MAYER, D. Analyzing the electroactive surface of gold nanopillars by electrochemical methods for electrode miniaturization. **Electrochimica Acta**, Oxford, v. 21, p. 6265–6272, 2008. DOI: 10.1016/j.electacta.2008.03.068.
5. PEGAN, J. D.; HO, A. Y.; BACHMAN, M.; KHINE, M. Flexible shrink-induced high surface area electrodes for electrochemiluminescent sensing. **Lab on a Chip**, Cambridge, v. 13, p. 4205–4209, 2013. DOI: 10.1039/C3LC50588J.
6. GABARDO, C. M.; ZHU, Y.; SOLEYMANI, L.; MORAN-MIRABAL, J. M. Bench-top fabrication of hierarchically structured high-surface-area electrodes. **Advanced Functional Materials**, Weinheim, v. 23, p. 3030–3039, 2013. DOI: 10.1002/adfm.201203220.
7. PARK, S.-J.; KIM, J.; CHU, M.; KHINE, M. Highly flexible wrinkled carbon nanotube thin film strain sensor to monitor human movement. **Advanced Materials Technologies**, Hoboken, v. 1, p. 1600053, 2016. DOI: 10.1002/admt.201600053.
8. CHU, M.; NGUYEN, T.; PANDEY, V.; ZHOU, Y.; PHAM, H. N.; BAR-YOSEPH, R.; RADOM-AIZIK, S.; JAIN, R.; COOPER, D. M.; KHINE, M. Respiration rate and volume measurements using wearable strain sensors. **npj Digital Medicine**, Berlin, v. 2, p. 1–9, 2019. DOI: 10.1038/s41746-019-0083-3.
9. KIM, J.; CHOU, E.-F.; LE, J.; WONG, S.; CHU, M.; KHINE, M. Soft wearable pressure sensors for beat-to-beat blood pressure monitoring. **Advanced Healthcare Materials**, Hoboken, v. 8, p. 1900109, 2019. DOI: 10.1002/adhm.201900109.
10. JIA, F.; YU, C.; AI, Z.; ZHANG, L. Fabrication of nanoporous gold film electrodes with ultrahigh surface area and electrochemical activity. **Chemistry of Materials**, Washington, v. 19, p. 3648–3653, 2007. DOI: 10.1021/cm070425l.

11. SCANLON, M. D.; SALAJ-KOSLA, U.; BELOCHAPKINE, S.; MACAODHA, D.; LEECH, D.; DING, Y.; MAGNER, E. Characterization of nanoporous gold electrodes for bioelectrochemical applications. **Langmuir**, Washington, v. 28, p. 2251–2261, 2012. DOI: 10.1021/la202945s.
12. ROUYA, E.; CATTARIN, S.; REED, M. L.; KELLY, R. G.; ZANGARI, G. Electrochemical characterization of the surface area of nanoporous gold films. **Journal of The Electrochemical Society**, Pennington, v. 159, p. K97, 2012. DOI: 10.1149/2.097204jes.
13. TAN, Y. H.; DAVIS, J. A.; FUJIKAWA, K.; GANESH, N. V.; DEMCHENKO, A. V.; STINE, K. J. Surface area and pore size characteristics of nanoporous gold subjected to thermal, mechanical, or surface modification studied using gas adsorption isotherms, cyclic voltammetry, thermogravimetric analysis, and scanning electron microscopy. **Journal of Materials Chemistry**, New York, v. 22, p. 6733–6745, 2012. DOI: 10.1039/C2JM16633J.
14. TRASATTI, S.; PETRII, O. A. Real surface area measurements in electrochemistry. **Pure and Applied Chemistry**, Berlin, v. 63, p. 711–734, 1991. DOI: 10.1351/pac199163050711.
15. COLLINSON, M. M. Nanoporous gold electrodes and their applications in analytical chemistry. **ISRN Analytical Chemistry**, London, v. 2013, p. e692484, 2013. DOI: 10.1155/2013/692484.
16. LIN, L.; CHU, M.; PARK, S.-J.; ZAKASHANSKY, J. A.; KHINE, M. Conformal stretch sensors for high resolution motion sensing and control. **Macromolecular Materials and Engineering**, Weinheim, v. 304, p. 1800520, 2019. DOI: 10.1002/mame.201800520.
17. PASTA, M.; LA MANTIA, F.; CUI, Y. Mechanism of glucose electrochemical oxidation on gold surface. **Electrochimica Acta**, Oxford, v. 55, p. 5561–5568, 2010. DOI: 10.1016/j.electacta.2010.04.069.
18. WITKOWSKA NERY, E.; KUNDYS, M.; JELEŃ, P. S.; JÖNSSON-NIEDZIÓŁKA, M. Electrochemical glucose sensing: is there still room for improvement? **Analytical Chemistry**, Washington, v. 88, p. 11271–11282, 2016. DOI: 10.1021/acs.analchem.6b03151.
19. TOI, P. T.; TRUNG, T. Q.; DANG, T. M. L.; BAE, C. W.; LEE, N.-E. Highly electrocatalytic, durable, and stretchable nanohybrid fiber for on-body sweat glucose detection. **ACS Applied Materials & Interfaces**, Washington, v. 11, p. 10707–10717, 2019. DOI: 10.1021/acsami.8b20583.
20. CHAN, Y.; SKRETA, M.; MCPHEE, H.; SAHA, S.; DEUS, R.; SOLEYMANI, L. Solution-processed wrinkled electrodes enable the development of stretchable electrochemical biosensors. **Analyst**, Cambridge, v. 144, p. 172–179, 2018. DOI: 10.1039/C8AN01637B.
21. SEDIGHI, A.; MONTAZER, M.; MAZINANI, S. Synthesis of wearable and flexible NiP0.1-SnOx/PANI/CuO/cotton towards a non-enzymatic glucose sensor. **Biosensors & Bioelectronics**, Oxford, v. 135, p. 192–199, 2019. DOI: 10.1016/j.bios.2019.04.010.

22. BAE, C. W.; TOI, P. T.; KIM, B. Y.; LEE, W. I.; LEE, H. B.; HANIF, A.; LEE, E. H.; LEE, N. E. Fully stretchable capillary microfluidics-integrated nanoporous gold electrochemical sensor for wearable continuous glucose monitoring. **ACS Applied Materials & Interfaces**, Washington, v. 11, p. 14567–14575, 2019. DOI: 10.1021/acsami.9b00848.
23. YOON, H.; XUAN, X.; JEONG, S.; PARK, J. Y. Wearable, robust, non-enzymatic continuous glucose monitoring system and its in vivo investigation. **Biosensors & Bioelectronics**, Oxford, v. 117, p. 267–275, 2018. DOI: 10.1016/j.bios.2018.06.008.
24. ZHAI, Q.; GONG, S.; WANG, Y.; LYU, Q.; LIU, Y.; LING, Y.; WANG, J.; SIMON, GEORGE. P.; CHENG, W. Enokitake mushroom-like standing gold nanowires toward wearable noninvasive bimodal glucose and strain sensing. **ACS Applied Materials & Interfaces**, Washington, v. 11, p. 9724–9729, 2019. DOI: 10.1021/acsami.8b19383.
25. ZHAO, Y.; ZHAI, Q.; DONG, D.; AN, T.; GONG, S.; SHI, Q.; CHENG, W. Highly stretchable and strain-insensitive fiber-based wearable electrochemical biosensor to monitor glucose in the sweat. **Analytical Chemistry**, Washington, v. 91, p. 6569–6576, 2019. DOI: 10.1021/acs.analchem.9b00152.
26. BANDODKAR, A. J.; JIA, W.; YARDIMCI, C.; WANG, X.; RAMIREZ, J.; WANG, J. Tattoo-based noninvasive glucose monitoring: a proof-of-concept study. **Analytical Chemistry**, Washington, v. 87, p. 394–398, 2015. DOI: 10.1021/ac504300n.
27. LEE, H.; SONG, C.; HONG, Y. S.; KIM, M. S.; CHO, H. R.; KANG, T.; SHIN, K.; CHOI, S. H.; HYEON, T.; KIM, D.-H. Wearable/disposable sweat-based glucose monitoring device with multistage transdermal drug delivery module. **Science Advances**, Washington, v. 3, p. e1601314, 2017. DOI: 10.1126/sciadv.1601314.
28. XUAN, X.; YOON, H. S.; PARK, J. Y. A wearable electrochemical glucose sensor based on simple and low-cost fabrication supported micro-patterned reduced graphene oxide nanocomposite electrode on flexible substrate. **Biosensors & Bioelectronics**, Oxford, v. 109, p. 75–82, 2018. DOI: 10.1016/j.bios.2018.02.054.
29. YANG, A.; LI, Y.; YANG, C.; FU, Y.; WANG, N.; LI, L.; YAN, F. Fabric organic electrochemical transistors for biosensors. **Advanced Materials**, Weinheim, v. 30, p. 1800051, 2018. DOI: 10.1002/adma.201800051.
30. LIN, K. C.; LIN, Y. C.; CHEN, S. M. A highly sensitive nonenzymatic glucose sensor based on multi-walled carbon nanotubes decorated with nickel and copper nanoparticles. **Electrochimica Acta**, Oxford, v. 96, p. 164–172, 2013. DOI: 10.1016/j.electacta.2013.02.098.
31. LIU, Y.; TENG, H.; HOU, H.; YOU, T. Nonenzymatic glucose sensor based on renewable electrospun Ni nanoparticle-loaded carbon nanofiber paste electrode. **Biosensors & Bioelectronics**, Oxford, v. 24, p. 3329–3334, 2009. DOI: 10.1016/j.bios.2009.04.032.
32. ALLER-PELLITERO, M.; FREMEAU, J.; VILLA, R.; GUIRADO, G.; LAKARD, B.; HIHN, J. Y.; DEL CAMPO, F. J. Electrochromic biosensors based on screen-printed Prussian blue electrodes. **Sensors and Actuators B: chemical**, Lausanne, v. 290, p. 591–597, 2019. DOI: 10.1016/j.snb.2019.03.100.

CHAPTER V

Electrochemical sensing devices for diagnosing COVID-19 in saliva samples

V.1. INTRODUCTION

With the advance of the COVID-19, the need for a faster and cheaper diagnosis to better counter the spread of the disease was evident. The gold standard for diagnosing COVID-19 is analyzing nucleic acid content in nasopharyngeal samples by RT-PCR, performed in clinical setups. During voluminous demand of testing, RT-PCR has struggled to analyze large number of samples in a short time. Besides, RT-PCR requires chemical supplies for the tests, which entails expensive diagnose for widespread testing. As previously discussed in *CHAPTER I*, POC testing has been exploited to diagnose diseases centered in the patient rather than in clinical setups, facilitating the widespread of the diagnosis. Although there are commercially available POC lateral-flow assays (LFA) for COVID-19, most of them consist of serological tests, of which cornerstone is the detection of the antibodies produced by the immune system against the virus. These antibody detection tests, however, can rarely inform the current state of the infection and give poor information for tracing the virus spread. On the other hand, antigen-based diagnosis, *i.e.*, detecting the whole virus or parts of it, is more appropriate to state the viral load in the patient. Since the pandemic began, many alternatives to PCR for diagnosing COVID-19 have been reported in the literature. Table V.1 summarizes the published works on POC for diagnosing COVID-19 based on detecting the antigen.

Table V.1 - Summary of peer-reviewed published works on antigen-based POC diagnosis for COVID-19. (To be continued)

Ref	Target analyte	Sample	Transduction	Description	Figures of merit
1	S1 subunit	NSS	Colorimetric	Lateral flow immunoassay with ACE2 and antibody against S1 subunit	LOD for virus In NSS: 1.86×10^5 copies mL ⁻¹
2	RBD and VLP	VTM, saliva, nasal fluid, and sputum	Fluorescence	SWCNT immobilized with ACE2 proteins	LOD for RBD In PBS: 12.6 nM LOD for VLP In 10% sucrose: 35 mg L ⁻¹ (corresponds to 17 nM of RBD)
3	S protein	PBS	Optical (plasmonic metasensor)	Plasmonic immunosensor based on toroidal electrodynamic with colloidal AuNP conjugates with antibody against S1 subunit	LOD for S protein In PBS: 319.2 fg mL ⁻¹
4	S1 subunit	Standard solution	Electrical	Electrodes with PDMS well in which the sample and the cell membrane with antibody against S1 subunit	LOD for S1 subunit Standard solution: 1 fg mL ⁻¹

Table V.1 - Summary of peer-reviewed published works on antigen-based POC diagnosis for COVID-19. (End)

Ref	Target analyte	Sample	Transduction	Description	Figures of merit
5	S protein and cultured virus	CTM, CM, NSS	Field-Effect-Transistor	Graphene-based FET with antibody against S protein	LOD for S protein In PBS: 1fg mL ⁻¹ In CTM: 100 fg mL ⁻¹ LOD for Virus In CM: 1.6 × 10 pfu mL ⁻¹ In NSS: 2.42 × 10 ² copies mL ⁻¹
6	S and N proteins	NSS	Field-Effect-Transistor	SWCNT-based FET functionalized with antibodies against S protein and N protein	LOD for S protein In PBS: 0.55 fg mL ⁻¹ LOD for N protein In PBS: 0.016 fg mL ⁻¹
7	S1 subunit	Saliva	Field-Effect-Transistor	SWCNT-based FET with antibody against S1 subunit	LOD for S1 subunit In buffer: 4.12 fg mL ⁻¹ Quantification range: In saliva: 0.1 to 5000 fg mL ⁻¹
8	S protein	PBS	Field-Effect Transistor	WSe2-based FET functionalized with antibody against S protein	LOD for S protein In PBS: 25 pg mL ⁻¹
9	S and N proteins, and virus	Untreated saliva	Electrochemical	Magnetic beads supporting immunological chain and secondary antibody with alkaline phosphatase as label. Enzymatic by-product detected by SPE modified with carbon black	LOD for S protein Untreated saliva: 19 ng mL ⁻¹ LOD for N protein Untreated saliva: 8 ng mL ⁻¹ LOD for virus (with anti-S antibody) In PBS: 6.5 pfu mL ⁻¹ (with anti-N antibody) In PBS: 6.5 × 10 ³ pfu mL ⁻¹
10	S protein and inactivated virus	Saliva, VTM, NSS	Electrochemical	Graphite leads modified with ACE2	LOD for S protein In PBS: 229 fg mL ⁻¹ LOD for inactivated virus In VTM: 2.07 pfu mL ⁻¹ (corresponds to 10 RNA copies mL ⁻¹)
11	RBD	Serum	Electrochemical	Electrochemical paper-based analytical device functionalized with SARS-CoV-2 IgM	LOD for RBD In PBS: 0.11 ng mL ⁻¹
12	S protein	PBS and viral lysis medium	Electrochemical	SPE modified with graphene layer and functionalized with antibody against S protein	LOD for S protein In PBS: 20 µg mL ⁻¹ LOD for virus In viral solution: 5.5 × 10 ⁵ pfu mL ⁻¹
13	N protein	PBS and fortified saliva	Colorimetric	Vertical-flow cellulose paper test with affinity pairs against N protein	LOD for N protein In PBS: 1.9 ng mL ⁻¹ In saliva: 3.8 ng mL ⁻¹

* ACE2 – Angiotensin converting enzyme 2; CM – Culture medium; CTM – Clinical transport medium; FET – Field-effect transistor; LOD – Limit of detection; NSS – Nasopharyngeal swab specimen; PBS – Phosphate buffer saline; RBD – Receptor-binding domain; SPE – Screen-printed electrode; VLP – Virus like particle; VTM – Virus transportation medium.

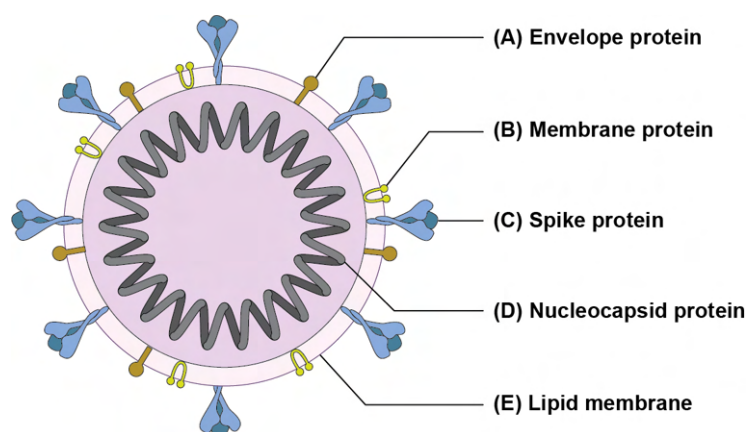
Another concern for promoting widespread testing is the sampling method. Invasive methods such as nasopharyngeal swabs require trained professionals for the sampling step, which are not abundantly available in low-resources setting and high-demand scenarios, such as a pandemic. Furthermore, the swab causes discomfort and induces coughing and bleeding, a hazardous exposure to the health care workers.¹⁴ Saliva arises as an interesting alternative as a biological fluid for diagnosing COVID-19 since it can be safely self-collected at home without requiring medical professionals, relieving the health care system.^{14,15} In fact, a study comparing nasopharyngeal swab specimens (NSS) and saliva showed higher rates of positive results in RT-PCR for the latter, inducing more sensitive diagnoses for COVID-19.¹⁵ Many POC related in the literature adopted saliva as a biofluid of analysis since it has been proven to be adequate for the diagnoses.

The most common target analyte to diagnose COVID-19 is the Spike (S) protein, which consists of the outermost protein of the virus (Figure V.1) and is responsible for initiating the cell infection. S protein consists of two subunits: S1 and S2. The S1 subunit contains the receptor-binding domain (RBD), which binds to the angiotensin-converting enzyme 2 (ACE2), an enzyme attached to the membranes of the cells in the host. Therefore, S1 is essential for initiating the viral entry in the host's cell. Meanwhile, the S2 subunit forms the stalk region and maintains the S fused to the viral membrane.¹⁶ In addition to the S protein, nucleocapsid (N) proteins are also investigated for diagnosing COVID-19. N proteins bind to the viral genome in a conformation resembling beads on a string and are located inside the virus, only released upon infection.¹⁶ The N protein has already been proved to be a reliable marker for early diagnoses of SARS-CoV,¹⁷ and studies suggest the same conclusion for SARS-CoV-2 as well.^{6,9,19} In fact, the detectability of the biosensors for N protein was better when compared to S protein.^{6,9} However, when tested to detect the whole virus, the biosensors with the antibody against N protein as bioreceptor showed less effective discrimination between positive and negative samples (higher false-negative output)⁶ as well as lesser detectability (high limit of detection).⁹ The poorer performance of the biosensor using the anti-N protein antibody for detecting the whole virus can be attributed to the lower amount of the N proteins on the SARS-CoV-2 virus compared to the S protein. Besides, their inner location in the virus limits their presence in unprocessed biological fluids.

Although LFA is commonly employed for serological tests, it can also be adapted for antigen detection. Lee *et al.* used two different bioreceptors for the sandwich-like detection of SARS-CoV-2: ACE2 and antibody against S1 subunit.¹ The ACE2 was immobilized in the nitrocellulose strip to capture the virus while the antibody was conjugated onto the colorimetric

probe (red cellulose nanobeads). The ACE2-based LFA for antigen detection detected down to 1.86×10^5 copies mL⁻¹ in NSS.¹ Although the adaptation of LFA for antigen detection is promising for widespread testing, there is still room for improvement regarding the limit of detection (LOD). Other optical transduction techniques such as fluorescence and plasmonic were reported for detecting the virus.^{2,3}

Figure V.1 - SARS-CoV-2 structure and main components: (A) Envelope protein, (B) membrane protein, (C) spike protein, (D) nucleocapsid protein, and (E) lipid membrane.



Source: Own authorship.

Commonly deployed transduction techniques in POC testing are electrochemical and electrical detection. These techniques are often chosen since they present great sensitivity and detectability, suitable for detecting low amounts of virus or its parts in biological fluids. Furthermore, their ease for miniaturization and integration to electronic systems enables device portability and data acquisition, ideal for widespread testing. Among the electrical transduction reported for POC testing of SARS-CoV-2, biosensors based on field-effect transistor (FET) have been widely employed. FET is a type of transistor consisting of three terminals: source, drain, and gate. At the latter, an electric field is applied, inducing a current change in the channel between the source and the drain terminals.²⁰ Carbon-based nanomaterials, such as graphene and carbon nanotubes (CNT), are introduced in the channel within the transistor structure to promote faster response time due to their enhanced conductive properties. In FET biosensors employing carbon-based nanomaterials, the virus is captured by bioreceptors immobilized on the nanomaterials, modifying the channel conductivity, detected at the output.²⁰ For the detection of SARS-CoV-2, graphene sheets and single-wall carbon nanotube (SWCNT) were used within the transistor structure.⁵⁻⁷ Low LOD in the order of femtogram (10^{-15}) per milliliter were reported for S protein. Seo *et al.* tested the graphene-based FET biosensor in NSS,

detecting the whole virus down to 2.42×10^2 copies mL^{-1} .⁵ Other materials have been exploited for FET since graphene can increase the off-state current leakage inducing false-signals. Fathi-Hafshejani *et al.* applied tungsten diselenide (WSe_2) in the FET structure to avoid the current leakage, and the biosensor detected the S protein at 25 pg mL^{-1} in PBS.⁸ For the detection of SARS-CoV-2, carbon-based FET showed better analytical features. In fact, the LOD was even comparable to the current molecular diagnostic tests, which range from approximately 50 – 100 copies.^{5,21}

As for electrochemical detection, different approaches were reported for detecting SARS-CoV-2, including using paper as substrate for diminishing the production cost, nanostructures and magnetic beads to improve detectability, and graphite lead as an alternative working electrode. Electrochemical paper-based analytical device (ePAD) is a suitable approach for diagnosing infectious disease since paper can be safely disposed of by incineration after its use. The ePAD developed by Yakoh *et al.* detected RBD at nanogram per milliliter range, above the detection level required to diagnose COVID-19 in real NSS.¹¹ Screen-printed electrodes (SPE) are commonly employed for POC testing due to their lightweight and portability. These electrodes can be modified with different nanomaterials, such as carbon-based nanostructures, to improve the analytical performance. Graphene was deposited onto the working electrode to enhance the conductivity and improve the performance compared to crude SPE. The limit of detection achieved with a graphene-modified SPE was at $20 \text{ } \mu\text{g mL}^{-1}$,¹² still not sensitive enough for detecting SARS-CoV-2 in biological fluids. SPE can be coupled with magnetic beads to improve the detectability of the sensor by concentrating the analyte at the detecting zone. Fabiani *et al.* detected the whole virus down to 6.5 pfu mL^{-1} using the magnetic beads as support for the immunological chain.⁹ Another low-cost, miniaturized electrochemical system was developed by Lima *et al.* with graphite leads as the working electrode and a plastic vial.¹⁰ The graphite leads were modified with ACE2 for the specific recognition of the S protein, detecting the virus in concentration as low as 2 pfu mL^{-1} , which corresponds to 10 RNA copies mL^{-1} .¹⁰ As can be seen, electrochemistry is a versatile transduction technique that can be applied in many different ways to detect the same analyte.

V.2. AIMS

This chapter presents two electrochemical approaches co-developed by the author for detecting SARS-CoV-2 in saliva:

Paper I. Detection of the SARS-CoV-2 spike protein in saliva with Shrinky-Dink® electrodes (DOI: [10.1039/D1AY00041A](https://doi.org/10.1039/D1AY00041A), full paper attached in ANNEX 3)

Paper II. Electrochemical immunosensors using electrochemically formed gold nanostructures for detecting the S proteins from both SARS-CoV and SARS-CoV-2. (DOI: [10.1007/s00216-022-03956-1](https://doi.org/10.1007/s00216-022-03956-1), full paper attached in ANNEX 4)

The works are compared, highlighting the differences between them as well as their advantages.

V.3. MAIN DIFFERENCES

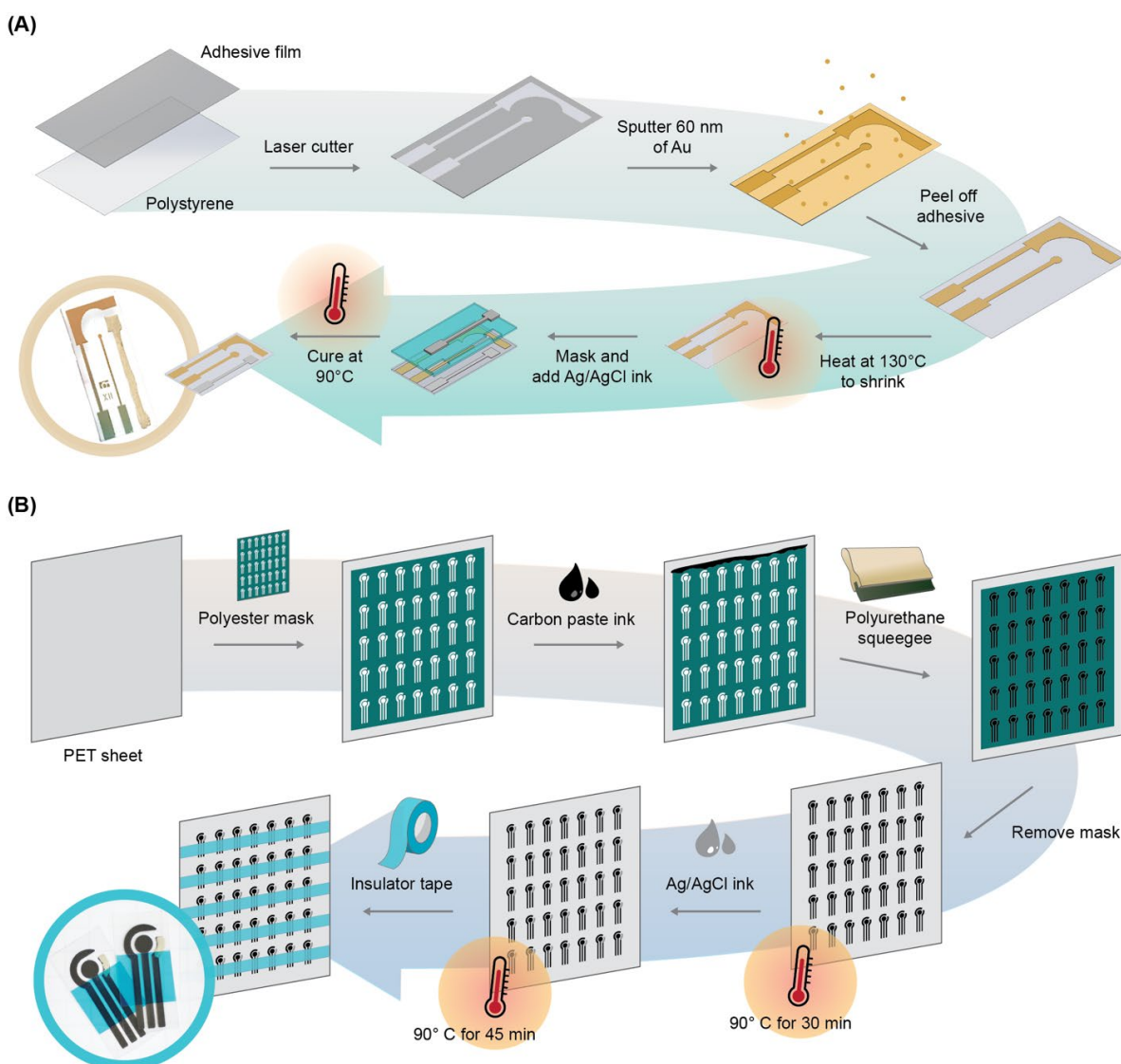
V.3.1. Fabrication method: Shrinky-Dinks vs. SPE

In paper I, the electrodes consisted of a set of wrinkled electrodes in a geometry similar to a common SPE for POC application, entitled *mini cells*. Thermoplastic polystyrene (PS) sheet was masked with laminating adhesive. The working and counter electrodes design was laser cut only in the adhesive layer, which was removed in the electrodes region to form a positive mask for the sputtering step. The gold was then sputtered to form working and counter electrodes with 60 nm layer. The PS sheet was heated in a convection oven at 130 °C to promote the shrinking of the electrodes. Then, a PDMS mask was placed on the shrunk PS for hand application of Ag/AgCl ink, forming the reference electrode. In paper II, the electrochemical cell consisted of screen-printed electrodes (SPE) on a polyethylene terephthalate (PET) sheet. A polyester mask was applied onto the PET sheet and a carbon paste ink was spread out with a squeegee. The mask was then removed for the curing step in an oven at 90 °C for 30 min. The Ag/AgCl ink was applied by hand and cured at 90 °C for 45 min. The working areas were isolated with an insulator tape. The fabrication steps for both types of electrodes are illustrated in Figure V.2.

In a lab setup, the SPEs are easily batch fabricated, with an outcome for dozens of electrodes per sheet of PET. The production of mini cells, on the other hand, are limited by the size of the chamber of the sputter machine. Besides, the peeling step of the laminating adhesive can be cumbersome. However, if scaled up for large production, industrial sputters can handle the sputtering of many electrodes at once, being less time-consuming.

In both works, the electrochemical analysis was performed in a drop, and required sample for the diagnosis in the order of microliters, promoting the POC application.

Figure V.2 - Fabrication processes of the (A) minicells and (B) SPEs.

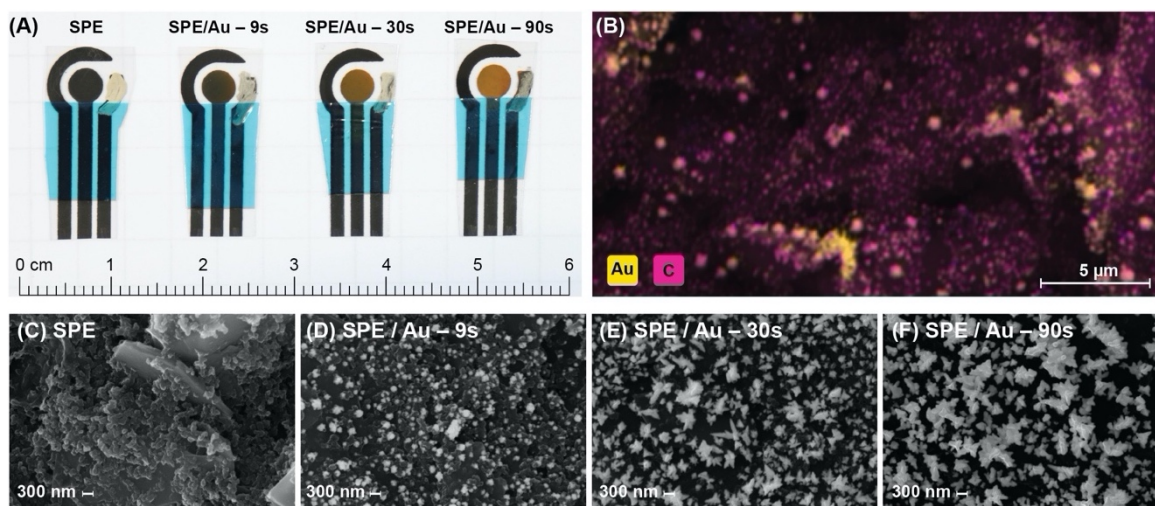


Source: (A) Reproduced from Zakashansky *et al.* *Anal. Methods*, 2021, 13, 874-883. © Royal Society of Chemistry 2022. DOI: 10.1039/D1AY00041A. (B) Own authorship.

V.3.2. Electrochemical modification

To improve the detectability of electrochemical transduction, two different approaches were evaluated. For the SPE, gold was electrochemically deposited in a form of nanostructures on the working electrode. The deposition was performed by applying a constant potential at -4 V in a solution of hydrogen tetrachloroaurate (III) in sulfuric acid for 9, 30, and 90 s (Figure V.3A). The increase in the deposition time resulted in larger amount of gold deposited on the working electrode surface, which can be observed on the color of the WE areas in Figure V.3A and on the SEM images in Figure V.3C - F. In the SEM images, the light spots correspond to the gold structures and the dark regions to carbon components from the ink. The gold structure changes with different deposition time, increasing the size of the agglomerates.

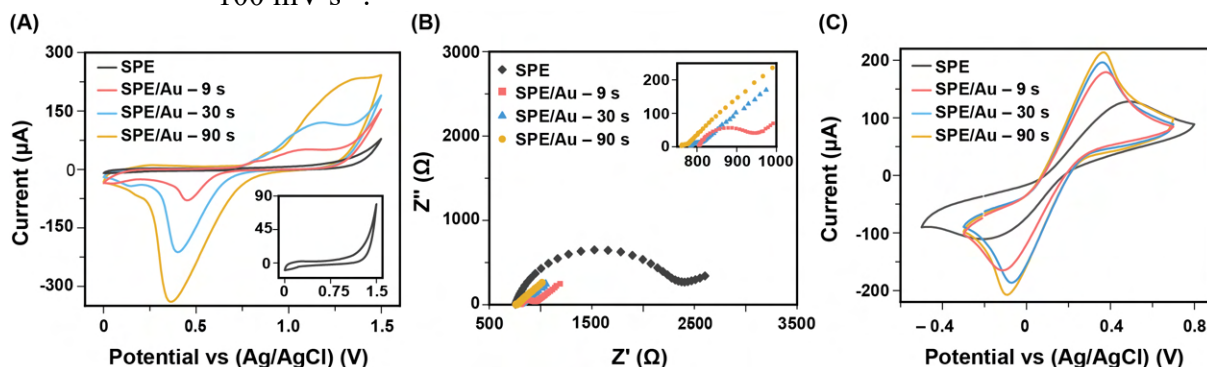
Figure V.3 - (A) SPE before and after electrodeposition of gold for 9, 30, and 90 s. (B) Elemental mapping of SPE after electrodeposition of gold for 9 s. Pink and yellow shades represent carbon and gold, respectively. SEM images of (C) bare SPE and modified with gold electrodeposited for (D) 9 s, (E) 30 s, and (F) 90 s.



Source: Own authorship.

The influence of the amount of gold deposited on the WE were evaluated by cyclic voltammetry (CV) and electrochemical impedance spectroscopy (EIS). The CV scans in H_2SO_4 from 0 to 1.5 V showed typical oxidation and reduction peaks profile for gold around 1.1 V and 0.4 V respectively after depositing the gold. In fact, the peak currents increased with longer deposition time, which indicate more gold at electrodes surface, corroborating with the SEM images. For the SPE without modification (in black in Figure V.4A), the voltammogram consisted of mostly capacitive current due to the absence of any electrochemical reactions at the surface of the electrode. The presence of gold also contributed to the conductivity of the electrodes, as can be observed in the EIS and CV measurements in $[\text{Fe}(\text{CN})_6]^{4-/3-}$ from Figure V.4B and C, respectively. The Nyquist plots consisted of semicircles and straight diffusion lines. The diameter of the semicircle corresponds to the resistance to charge transfer (R_{CT}). The SPE initially present a large R_{CT} since carbon-based electrodes are not quite conductive. With the deposition of gold, the R_{CT} decreased monotonically due to the presence of sites of gold that enhanced the electron transfer. The improved electron transfer can also be inferred from the CV measurements in Figure V.4C. The larger peak currents from oxidation and reduction of $[\text{Fe}(\text{CN})_6]^{4-/3-}$ are indicative of lower resistance of electron transfer in electrochemical reactions. Furthermore, the presence of gold structures increased the roughness of the electrode surface, as can be observed in the SEM images Figure V.3D - F, increasing the electrochemically active surface area (EASA), which also contributes to enhancing the current related to electrochemical reactions.

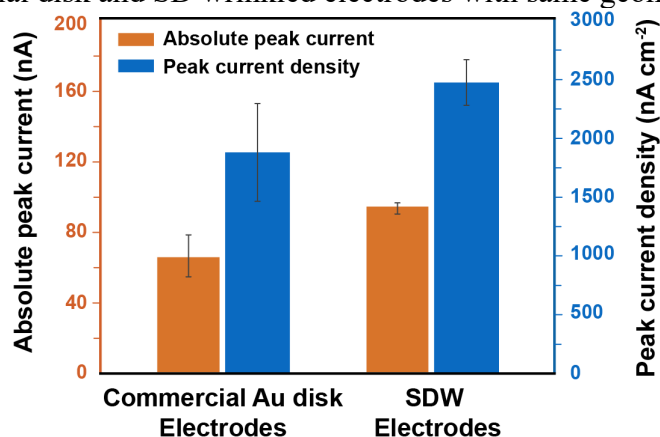
Figure V.4 - Electrochemical characterization of the SPE (black) modified with gold electrodeposited for 9s (red), 30s (blue), and 90s (yellow). (A) CVs in H_2SO_4 at 100 mV s^{-1} . Insert shows a zoomed view of the CV of SPE. (B) Nyquist plots in $[\text{Fe}(\text{CN})_6]^{4-/3-}$ from 10 kHz to 10 mHz. (C) CVs in $[\text{Fe}(\text{CN})_6]^{4-/3-}$ at 100 mV s^{-1} .



Source: Own authorship.

For the mini cells, the enhancement on the EASA was achieved by the wrinkling of the gold thin film with the shrinking of the pre-stressed thermoplastic. The wrinkled electrode, as discussed in *CHAPTER IV*, showed an enhanced current in comparison to an electrode with same geometrical area. When compared to commercial disk electrodes with same geometric area, the Shrinky-Dink (SD) wrinkled electrodes showed enhanced peak current and current density of the redox probe (Figure V.5). The increase in the peak current is attributed to more redox probe tethered at the larger surface area of the Shrinky-Dink wrinkled electrodes. The increase in the current density comes from the larger EASA by the shrinking of the metal film, as extensively discussed in *CHAPTER IV*. The increased EASA is achieved during the fabrication process, not requiring any treatment or deposition of materials on the electrodes, like for the SPE.

Figure V.5 - Peak currents and peak current densities of redox probe methylene blue in commercial disk and SD wrinkled electrodes with same geometric areas.



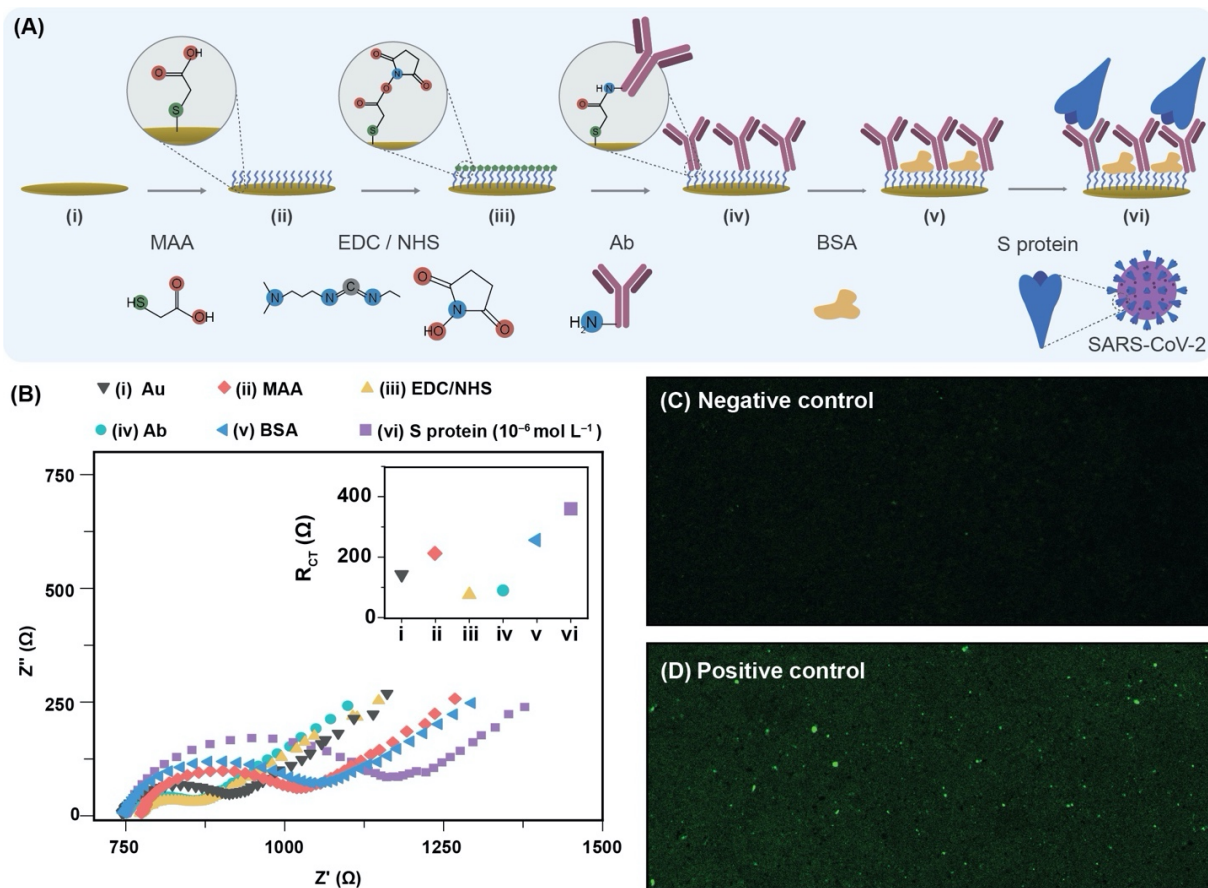
Source: Reproduced from Zakashansky *et al.* *Anal. Methods*, 2021, 13, 874-883. © Royal Society of Chemistry 2022. DOI: 10.1039/D1AY00041A.

V.3.3. Bioreceptor

SARS-CoV-2 virus was recognized by different bioreceptors in the works discussed in this chapter. The SPE/Au electrodes were modified with monoclonal antibodies specific to the S protein of the SARS-CoV. Although they are different viruses, the S protein from the first variant of SARS-CoV-2 (Wuhan-Hu-1 strain) retains 76% of overall protein sequence identity from SARS-CoV and the antibody can recognize the former at some extent.²² The mini cells, on the other hand, were functionalized with aptamers specific for the RBD of the S1 protein. Since the RBD is indispensable for the infection and is responsible for the specificity of the virus, an aptamer produced to recognize this region rather than the entire S protein will likely decrease cross-reactions with other coronaviruses and enhance the specificity of the biosensor.²³ As extensively discussed in *CHAPTER I*, antibodies and aptamers have similar affinity reactions to recognize the antigen and target analyte respectively. However, aptamers are smaller than antibodies which can result in more dense recognition sites in same area. In fact, the aptamer used for the detection of S1 protein consisted of 51 bases with molar weight of 15.8 kDa.²³ IgG antibodies typically present a molar weight of 150 kDa. Moreover, aptamers are cheaper to produce and can be easily modified with functional groups and probes.

The gold in the SPE not only improved the electrode conductivity but also contributed for the immobilization of the antibodies. For the immobilization, mercaptoacetic acid (MAA) was used to form the monolayer on top of the gold structures. Then, the carboxylic groups from the MAA were activated by the pair 1-ethyl-3-(3-dimethylamino-propyl) carbodiimide (EDC) and N-hydroxysuccinimide (NHS) to facilitate the anchoring of the antibodies through imide bond. Finally, the surface was blocked with bovine serum albumin (BSA) to avoid nonspecific interactions (Figure V.6A). The modification of the surface of the electrode was followed by EIS measurements. Overall, the R_{CT} increased with the addition of layers of organic compounds on the electrode (Figure V.6B), except after EDC/NHS activation step, which can be explained by the change in the pH (from 7.4 to 6) during the activation. The R_{CT} also increased after incubating the electrodes in PBS solution with S protein for 30 min. In fact, the presence of the S protein from SARS-CoV was confirmed by confocal fluorescence microscopy. S protein was labelled with fluorescein and incubated in the functionalized electrode. The SPE before incubation has not showed any fluorescence signals (Figure V.6C), meanwhile, after the incubation, fluorescence was observed at the surface (Figure V.6D).

Figure V.6 - Functionalization of the SPE. (A) Steps of the modifications on the SPE: (i) Bare Au; (ii) MAA; (iii) EDC-NHS; (iv) Ab; (v) BSA; (vi) S protein. (B) Nyquist plots of the SPE after each functionalization step. Fluorescence images of the electrode with (C) MAA/EDC-NHS/Ab, and (D) after incubation with fluorescein-labeled protein S from SARS-CoV. Amplification 20 \times .

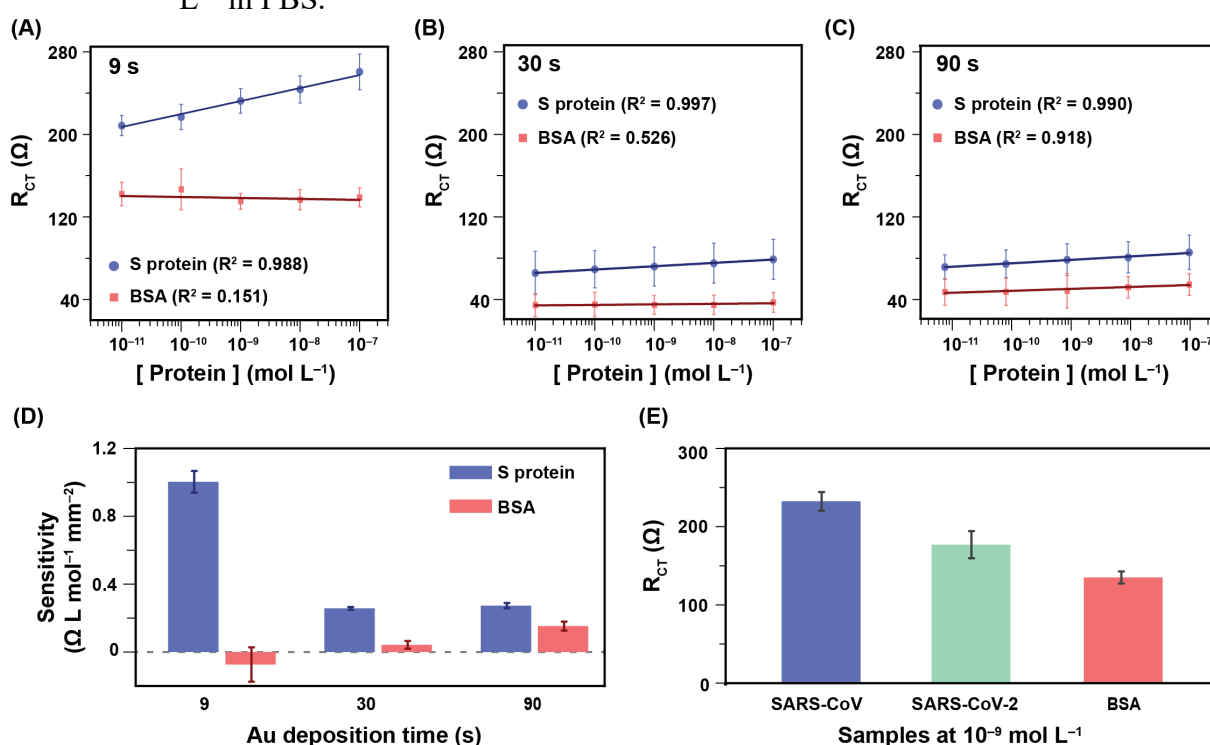


Source: Own authorship.

The analytical signal for the quantification of the SARS-CoV viruses consisted of R_{CT} . The R_{CT} increased with larger concentrations of S protein for SPE with gold deposited for 9, 30, and 90 s (Figure V.7A – C). All electrodeposition conditions differentiated the S protein from the BSA, negative control. However, the Au deposition time affected the sensitivity of the detection of the S protein. Electrodeposition of 9 s showed spherical and homogenous gold deposition, as shown in the MEV from Figure V.3D, which positively influenced the electroanalytical performance of the electrode. Furthermore, the analytical signal is based on an impedance measurement, which is inversely related to conductivity. Although 9 s of deposition time showed minor increase in the faradaic currents (Figure V.4A and C), these electrodes responded better for the detection of S protein since the analytical signal is based on impedance. For same concentrations of S protein from SARS-CoV and SARS-CoV-2, and BSA, the electrodes yielded different values of R_{CT} . The R_{CT} values for the SARS-CoV-2 was lower

than from SARS-CoV since the antibody is specific for the latter. However, it was specific enough to distinguish from the negative control (BSA). To improve the biosensor's selectivity towards COVID-19, the antibody can be switched to one specific for the SARS-CoV-2. The immobilization protocol would remain the same. Furthermore, antibodies specific for other strains of the virus can be applied for the detection of other variants, if necessary.

Figure V.7 - Calibration curves of S protein and BSA for different Au deposition times: 9 (A), 30 (B), and 90 s (C). S protein and BSA were incubated for 30 min prior to EIS measurements. (D) Sensitivities for S protein and BSA for each Au deposition condition. (E) R_{CT} signals from SARS-CoV, SARS-CoV-2, and BSA at 10^{-9} mol L^{-1} in PBS.

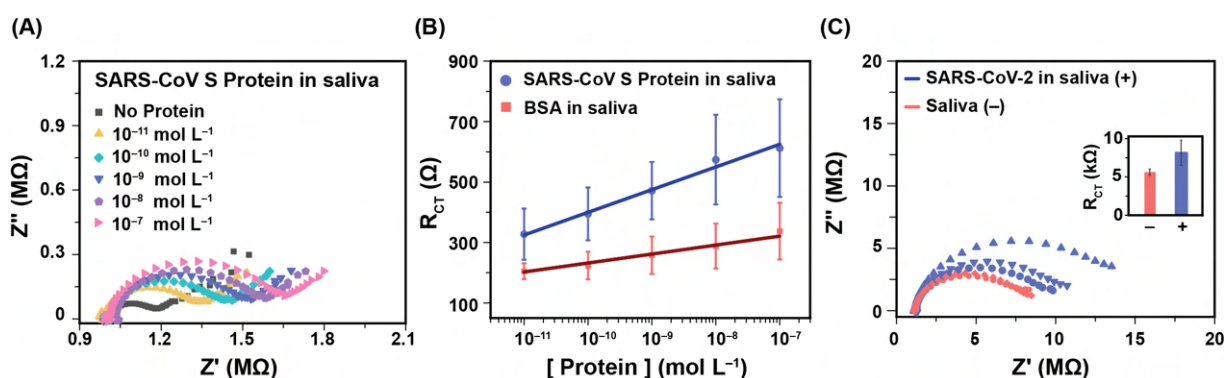


Source: Own authorship.

The SPEs modified for 9s of electrodeposition were also tested for the detection of the S protein in processed saliva, which consisted of the supernatant of the centrifuged saliva samples (Figure V.8A). The R_{CT} increased linearly with increasing concentration of S protein spiked in saliva (Figure V.8B) from 10^{-11} to 10^{-7} mol L^{-1} (equivalent to 0.35 ng mL^{-1} – 3.5 μ g mL^{-1} considering a molar weight of 35.1 kDa for the S protein). As negative control, BSA spiked in saliva was also tested. The increase in R_{CT} for successive incubations of BSA was higher than in PBS, resulting from other components in saliva. It is important to state that in saliva, there are inherent proteins, including human serum albumin. The addition of BSA in saliva was to ensure the higher R_{CT} detected for the S protein. The electrode was also tested for

inactivated SARS-CoV-2 viruses at 10^6 PFU mL^{-1} in saliva (Figure V.8C). The increase in the R_{CT} again was larger for samples with the viruses over just saliva. The typical physiological concentration of the virus in saliva for positive patients ranges from 10^5 to 10^7 PFU mL^{-1} , showing the applicability of diagnosing COVID-19 in saliva.²⁴

Figure V.8 - Application of the proposed immunosensor in biological samples. (A) Nyquist plots after incubation of S protein from SARS-CoV from 10^{-11} to 10^{-7} mol L^{-1} in saliva samples. (B) Calibration curves for S protein from SARS-CoV and BSA in saliva. (C) Nyquist plot for detection of inactivated SARS-CoV-2 viruses in saliva. The inset shows the R_{CT} obtained for negative (in the absence of the virus) and positive (in the presence of 10^6 PFU mL^{-1} of the virus) samples.

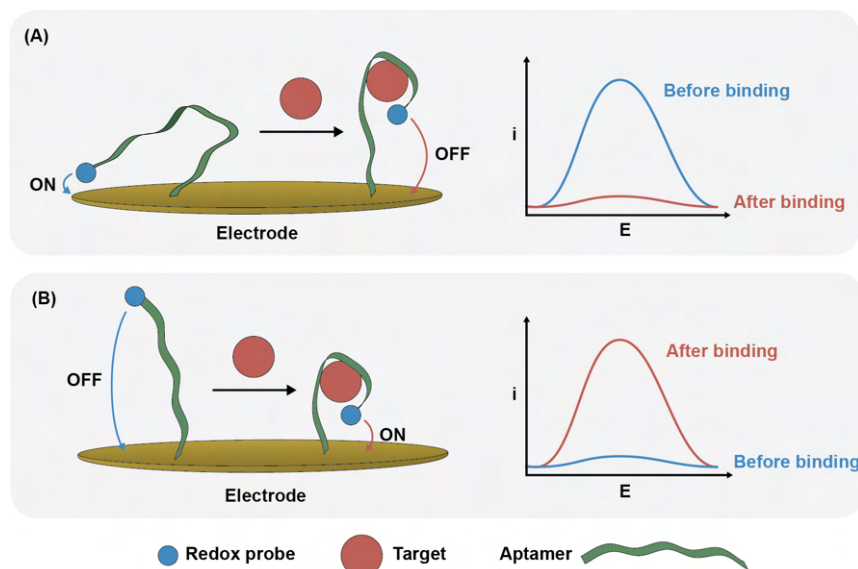


Source: Own authorship.

Aptamer-based biosensor was based on a different detection strategy. The aptamer was labelled with an electrochemical redox probe, methylene blue (MB). The labelling process can be costly, however, it dispenses the use of electrochemical redox pair solutions such as $[\text{Fe}(\text{CN})_6]^{4-/3-}$ and generates the output in common buffer, or even in the sample itself. Moreover, the labelling enables reversible and continuous electrochemical measurements by regenerating the aptamer after every binding event.²³ Electrochemical aptamer-based (EAB) sensors rely on the binding-induced conformational change of the aptamer, which results in the change of the electron transfer rate of the redox probe. The electron transfer rate depends on the distance from the redox probe to the surface of the electrode as well as the presence of any obstructions in the way. The closer the redox probe is at the surface and the less obstructive is the passage, the faster the electron transfer rate will be, which is showed by larger peak current. The conformational change of the aptamer can lead to a decrease (Figure V.9A) or increase (Figure V.9B) in the electron transfer, depending on the oligonucleotide structure and interaction with the target analyte. The electron transfer rate then can be accessed by chronoamperometry, cyclic voltammetry, pulsed voltammetry, and electrochemical impedance spectroscopy. In this work, a type of pulsed voltammetry, square wave voltammetry (SWV),

was chosen because of the minimal charging current (reduced non-Faradaic current) and enhanced detectability.

Figure V.9 - Simple schematic of binding-induced conformational change of an aptamer and the effect on the current. Binding to a target leads to a (A) decrease or (B) increase in electron transfer rate and consequently, on current.



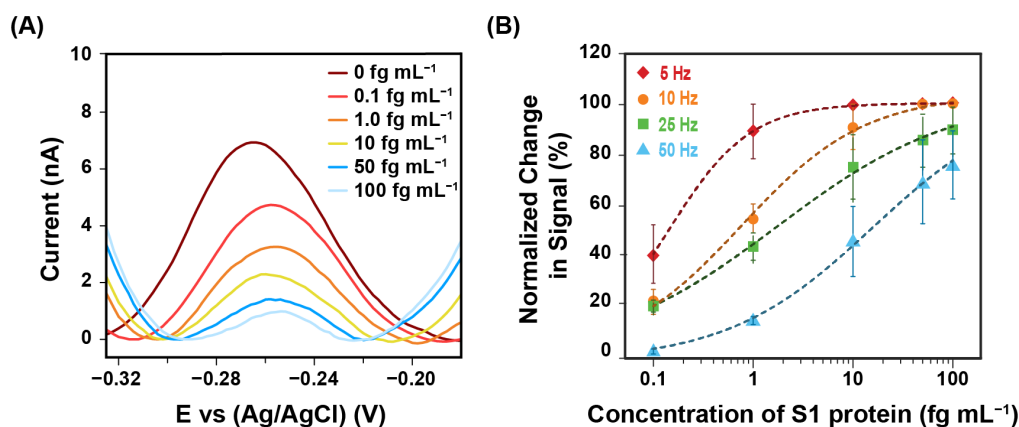
Source: Own authorship.

Firstly, the aptamer response to S1 protein was studied in a conventional electrochemical cell, composed of commercial disk gold electrode as the working electrode, Pt wire as counter electrode, and Ag/AgCl as reference electrode. The working electrode was functionalized with aptamer by forming the sulfide bond between the gold surface and the sulfur from the 3' end. To avoid any nonspecific interactions, the electrode was further incubated in mercaptohexanol (MCH) to form a monolayer. The monolayer also confer biocompatibility to the bioelectronic interface.²⁵ Upon addition of S1 protein, the peak current from the MB decreased in intensity (Figure V.10A). Since the binding-induced conformational change of the aptamer was not confirmed, the change in peak current might be due to the obstruction of the electron transfer in the presence of the S1 protein.

EAB sensors are highly dependent to the frequency. The output of an electrochemical methods is composed of electrokinetic, faradaic, mass, and charge transport phenomena, which are generated by applying a voltage at the bioelectronic interface. Each one of the physicochemical phenomena has a time constant. The phosphate groups of the nucleotides result in a negatively charged backbones that move according to the field caused by the voltage perturbation. Depending on the voltage, the backbone moves toward or away from the electrode surface, disturbing the frequency of electron transfer and, consequently, affecting the current

measured.²⁵ To optimize the analytical parameters of the biosensor, the frequency of the square-wave voltammetry was evaluated (Figure V.10B).

Figure V.10 - Response of commercial disk gold electrodes functionalized with the aptamer upon addition of S1 protein. (A) SWVs upon addition of S1 protein at 10 Hz. (B) Titration curves at different frequencies. Error bars represent the standard error from three electrodes.



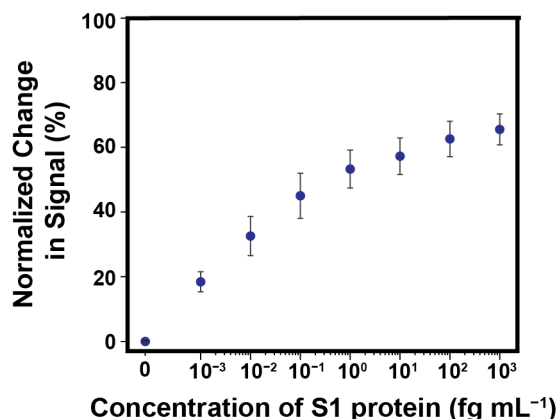
Source: Reproduced from Zakashansky *et al.* Anal. Methods, 2021, 13, 874-883. © Royal Society of Chemistry 2022. DOI: 10.1039/D1AY00041A.

For each frequency, a non-linear fit was applied, known as Hill-Langmuir isotherm:

$$\theta = \frac{[T]^n}{(K_D + [T]^n)} \quad \text{Eq V-1}$$

where θ is the fraction of the receptor bound to the target, $[T]$ is the target concentration, K_D is the dissociation constant of the receptor, and n is the Hill coefficient, which establishes the extent of the interaction between the receptor and the target. For example, at 5 Hz, the n was approximately equivalent to 1, indicating a single binding event per receptor. However, a narrower dynamic range was achieved in this condition. To compromise between the aptamer's affinity and high sensitivity, frequency of 10 Hz was chosen. Once the square wave voltammetry frequency was optimized, the mini cells were functionalized with the aptamers and MCH. The mini cells were then incubated in samples of 10% saliva spiked with increasing concentrations of S1 protein, as shown in Figure V.11. The zero point in the Figure V.11 represents the first incubation of 10% saliva without S1 protein. For the saliva samples containing S1 protein, the signal changes were normalized to the zero point. The EAB mini cell quantified down to 1 ag mL⁻¹ of S1 protein, the lowest concentration reported for an antigen-based detection for SARS-CoV-2 (Table V.1).

Figure V.11 - Titration curve of S1 protein performed at 10 Hz in 10% saliva. Error bars represent standard error of the mean among five SD wrinkled mini cells.



Source: Reproduced from Zakashansky *et al.* *Anal. Methods*, 2021, 13, 874-883. © Royal Society of Chemistry 2022. DOI: 10.1039/D1AY00041A.

V.4. CONCLUSION

Two electrochemical biosensors for diagnosing SARS-CoV-2 were described in this chapter. The main differences of the biosensors are in the fabrication and electrochemical modification of the electrodes, and in the bioreceptor chosen to detect the virus. One of the approaches based on the SPE modified with electrodeposited gold nanostructures to enhance the electrochemical output and promote the immobilization of antibodies as bioreceptor. The fabrication of SPE is simple, requiring equipment that are commonly available in a low-resource lab. The biosensor distinguished the SARS-CoV from the negative control (BSA), both spiked in saliva. Even though the SPE/Au applied antibodies specific for the S protein of SARS-CoV, it detected the inactivated SARS-CoV-2 virus in processed saliva down to 10^6 PFU mL⁻¹.

The second biosensor consisted of the Shrinky-Dink wrinkled electrodes, which present larger EASA due to the shrinking process of metal films in the fabrication process. The larger EASA actuated to enhance the electrochemical signal and to accommodate larger number of bioreceptors, creating a surface with denser recognition sites. For the fabrication of these electrodes, a sputtering chamber is required, and the production outcome is limited by the size of the chamber. Moreover, the peeling of the adhesive during the fabrication can be an intricate process. Although the fabrication of the Shrinky-Dink wrinkled electrodes can be cumbersome, the signal amplification for more sensitive electrochemical detection is inherent to the process, not requiring further modification. For recognition of the SARS-CoV-2, an aptamer specific for the RBD region of the S1 protein was used. The analytical signal for the mini cells consisted of

redox probe MB attached to one of the ends of the aptamer. The functionalized mini cells quantified S1 protein down to 1 ag mL^{-1} in 10% saliva samples, in contrast to the Au-modified SPE that quantified down to 0.35 ng mL^{-1} in processed saliva. The higher detectability of the mini cells is attributed to the higher surface area of the electrodes, enhancing the faradaic current from the MB and the bioreceptor density at the surface. Unfortunately, it was not possible to evaluate the mini cells for detecting the whole virus, as was performed for the SPE.

The aptamer has shown great advantages over the antibodies. Firstly, the aptamers used in the mini cells were specific for the RBD region, which ensures higher specificity to the SARS-CoV-2 rather than to other coronaviruses. However, the binding mechanism of this aptamer has not been fully understood since it consists of new oligonucleotide sequence. The binding mechanism of an aptamer is crucial to many EAB sensors that rely on the conformational change upon binding to the target to produce the analytical signals. Nonetheless, the aptamer for RBD provided monotonical changes in signal for the mini cells, capable of correlating with S protein concentrations. Other advantage of the aptamers is the synthetic production, resulting in lower batch-to-batch variation, and enabling precise modifications, such as addition of tailing groups to immobilize at different surfaces and probes for several transduction techniques, colorimetric, electrochemical, fluorescence, and others. The addition of the redox probe MB to the aptamer provided an inherent source of the analytical signal without the need of electrochemical redox pair, such as the $[\text{Fe}(\text{CN})_6]^{4-/3-}$, which are light and time sensitives.

Although the two biosensors differed in many aspects, both analyzed small volume of samples, at microliter range. Their small feature and the availability of portable potentiostat enable the diagnosing of COVID-19 in the POC. These biosensors are cheaper and do not require further chemical supplies, unlike the PCR technology. The use of saliva instead of the NSS as sample also illustrates the possibility of applying them with minor risk for the health care works or even applying outside clinical setups. Finally, this chapter demonstrated the diversity of the electrochemical detection as a transduction method for POC sensors and how the biorecognition element plays an important role in the performance of a biosensor.

V.5. REFERENCES

1. LEE, J.-H.; CHOI, M.; JUNG, Y.; LEE, S. K.; LEE, C.-S.; KIM, J.; KIM, J.; KIM, N. H.; KIM, B.-T.; KIM, H. G. A novel rapid detection for SARS-CoV-2 spike 1 antigens using human angiotensin converting enzyme 2 (ACE2). **Biosensors & Bioelectronics**, Oxford, v. 171, p. 112715, 2021. DOI: 10.1016/j.bios.2020.112715.
2. PINALS, R. L.; LEDESMA, F.; YANG, D.; NAVARRO, N.; JEONG, S.; PAK, J. E.; KUO, L.; CHUANG, Y. C.; CHENG, Y.-W.; SUN, H.-Y.; LANDRY, M. P. Rapid SARS-CoV-2 spike protein detection by carbon nanotube-based near-infrared nanosensors. **Nano Letters**, Washington, v. 21, p. 2272–2280, 2021. DOI: 10.1021/acs.nanolett.1c00118.
3. AHMADIVAND, A.; GERISLIOGLU, B.; RAMEZANO, Z.; KAUSHIK, A.; MANICKAM, P.; GHOREISHI, S. A. Functionalized terahertz plasmonic metasensors: femtomolar-level detection of SARS-CoV-2 spike proteins. **Biosensors & Bioelectronics**, Oxford, v. 177, p. 112971, 2021. DOI: 10.1016/j.bios.2021.112971.
4. MAVRIKOU, S.; MOSCHOPOULOU, G.; TSEKOURAS, V.; KINTZIOS, S. Development of a portable, ultra-rapid and ultra-sensitive cell-based biosensor for the direct detection of the SARS-CoV-2 S1 spike protein antigen. **Sensors**, Basel, v. 20, p. 3121, 2020. DOI: 10.3390/s20113121.
5. SEO, G.; LEE, G.; KIM, M. J.; BAEK, S.-H.; CHOI, M.; KU, K. B.; LEE, C.-S.; JUN, S.; PARK, D.; KIM, H. G.; KIM, S.-J.; LEE, J.-O.; KIM, B. T.; PARK, E. C.; KIM, S. I. Rapid detection of COVID-19 causative virus (SARS-CoV-2) in human nasopharyngeal swab specimens using field-effect transistor-based biosensor. **ACS Nano**, Washington, v. 14, p. 5135–5142, 2020. DOI: 10.1021/acsnano.0c02823.
6. SHAO, W.; SHURIN, M. R.; WHEELER, S. E.; HE, X.; STAR, A. Rapid detection of SARS-CoV-2 antigens using high-purity semiconducting single-walled carbon nanotube-based field-effect transistors. **ACS Applied Materials & Interfaces**, Washington, v. 13, p. 10321–10327, 2021. DOI: 10.1021/acsnano.0c22589.
7. ZAMZAMI, M. A.; RABBANI, G.; AHMAD, A.; BASALAH, A. A.; AL-SABBAN, W. H.; AHN, S. N.; CHOUDHR, H. Carbon nanotube field-effect transistor (CNT-FET)-based biosensor for rapid detection of SARS-CoV-2 (COVID-19) surface spike protein S1. **Bioelectrochemistry**, Lausanne, p. 107982, 2021. DOI: 10.1016/j.bioelechem.2021.107982
8. FATHI-HAFSHEJANI, P.; AZAM, N.; WANG, L.; KURODA, M. A.; HAMILTON, M. C.; HASIM, S.; MAHJOURI-SAMANI, M. Two-dimensional-material-based field-effect transistor biosensor for detecting COVID-19 virus (SARS-CoV-2). **ACS Nano**, Washington, v. 15, p. 11461–11469, 2021. DOI: 10.1021/acsnano.1c01188.
9. FABIANI, L.; SAROGLIA, M.; GALATÀ, G.; DE SANTIS, R.; FILLO, S.; LUCA, V.; FAGGIONI, G.; D'AMORE, N.; REGALBUTO, E.; SALVATORI, P.; TEROVA, G.; MOSCONE, D.; LISTA, F.; ARDUINI, F. Magnetic beads combined with carbon black-based screen-printed electrodes for COVID-19: a reliable and miniaturized electrochemical immunosensor for SARS-CoV-2 detection in saliva. **Biosensors & Bioelectronics**, Oxford, v. 171, p. 112686, 2021. DOI: 10.1016/j.bios.2020.112686.

10. LIMA, L. F. DE; FERREIRA, A. L.; TORRES, M. D. T.; ARAUJO, W. R. DE; FUENTE-NUNEZ, C. DE LA. Minute-scale detection of SARS-CoV-2 using a low-cost biosensor composed of pencil graphite electrodes. **Proceedings of the National Academy of Sciences**, Washington, v. 118, 2021. DOI: 10.1073/pnas.2106724118.
11. YAKOH, A.; PIMPITAK, U.; RENGPIPAT, S.; JIRANKARN, N.; CHAILAPAKUL, O.; CHAIYO, S. Paper-based electrochemical biosensor for diagnosing COVID-19: detection of SARS-CoV-2 antibodies and antigen. **Biosensors & Bioelectronics**, Oxford, p. 112912, 2020. DOI: 10.1016/j.bios.2020.112912.
12. MOJSOSKA, B.; LARSEN, S.; OLSEN, D. A.; MADSEN, J. S.; BRANDSLUND, I.; ALATRAKTCHI, F. A. Rapid SARS-CoV-2 detection using electrochemical immunosensor. **Sensors**, Basel, v. 21, p. 390, 2021. DOI: 10.3390/s21020390.
13. KIM, S.; YEE, E.; MILLER, E. A.; HAO, Y.; TAY, D. M. Y.; SUNG, K. J.; JIA, H.; JOHNSON, J. M.; SAEED, M.; MACE, C. R.; YURT, D. Y.; SIKES, H. D. Developing a SARS-CoV-2 antigen test using engineered affinity proteins. **ACS Applied Materials & Interfaces**, Washington, v. 13, p. 38990-39002, 2021. DOI: 10.1021/acsami.1c08174.
14. BASSO, D.; AITA, A.; PADOAN, A.; COSMA, C.; NAVAGLIA, F.; MOZ, S.; CONTRAN, N.; ZAMBON, C.-F.; CATTELAN, A. M.; PLEBANI, M. Salivary SARS-CoV-2 antigen rapid detection: a prospective cohort study. **Clinica Chimica Acta**, Amsterdam, v. 517, p. 54–59, 2021. DOI: 10.1016/j.cca.2021.02.014.
15. TEO, A. K. J.; CHOUDHURY, Y.; TAN, I. B.; CHER, C. Y.; CHEW, S. H.; WAN, Z. Y.; CHENG, L. T. E.; OON, L. L. E.; TAN, M. H.; CHAN, K. S.; HSU, L. Y. Saliva is more sensitive than nasopharyngeal or nasal swabs for diagnosis of asymptomatic and mild COVID-19 infection. **Scientific Reports**, Berlin, v. 11, p. 3134, 2021. DOI: 10.1038/s41598-021-82787-z.
16. HUANG, Y.; YANG, C.; XU, X.; XU, W.; LIU, S. Structural and functional properties of SARS-CoV-2 spike protein: potential antiviral drug development for COVID-19. **Acta Pharmacologica Sinica**, London, v. 41, p. 1141–1149, 2020. DOI: 10.1038/s41401-020-0485-4.
17. FEHR, A. R.; PERLMAN, S. Coronaviruses: an overview of their replication and pathogenesis. *In: Coronaviruses: methods and protocols*. New York: Springer, 2015. p. 1–23. DOI: 10.1007/978-1-4939-2438-7_1
18. DI, B.; HAO, W.; GAO, Y.; WANG, M.; WANG, Y.; QIU, L.; WEN, K.; ZHOU, D.; WU, X.; LU, E.; LIAO, Z.; MEI, Y.; ZHENG, B.; CHE, X. Monoclonal antibody-based antigen capture enzyme-linked immunosorbent assay reveals high sensitivity of the nucleocapsid protein in acute-phase sera of severe acute respiratory syndrome patients. **Clinical and Vaccine Immunology**, Washington, v. 12, p. 135–140, 2005. DOI: 10.1128/CDLI.12.1.135-140.2005.
19. DIAO, B.; WEN, K.; ZHANG, J.; CHEN, J.; HAN, C.; CHEN, Y.; WANG, S.; DENG, G.; ZHOU, H.; WU, Y. Accuracy of a nucleocapsid protein antigen rapid test in the diagnosis of SARS-CoV-2 infection. **Clinical Microbiology and Infection**, Oxford, v. 27, p. 289.e1-289.e4, 2021. DOI: 10.1016/j.cmi.2020.09.057.

20. SENGUPTA, J.; HUSSAIN, C. M. Graphene-based field-effect transistor biosensors for the rapid detection and analysis of viruses: a perspective in view of COVID-19. **Carbon Trends**, Amsterdam, v. 2, p. 100011, 2021. DOI: 10.1016/j.cartre.2020.100011.
21. JUNG, Y.; PARK, G.S.; MOON, J. H.; KU, K.; BEAK, S.-H.; LEE, C.-S.; KIM, S.; PARK, E. C.; PARK, D.; LEE, J.-H.; BYEON, C. W.; LEE, J. J.; MAENG, J.-S.; KIM, S.-S.; KIM, S. I.; KIM, B.-T.; LEE, M. J.; KIM, H. G. Comparative analysis of primer–probe sets for RT-qPCR of COVID-19 causative virus (SARS-CoV-2). **ACS Infectious Diseases**, Washington, v. 6, p. 2513–2523, 2020. DOI: 10.1021/acsinfecdis.0c00464.
22. JAIMES, J. A.; ANDRÉ, N. M.; CHAPPIE, J. S.; MILLET, J. K.; WHITTAKER, G. R. Phylogenetic analysis and structural modeling of SARS-CoV-2 spike protein reveals an evolutionary distinct and proteolytically sensitive activation loop. **Journal of Molecular Biology**, London, v. 432, p. 3309–3325, 2020. DOI: 10.1016/j.jmb.2020.04.009.
23. SONG, Y.; SONG, J.; WEI, X.; HUANG, M.; SUN, M.; ZHU, L.; LIN, B.; SHEN, H.; ZHU, Z.; YANG, C. Discovery of aptamers targeting the receptor-binding domain of the SARS-CoV-2 spike glycoprotein. **Analytical Chemistry**, Washington, v. 92, p. 9895-9900, 2020. DOI: 10.1021/acs.analchem.0c01394.
24. LESCURE, F. X.; BOUADMA, L.; NGUYEN, D.; PARISEY, M.; WICKY, P. H.; BEHILLIL, S.; GAYMARD, A.; BOUSCAMBERT-DUCHAMP, M.; DONATI, F.; HINGRAT, Q. L.; ENOUF, V.; HOUHOU-FIDOUH, N.; VALETTE, M.; MAILLES, A.; LUCET, J. C.; MENTRE, F.; DUVAL, X.; DESCAMPS, D.; MALVY, D.; TIMSIT, J. F.; LINA, B.; VAN-DER-WERF, S.; YAZDANPANA, Y. Clinical and virological data of the first cases of COVID-19 in Europe: a case series. **Lancet Infectious Disease**, Oxford, v. 20, p. 697-706, 2020. DOI: 10.1016/S1473-3099(20)30200-0.
24. PELLITERO, M. A.; SHAVER, A.; ARROYO-CURRÁS, N. Critical review: approaches for the electrochemical interrogation of DNA-based sensors: a critical review. **Journal of the Electrochemical Society**, Pennington, v. 167, p. 037529, 2020. DOI: 10.1149/2.0292003JE.

FINAL REMARKS AND PERSPECTIVES

In this dissertation, the challenges on miniaturization of biosensors were discussed in Chapter I and pointily addressed under the chemical aspect. Chapter II optimized the immobilization of biomolecules on paper by oxidating the cellulose with NaIO_4 . The oxidation was extensively characterized since it affected the physicochemical properties of the paper. Changes in size, cellulose structure, mechanical properties, capillarity, and chemical groups density were observed. Moreover, the oxidized paper quantified the protein amount in urine, detecting early cases of microalbuminuria. The oxidation promoted covalent bonding of biomolecules to the paper, a commonly used substrate as platforms for analytical devices to detect important biomarkers in many biological fluids. The stronger attachment of biological components on paper ensures the development of more robust and reproducible μPADs .

Chapter III described an alternative fabrication method for wearable microfluidic devices using the toy Shrinky-Dinks (SD), which consists of a thermoplastic sheet that shrinks by heating above the glass transition temperature, decreasing the drawn or printed features on the surface. The SD wearable devices dispense photolithography, an expensive method that requires a cleanroom. As a proof-of-concept, a wearable colorimetric device for glucose and lactate was demonstrated. Although the assays lacked detectability and sensitivity to detect glucose and lactate in sweat, the SD-based microfluidic channels demonstrated the capability of continuously collecting sweat without disturbing the user. The SD-based molds enable easy fabrication of wearable devices, which lead the health care for personalized medicine.

For more sensitive detection of biomarkers in sweat, the SD wearable device can be coupled with wrinkled electrodes, described in Chapter IV. The wrinkled electrodes were fabricated by the same premise of SD wearable devices. By heating a thin layer of metal on a thermoplastic sheet, the metal crumpled to follow the shrinking of the plastic. Consequently, the final electrode has a smaller geometric area with a high surface area due to the wrinkles. Since the electrochemical current is proportional to the surface area of the electrode, the wrinkled electrodes demonstrated higher current density compared to electrodes with the same geometric area. The wrinkled metal was further transferred to an elastomer, resulting in flexible and stretchable electrodes, ideal for wearable applications. The stretchable wrinkled electrodes quantified glucose at broader concentration range from $0.1 \mu\text{mol L}^{-1}$ to 0.1mmol L^{-1} in physiological pH. A fully integrated device for continuous sensing of glucose in sweat can be achieved by coupling the SD wearable microfluidic channels with the stretchable electrodes. The improved sensitivity of these electrodes allows the detection of biomarkers at low

concentration in small volume of biological fluids, which is one of the concerns on miniaturization of clinical analysis.

With the COVID-19 outbreak, the scientific community urged to develop new technologies to counter the spread of the disease. Chapter V described two studies co-developed by the author during the pandemic aiming for faster and more accessible diagnosis tools for widespread testing for COVID-19. Both were based on electrochemical transduction methods, but they differed in fabrication, electrochemical modifications, and the bioreceptors. Although differently approached, both biosensors detected the S protein in a small sample volume, (microliter range), without requiring chemical supplies, unlike the gold standard PCR. Furthermore, their small features and the availability of portable potentiostat enable the diagnosing of COVID-19 at the POC.

The diversity of the studies described in this dissertation enlightens the many opportunities in the field of biosensors. Although none of the biosensors described in this dissertation have reached the market, hopefully, the improvements obtained on immobilization, microfabrication process, and sensitivity will contribute to further works on the development of biosensors to finally reach commercial ends and wide spread the diagnostic tools to broaden the access to health care.

CURRICULUM VITAE

Amanda Hikari Imamura | amandahimamura@gmail.com

EDUCATION

São Carlos Institute of Chemistry, University of São Paulo, São Carlos/SP, Brazil

Ph.D. in Chemistry, March 2022.

Advisor: Dr. Emanuel Carrilho

Henry Samueli School of Engineering, University of California, Irvine/CA, United States

Visiting Ph.D. Candidate in Chemistry, 2019.

Advisor: Dr. Michelle Khine

São Carlos Institute of Chemistry, University of São Paulo, São Carlos/SP, Brazil

B.S. in Chemistry, December 2015.

RESEARCH EXPERIENCE

2016 – 2022: BioMicS / USP

Ph.D. Candidate | Advisor: Dr. Emanuel Carrilho

Fabrication of paper-based microfluidics with wax printing and laser cutting. Surface modification of paper, gold, and carbon-based materials for biomolecules immobilization. Detection of common biomarkers by colorimetric reactions and electrochemical techniques (cyclic voltammetry, pulse voltammetry, chronoamperometry, electrochemical impedance spectroscopy, and contactless conductivity). Soft lithography by printer-based techniques. Automatization of data analysis in MATLAB.

2019 – 2020: Khine Lab / UCI

Visiting Ph.D. Candidate | Advisor: Dr. Michelle Khine

Microfabrication of highly stretchable wrinkled electrodes for wearable application. Electrochemical characterization of wrinkled electrodes under strain. Electrochemical detection of biomarkers, specifically glucose.

2012 – 2014: CROMA (Chromatography Lab) / USP

Undergraduate Research Fellow | Advisor: Dr. Álvaro José dos Santos Neto

Oxidative degradation of pharmaceutical components (*e.g.*, antibiotics) in water and synthetic wastewater. Optimization of sample treatment by solid phase extraction and analysis of the degradation compounds by high performance liquid chromatography coupled with mass spectrometry (HPLC-MS).

HONORS AND AWARDS

- Awarded Honorable Mention at 2nd Postgraduate Video Award promoted by USP *Pró-Reitoria de Pós-Graduação* and Father Anchieta Foundation – TV *Cultura* in **2020**.
- Awarded Best Poster award in Electrochemistry and Electroanalysis at 19th ENQA (*Encontro Nacional de Química Analítica*) and 7th CIAQA (*Congresso Iberoamericano de Química Analítica*) in **2018**.

PUBLICATIONS

- IMAMURA, A.; ZAKASHANSKY, J.; CHO, K.; LIN, L.; CARRILHO, E.; KHINE, M. Stretchable Sensors for Nanomolar Glucose Detection. **Advanced Materials Technology**, v. 5, 1900843, 2020. DOI: [10.1002/admt.201900843](https://doi.org/10.1002/admt.201900843)
- IMAMURA, A. H.; SEGATO, T. S.; DE OLIVEIRA, L. J. M.; HASSAN, A.; CRESPILO, F. N.; CARRILHO, E. Monitoring cellulose oxidation for protein immobilization in paper-based low-cost biosensors. **Microchimica Acta**, v. 187, 272, 2020. DOI: [10.1007/s00604-020-04250-6](https://doi.org/10.1007/s00604-020-04250-6)
- ZAKASHANSKY, J. A.; IMAMURA, A. H.; SALGADO, D. F.; ROMERO MERCECA, H. C.; AGUAS, R. F. L.; LAO, A. M.; PARISER, J.; ARROYO-CURRÁS, N.; M. KHINE. Detection of the SARS-CoV-2 spike protein in saliva with Shrinky-Dink© electrodes. **Analytical Methods**, v. 13, 874-883, 2021. DOI: [10.1039/D1AY00041A](https://doi.org/10.1039/D1AY00041A)
- BRAZACA, C. L.; IMAMURA, A. H.; GOMES, N. O.; ALMEIDA, M. B.; SCHEIDT, D. T.; RAYMUNDO-PEREIRA, P. A.; OLIVEIRA JR, O. N.; JANEGITZ, B. C.; MACHADO, S. A. S.; CARRILHO, E. Electrochemical immunosensors using electrodeposited gold nanostructures for detecting the S proteins from SARS-CoV and SARS-CoV-2. **Analytical and Bioanalytical Chemistry**. DOI: [10.1007/s00216-022-03956-1](https://doi.org/10.1007/s00216-022-03956-1)

- BRAZACA, C. L.; **IMAMURA, A. H.**; BLASQUES, R. V.; CAMARGO, J. R.; JANEGITZ, B. C.; WHITESIDES, G.; CARRILHO, E. Low-cost paper-based platforms for the diagnosis of important diseases: a critical review. *In preparation.*
- BRAZACA, C. L.; **IMAMURA, A. H.**; ALMEIDA, M. B.; CARRILHO, E. Application of smart materials in biosensors for cancer diagnosis. In: *New Trends in Smart Nanostructures Biomaterials in Health Sciences. In preparation.*

ANNEX 1

Monitoring cellulose oxidation for protein immobilization in paper-based low-cost biosensors



Monitoring cellulose oxidation for protein immobilization in paper-based low-cost biosensors

Amanda Hikari Imamura^{1,2} · Thiago Pinotti Segato^{1,2} · Leticia Jordão Marques de Oliveira^{1,2} · Ayaz Hassan¹ · Frank Nelson Crespillo¹ · Emanuel Carrilho^{1,2}

Received: 4 September 2019 / Accepted: 30 March 2020 / Published online: 15 April 2020
© Springer-Verlag GmbH Austria, part of Springer Nature 2020

Abstract

The oxidation of paper by periodate was investigated and systematically characterized by Fourier-transform infrared (FTIR) spectroscopy, scanning electron microscopy, X-ray diffraction, goniometry, and dynamic mechanical analysis. For the first time, in situ FTIR microscopy analysis was performed, yielding chemical images of carbonyl groups on the cellulose fibers. The enhancement of protein immobilization on oxidized paper was quantified by a colorimetric assay with Ponceau dye, demonstrating that 0.5-h oxidation suffices to functionalize the paper-based devices. The oxidized paper was applied as a sensor for protein quantification in urine, a test able to detect levels of proteinuria and even microalbuminuria. The quantification was based on the capture of proteins through covalent bonds formed with the carbonyl groups on the oxidized paper followed by the staining of the region with Ponceau dye. There is a linear dependency between human serum albumin (HSA) concentration and the length of the stained blot from 0.1 to 3 mg mL⁻¹. This method correlated linearly with a reference method showing a higher sensitivity (0.866 cm mL mg⁻¹) than the latter. The limit of quantification was 0.1 mg mL⁻¹, three times lower than that of the commercial strip.

Keywords Paper-based analytical devices · Periodate · Protein immobilization · Proteinuria · Microalbuminuria · Colorimetric assay

Introduction

The use of paper as a substrate for analytical purposes has been reported since the 1850s with the creation of urine test strips [1]. In the early 1900s, paper began to be widely used for chromatography and electrophoresis [2], and a few years later, the pH paper test was introduced and commercialized [3]. However, 10 years ago, Whitesides and co-workers reintroduced paper as a low-cost substrate for inexpensive, low-volume, portable, and multiple assay microfluidic devices

[4]. Since then, several studies centered on the use of paper as a substrate for point-of-care (POC) testing have been published, and the field of paper microfluidics has emerged.

The popularity of the microfluidic paper-based analytical devices (μ PADs) is mainly due to its capacity of explore the capillarity of the paper to transport fluid, besides other natural properties as lightness, flexibility, and possibility of physical and chemical modifications [5, 6]. During the fabrication process of μ PADs, several instruments and materials can be explored to pattern paper into channels and adequate the sample zone for assays [5, 7, 8]. Thus far, a large number of works have employed colorimetric assays, which produce a response easily visualized by eye or digital images [9]. For biorecognition of the analyte, biomolecules such as enzymes, antibodies, and aptamers have been immobilized on the surface as a bioreceptor to provide specificity [5, 10, 11]. The bioreceptor plays a significant role, since it recognizes a specific target molecule, and its concentration is of interest. Furthermore, to prevent nonspecific bonding, generic proteins can be added to block the cellulose surface [12, 13].

The immobilization of the bioreceptor is a crucial step to guarantee the reproducibility and robustness of the device.

Electronic supplementary material The online version of this article (<https://doi.org/10.1007/s00604-020-04250-6>) contains supplementary material, which is available to authorized users.

✉ Emanuel Carrilho
emanuel@iqsc.usp.br

¹ Instituto de Química de São Carlos, Universidade de São Paulo, Av. Trabalhador São-Carlense, 400, São Carlos, SP 13566-590, Brazil

² Instituto Nacional de Ciência e Tecnologia em Bioanalítica – INCTBio, Campinas, SP 13083-970, Brazil

The main immobilization techniques on cellulose surface are adsorption, bioaffinity interaction, covalent immobilization, or a combination of the three [10]. The performance of the immobilization is evaluated by the final biomolecule stability, conformation, activity, and orientation on the surface. Based on these criteria, the covalent immobilization can be pointed out as the most stable approach, because it provides a uniform adhesion of the biomolecules [10]. However, such approach firstly requires a chemical activation to yield functional groups on the paper surface, through which the covalent bonding will be established [10, 14]. Since paper is a substrate typically composed by compressed fibers of cellulose, a treatment with periodate (IO_4^-) promotes oxidation of hydroxyl groups of the glucose monomers to aldehyde groups, which are more reactive. The resulting oxidized species react with amine groups of the proteins in a given assay preparation [10, 15].

Although the oxidative treatment has been frequently claimed as a promising one [15–17], the literature lacks an in-depth characterization and standardization of this process. Because of this, the origin and the progress of the oxidation process and its impact on the protein immobilization remain unanswered. Here, we widely characterize physical characteristics of Whatman chromatography paper (CHR #1) after the oxidation with sodium periodate (NaIO_4), including a new approach based on microspectroscopic chemical images (microscopy – Fourier-transform infrared/FTIR spectroscopy) introduced for the first time. We evaluated the immobilization of bovine serum albumin (BSA) as a model protein on the oxidized substrate for development of paper-based sensing devices. The oxidized paper was applied for a protein quantification strategy as an alternative assay for proteinuria, a condition defined by the excess of protein in the urine that can be diagnostic for diseases [18].

Materials and methods

Chemicals and solutions

Sodium meta-periodate (NaIO_4), bovine albumin serum (BSA), and human albumin serum (HSA) were purchased from Sigma-Aldrich (<https://www.sigmaaldrich.com>). Sodium phosphate dibasic and monobasic were purchased from J. T. Baker (<https://us.vwr.com>). Supersaturated NaIO_4 solutions at 0.5 M were prepared in ultrapure water before the oxidation. Whereas higher concentrations were not possible, lower concentrations of NaIO_4 were not evaluated since longer oxidation time would be required to achieve the same oxidation efficiency. The phosphate buffer 10 mM was prepared in ultrapure water at pH 3.8, 4.8, and 5.8. The BSA solutions were prepared in ultrapure water before the immobilization protocol. The distaining solution was 10%

(v/v) of acetic acid in distilled water. The Ponceau 0.1% (w/v) solution was prepared in the same distaining solution.

Paper oxidation with NaIO_4 and characterization

The chromatography paper was oxidized in NaIO_4 solution for predetermined time: 0.5, 1.0, 2.0, 4.0, 8.0, 12, and 24 h. The paper was totally immersed in 25 mL of NaIO_4 0.5 M solution and then kept away from the light. After the established time, the paper was washed abundantly with distilled water and then left to dry in the desiccator. After the oxidation, the paper dimensions were measured with a digital caliper Mitutoyo, ABSOLUTE Super Caliper SERIES 500 (<https://www.mitutoyo.com>).

The functional groups of the native and oxidized paper were evaluated by infrared spectroscopy PerkinElmer Spectrum Frontier (www.perkinelmer.com) with universal attenuated total reflection (ATR) accessory (diamond/ZnSe crystal). Spectra were recorded between 4000 and 600 cm^{-1} by accumulation of 32 scans with a resolution of 4 cm^{-1} . We also evaluated the distribution of functional groups along the cellulose fibers by micro-FTIR spectroscopy using an FTIR spectrometer (Vertex 70v) coupled with an FTIR microscope Hyperion 3000, Bruker (<https://www.bruker.com>). The measurements with this equipment were performed in the transmittance mode using a spectral resolution of 4 cm^{-1} and 256 scans in the mid infrared (4000–600 cm^{-1}) spectral range. The FTIR microscope was equipped with liquid N_2 cooled, a 64 × 64 elements focal plane array (FPA) detector. Each element of the FPA worked as an individual detector, making possible the measurement of 4096 spectra from the probed sample area in a single detection with a spatial resolution of approximately 2.5 μm . The 2D and 3D chemical images were obtained by integrating the area under the peak corresponding to a specific vibrational mode in the FTIR spectrum. A piece of the sample was cut and placed directly on the IR transparent CaF₂ window for the measurements. All the FTIR spectra shown are the difference spectra, in which the absorption signals corresponding to the background were subtracted from those of the samples.

The native and oxidized papers were evaluated by X-ray diffraction Bruker, Model D8 Advance (<https://www.bruker.com>). The diffractograms were acquired in interval from 5 to 60 degrees with step of 0.02 degree and irradiation time of 0.5 s. The contact angle of the paper with water was measured for the native and oxidized paper for 12 h in a goniometer (KSV CAM 200) equipped with CAM 2008 software. The surfaces of the native chromatography paper and oxidized for 24 h were visualized by scanning electron microscopy (SEM; Zeiss LEO-440). The samples were sputter coated with gold before the SEM analysis. Dynamic mechanical analysis (DMA, TA Instruments Q800 <https://www.tainstruments.com>) using the tension film clamps

characterized the native and oxidized (for 24 h) papers. For this analysis, the native paper was cut in the dimensions of 30×3 mm and 54.5×1.76 mm. The larger specimen was oxidized for 24 h, as described in the protocol above. After the oxidation, the specimen shrunk to the same dimensions of the smaller native paper.

BSA immobilization assay

The performance of the oxidative treatment on paper was evaluated by the capacity of the paper as a platform to immobilize bovine serum albumin (BSA). The BSA was chosen as a proof of concept for immobilization since it is a well-studied and widely used protein in the bioanalytical field. Due to the shrinkage of the paper, only the paper samples oxidized up to 4 h were evaluated for protein immobilization. BSA concentrations of 1 to 8 mg mL⁻¹ were tested on all the samples of paper. The pH of the phosphate buffer used on the percolation step was BSA pI ± 1 (3.8, 4.8, and 5.8). Each combination of oxidation time and BSA concentration was made in triplicate.

For the protein immobilization assay, 0.5 μ L of the protein solution was dropped 0.5 cm above the first circle ($d = 0.8$ mm). Then, the paper chip was stood up with the first circle immersed in a phosphate buffer until almost all the waste circle ($d = 15$ mm) was wet. The device was immersed quickly in a Ponceau solution and then washed 3 times with 10 mL of the destaining solution. The paper was dried in an oven at 80 °C with an absorbent paper on it. The dried paper was scanned by a digital scanner HP® Scanjet 200 Flatbed (<https://www.hp.com>) and then analyzed on ImageJ® software, by which the lengths of the blot and the color intensity on the protein application spot were measured.

Quantification of HSA in human urine

For this experiment, chromatography paper chips with narrower channel (2 mm) were oxidized for 4 h. The members of our research group donated the urine samples for the assay. All the 7 samples were mixed together to create a urine pool which was used for the analysis. The urine pool was spiked with HSA to result a final concentration of 10 mg mL⁻¹ from which concentrations of 0.1, 0.5, 1.0, 1.5, 2.0, 3.0, and 5.0 were prepared by dilution in urine pool. 0.5 μ L of the sample was spot in the oxidized paper chip, and the protocol for BSA immobilization described above was applied.

The urine samples were analyzed by Bradford method, considered as a reference method to quantify proteins. For this analysis, 2 μ L of the urine sample were mixed with 798 μ L of water and 200 μ L of Bradford reagent. The mix reacted for 20 min before the measurement on ThermoFisher NanoDrop 2000c spectrophotometer (<https://www.thermofisher.com>) at 595 nm in a quartz cuvette of 10 mm wide. The urine samples were measured in triplicate.

Results and discussion

Characterization of oxidized paper by NaIO₄

The exposure of the cellulose to the periodate results in the opening of the D-glucose rings, the cellulose monomer, by oxidizing the hydroxyl groups of C2 and C3 to aldehydes. The papers oxidized for 0.5 and 2 h were analyzed by micro-FTIR spectroscopy, which yielded 2D and 3D chemical images of the samples, shown in Fig. 1. It is worth mentioning that micro-FTIR spectroscopy has been introduced as one of the most promising techniques for understanding surface redox chemistry [19–21]. For the oxidation process, chemical maps showing the surface changes can be obtained by selecting specific vibrational modes with a focal plane array detector, which allows the simultaneous collection of IR spectra from 4096 microscopic regions. Here, in a pioneering way, we expanded the micro-FTIR spectroscopy for in situ and on-a-paper analysis to understand how the oxidation process affects the chemical composition in specific 2D spatially resolved regions. First, we acquired a photomicrograph of the sample, as shown in Fig. 1a and Fig. 1b for the paper oxidized for 0.5 and 2 h, respectively. The infrared data measured within the scanned area resulted in individual spectra as shown in Fig. 1c and d, where the >C=O stretch band at 1733 cm⁻¹ is observed (the chemical groups of the samples oxidized for 0.5 to 24 h were also analyzed by a regular FTIR equipment, shown on Fig. S1.) The area under this peak was integrated to yield the 2D (Fig. 1e and f) and 3D chemical images (Fig. 1g and h), where we observed the carbonyl bond distribution along the cellulose fibers. As the native paper does not contain the aldehyde group, it was not possible to reconstruct the image. The blue regions represent the absence of carbonyl group, and they correspond to the pores in the micrograph. The region in red shows the aldehyde group on the fibers. The distribution of the red color is not homogenous at this magnification scale, and further and deeper characterization is required to infer about homogeneity. There was no significant change in the aldehyde group distribution between the 0.5- and 2-h oxidation. This is further evidenced on the BSA immobilization assay.

The cleavage of the glucose ring, however, can modify the physicochemical properties of the paper. In fact, the paper shrunk after long periods of exposure to periodate (Fig. 2a), as described by Martinez et al. [22]. The decrease in the geometric area was more significant than in the volume because of a slight increase in the thickness of the paper, from 0.18 mm in the native paper to 0.43 mm in the 24-h oxidized paper (Fig. 2b). It is important to note that there was no evidence for significant mass decrease (data not shown). Therefore, the shrinking is mainly attributed to the aggregation of the fibers and reducing the pores size, as observed in the micrographs in Fig. 2a.

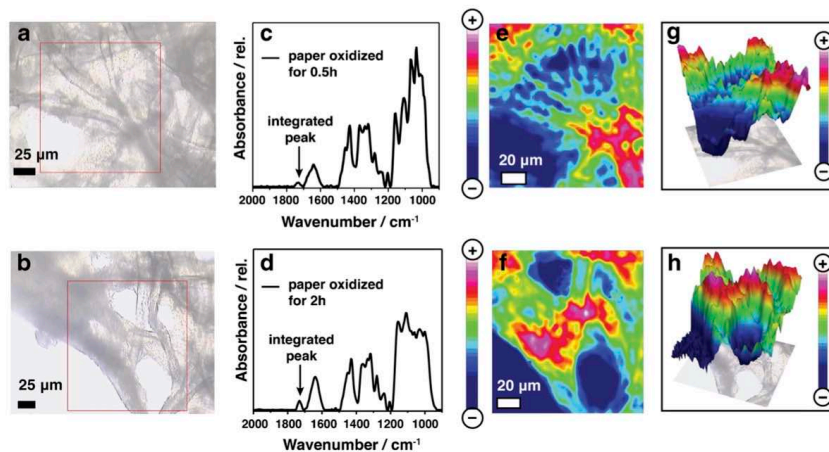


Fig. 1 Micro-FTIR spectroscopy of the paper treated for 0.5 h (**a, c, e, g**) and 2 h (**b, d, f, h**) recorded with focal plane array (FPA) detector in the spectral range from 4000 to 900 cm^{-1} at spectral resolution of 4 cm^{-1} with 256 spectra co-added. **a, b** Optical image showing a part of the sample paper, where fibers are easily seen. The area marked in red was selected

for the extraction of the spectra and consequent chemical images. **c, d** Micro-FTIR spectra of the treated paper with the integrated spectral bands highlighted. **e, f** 2D chemical image showing the distribution of C=O (carbonyl) spectral band along the cellulose fibers. **g, h** 3D chemical image

Furthermore, the paper also showed increased rigidity. To characterize the mechanical properties of the paper oxidized for 24 h, the tensile test was performed. The strain vs. stress profile of the 24-h oxidized paper was unique, with a region of negative strain (Fig. 3a). Even with the negative strain region, the oxidized paper required a higher pressure (15.3 ± 1.6 mPa) to promote the rupture of a strip with same dimensions of the non-oxidized strip (10.3 ± 1.2 mPa), showing that the oxidation increased the stiffness. This is explained by the higher density of fibers on the oxidized paper than on the native one, as their sizes were kept the same for this experiment.

The conversion of hydroxyl to carbonyl groups results in the disarrangement of the cellulose chains, structured by the intra- and interchain hydrogen bonds between monomer units.

In addition, the opening of the glucose ring disarranges the linear pattern of the chains. All these effects contribute to decrease the cellulose crystallinity along with the course of the oxidation by periodate, as can be observed on Fig. 3b.

The capillarity of liquids occurs through the hydrogen bonds between the water molecules and the β -D-glucopyranoside hydroxyl groups. With the decrease of hydrogen bonding sites, the paper exposed to periodate for prolonged times absorbed water more slowly (Fig. 3c). Also, the hydrophilicity of the cellulose diminishes with loss of hydroxyl groups, resulting in an increased contact angle for the paper oxidized for 12 h (Fig. 3c). Therefore, an excessive oxidation of the paper by periodate hindered the capillarity, which enables the solutions to flow without pumping.

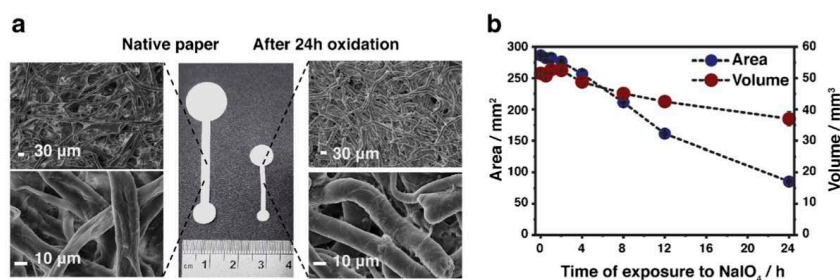


Fig. 2 **a** Shrinking of the paper chip after 24 h of exposure on 0.5 M of IO_4^- (middle) and micrographs in 500 and 3000 times of magnification of the native chromatography paper (left) and of the oxidized paper (right). **b**

Plot of the geometrical area (●) and volume (●) decrease along the time of exposure to NaIO_4

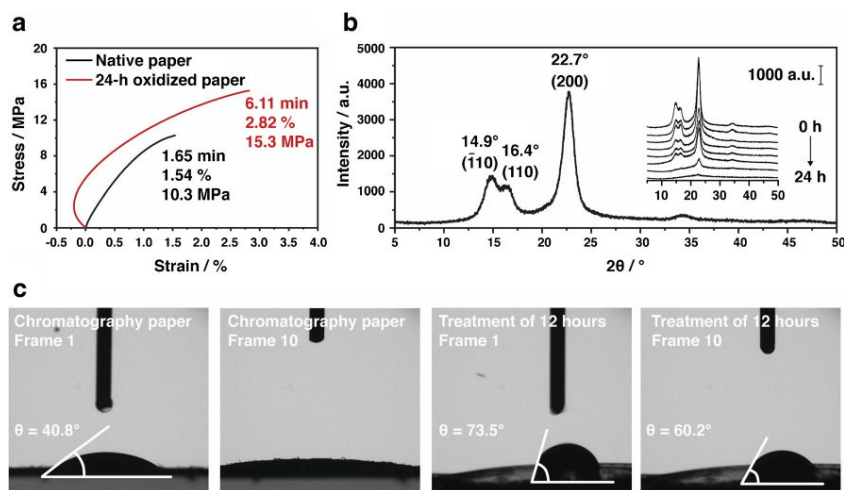


Fig. 3 **a** Stress-strain curve for chromatography paper without (—) and after (—) exposure to periodate for 24 h; specimen dimensions: 30×3 mm. **b** Whatman N° 1 chromatography paper diffractogram, with the index peaks of the crystalline planes, and in the insertion,

diffractograms of the oxidation progress. **c** 1st and 10th frames of a water drop above native chromatography paper and after oxidation of 12 h; contact angles inserted on the frames

BSA immobilization assay

With the aldehyde groups on the oxidized paper, the protein covalently binds through their amine groups, forming a Schiff base (imine bond). During the percolation of phosphate buffer, the unbound proteins at the application spot were carried away through the strip until finding a free binding site on the paper to immobilize. After spotting the protein in the paper, it did not require a rigid time control as in typical adsorption protocols, which usually let the protein adsorb for at least 30 min [21, 23]. For the visualization of protein in the device, Ponceau staining was used. Ponceau bonded specifically with protein through electrostatic interaction, defining a red-colored area on paper where the protein is bound, as shown in the Fig. 4a. The signal change in this system consisted on the blot length rather than the color density since the proteins were allowed to diffuse through the channel and not confined in a delimited space such as for spot tests. There is an adsorption process that is dependent on the number of active sites, resembling frontal chromatography; on the equilibrium regime, the proteins adsorb to all available adsorption sites, and as there is local saturation, the increase in concentration makes the front to advance. As the BSA concentration increased, the blot extension also increased (independent of the paper oxidation), demonstrating a correlation between the amount of the protein and the extension of the blot, as shown in the Fig. 4b. Looking at the same BSA concentration, there was a decrease of the blot size after the oxidative treatment. This indicated a reduced

displacement of the protein because of the improvement on the protein immobilization on the cellulose surface upon contact. There was no significant difference in the blot length after treatments, indicating that the exposure of the paper for 0.5-h sufficed to promote the immobilization of any concentration of BSA on Whatman CHR #1 paper (this was confirmed by two-way ANOVA and Tukey's test, Tables S1–S6). The number of active sites at 0.5 h was enough to immobilize all the protein available at any concentration, which led to a possible steric hindrance. Reaction might continue; however, because proteins are such large molecules, the immobilization is limited by the availability of the pores and not by the density of aldehyde groups anymore.

For 1 mg mL^{-1} BSA concentration, there was no significant difference on the blot length even for the non-treated paper, as can be seen in the bars in Fig. 4b and in Table S3. This is explained by the low total amount of protein. For small concentration of protein, the device required more sensibility to distinguish the blot from different concentrations and oxidation times. One strategy to increase the sensibility of the assay in a range of low protein concentration is to narrow the width of the channel, as we did for the urine protein assessment. Although the blot length did not differ from each other, there was a less intense color on the blot for the non-treated paper, even for the BSA 1 mg mL^{-1} (Fig. S2). This illustrated that the oxidation of the paper changes the properties on the immobilization of proteins. It is important to state that these results are characteristic of this experimental

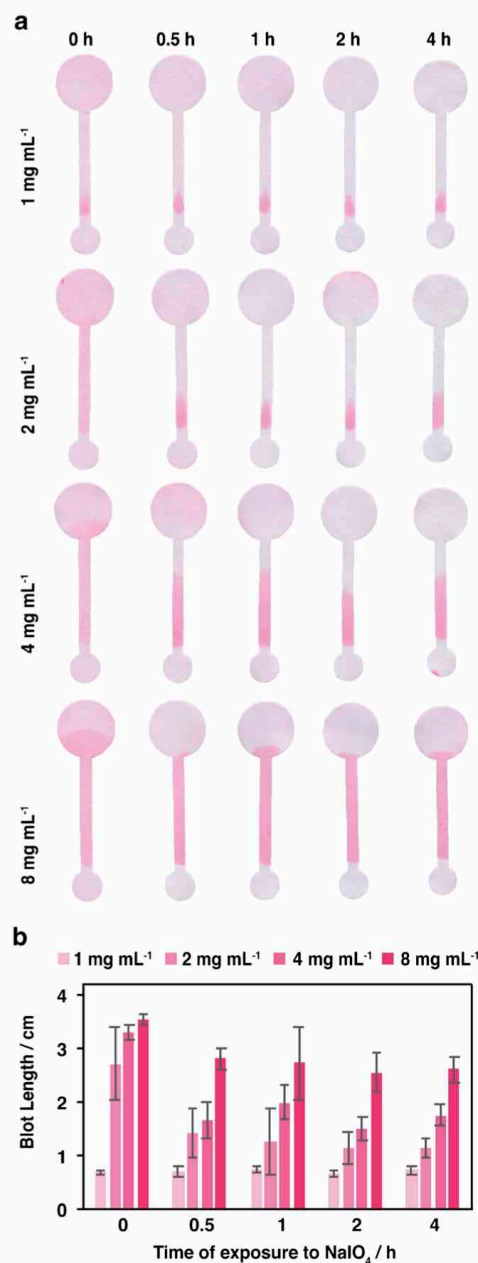


Fig. 4 **a** Paper chips from native (0 h) and oxidized papers for 0.5, 1.0, 2.0, and 4.0 h after the immobilization with 0.5 μ L of BSA at 1.0, 2.0, 4.0, and 8.0 mg mL^{-1} solutions. **b** Graphical relation between oxidation time, BSA concentration, and the blot length

set up and may vary from different type of papers, treatments, and proteins.

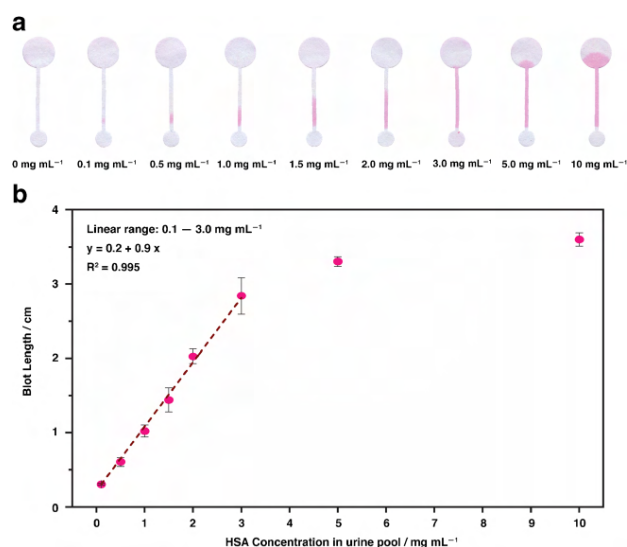
The pH of the buffer solution was evaluated in the immobilization of BSA 4 and 8 mg mL^{-1} . The blot length was smaller in the $\text{pH} = \text{pI}$ (Fig. S3). This result agrees with the work of Garcia et al. [23], which studied the BSA adsorption on chromatography paper 3 MM. In line with their work, the area where protein was immobilized in pH further from pI was led by the repulsion between the charged proteins. Once a protein was bonded to the paper, the next protein was repelled by the mutual charges, resulting in a monolayer distribution of the protein and spreading of the blot. At the pI, even with the protein attached to the paper, the next protein can immobilize in a near binding site of the oxidized paper, stacking the proteins and exploring more binding sites of the paper. Also, the proteins at their pI aggregate furthering the immobilization of proteins in proximity.

Although the treatment for 0.5 h in periodate was enough to promote the protein immobilization on CHR paper, the oxidation of the paper during 4 h exhibited better repeatability between blot lengths, as can be seen in Fig. 4b, and presented a high linear correlation between the BSA concentration and the blot length (Fig. S4). Prolonged times of exposure to NaIO_4 promoted a more homogenous oxidation of the cellulose, resulting in a minor variation of the blot length. Therefore, the paper oxidized for 4 h was evaluated as a platform for determining protein in urine.

Quantification of HSA in urine

As an application of oxidized paper device, we tested it as a sensor for quantification of total protein in human urine. The level of protein in urine from health individuals is less than 30 mg per day, considering the daily volume of urine is from 1 to 3 L [24]. High levels of protein are characterized as microalbuminuria (the protein concentration ranges from 0.01 to 0.3 mg mL^{-1}) and proteinuria (the protein concentration is above 0.3 mg mL^{-1}) [18]. The pool of all samples resulted in no blot in the channel (as shown in the first device of the Fig. 5a), indicating healthy levels of protein. Thus, to simulate a proteinuria sample, the urine pool was spiked with human serum albumin (HSA) to reach concentrations of 0.1, 0.5, 1.0, 1.5, 2.0, 3.0, 5.0, and 10.0 mg mL^{-1} . At HSA levels lower than 0.1 mg mL^{-1} , it was not possible to visualize any color; therefore, the limit of quantification of HSA in this device was 0.1 mg mL^{-1} . In the analytical curve illustrated in Fig. 5b, there are two regions of correlation between the

Fig. 5 **a** Paper chips oxidized for 4 h after the immobilization of 0.5 μL of HSA 0, 0.1, 0.5, 1.0, 1.5, 2.0, 3.0, 5.0, and 10.0 mg mL^{-1} in urine pool. **b** Plot of blot length vs. HSA concentration in urine pool; error bars indicate the standard deviation from 5 chips



HSA concentration and blot length. The first region that includes concentrations from 0.1 to 3.0 mg mL^{-1} is linear ($R^2 = 0.995$). In this region, the blots spread within the channel, where there is a direct correlation to the length. For higher concentrations, the linearity was lost because the blot reached the drain pad and the lateral spreading of protein attenuated the length-increasing rate. This was characterized as a saturation region. In practice, if a urine sample results in a blot that reaches the saturation circle, the subject is under a severe proteinuria case. Increasing the channel length increases the dynamic range of this assay. For analytical comparison, the quantification of protein in urine was also performed by Bradford method, which consists in the colorimetric reaction between the peptide bonds of the protein with the Bradford reagent. The increase in the concentration of protein enhances the color intensity, which can be measured by UV/vis spectroscopy at 595 nm. The same range of HSA levels in urine was analyzed by the Bradford method, and the analytical curve is shown in Fig. S5. The signal obtained by the paper chip method was plotted against the absorbance signal from Bradford method, as shown in the Fig. S6. The Pearson's correlation of 0.9942 indicated that the proposed method correlated with the reference Bradford method, validating the paper chip method to quantify protein in urine. Despite the lower limit of quantification achieved by the Bradford method ($\text{LOQ} = 0.02 \text{ mg mL}^{-1}$), the paper chip method showed a better sensitivity (Fig. S7) and does not require a spectrophotometer or large amount of Bradford reagent. The figures of merit from both methods are summarized on Table S7.

In a commercial urine test strip, the protein level is given by a color scale in semi-quantitative values of 0.3, 1.0, 3.0, and 20 mg mL^{-1} . A color less intense than the corresponding 0.3 mg mL^{-1} is considered as a trace. Therefore, the urine dipstick is not sensitive enough to distinguish normal levels of protein from microalbuminuria, which is a clinical marker for early diabetic nephropathy and concomitant cardiovascular disease [18]. Our device quantitatively determined levels of protein three times lower than the commercial strip, yielding early symptoms of health problems. Moreover, our chip can be applied for detection of any protein in general that binds to the aldehyde groups of the oxidized cellulose and is stained by Ponceau dye, unlike the commercial test in which colorimetric reagents are specific for albumin.

Conclusion

By understanding the oxidation of the paper by periodate, we enhanced the immobilization of proteins, which is an important construction step of biosensing devices in both lateral flow and flow-through assays. The oxidation for 0.5 h was enough to promote the BSA immobilization on paper. However, the oxidation process must be controlled and well-characterized; otherwise, it can drastically modify the physical properties of the paper, as highlighted in this work. The prolonged exposition of the paper to periodate resulted in the reduction of capillarity, loss of crystallinity, and shrinkage of the substrate. We introduced a new approach to characterize

the paper by visualizing the distribution of the chemical groups along the cellulose fibers. This work evidenced the importance of an in-depth characterization of the surface modification of the substrate to apply as an analytical device, encouraging future practices to deeply investigate other chemical processes in paper or other substrates. An alternative device for proteinuria diagnosis was also developed, which is instrument-free and straightforward. Although there is already a commercial urine dipstick for protein screening, our device arises as a quantitative determination for total protein, and it diagnosed microalbuminuria. The analysis by the presented device requires multiple steps that are being optimized for practical purposes, as well as the device layout, but it showed a potential diagnose technology.

Associated content The following files are available free of charge. FTIR spectra for all oxidized papers; ANOVA and Tukey's analysis; variation of color intensity in the protein application spot; variation of the blot length with phosphate buffer pH; correlation of the blot length with increase of BSA concentration; analysis of HSA in urine by Bradford method and comparison between methods (PDF).

Funding information AHI, AH, and FNC gratefully acknowledge the financial support provided by the FAPESP under the grant numbers 2017/05362-9, 2016/25806-6, and 2013/14262-7, respectively. LJMO thanks the financial support by the Coordenação de Aperfeiçoamento de Pessoal de Nível Superior – Brasil (CAPES) – Finance Code 001. TPS gratefully acknowledges financial support from the Conselho Nacional de Desenvolvimento Científico e Tecnológico (CNPq #154064/2016-5). EC is grateful for the INCTBio grants (FAPESP #2014/50867-3 and CNPq #465389/2014-7).

Compliance with ethical standards All procedures performed in studies involving human participants were in accordance with the ethical standards of the institutional and/or national research committee and with the 1964 Helsinki Declaration and its later amendments or comparable ethical standards.

Conflict of interest The authors declare that they have no conflict of interests.

References

- Hu J, Wang S, Wang L, Li F, Pingguan-Murphy B, Lu TJ, Xu F (2014) Advances in paper-based point-of-care diagnostics. *Biosens Bioelectron* 54:585–597
- Nanthasurasak P, Cabot JM, See HH, Gujtt RM, Breadmore MC (2017) Electrophoretic separations on paper: past, present, and future - a review. *Anal Chim Acta* 985:7–23
- Foster LS, Gruntfest IJ (1937) Demonstration experiments using universal indicators. *J Chem Educ* 14:274–276
- Martinez AW, Phillips ST, Butte MJ, Whitesides GM (2007) Patterned paper as a platform for inexpensive, low-volume, portable bioassays. *Angew Chemie - Int Ed* 46:1318–1320
- Tang RH, Liu LN, Zhang SF, He XC, Li XI, Xu F, Ni YH, Li F (2019) A review on advances in methods for modification of paper supports for use in point-of-care testing. *Microchim Acta* 186:521
- Martinez AW, Phillips ST, Whitesides GM, Carrilho E (2010) Diagnostics for the developing world: microfluidic paper-based analytical devices. *Anal Chem* 82:3–10
- Xia Y, Si J, Li Z (2016) Fabrication techniques for microfluidic paper-based analytical devices and their applications for biological testing: a review. *Biosens Bioelectron* 77:774–789
- Li X, Ballerini DR, Shen W (2012) A perspective on paper-based microfluidics: current status and future trends. *Biomicrofluidics* 6: 011301–011301-13
- Nery EW, Kubota LT (2013) Sensing approaches on paper-based devices: a review. *Anal Bioanal Chem* 405:7573–7595
- Kong F, Hu YF (2012) Biomolecule immobilization techniques for bioactive paper fabrication. *Anal Bioanal Chem* 403:7–13
- Rusmini F, Zhong Z, Feijin J (2007) Protein Immobilization Strategies for Protein Biochips. *Biomacromolecules* 8:1775–1789
- Yamada K, Shibata H, Suzuki K, Citterio D (2017) Toward practical application of paper-based microfluidics for medical diagnostics: state-of-the-art and challenges. *Lab Chip* 17:1206–1249
- Scida K, Li B, Ellington AD, Crooks RM (2013) DNA detection using origami paper analytical devices. *Anal Chem* 85:9713–9720
- Kim D, Herr AE Protein immobilization techniques for microfluidic assays. *Biomicrofluidics* 6:041501
- Su S, Nutiu R, Filipe CDM, Li R, Pelton R (2007) Adsorption and covalent coupling of ATP-binding DNA Aptamers onto cellulose. *Langmuir* 23:1300–1302
- Wang S, Ge L, Song X, Yan M, Ge S, Yu J, Zeng F (2012) Simple and covalent fabrication of a paper device and its application in sensitive chemiluminescence immunoassay. *Analyst* 137:3821–3827
- Garcia PT, Cardoso TMG, Garcia CD, Carrilho E, Coltro WKT (2014) A handheld stamping process to fabricate microfluidic paper-based analytical devices with chemically modified surface for clinical assays. *RSC Adv* 4:37637–37644
- Barratt J, Topham P (2007) Urine proteomics: the present and future of measuring urinary protein components in disease. *CMAJ* 177: 361–368
- Khalid M, Hassan A, Honorato AMB, Crespihlo FN, Varela H (2018) Nano-flocks of a bimetallic organic framework for efficient hydrogen evolution electrocatalysis. *Chem Commun* 54:11048–11051
- Macedo LJA, Lima FCDA, Amorim RG, Freitas RO, Yadav A, Iost RM, Balasubramanian K, Crespihlo FN (2018) Interplay of non-uniform charge distribution on the electrochemical modification of graphene. *Nanoscale* 10:15048–15057
- Macedo LJA, Crespihlo FN (2018) Multiplex infrared spectroscopy imaging for monitoring spatially resolved redox chemistry. *Anal Chem* 90:1487–1491
- Strong EB, Kirschbaum CW, Martinez AW, Martinez NW (2018) Paper miniaturization via periodate oxidation of cellulose. *Cellulose* 25:3211–3217
- McCann L, Benavidez TE, Holtsclaw S, Garcia CD (2017) Addressing the distribution of proteins spotted on μ PADs. *Analyst* 142:3899–3905
- Julian BA, Suzuki H, Suzuki Y, Tomino Y, Spavoski G, Novak J (2009) Sources of urinary proteins and their analysis by urinary proteomics for the detection of biomarkers of disease. *Proteomics Clin Appl* 3:1029–1043

Publisher's note Springer Nature remains neutral with regard to jurisdictional claims in published maps and institutional affiliations.

ANNEX 2

Stretchable Sensors for Nanomolar detection of Glucose

Stretchable Sensors for Nanomolar Glucose Detection

Amanda Imamura, Julia Zakashansky, Kenny Cho, Lancy Lin, Emanuel Carrilho, and Michelle Khine*

Biosensors that detect analytes in sweat face the challenge of maintaining sensitivity upon miniaturization. Various materials and processes have been developed to create nanostructured electrodes with high surface areas to mitigate this issue. The need remains, however, for biocompatible materials that can be scalably integrated into wearable devices. This paper details a gold thin-film electrode fabricated using a thermoplastic shape memory polymer to create hierarchical wrinkled structures via the miniaturization process, followed by transfer onto a soft, stretchable substrate. The final stretchable electrode, which is $\gg 30$ times smaller than that of the original, unshrunk electrode, retains its original surface area. Even more remarkably, further enhancement in current density is achieved upon stretching the electrode to 210% of its original length; improved sensitivity remains stable after relaxation of the polymer. Stretching aids diffusion limited reactions, such as the reduction and oxidation of $[\text{Fe}(\text{CN})_6]^{3-/4-}$. The stretchable electrodes sensitively detect glucose without enzymes or additional labels at physiological pH in the range of 1×10^{-7} – 1×10^{-4} M with a calculated limit of detection of 2.22×10^{-8} M, among the lowest reported for a flexible, enzyme-free sensor.

Wearable technology has been widely developed with increasing interest in continuous physiological monitoring during daily activities.^[1–4] More insight into the user's health state can be obtained at molecular level with analysis of biomarkers present in sweat, such as glucose, ethanol, lactic acid, ions, cortisol, and small proteins.^[5–7] Electrochemical detection of these biomarkers is attractive because it can achieve clinically relevant sensitivity and accuracy and is easily integrated into electronic systems.^[8–11]

Integrating electrochemical transducers into wearable devices necessitates miniaturization of the electrodes. This negatively impacts the signal-to-noise ratio (SNR) of the electrical response, as current is directly related to the sensing electrode

surface area.^[12,13] To overcome this issue, nanostructured electrodes with small geometric footprints have been fabricated to achieve higher surface area than their planar counterparts.^[14–17] Wearable sensors in particular should be biocompatible and withstand physiological strains due to motion and deformation of human skin, which is $\approx 30\%$.^[18,19]

Stretchable gold electrodes have been evaluated as glucose detection platforms. Chan et al. demonstrated stability at strains up to 230% with their solution-processed wrinkled gold glucose sensor, with a limit of detection (LOD) of 1×10^{-3} M in artificial sweat.^[20] Zhai et al. reported gold nanowire-based electrodes functionalized with glucose oxidase that were stretched to 20% strain to detect glucose concentrations of 1×10^{-4} M in a solution of NaOH, while Zhao et al. demonstrated a gold-fiber based sensor functionalized with glucose oxidase capable of detecting 6×10^{-6} M glucose in phosphate-buffered solution


(PBS) under strains up to 200%.^[21,22] It is critical to have low detection limits and high sensitivity due to lower concentration of glucose in sweat in comparison with other biological fluids. In this work, we introduce a highly stretchable electrode with the lowest limit of detection to the best of our knowledge for flexible enzyme-free glucose sensing at physiological pH.

We introduce stretchable wrinkled electrodes for electrochemical sensing by depositing thin gold metal thin film on polyolefin (PO), which shrinks to 5% of its original area. During the shrinking process, the stiffness mismatch between the polymer and the gold thin film leads to buckling of the gold and results in hierarchical, wrinkled structures. The shrinking factor (the ratio of the average unshrunk electrode's geometric area to that of the processed electrode) of the pre-stressed thermoplastic PO is 21.8. The wrinkled thin film is then transferred to an elastomer. The transfer of the electrode from shape-memory polymer to elastomer results in additional shrinking due to lift-off process, with a total shrinking factor of 33.4 (Figure 1a). The transferred electrodes retain the wrinkled structures (Figure 1b–d) and upon application of strain, the wrinkles stretch and separate from each other as cracks are sustained in the gold thin film (Figure 1e–g).

Electrochemical properties of the wrinkled electrodes were characterized by measuring the electrochemical active surface area (EASA) in different solutions. The wrinkled structures contribute to high surface area, which directly correlates

A. Imamura, J. Zakashansky, K. Cho, L. Lin, Prof. M. Khine
Materials Science and Engineering
Biomedical Engineering
University of California, Irvine
Irvine, CA 92697, USA
Email: mkhine@uci.edu

A. Imamura, Prof. E. Carrilho
Instituto de Química de São Carlos
Universidade de São Paulo
São Carlos, São Paulo 13566-590, Brazil

 The ORCID identification number(s) for the author(s) of this article can be found under <https://doi.org/10.1002/admt.201900843>.

DOI: 10.1002/admt.201900843

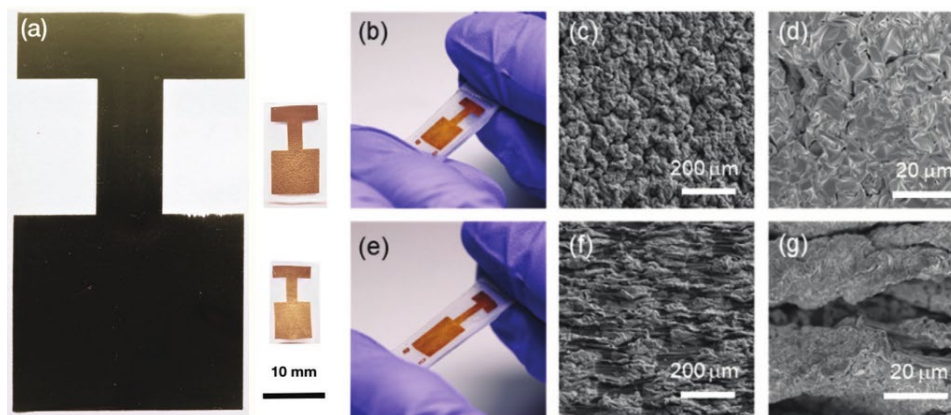


Figure 1. a) Photo of the gold electrodes, from left to right: Unshrunk electrode, shrunk electrode on PO and shrunk electrode on elastomer substrate. b) Photo of electrode transferred to elastomer substrate. SEM of the unstretched, transferred electrode at c) 1.1 and d) 12.9 k \times magnification. e) Transferred electrode being stretched. SEM of the stretched transferred electrode at f) 1.1 and g) 12.9 k \times magnification.

with the Faradaic current. The electrodes were measured by cyclic voltammetry in H_2SO_4 and $[\text{Fe}(\text{CN})_6]^{3-/4-}$ solutions (Figure S1, Supporting Information) and the current densities were obtained by dividing the current by the geometric area (Figure 2a,b). The current densities of shrunk and transferred electrodes were observed to be greater than the unshrunk, planar electrode in both solutions. In our previous work,^[23] a 6.6-fold increase in electrochemical signal was observed in H_2SO_4 for an electrode that had a 20-fold reduction in size, indicating that only a portion of the theoretical surface area was electrochemically active. Even with the application of a hydrophilic polymer to the electrode surface,^[12] the EASA increased only by twofold, therefore not fully achieving access to the original surface area available before shrinking.^[12] Better surface wettability was achieved in this work by modifying the wrinkled surface with oxygen plasma. This method renders the surface hydrophilic and improves surface wetting, removing the need for the hydrophilic polymer coating.

In H_2SO_4 , signal enhancements (the ratio of current densities of processed electrodes to unshrunk electrodes) of 21- and 32-fold were achieved for shrunk and transferred electrodes, respectively (Figure 2c), an improvement of 2.5-fold over our previous work.^[12] The diffusion-independent reaction occurring in the H_2SO_4 solution is the oxidation of gold to gold oxide starting at 1.0 V and the reduction of gold oxide to gold at 0.7 V. The surface area of the shrunk and transferred Au electrodes were calculated by the charge corresponding to the reduction of gold oxide (Table S1, Supporting Information). The calculated surface areas match well with the initial geometric area of unshrunk electrodes (10.5 cm^2). Therefore, the signal enhancements of 21- and 32-fold in H_2SO_4 match the shrinking factor, suggesting that access to the original surface area was preserved.

Interestingly, the signal enhancements are different depending on the solution in which the measurement was performed. The signal enhancements in the $[\text{Fe}(\text{CN})_6]^{3-/4-}$ solution

are \approx 14- and 13-fold for shrunk and transferred electrodes, respectively. The lower signal enhancement in this solution is due to the $[\text{Fe}(\text{CN})_6]^{3-/4-}$ reaction being a diffusion-limited process with relatively fast electron transfer kinetics. As the potential is applied, the concentration of $[\text{Fe}(\text{CN})_6]^{3-/4-}$ at the outermost surface of the electrode approaches zero, and a concentration gradient forms in the solution. Diffusion takes place at the surface of the electrodes as the reaction proceeds; however, the diffusion of electroactive species is impeded by the morphology of the wrinkles. A significant portion of the inner surface of the gold wrinkles is therefore not accessed by the $[\text{Fe}(\text{CN})_6]^{3-/4-}$ ions because the time for diffusion deep into the wrinkles is not sufficient, leading to the disagreement between signal enhancement and shrinking factor. Similarly, the electrochemical behavior of nanoporous gold was reported by Collinson,^[24] Jia,^[25] and Scanlon,^[26] wherein high-surface area, porous electrodes were shown to be biased against redox couples like $[\text{Fe}(\text{CN})_6]^{3-/4-}$. A high dependence of signal enhancement on scan rate was more evident for the diffusion-limited reaction in $[\text{Fe}(\text{CN})_6]^{3-/4-}$ than for H_2SO_4 ; higher signal enhancement can be achieved at greater scan rates (Figure S2, Supporting Information).

The electrochemical behavior of the transferred, stretchable electrodes with applied strain was characterized by stretching the electrodes in H_2SO_4 and $[\text{Fe}(\text{CN})_6]^{3-/4-}$ up to 210% of its length in increments of 30% (Figure 2d,e). Two separate phenomena are occurring simultaneously upon stretching the electrode: 1) an increase in crack formation that eventually stabilizes at a certain number of stretching cycles; and 2) the cracking leads to an increase in EASA. We confirmed both hypotheses as follows. For 1), we cycled the electrodes outside of solution and witnessed an increase in resistance upon cycles (Table S2, Supporting Information) which eventually plateaus (when the cracks are formed). Our previous work detailed this phenomenon for strain sensor applications.^[27] For 2), we witnessed higher electrochemical current after

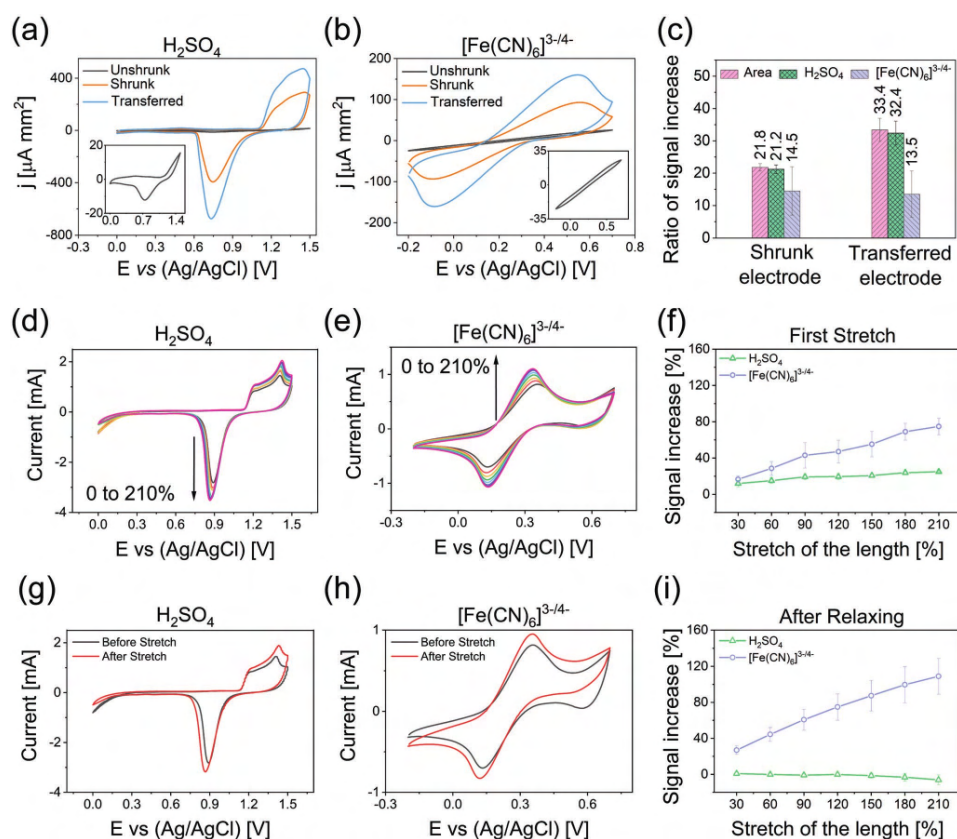


Figure 2. Current density voltammograms of unshrunk, shrunk, and transferred electrodes in a) H₂SO₄ and b) [Fe(CN)₆]^{3-/4-}. c) Shrinking factor and signal enhancement for shrunk and transferred gold electrode expressed as ratios. Cyclic voltammograms of transferred gold electrode stretched up to 0–210% of its length in d) H₂SO₄ and e) [Fe(CN)₆]^{3-/4-}. f) Signal increase as measured by peak height before and after stretching up to 210% of its length and gain in signal in H₂SO₄ and [Fe(CN)₆]^{3-/4-}. Cyclic voltammograms of transferred gold electrodes in g) H₂SO₄ and h) [Fe(CN)₆]^{3-/4-} before and after stretching to 210% of its length and relaxing overnight. i) After relaxing the electrodes overnight, the procedure in (f) was repeated in H₂SO₄ and [Fe(CN)₆]^{3-/4-}.

stretching. As shown in the voltammograms in Figure 2d,e, stretching the electrode resulted in a greater peak height for the faradaic current without significant increase in the capacitive current. Since the faradaic current scales with surface area, the increase in signal can be explained by newly exposed surface area due to crack formation. A 20% increase in signal was observed in H₂SO₄ (Figure 2f); however, the enhancement to signal after stretching was greater in the [Fe(CN)₆]^{3-/4-} solution than in H₂SO₄ (Figure 2f). This indicated that crack-based formation of new surfaces was not the only phenomenon contributing to the 60% signal enhancement in the [Fe(CN)₆]^{3-/4-} solution. We hypothesize that stretching the wrinkled surface leads to the exposure of wrinkle “pockets” that were previously isolated from the solution and thus not accessed by

[Fe(CN)₆]^{3-/4-}. This, combined with the newly exposed areas caused by the formation of cracks, resulted in additional reactive surface area being accessed by [Fe(CN)₆]^{3-/4-} and a subsequent increase in current (Figure 2f). It was visually evident in scanning electron microscopy (SEM) images (Figure 1f,g) that the larger-scale wrinkles deform to accommodate the stretching of the substrate at high strains. This results in surface that is less rough and the [Fe(CN)₆]^{3-/4-} ions are able to more easily access the inner surface.^[24] The total enhancement to current density increases to approach the shrinking factor as in the H₂SO₄ solution. The stretched, wrinkled electrode therefore behaves more similar to a planar electrode at high strains and allows us to overcome the diffusion limitation of the [Fe(CN)₆]^{3-/4-} reaction described above.

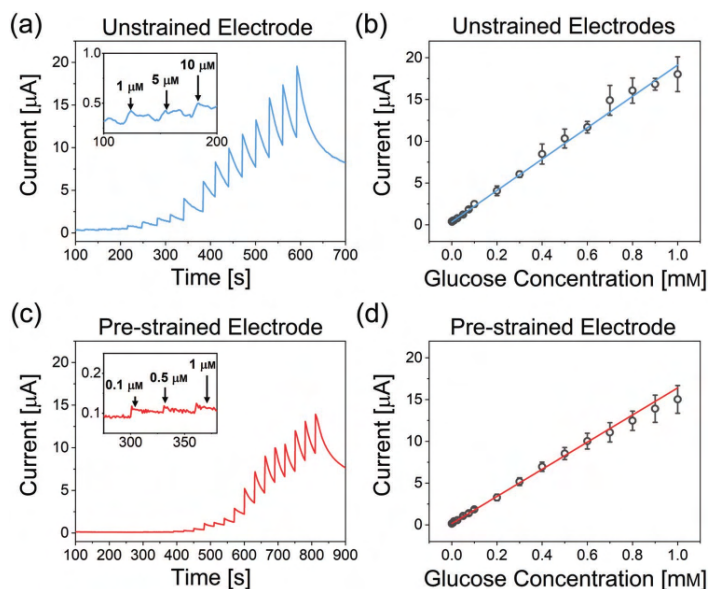


Figure 3. a) Amperometry detection of glucose from 1×10^{-6} – 1×10^{-3} M in PBS using unstrained electrode. b) Linear correlation of current values with glucose concentration in unstrained electrode ($R^2 = 0.99$). c) Amperometry detection of glucose from 1×10^{-7} – 1×10^{-3} M in PBS using prestrained electrode. d) Linear correlation of current values with glucose concentration in prestrained electrode ($R^2 = 0.99$).

Importantly, comparing the voltammograms of unstrained electrodes before and after stretching, we observe a gain in signal of 16% and 13% in H_2SO_4 and $[\text{Fe}(\text{CN})_6]^{3-/4-}$, respectively (Figure 2 g,h). This gain in signal can be attributed to the cracks formed during the straining protocol. Further evidence of wrinkled deformation facilitating diffusion in $[\text{Fe}(\text{CN})_6]^{3-/4-}$ is that after initial crack formation and relaxation, stretching the electrode again continues to increase the current in $[\text{Fe}(\text{CN})_6]^{3-/4-}$ solution. Conversely, in H_2SO_4 the current does not significantly increase with strain upon subsequent stretching of the electrode (Figure 2i). The increase in current with strain in the $[\text{Fe}(\text{CN})_6]^{3-/4-}$ solution after relaxation demonstrated that access to the surface area can be controlled by stretching the electrode to facilitate diffusion and increase EASA. Straining the electrode was thus used as a preconditioning step to maximally increase the electrical response of the transferred electrodes, which can further improve detection of biomarkers at low concentration in sweat.

The transferred electrodes were thus evaluated for label- and enzyme-free electrochemical detection of glucose in the clinically relevant concentration range found in sweat, saliva, and tears. Glucose is a commonly studied biomarker, and as a proof of concept, the measurements were taken at physiological pH. The transferred electrode detects glucose without the use of enzymes through its oxidation mechanism at 0.3 V (Figure S4, Supporting Information).^[28]

Chronoamperometry was used to measure sequential addition of glucose to PBS pH 7.2 (Figure 3). The unstrained, transferred electrode showed a LOD of 2.68×10^{-7} M which is adequate for glucose detection in the sweat of hypoglycemic and hyperglycemic patients (2×10^{-3} – 6×10^{-4} M).^[29] The detection of glucose using prestrained electrodes was evaluated after being stretched up to 210% of its length. The prestrained electrodes exhibited a broader linear range of detection (1×10^{-7} – 1×10^{-3} M) due to a significant improvement to SN) of an order of magnitude. The corresponding LOD of prestrained electrodes was 2.22×10^{-8} M, an order of magnitude lower than in unstrained electrodes. We hypothesize that the improved LOD is due to an improvement in SNR, attributed to the mechanical stabilization of the wrinkled thin film. Before the strain cycling, cracks are continuously introduced to the metal film (from handling and natural stress release) and the electrode is mechanically dynamic. By driving crack formation (illustrated in the schematic in Figure S3, Supporting Information), the metal film and electron pathways are stabilized, which also likely reduces the noise during electrochemical measurement of surface activity. After straining the electrode outside of the solution, the standard deviation of noise of resistance measurements decreased by almost sixfold, on average, while the standard deviation of the noise of an electrode measured before a glucose injection in solution decreased by an order of magnitude after straining.

The achieved LOD is lower than those reported for electrodes utilizing structures with nanoparticles of gold, platinum, or other alloy combinations with carbon,^[10,30,31] as well as for nanoporous substrates and electrodes functionalized with glucose oxidase.^[32–37] Table S3 (Supporting Information) compares the figures of merit obtained in this paper with other published works investigating flexible, glucose sensors. The range of detection achieved using the flexible, prestrained electrodes is relevant for monitoring blood sugar via sweat in diabetic patients, as well as for noninvasive methods utilizing saliva, tears, or any application that requires detection of small changes in glucose concentration.^[38–40]

In summary, we introduce high surface area electrodes on soft, stretchable substrates for electrochemical detection of nanomolar quantities of glucose at physiological pH. The method for fabricating the enhanced EASA electrodes requires neither a cleanroom, nor specialty materials or equipment. The wrinkled, transferred gold electrode shows a 32-fold increase in current density compared to a planar electrode of equal geometric size. Stretching the electrode introduces cracks to the wrinkled film and provides additional surface area. Stretching the electrode also resulted in the “unfolding” of some of the wrinkles, which facilitated electroactive species to reach areas not accessed otherwise in reactions limited by diffusion, such as in the redox reaction of $[\text{Fe}(\text{CN})_6]^{3-/4-}$.

Straining the electrode therefore functions as a preconditioning step to improve the SNR and enhance the LOD by an order of magnitude over unstrained electrodes. These improvements are crucial for overcoming the challenge of detecting low concentrations of biomarkers. The prestrained, wrinkled gold electrodes demonstrate a LOD of 2.22×10^{-8} M, among the lowest reported for enzyme-free glucose detection. Further investigation into the detection of other biomarkers of clinical interest is currently being developed based on these findings.

Experimental Section

Fabrication and Transfer of Wrinkled Electrodes: Detailed protocol is described in the Supporting Information. The average geometric area of the shrunk and transferred electrode were 0.48 and 0.31 cm², respectively. Samples were prepared for SEM imaging with sputtered iridium (6 nm) and were taken using the GAIA Tescan system (8 kV, 0.20 pA).

Electrochemical Characterization: Electrochemical characterization was performed on a Reference 600 potentiostat (Gamry Instruments) with the unshrunk, shrunk, and transferred electrodes as working electrodes, Pt wire as the counter electrode and Ag/AgCl as the reference electrode. Cyclic voltammetry was first performed in a H₂SO₄ 0.5 M solution from 0 to 1.5 V at 10, 25, 50, 100, 250, 500, and 1000 mV s⁻¹. The process was repeated in 0.005 M $[\text{Fe}(\text{CN})_6]^{3-/4-}$ solution in 0.05 M PBS solution at pH 7.4 from -0.2 to 0.7 V.

Electrochemical Characterization of Transferred Electrodes Under Strain: A stretching system was developed to maintain the flexible electrodes under strain, while an electrochemical measurement was performed. Cyclic voltammetry was performed at every 30% strain of electrode length in H₂SO₄ and $[\text{Fe}(\text{CN})_6]^{3-/4-}$ solutions until it reached 210% of its original length. The electrode was allowed to relax overnight before repeating the stretching procedure.

Glucose Detection with Stretchable Electrode: The glucose oxidation potential was measured in a 5×10^{-3} M solution of glucose in PBS (pH 7) by cyclic voltammetry. Chronoamperometry was performed at 0.3 V and glucose was titrated into 20 mL of PBS (pH 7.4) every

30 s. The titration was performed for nonstrained electrodes ($n = 3$) and prestrained electrodes ($n = 3$). An analytical calibration curve was plotted using current values corresponding to sequential additions of glucose. The sensitivity was obtained from the slope and the limit of detection was calculated according to IUPAC.

Supporting Information

Supporting Information is available from the Wiley Online Library or from the author.

Acknowledgements

A.I. and J.Z. contributed equally to this work. The authors thank Heather Carmen Romero Mercieca, Richard Chang, and Chuangyuan Lee. A.I. gratefully acknowledges the financial support provided by the FAPESP under Grant No. 2018/19749-5.

Conflict of Interest

The authors declare no conflict of interest.

Keywords

flexible electrodes, glucose detection, high surface area, rough surface, signal enhancement

Received: September 25, 2019

Revised: December 13, 2019

Published online: February 17, 2020

- [1] K. Guk, G. Han, J. Lim, K. Jeong, T. Kang, E.-K. Lim, J. Jung, *Nanomaterials* **2019**, *9*, 813.
- [2] J. Heikenfeld, A. Jajack, J. Rogers, P. Cutruf, L. Tian, T. Pan, R. Li, M. Khine, J. Kim, J. Wang, J. Kim, *Lab Chip* **2018**, *18*, 217.
- [3] K. Xu, Y. Lu, K. Takei, *Adv. Mater. Technol.* **2019**, *4*, 1800628.
- [4] L. Manjakkal, D. Shakhthivel, R. Dahiya, *Adv. Mater. Technol.* **2018**, *3*, 1800252.
- [5] Z. Sonner, E. Wilder, J. Heikenfeld, G. Kasting, F. Beyette, D. Swaile, F. Sherman, J. Joyce, J. Hagen, N. Kelley-Loughnane, R. Naik, *Biomicrofluidics* **2015**, *9*, 031301.
- [6] M. Bariya, Z. Shahpar, H. Park, J. Sun, Y. Jung, W. Gao, H. Y. Y. Nyein, T. S. Liaw, L.-C. Tai, Q. P. Ngo, M. Chao, Y. Zhao, M. Hettick, G. Cho, A. Javey, *ACS Nano* **2018**, *12*, 6978.
- [7] J. Kim, J. R. Sempionatto, S. Imani, M. C. Hartel, A. Barfidokht, G. Tang, A. S. Campbell, P. P. Mercier, J. Wang, *Adv. Sci.* **2018**, *5*, 1800880.
- [8] W. Gao, S. Emaminejad, H. Y. Y. Nyein, S. Challa, K. Chen, A. Peck, H. M. Fahad, H. Ota, H. Shiraki, D. Kiriya, D.-H. Lien, G. A. Brooks, R. W. Davis, A. Javey, *Nature* **2016**, *529*, 509.
- [9] J. Kim, A. S. Campbell, J. Wang, *Talanta* **2018**, *177*, 163.
- [10] A. Sedighi, M. Montazer, S. Mazinani, *Biosens. Bioelectron.* **2019**, *135*, 192.
- [11] S. K. Vashist, *Anal. Chim. Acta* **2012**, *750*, 16.
- [12] A. Hauke, L. S. S. Kumar, M. Y. Kim, J. Pegan, M. Khine, H. Li, K. W. Plaxco, J. Heikenfeld, *Biosens. Bioelectron.* **2017**, *94*, 438.
- [13] E. Huigen, A. Peper, C. A. Grimbergen, *Med. Biol. Eng. Comput.* **2002**, *40*, 332.

- [14] D. M. Cox, in *Nanostructure Science and Technology: R&D Status and Trends in Nanoparticles Nanostructured Materials and Nanodevices* (Eds.: R. W. Siegel, E. Hu, D. M. Cox, H. Goronkin, L. Jelinski, C. C. Koch, J. Mendel, M. C. Roco, D. T. Shaw), Springer Netherlands, Dordrecht, 1999, pp. 49–66.
- [15] P. T. Toi, T. Q. Trung, T. M. L. Dang, C. W. Bae, N.-E. Lee, *ACS Appl. Mater. Interfaces* **2019**, *11*, 10707.
- [16] F. Schröper, D. Brüggemann, Y. Mourzina, B. Wolfrum, A. Offenhäusser, D. Mayer, *Electrochim. Acta* **2008**, *53*, 6265.
- [17] N. Arroyo-Currás, K. Scida, K. L. Ploense, T. E. Kippin, K. W. Plaxco, *Anal. Chem.* **2017**, *89*, 12185.
- [18] D.-H. Kim, N. Lu, R. Ma, Y.-S. Kim, R.-H. Kim, S. Wang, J. Wu, S. M. Won, H. Tao, A. Islam, K. J. Yu, T. Kim, R. Chowdhury, M. Ying, L. Xu, M. Li, H.-J. Chung, H. Keum, M. McCormick, P. Liu, Y.-W. Zhang, F. G. Omenetto, Y. Huang, T. Coleman, J. A. Rogers, *Science* **2011**, *333*, 838.
- [19] A. Ni Annaidh, K. Bruyère, M. Destrade, M. D. Gilchrist, M. Otténio, *J. Mech. Behav. Biomed. Mater.* **2012**, *5*, 139.
- [20] Y. Chan, M. Skreta, H. McPhee, S. Saha, R. Deus, L. Soleymani, *Analyst* **2018**, *144*, 172.
- [21] Q. Zhai, S. Gong, Y. Wang, Q. Lyu, Y. Liu, Y. Ling, J. Wang, G. P. Simon, W. Cheng, *ACS Appl. Mater. Interfaces* **2019**, *11*, 9724.
- [22] Y. Zhao, Q. Zhai, D. Dong, T. An, S. Gong, Q. Shi, W. Cheng, *Anal. Chem.* **2019**, *91*, 6569.
- [23] J. D. Pegan, A. Y. Ho, M. Bachman, M. Khine, *Lab Chip* **2013**, *13*, 4205.
- [24] M. M. Collinson, *ISRN Anal. Chem.* **2013**, *2013*, 692484.
- [25] F. Jia, C. Yu, Z. Ai, L. Zhang, *Chem. Mater.* **2007**, *19*, 3648.
- [26] M. D. Scanlon, U. Salaj-Kosla, S. Belochapkin, D. MacAodha, D. Leech, Y. Ding, E. Magner, *Langmuir* **2012**, *28*, 2251.
- [27] L. Lin, M. Chu, S.-J. Park, J. A. Zakashansky, M. Khine, *Macromol. Mater. Eng.* **2019**, *304*, 1800520.
- [28] M. Pasta, F. La Mantia, Y. Cui, *Electrochim. Acta* **2010**, *55*, 5561.
- [29] E. Witkowska Nery, M. Kundys, P. S. Jeleń, M. Jönsson-Niedziółka, *Anal. Chem.* **2016**, *88*, 11271.
- [30] J. Ryu, K. Kim, H.-S. Kim, H. T. Hahn, D. Lashmore, *Biosens. Bioelectron.* **2010**, *26*, 602.
- [31] K.-C. Lin, Y.-C. Lin, S.-M. Chen, *Electrochim. Acta* **2013**, *96*, 164.
- [32] A. J. Bhandodkar, W. Jia, C. Yardımcı, X. Wang, J. Ramirez, J. Wang, *Anal. Chem.* **2015**, *87*, 394.
- [33] H. Lee, C. Song, Y. S. Hong, M. S. Kim, H. R. Cho, T. Kang, K. Shin, S. H. Choi, T. Hyeon, D.-H. Kim, *Sci. Adv.* **2017**, *3*, e1601314.
- [34] X. Xuan, H. S. Yoon, J. Y. Park, *Biosens. Bioelectron.* **2018**, *109*, 75.
- [35] A. Yang, Y. Li, C. Yang, Y. Fu, N. Wang, L. Li, F. Yan, *Adv. Mater.* **2018**, *30*, 1800051.
- [36] H. Yoon, X. Xuan, S. Jeong, J. Y. Park, *Biosens. Bioelectron.* **2018**, *117*, 267.
- [37] C. W. Bae, P. T. Toi, B. Y. Kim, W. I. Lee, H. B. Lee, A. Hanif, E. H. Lee, N.-E. Lee, *ACS Appl. Mater. Interfaces* **2019**, *11*, 14567.
- [38] P. Abikshyeet, V. Ramesh, N. Oza, *Diabetes, Metab. Syndr. Obes.: Targets Ther.* **2012**, *5*, 149.
- [39] J. Moyer, D. Wilson, I. Finkelshtein, B. Wong, R. Potts, *Diabetes Technol. Ther.* **2012**, *14*, 398.
- [40] Q. Liu, Y. Liu, F. Wu, X. Cao, Z. Li, M. Alharbi, A. N. Abbas, M. R. Amer, C. Zhou, *ACS Nano* **2018**, *12*, 1170.

ANNEX 3

Detection of the SARS-CoV-2 spike protein in saliva with Shrinky-Dink© electrodes



Cite this: DOI: 10.1039/d1ay00041a

Received 8th January 2021
Accepted 2nd February 2021

DOI: 10.1039/d1ay00041a

rsc.li/methods

Detection of the SARS-CoV-2 spike protein in saliva with Shrinky-Dink® electrodes†

Julia A. Zakashansky,^a Amanda H. Imamura,^b Darwin F. Salgado, II,^c Heather C. Romero Mercieca,^c Raphael F. L. Aguas,^c Angelou M. Lao,^c Joseph Pariser,^c Netzahualcōyotl Arroyo-Currás^{b,de} and Michelle Khine^{b,*c}

Using the children's toy, Shrinky-Dink®, we present an aptamer-based electrochemical (E-AB) assay that recognizes the spike protein of SARS-CoV-2 in saliva for viral infection detection. The low-cost electrodes are implementable at population scale and demonstrate detection down to 1 ag mL⁻¹ of the S1 subunit of the spike protein.

already been reported in recent literature.²⁻⁴ Due to the high transmission rate, measures such as “lockdowns” and “self-quarantining” were adopted, but the number of confirmed cases is still rising in many countries, including the United States. The widespread shortages of medical resources and materials reflect the overwhelming nature of the spread of this illness.

Introduction

In 2020, the World Health Organization (WHO) announced the respiratory disease COVID-19 outbreak to be a pandemic.¹ The first cases of COVID-19 were in the Chinese city of Wuhan and it quickly spread to other continents. The high infection rate of the pathogen, severe acute respiratory syndrome coronavirus-2 (SARS-CoV-2), makes the management of the disease more difficult than previous coronaviruses, such as SARS-CoV-1 and MERS-CoV. Human-to-human transmission of SARS-CoV-2 can occur through droplets like other coronaviruses; however, there is a critical difference in SARS-CoV-2 viral load distribution throughout the time of infection that contributes to its rapid spread. Unlike SARS-CoV-1 or the common flu, whose viral loads are associated with the symptom onset, the high shedding of SARS-CoV-2 even among pre-symptomatic patients increases the risk of transmission of the virus. Several studies on the transmission of COVID-19 by asymptomatic patients have

Due to the mode of transmission of COVID-19, the implementation of population-scale testing including asymptomatic people is recommended.⁵ Although the WHO recommends immediate diagnosis as a crucial management step to thwart the spread of infectious diseases, a massively deployable diagnostic for SARS-CoV-2 has yet to be realized.

In the U.S., more than 1.6 million tests are performed per day with a daily positive rate of 13.4% as of January 7, 2020.^{6,7} The gold standard methods for diagnosing COVID-19 are based on polymerase chain reaction (PCR), including reverse transcription polymerase chain reaction (RT-PCR), which is a complex and expensive technique performed in centralized clinical laboratories. The turnaround time can be days, if not weeks, due to the currently overwhelming demand placed on laboratory equipment and manpower necessary to analyse specimens. Additionally, a major concern regarding the PCR-based tests is the high rate of false-negatives. Another concern regarding current tests is the invasive sampling method. Nasopharyngeal swabs induce coughing and occasionally cause bleeding, which is a risk of transmission to healthcare workers. An easier and more accessible fluid is saliva. Using saliva not only removes the discomfort and increases the accessibility of current tests, but could provide results when nasopharyngeal swabs cannot.⁸ Yet, there still has not been (at the time of completion of this manuscript) a single screening or diagnostic test approved for over-the-counter (OTC) use by the FDA, which would allow users to collect their own saliva specimens, without having to mail them to a centralized laboratory for processing, and read results on the spot.

One alternative diagnostic approach is immunoassays, which detect the antibodies against SARS-CoV-2; however, these

^aMaterials Science and Engineering, University of California – Irvine, Irvine, California 92697, USA. E-mail: mkhine@uci.edu

^bInstituto de Química de São Carlos, Universidade de São Paulo, São Carlos, São Paulo, 13566-590 Brazil

^cBiomedical Engineering, University of California – Irvine, Irvine, California 92697, USA

^dDepartment of Pharmacology and Molecular Sciences, Johns Hopkins School of Medicine, Baltimore, Maryland 21205, USA

^eDepartment of Chemical and Biomolecular Engineering, Whiting School of Engineering, & Institute for Nanobiotechnology, Johns Hopkins University, Baltimore, MD 21218, USA

† Electronic supplementary information (ESI) available. See DOI: 10.1039/d1ay00041a

View Article Online

Analytical Methods

Communication

are more suitable to establish whether an individual was previously infected with COVID-19 and are not recommended as a diagnostic tool or for contact tracing the spread of the disease.⁹ In contrast, during the critical first few days post infection, the detectable viral load peaks. With no indication of infection, the asymptomatic individual can effectively spread the virus to many people. Recent studies indicate that approximately 20% of infected patients remain asymptomatic but are infectious.^{9,10}

We note that virus copies present in saliva range from 10^2 – 10^{11} copies per mL throughout the duration of the infection.^{8,11–16} Because these numbers are low, it is critical to establish an adequately low limit of detection for the assay. Here, we demonstrate an innovative platform that obviates the need for specimen processing and uses nucleic acid aptamers to recognize viral spike protein within clinically relevant concentration ranges.

Critical to the development of sensitive diagnostic assays, aptamers have a significant advantage: the kinetic parameters of aptamer–target binding can be easily tuned to invoke a specific and measurable response.¹⁷ By tagging aptamers with a redox indicator such as methylene blue (MB), the change in MB electron transfer rate upon binding to the target molecule can be measured. Specifically, electrochemical aptamer-based (E-AB) sensors use this strategy to achieve response times on the order of seconds or faster and provide equilibrium results within 30 minutes.¹⁸ The limit of detection (LOD) for E-AB virus sensors depends on the target analyte, aptamer and most importantly, sensor design; the LOD can be brought to lower ranges through amplification methods to accommodate the low concentrations (aM–nM) of analyte present in physiological conditions.^{19–21} In 2009, an E-AB sensor was used to detect the nucleocapsid protein of the SARS-CoV virus with a LOD of 2 pg mL^{-1} , which falls in the lower range of concentrations of detectable viral load in nasopharyngeal and saliva samples.^{22,23} Most recently, several publications have reported sensors for the detection of the SARS-CoV-2 virus in various media utilizing both antibody- and oligonucleotide-based capture methods. The detection scheme presented by Moitra *et al.* results in an easy-to-read optical signal; however, the limit of detection achieved using this method is 10^3 ng mL^{-1} , which is significantly higher than the concentration of spike protein found in saliva.²⁴ Chen *et al.* have also recently investigated three single-stranded DNA probes for the detection of the N-protein of SARS-CoV-2 with a reported LOD of 10 ng mL^{-1} . Among the diagnostic methods using antibodies for antigen recognition, a field-effect transistor sensor was reported by Seo *et al.* to have a LOD of 100 fg mL^{-1} in buffer solution, and an electrochemical sensor was reported by Eissa *et al.* to have an LOD of 0.8 pg mL^{-1} .^{25,26} A study was also recently published in which an oligonucleotide targeting four different regions within the N-gene of the SARS-CoV-2 virus was used to detect SARS-CoV-2 viral RNA.²⁷ The N-gene of the SARS-CoV-2 virus is located inside the virus and is released upon infection of cells. By contrast, each virus is thought to contain up to 100 spike proteins, based on the evaluation of genetically similar SARS-CoV viruses, each with a receptor binding domain (RBD)

capable of binding to an oligonucleotide specific to that region.^{5,28–30} For this reason, we chose the S1 subunit of the spike protein, which contains the RBD, as the detection target.

Recently, Song *et al.* discovered two aptamers targeting the RBD from SARS-CoV-2 by using an ACE2 receptor competition-based selection strategy (SELEX).³¹ For the biorecognition of our sensor, we selected the hairpin-structured 51-base aptamer called CoV2-RBD-1C with a dissociation constant of 5.8 nM, which is comparable to that of existing antibodies raised against the spike protein. The measurements performed by Song *et al.* suggest that the aptamer binds to several amino acids of the RBD, which is essential for highly specific detection.³¹ The current diagnostic methods for COVID-19 often face shortages of chemicals and involve invasive sampling methods. We propose here a point-of-care E-AB platform based on high-surface area Shrinky-Dink® electrodes, which are broadly available and can be manufactured at large scales without extensive surface modification. An aptamer proven to be specific to the RBD region was chosen to enable non-invasive detection of SARS-CoV-2 spike protein in saliva.

Results and discussion

We have previously demonstrated signal enhancement in the form of greater dynamic range of detection on electrodes made using the 80's children's toy, Shrinky-Dink®, which saturates the color of a drawing made on a thermoplastic polystyrene sheet that shrinks when heated (Fig. 1).^{32,33} Our group published on Shrinky-Dink Microfluidics in Lab-on-a-Chip in 2008 and it has since become a workhorse in laboratories around the world.^{34,35} In this study, we demonstrate using Shrinky-Dink wrinkled (SDW) electrodes for sensitive detection of the S1 subunit of the spike protein of SARS-CoV-2 with the purpose of providing a low-cost screening and diagnostic device for the COVID-19 infection. Fig. 1 demonstrates the fabrication process of SDW electrodes, beginning with sputtering pre-stressed polystyrene with gold, followed by shrinking and immobilization of aptamers and 6-mercaptohexanol (MCH). The structured surface of the SDW gold electrode, shown in the scanning electron microscopy image, supports a high surface area for loading of MB-modified aptamers, which respond to the S1 protein domain by decreasing electron transfer currents from MB. The wrinkled gold surface has been extensively investigated in previous publications from our group and others.^{32,33,36–40}

To determine the functionality and affinity of the aptamers in the E-AB format, all initial experiments were first performed on commercial disc (CD) Au electrodes (CH Instruments, 2 mm diameter) in a standard 3-electrode electrochemical cell (Fig. 2A). The commercial gold electrodes were functionalized with the aptamers and backfilled with blocking MCH monolayers. Upon exposure of the electrode surface to a buffered solution containing S1 protein, we observed a decrease in the MB peak height of square wave voltammograms (Fig. 2B). The binding of a relatively large protein, such as the S1 protein (78.3 kDa), to the MB-modified aptamer produces an increase in resistance to the transfer of electrons from MB to the electrode (presumably *via* steric hindrance), leading to a decrease in the

Communication

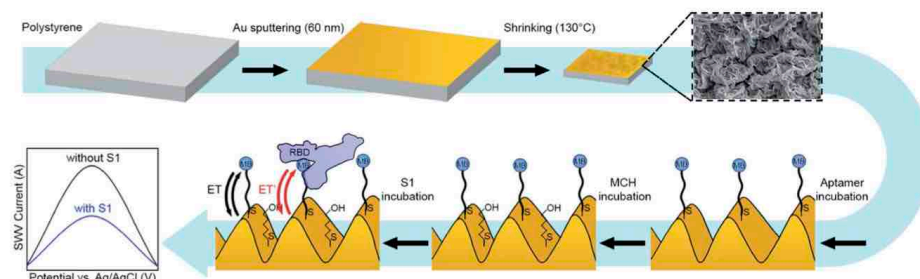
View Article Online
Analytical Methods

Fig. 1 Process flow to create SDW E-AB sensors. First, a thin layer of gold is sputtered onto polystyrene plastic, which is shrunk to create wrinkles (SEM inset shows representative wrinkle morphology). The wrinkled surface is incubated with aptamers conjugated with MB, then incubated with MCH as the blocking molecule. After functionalization, the wrinkled surface was exposed to the S1 protein. Arrows indicate change in electron transfer with and without the spike protein attached (through the RBD). Graph illustrates change in current due to the change in electron transfer for spike bound MB on SDW electrodes upon addition of S1 protein.

MB peak similar to that presented in the work of Kang *et al.*⁴¹ In the E-AB sensors, the mechanism of detection relies on binding-induced conformational changes that, in turn, alter the electron transfer rate between a redox reporter and the surface of the electrode.^{42,43} The distance between the reporter and the electrode surface directly affects electron transfer kinetics in the system; at small distances, and with little obstruction, electron transfer occurs at a faster rate than at greater distances or in the presence of obstructing molecules. These differences in electron transfer rates translate to differing time constants of current passed, which become relevant when considering measurement parameters.⁴⁴ For the SARS-CoV-2 RBD aptamer used in this study, no conformational change has yet been demonstrated. Thus, we speculate that the changes in signal observed in this study upon target binding are due to the physical obstruction of electron transfer from the reporter to the gold surface by bound spike proteins.

The change in peak current correlates with increasing concentrations of S1 protein, as shown in Fig. 2B. We evaluated

the change in signal in response to increasing S1 protein concentrations on CD Au electrodes by performing a titration curve in phosphate-buffered solution (Fig. 2C). Measurements were taken at square-wave frequencies ranging from 5 to 50 Hz. Non-linear regression using the Hill isotherm was used to determine the optimal square-wave frequency producing maximum signal gain and broadest dynamic range. This analysis resulted in Hill parameters that reported varying receptor-ligand affinity (K_D) and binding stoichiometry with square-wave frequency. The Hill coefficient n was ~ 1 at 5 Hz and the data displayed highest sigmoidicity at this frequency, indicating single binding site physics for the interaction between the S1 protein and the aptamer. Frequencies above 5 Hz produced isotherms with slightly lower n values (*e.g.*, $n = 0.78$ at 50 Hz) but broader dynamic range. Based on these calibrations, 10 Hz was chosen as the optimal compromise between sensor affinity and sensitivity for our platform.

The signal change in response to addition of S1 protein on CD electrodes confirmed the viability of the chosen aptamer

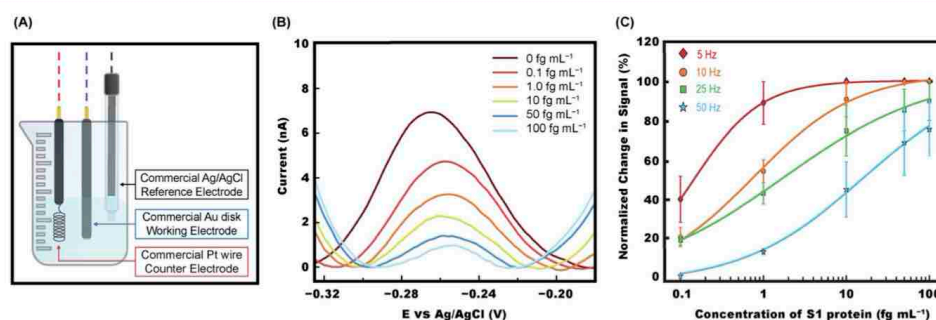


Fig. 2 (A) Beaker cell configuration with CD electrode. (B) Raw peak height change in current with increasing concentrations of S1 protein in phosphate buffer solution on CD electrodes. (C) Titration curves collected at various frequencies. Error bars represent standard error of the mean among three electrodes.

Analytical Methods

View Article Online
Communication

probes; however, using CD electrodes for screening and diagnostic applications is not feasible. CD electrodes cost \$90 each, and given the contagious nature of the disease, reusing them presents significant practical challenges. For a truly deployable and scalable approach, the entire sensor must be disposable. With such considerations of cost of production and scaling in mind, we investigated electrodes fabricated with a simple sputtering deposition process on a commercial polystyrene substrate. Before the shrinking process, the adhesion of sputtered gold on polystyrene is too weak and the gold thin film can delaminate. When shrunk, however, the resulting SDW electrodes are extremely robust and retain their original surface area, resulting in enhanced current density and dynamic range.⁴⁵ Because of the advantages in cost and performance, we initiated experiments on SDW gold electrodes (Fig. 3A) with the goal of detecting the S1 protein directly in saliva.

The total accessible electrochemically active surface area (EASA) of SDW electrodes was confirmed to be greater than that of CD electrodes, as calculated by integration of the reduction

peak of gold oxide in sulfuric acid for the respective electrode types (Fig. S1†). The electrodes were of equivalent geometric areas. The wrinkles provide a diffusion-based challenge to surface coverage, as previously described.³² With longer incubation time, however, this limitation was overcome. The outcome was a greater number of moles of aptamers tethered to the surface of SDW electrodes relative to the same geometric area of CD electrodes. The increased aptamer density resulted in greater absolute MB peak heights on SDW electrodes. Fig. 3B demonstrates the MB peak current densities of CD and SDW electrodes are comparable, with the CD electrodes displaying greater variability as measured by the magnitude of the standard deviation between 3 independent electrodes.

To determine whether the introduction of S1 protein to saliva would produce a differentiable signal change relative to untreated saliva, titration curves were built by measuring square wave voltammograms at 10 Hz with SDW electrodes exposed to varying concentrations of S1 protein. The change in signal with increasing concentrations of S1 protein is shown in

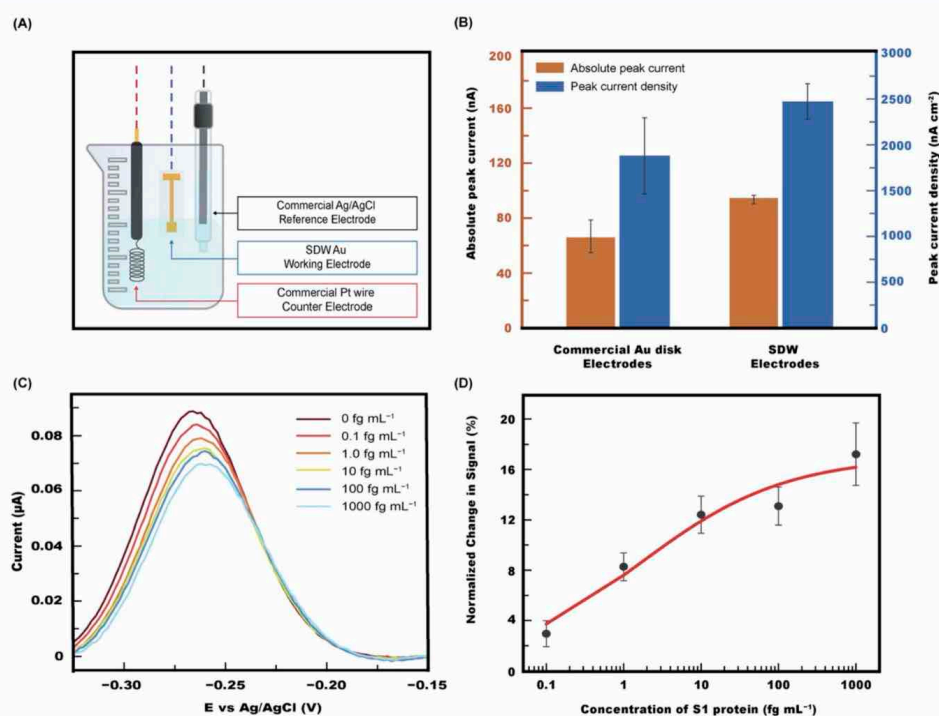


Fig. 3 (A) Beaker cell configuration with SDW electrode. (B) Methylene blue absolute peak current and peak current density comparison between CD and SDW electrodes with equivalent geometric areas. (C) Raw peak height change in current with increasing concentrations of S1 protein in 10% saliva on SDW electrodes. (D) Normalized change in signal produced from sequential incubations of saliva spiked with increasing concentrations of S1 protein minus signal from sequentially incubated blank saliva samples. Hill fit represented in red. Error bars represent standard error of the mean calculated from the propagated standard deviation of the two data sets at each point.

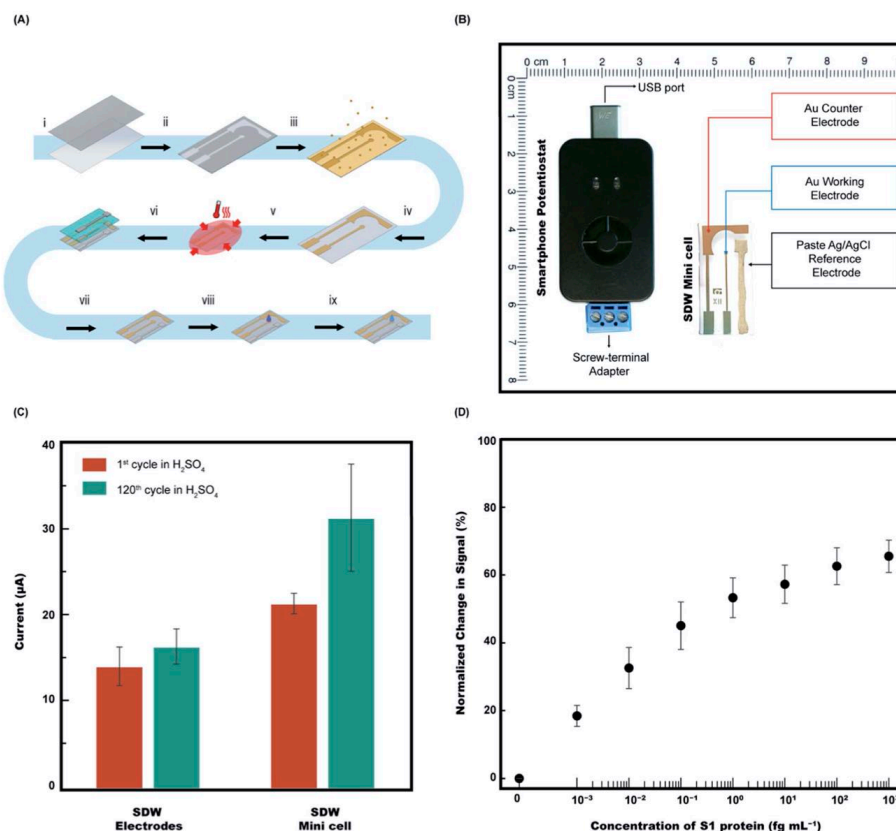


Fig. 4 (A) Process workflow for fabrication of mini cells beginning with (i) laminating adhesive masking film onto pre-stressed polystyrene, followed by (ii) laser cutting working and counter electrode designs, (iii) sputtering 60 nm Au, (iv) peeling away film, (v) shrinking at $130\text{ }^\circ\text{C}$, (vi) applying PDMS mask and Ag/AgCl ink comprising the reference electrode, (vii) curing the Ag/AgCl ink, and functionalizing the working electrode surface with (viii) aptamers and (ix) MCH. (B) Sensit Smart (PalmSens) potentiostat next to a SDW mini cell with scale provided in centimeters. Electrode arrangement (left to right): counter (60 nm Au), working (60 nm Au) and reference (Ag/AgCl ink). (C) Comparison of change in peak height of the gold reduction peak during cycling in sulfuric acid between individual SDW electrodes and SDW mini cells. Peak height and area under the peak stabilized by 120 cycles at 1000 mV s^{-1} . (D) Titration curve of S1 protein performed at 10 Hz in 10% saliva. The zero point represents the first incubation of 10% saliva with no S1 protein and all subsequent signal changes with sequential S1 additions were normalized to the zero point. Error bars represent standard error of the mean among five SDW mini cells.

Fig. 3C. A slight shift in the reduction voltage of MB was observed and attributed to binding-induced changes in the local pH at the surface of the electrode. The titration curve displayed in Fig. 3D was derived from two electrode sets. One set was incubated in saliva, and the second in saliva spiked with S1 protein. Both sets were incubated in saliva for the same total amount of time. The two separate datasets can be found in Fig. S2.†

As evidenced from Fig. 3D, SDW electrodes showed a smaller overall signal change than CD electrodes; we attribute this to

the SDW electrode measurements being performed in saliva, as opposed to buffer solution as in Fig. 2. A loss of signal gain in measurements collected from human media compared to buffer solution has been documented previously.⁴⁶

To improve the portability of our sensor, we next fabricated an entire miniaturized electrochemical cell, abbreviated as "mini cell", using the same shrinking process used for individual SDW electrodes (Fig. 4A). The SDW mini cells' working and counter electrodes were created by sputtering gold onto the pre-stressed polymer a reference electrode on the shrunk

Analytical Methods

substrate; thus, all three electrodes were located on one substrate, allowing electrochemical measurements within a 250 μL droplet instead of the 20 mL used in the beaker cell. The performance of the SDW mini cell was evaluated by characterizing the gold oxidation and reduction in sulfuric acid. Compared to measurements collected using the commercial reference and counter electrodes, the SDW mini cell demonstrated similar performance, with slightly increased peak-to-peak separation (ΔE_p) between oxidation and reduction peaks (Fig. S3†). The SDW mini cell was connected to a PalmSens USB drive-sized potentiostat (Fig. 4B) with alligator clips to demonstrate collection of measurements in any location (non-lab environment).

We observed that during the cleaning protocol performed in sulfuric acid, the area under the peak and peak height of the SDW mini cell increased more than that of individual SDW electrodes (Fig. 4C). We hypothesize that because the SDW mini cell contains an additional source of gold (the counter electrode), there may be a greater rate of gold deposition onto the working electrode occurring during the sulfuric acid cycling, leading to a greater final EASA in the SDW mini cell. The peak height stabilized by the 120th cycle, after which the functionalization of the working electrode on the mini cell proceeded in the same way as for SDW electrodes. We next evaluated the SDW mini cell for detection of the S1 protein in saliva.

The signal gain of more than 60% at the highest concentration of spike protein was greater in the SDW mini cells than in the individual SDW electrodes, in which the maximum change was approximately 16% (Fig. 4D). Because the aptamer functionalization protocol (incubation time, aptamer and MCH concentrations) was the same for both individual SDW electrodes and SDW mini cells, the larger surface area of the SDW mini cell working electrode resulted in a lower probe density. This was also reflected in the differences in peak current densities of MB between individual SDW electrodes and SDW mini cells. Previous studies have shown that a lesser probe density can contribute to greater sensitivity to signal change, which was found to be the case in this study.^{37,48} We therefore demonstrate the detection of the S1 protein with greater signal change in the SDW mini cells than individual SDW electrodes. From these results, we believe the SDW mini cell to be a promising option for further investigation of portable individual tests.

The SDW mini cell demonstrated detection of as little as 1 ag mL^{-1} S1 protein in 10% saliva, with the full comparison to system noise described in the SI. This is thus far, to the best of our knowledge, the lowest limit of quantification reported for the detection of the SARS-CoV-2 antigen using an E-AB sensor. Additionally, our low-complexity process does not involve the use of costly materials and does not rely on enzymatic reactions or biotinylation, which is known to cause interference with clinical samples.

Conclusions

Although biosensors have largely utilized antibodies to recognize target molecules or pathogens in the previous decades, an

equally specific alternative has recently emerged. Aptamers that selectively bind to specific targets have extensively been demonstrated to be promising as a diagnostic tool for disease detection through molecular recognition, and have been prominently investigated.^{19,46,49–55} In this study, an aptamer specific to the RBD region of the SARS-CoV-2 spike protein was selected as the probe for the detection of the SARS-CoV-2 in saliva.

The SDW electrodes used in this study demonstrated sensitive detection of the S1 protein at 1 ag mL^{-1} in pooled saliva diluted to 10%. The facile fabrication process and the sensitivity to low concentrations of S1 protein indicate a promising opportunity to increase the accessibility of SARS-CoV-2 screening and widespread testing of asymptomatic people. The biosensor still needs to be validated to detect the whole virus but given the location of the S1 protein at the outermost layer of the virus, we expect that this should not be an issue.³⁷

In future studies, the varying performance at different frequencies as well as different probe densities should be investigated to better understand aptamer behaviour on the molecular level. Additionally, we expect using aptamers specifically designed for binding-induced conformational changes would produce even more sensitive results than with the aptamer used in this study, which has no confirmed conformational change upon binding with the S1 protein. Importantly, this SDW platform allows for ease in substituting different aptamers, enabling detection of a wide range of analytes for future epidemics.

Materials and methods

Chemicals

DNA aptamers were chosen according to prior literature.³¹ The oligonucleotide modified with methylene blue at the 5' end and a thiol group at the 3' end was purchased from Integrated DNA Technologies, Inc with the following sequence: /5MeBIN/CA GCA CCG ACC TTG TGC TTT GGG AGT GCT GGT CCA AGG GCG TTA ATG GAC A/3ThioMC3-D/.

Aptamer reducing buffer was purchased from Base Pair Biotechnologies. Aptamers were diluted in phosphate buffer solution. The S1 protein was purchased from GenScript (Cat. no. Z03501). 6-Mercaptohexanol (MCH), monobasic potassium phosphate (KH_2PO_4) and dibasic potassium phosphate (K_2HPO_4) were purchased from Sigma Aldrich. Pooled saliva was purchased from CellSciences.

Phosphate buffer solution was prepared with KH_2PO_4 and K_2HPO_4 at 0.1 M. Sulfuric acid (H_2SO_4 – Sigma Aldrich) was prepared in water at 0.5 M. In experiments involving saliva, the saliva was diluted to a final concentration of 10% in phosphate buffer.

SDW electrode fabrication

The electrode design was created by applying an adhesive polymer (Grafix Frisket Film, Grafix Arts, OH) shadow mask stencil to the polystyrene (Grafix Shrink Film KSF50-C, Grafix Arts, OH) prior to sputtering. A Q150R Plus – Rotary Pumped

Coater was used to sputter 60 nm of gold onto the pre-stressed polystyrene to create the working electrode. The substrate was de-masked and placed into a conventional oven at 130 °C for 13 minutes until fully shrunk. Following this step, the electrode was treated with oxygen plasma for 3 minutes to achieve temporary hydrophilicity to ensure full surface wettability during the following cleaning step.

SDW mini cell fabrication

The SDW mini cells' working electrode and counter electrodes were created by applying an adhesive mask to the polystyrene prior to sputtering. Following the same protocol as for individual SDW electrodes, 60 nm of gold was sputtered onto the pre-stressed polystyrene to create the working and counter electrode. The substrate was then de-masked and placed into a conventional oven at 130 °C for 13 minutes until fully shrunk. Following this step, the reference electrode was painted onto the shrunk polystyrene using commercially available Ag/AgCl ink (Creative Materials). The working and counter electrodes were treated with oxygen plasma for 3 minutes to achieve temporary hydrophilicity, while the Ag/AgCl electrode was covered to prevent oxidation.

Cleaning electrodes

Commercial electrodes were polished using the 0.5 µm-sized alumina particles included in the kit provided with the electrodes prior to cycling in sulfuric acid. The electrodes were then individually immersed in a 0.5 M solution of H₂SO₄ and subjected to 120 cycles at 1000 mV s⁻¹ followed by five cycles at 100 mV s⁻¹ in the potential window of 0–1.5 V.

Individual SDW electrodes were similarly immersed in a 0.5 M solution of H₂SO₄ and subjected to 120 cycles at 1000 mV s⁻¹ followed by five cycles at 100 mV s⁻¹ in the potential window of 0–1.5 V.

SDW mini cell electrodes were cleaned by drop-casting a 250 µL drop of 0.5 M solution of H₂SO₄ onto the surface, ensuring coverage of all three electrodes' working areas, and subjected to 120 cycles at 1000 mV s⁻¹ followed by five cycles at 100 mV s⁻¹ in the potential window of 0–1.5 V.

The last cycle at 1000 mV s⁻¹ for each electrode type is shown in Fig. S3.†

Aptamer preparation

Aptamers were received in liquid form and diluted to a concentration of 100 µM. For each experiment, a small volume of aptamer solution (100 µM) was combined with a reducing buffer (Basepair Technologies) at a 1 : 2 volume ratio for one hour to reduce the 3' ends of the aptamers. Following the reduction step, the solution was diluted with phosphate buffer solution to a final concentration of 1 µM. 1 µM is an excessive concentration to use, but additional studies must be carried out to determine optimal concentration of probes for incubation. Optimal probe density must also be investigated in order to confirm optimal sensor sensitivity. Probe density affects the magnitude of signal change and is assumed to be a function not only of initial concentration of applied aptamers, but also of

incubation time and temperature.³⁶ In the case of oligonucleotides greater than 24 bases, such as in this investigation, the probe density is greatly affected by incubation time.⁴⁷ From the SDW mini cell experiments, it was evident that a lesser probe density contributed to enhanced signal gain.

Functionalization of electrodes with aptamers

A 30 µL drop of the aptamer solution at 1 µM was applied to each electrode and allowed to incubate 4 and 8 hours, respectively, for CD and SDW electrodes, at room temperature. The aptamer incubation time was optimized for SDW electrodes; from previous investigations, it is clear that the wrinkled morphology presents diffusion limitations for molecular access to the surface.³² Thus, the incubation time of aptamers was increased to ensure adequate surface coverage by the aptamer probes. During this time, the aptamers formed thiol bonds with the gold surface. The presence of the characteristic MB peak at -0.28 V confirmed the attachment of the aptamer to the gold surface. The peak height collected from each type of electrode (CD, SDW individual and mini cell) was normalized to their respective EASA for comparison of current density. The current density was assumed to correlate with the density of MB and the aptamer probes to which it is attached on the electrode surface. The results of a two-sample *t*-test show a rejection of the null hypothesis at the 5% significance level that the current densities of CD electrodes and individual SDW electrodes have an equal mean, indicating that the individual SDW electrodes may have a greater probe density. We believe this may be attributed to the longer incubation time chosen for SDW electrodes to compensate for diffusion limitations posed by wrinkles. In contrast, due to the greater EASA of the SDW mini cell working electrodes, the probe density was found to be lesser than that of individual SDW electrodes.

Blocking of electrodes with MCH

Blocking the electrode surface avoids nonspecific binding with interfering species in real samples, enhances the stability of aptamers, and passivates any remaining EASA. A six-carbon blocking molecule, MCH, was chosen as the blocking agent because it has been shown to create more stable monolayers than a 2- or 3-carbon molecule, although at the expense of greater conductivity of the SAM achieved using shorter chains.⁴⁷ After the incubation with the aptamers, the electrodes were rinsed and incubated with 30 µL of 3 mM MCH in phosphate buffer for 18 and 39 hours, respectively, for CD and SDW electrodes (both individual and mini cell), at 4 °C.

Titration curve of S1 protein on CD electrodes

After functionalization and blocking, the commercial gold electrodes were measured in 20 mL of phosphate buffer with a Gamry Reference 600 potentiostat with a commercial Ag/AgCl reference electrode (Gamry) and a platinum coil (BASi) as the counter electrode. Following the collection of a baseline measurement, the electrodes were incubated for one hour with increasing concentrations of S1 protein in phosphate buffer solution.

View Article Online

Communication

Analytical Methods

Titration curve of S1 protein on SDW gold electrodes

Six SDW gold electrodes were incubated with aptamers and blocked with MCH, as described above. All six electrodes' MB peak heights were measured after every functionalization step in phosphate buffer solution with the same setup for commercial electrodes. Three of the electrodes were incubated for one hour with 10% pooled saliva in phosphate buffer then rinsed carefully with phosphate buffer solution. The three remaining electrodes were incubated for one hour with 10% pooled saliva containing 0.1 fg mL^{-1} S1 protein. The MB signal from all six electrodes was measured again in phosphate buffer solution. Subsequent incubation steps were performed in the same way, with all electrodes incubated with either un-spiked saliva or saliva containing increasing concentrations of S1 protein with every incubation. All electrodes were rinsed before all measurements. Measurements were collected after establishing signal stability across 10 consecutive measurements in phosphate buffer solution at 10 Hz (Fig. S4[†]) to ensure signal stability was within 5% normalized change. The same protocol was performed after saliva addition to ensure no signal drift prior to performing subsequent S1 protein titrations (Fig. S5[†]).

Titration curve of S1 protein on SDW mini cells

The working electrodes of the SDW mini cells were incubated with 10% saliva for 1 hour containing no S1 protein to constitute the zero point of the titration curve. The SDW mini cells were then incubated with 10% saliva containing the following concentrations of S1: 0.001, 0.01, 0.1, 1.0, 10, 100, and 1000 fg mL^{-1} . The SDW mini cell was rinsed following each incubation period at 1 hour, and a 250 μL drop-cast of phosphate buffered solution was applied to cover all three electrodes to collect measurements from the PalmSens Sensit Smart.

Electrochemical measurements

Gamry Reference 600 potentiostat. Conventional potentiostat settings were measured in a phosphate buffer solution with a potential window starting from -0.7 to -0.35 V. Frequencies measured at: 5, 10, 25, 50, 75, 100, 150, 200 and 250 Hz. The amplitude was set to 25 mV with a step size of 2 mV.

PalmSens Sensit Smart. All mini cell measurements were measured in a phosphate buffer (pH 7.4) solution with a potential window starting from -0.7 to -0.35 V. Frequencies measured at: 5, 10, 25, 50, 75, 100, 150, 200 and 250 Hz. The amplitude was set to 25 mV with a step size of 2 mV.

Author contributions

Julia Alice Zakashansky conceptualized the assay and designed the experiments with Amanda Hikari Imamura and Dr Michelle Khine. Julia ran the experiments, analyzed the data, and wrote the manuscript. Amanda Hikari Imamura contributed to interpretation of results, visualization of results, manuscript drafting, and critical commentary. Darwin Franklin Salgado III identified aptamers and assisted in mini cell fabrication and titration curve experiments. Heather Carmen Romero Mercieca contributed to data visualization scripts, peak analysis scripts,

and formulation of figures. Raphael Francis Laxamana Aguas created scripts for peak analyses and data visualization. Angele Marie Lao assisted in signal stability characterization and mini cell titration curve experiments. Joseph Pariser developed a Python script for baseline correction visualization for formulation of figures. Netzahualcōyotl Arroyo-Currás made critical written contributions and advised on data interpretation. Michelle Khine was the principal investigator of the study and as such oversaw the students, experiments, analysis of data, and editing of manuscript.

Conflicts of interest

There are no conflicts to declare.

Acknowledgements

We would like to thank Hui Li for graciously providing guidance on signal stability. We thank Xinlei Chen for providing much appreciated assistance during the final titration experiments. We thank Julien Goavec for the initiation of mini cell experimentation. HCRM gratefully acknowledges the support provided by the National Institute of Health through the NIH-MARC U-STAR training grant T34GM136498. AHI acknowledges the financial support from grant #2017/05362-9, São Paulo Research Foundation (FAPESP).

References

- 1 D. Cucinotta and M. Vanelli, *Acta Bio Med. Atenei Parmensis*, 2020, **91**, 157–160.
- 2 M. M. Arons, K. M. Hatfield, S. C. Reddy, A. Kimball, A. James, J. R. Jacobs, J. Taylor, K. Spicer, A. C. Bardossy, L. P. Oakley, S. Tanwar, J. W. Dyal, J. Harney, Z. Chisty, J. M. Bell, M. Methner, P. Paul, C. M. Carlson, H. P. McLaughlin, N. Thornburg, S. Tong, A. Tamin, Y. Tao, A. Uehara, J. Harcourt, S. Clark, C. Brostrom-Smith, L. C. Page, M. Kay, J. Lewis, P. Montgomery, N. D. Stone, T. A. Clark, M. A. Honein, J. S. Duchin and J. A. Jernigan, *N. Engl. J. Med.*, 2020, **382**, 2081–2090.
- 3 S. Hoehl, H. Rabenau, A. Berger, M. Kortenbusch, J. Cinatl, D. Bojkova, P. Behrens, B. Böttchinghaus, U. Götsch, F. Naujoks, P. Neumann, J. Schork, P. Tiarks-Jungk, A. Walczok, M. Eickmann, M. J. G. T. Vehreschild, G. Kann, T. Wolf, R. Gottschalk and S. Ciesek, *N. Engl. J. Med.*, 2020, **382**, 1278–1280.
- 4 Y. Bai, L. Yao, T. Wei, F. Tian, D.-Y. Jin, L. Chen and M. Wang, *JAMA, J. Am. Med. Assoc.*, 2020, **323**, 1406–1407.
- 5 R. Weissleder, H. Lee, J. Ko and M. J. Pittet, *Sci. Transl. Med.*, 2020, **12**(546), eabc1931.
- 6 *Coronavirus (COVID-19) Testing – Statistics and Research*, <https://ourworldindata.org/coronavirus-testing>, accessed June 11, 2020.
- 7 *Daily Testing Trends in the US – Johns Hopkins*, <https://coronavirus.jhu.edu/testing/individual-states>, accessed October 24, 2020.

- 8 A. L. Wyllie, J. Fournier, A. Casanovas-Massana, M. Campbell, M. Tokuyama, P. Vijayakumar, J. L. Warren, B. Geng, M. C. Muenker, A. J. Moore, C. B. F. Vogels, M. E. Petrone, I. M. Ott, P. Lu, A. Venkataraman, A. Luculligan, J. Klein, R. Earnest, M. Simonov, R. Datta, R. Handoko, N. Naushad, L. R. Sewanan, J. Valdez, E. B. White, S. Lapidus, C. C. Kalinich, X. Jiang, D. J. Kim, E. Kudo, M. Linehan, T. Mao, M. Moriyama, J. E. Oh, A. Park, J. Silva, E. Song, T. Takahashi, M. Taura, O.-E. Weizman, P. Wong, Y. Yang, S. Bermejo, C. D. Odio, S. B. Omer, C. S. Dela Cruz, S. Farhadian, R. A. Martinello, A. Iwasaki, N. D. Grubaugh and A. I. Ko, *N. Engl. J. Med.*, 2020, **383**, 1283–1286.
- 9 CDC, *Coronavirus Disease 2019 (COVID-19)*, <https://www.cdc.gov/coronavirus/2019-ncov/testing/serology-overview.html>, accessed October 25, 2020.
- 10 D. Buitrago-Garcia, D. Egli-Gany, M. J. Counotte, S. Hossmann, H. Imeri, A. M. Ipekci, G. Salanti and N. Low, *PLoS Med.*, 2020, **17**, e1003346.
- 11 R. Xu, B. Cui, X. Duan, P. Zhang, X. Zhou and Q. Yuan, *Int. J. Oral Sci.*, 2020, **12**, 1–6.
- 12 K. K.-W. To, O. T.-Y. Tsang, W.-S. Leung, A. R. Tam, T.-C. Wu, D. C. Lung, C. C.-Y. Yip, J.-P. Cai, J. M.-C. Chan, T. S.-H. Chik, D. P.-L. Lau, C. Y.-C. Choi, L.-L. Chen, W.-M. Chan, K.-H. Chan, J. D. Ip, A. C.-K. Ng, R. W.-S. Poon, C.-T. Luo, V. C.-C. Cheng, J. F.-W. Chan, I. F.-N. Hung, Z. Chen, H. Chen and K.-Y. Yuen, *Lancet Infect. Dis.*, 2020, **20**(5), 565–574.
- 13 Y. Pan, D. Zhang, P. Yang, L. L. M. Poon and Q. Wang, *Lancet Infect. Dis.*, 2020, **20**, 411–412.
- 14 C. Lucia, P.-B. Federico and G. C. Alejandra, *An ultrasensitive, rapid, and portable coronavirus SARS-CoV-2 sequence detection method based on CRISPR-Cas12*, *Molecular Biology*, 2020.
- 15 W.-K. Wang, S.-Y. Chen, I.-J. Liu, Y.-C. Chen, H.-L. Chen, C.-F. Yang, P.-J. Chen, S.-H. Yeh, C.-L. Kao, L.-M. Huang, P.-R. Hsueh, J.-T. Wang, W.-H. Sheng, C.-T. Fang, C.-C. Hung, S.-M. Hsieh, C.-P. Su, W.-C. Chiang, J.-Y. Yang, J.-H. Lin, S.-C. Hsieh, H.-P. Hu, Y.-P. Chiang, J.-T. Wang, P.-C. Yang and S.-C. Chang, *Emerging Infect. Dis.*, 2004, **10**, 1213–1219.
- 16 K. K.-W. To, O. T.-Y. Tsang, C. C.-Y. Yip, K.-H. Chan, T.-C. Wu, J. M.-C. Chan, W.-S. Leung, T. S.-H. Chik, C. Y.-C. Choi, D. H. Kandamby, D. C. Lung, A. R. Tam, R. W.-S. Poon, A. Y.-F. Fung, I. F.-N. Hung, V. C.-C. Cheng, J. F.-W. Chan and K.-Y. Yuen, *Clin. Infect. Dis.*, 2020, **71**(15), 841–843.
- 17 S. D. Jayasena, *Clin. Chem.*, 1999, **45**, 1628–1650.
- 18 A. M. Downs, J. Gerson, K. L. Ploense, K. W. Plaxco and P. Dauphin-Ducharme, *Anal. Chem.*, 2020, **92**, 14063–14068.
- 19 X. Zou, J. Wu, J. Gu, L. Shen and L. Mao, *Front. Microbiol.*, 2019, **10**, 1462.
- 20 M. A. Pellitero, A. Shaver and N. Arroyo-Currás, *J. Electrochem. Soc.*, 2020, **167**, 037529.
- 21 S. O. Kelley, *ACS Sens.*, 2017, **2**, 193–197.
- 22 I. F. N. Hung, V. C. C. Cheng, A. K. L. Wu, B. S. F. Tang, K. H. Chan, C. M. Chu, M. M. L. Wong, W. T. Hui, L. L. M. Poon, D. M. W. Tse, K. S. Chan, P. C. Y. Woo, S. K. P. Lau, J. S. M. Peiris and K. Y. Yuen, *Emerging Infect. Dis.*, 2004, **10**, 1550–1557.
- 23 D.-G. Ahn, I.-J. Jeon, J. D. Kim, M.-S. Song, S.-R. Han, S.-W. Lee, H. Jung and J.-W. Oh, *Analyst*, 2009, **134**, 1896–1901.
- 24 P. Moitra, M. Alafeef, K. Dighe, M. B. Frieman and D. Pan, *ACS Nano*, 2020, **14**, 7617–7627.
- 25 G. Seo, G. Lee, M. J. Kim, S.-H. Baek, M. Choi, K. B. Ku, C.-S. Lee, S. Jun, D. Park, H. G. Kim, S.-J. Kim, J.-O. Lee, B. T. Kim, E. C. Park and S. I. Kim, *ACS Nano*, 2020, **14**, 5135–5142.
- 26 S. Eissa and M. Zourob, *Anal. Chem.*, 2021, **93**(3), 1826–1833.
- 27 M. Alafeef, K. Dighe, P. Moitra and D. Pan, *ACS Nano*, 2020, **14**(12), 17028–17045.
- 28 B. W. Neuman, B. D. Adair, C. Yoshioka, J. D. Quispe, G. Orca, P. Kuhn, R. A. Milligan, M. Yeager and M. J. Buchmeier, *J. Virol.*, 2006, **80**, 7918–7928.
- 29 Y. Huang, C. Yang, X. Xu, W. Xu and S. Liu, *Acta Pharmacol. Sin.*, 2020, **41**, 1141–1149.
- 30 Z. Ke, J. Oton, K. Qu, M. Cortese, V. Zila, L. McKeane, T. Nakane, J. Zivanov, C. J. Neufeldt, B. Cerikan, J. M. Lu, J. Peukes, X. Xiong, H.-G. Kräusslich, S. H. W. Scheres, R. Bartenschlager and J. A. G. Briggs, *Nature*, 2020, 1–5.
- 31 Y. Song, J. Song, X. Wei, M. Huang, M. Sun, L. Zhu, B. Lin, H. Shen, Z. Zhu and C. Yang, *Anal. Chem.*, 2020, **92**(14), 9895–9900.
- 32 A. Imamura, J. Zakashansky, K. Cho, L. Lin, E. Carrilho and M. Khine, *Adv. Mater. Technol.*, 2020, **5**, 1900843.
- 33 A. Hauke, L. S. S. Kumar, M. Y. Kim, J. Pegan, M. Khine, H. Li, K. W. Plaxco and J. Heikenfeld, *Biosens. Bioelectron.*, 2017, **94**, 438–442.
- 34 C.-S. Chen, D. N. Breslauer, J. I. Luna, A. Grimes, W. Chin, L. P. Lee and M. Khine, *Lab Chip*, 2008, **8**, 622–624.
- 35 S. Lin, E. K. Lee, N. Nguyen and M. Khine, *Lab Chip*, 2014, **14**, 3475–3488.
- 36 J. D. Pegan, A. Y. Ho, M. Bachman and M. Khine, *Lab Chip*, 2013, **13**, 4205–4209.
- 37 S. Saem, O. Shahid, A. Khondker, C. Moran-Hidalgo, M. C. Rheinstädter and J. Moran-Mirabal, *Sci. Rep.*, 2020, **10**, 4595.
- 38 Y. Chan, M. Skreta, H. McPhee, S. Saha, R. Deus and L. Soleymani, *Analyst*, 2018, **144**, 172–179.
- 39 G. Seo, M. J. Kim, S. H. Baek, M. Choi, K. B. Ku, C. S. Lee, S. Jun, D. Park, H. G. Kim, S. J. Kim, J. O. Lee, B. T. Kim, E. C. Park and S. I. Kim, *ACS Nano*, 2020, **14**(4), 5135–5142.
- 40 S. M. Woo, C. M. Gabardo and L. Soleymani, *Anal. Chem.*, 2014, **86**, 12341–12347.
- 41 D. Kang, C. Parolo, S. Sun, N. E. Ogden, F. W. Dahlquist and K. W. Plaxco, *ACS Sens.*, 2018, **3**, 1271–1275.
- 42 E. Farjami, R. Campos and E. E. Ferapontova, *Langmuir*, 2016, **32**, 928.
- 43 E. Farjami, L. Clima, K. V. Gothelf and E. E. Ferapontova, *Analyst*, 2010, **135**, 1443–1448.
- 44 R. J. White and K. W. Plaxco, *Anal. Chem.*, 2010, **82**, 73–76.
- 45 C.-C. Fu, A. Grimes, M. Long, C. G. L. Ferri, B. D. Rich, S. Ghosh, S. Ghosh, L. P. Lee, A. Gopinathan and M. Khine, *Adv. Mater.*, 2009, **21**, 4472–4476.

Analytical Methods

[View Article Online](#)
Communication

- 46 N. Arroyo-Currás, P. Dauphin-Ducharme, K. Scida and J. L. Chávez, *Anal. Methods*, 2020, **12**, 1288–1310.
- 47 R. J. White, N. Phares, A. A. Lubin, Y. Xiao and K. W. Plaxco, *Langmuir*, 2008, **24**, 10513–10518.
- 48 Y. Xiao, R. Y. Lai and K. W. Plaxco, *Nat. Protoc.*, 2007, **2**, 2875–2880.
- 49 B. Kang, S. V. Park, H. T. Soh and S. S. Oh, *ACS Sens.*, 2019, **4**, 2802–2808.
- 50 Y. Wu, B. Midinov and R. J. White, *ACS Sens.*, 2019, **4**, 498–503.
- 51 D. Ruiz Ciancio, M. R. Vargas, W. H. Thiel, M. A. Bruno, P. H. Giangrande and M. B. Mestre, *Pharmaceuticals*, 2018, **11**(3), 86.
- 52 K. Ikebukuro, C. Kiyohara and K. Sode, *Anal. Lett.*, 2004, **37**, 2901–2909.
- 53 M. Ilgu, R. Fazlioglu, M. Ozturk, Y. Ozsurekci and M. Nilsen-Hamilton, *Recent Adv. Anal. Chem.*, 2019.
- 54 D. N. Mazaafrianto, M. Maeki, A. Ishida, H. Tani and M. Tokeshi, *Micromachines*, 2018, **9**(5), 202.
- 55 W. Zhou, P.-J. J. Huang, J. Ding and J. Liu, *Analyst*, 2014, **139**, 2627–2640.
- 56 F. Ricci, R. Y. Lai, A. J. Heeger, K. W. Plaxco and J. J. Sumner, *Langmuir*, 2007, **23**, 6827–6834.

ANNEX 4

Electrochemical immunosensors using electrodeposited gold nanostructures for detecting the S proteins from SARS-CoV and SARS-CoV-2



Electrochemical immunosensors using electrodeposited gold nanostructures for detecting the S proteins from SARS-CoV and SARS-CoV-2

Lais Canniatti Brazaca^{1,2} · Amanda Hikari Imamura^{1,2} · Nathalia Oezau Gomes¹ · Mariana Bortholazzi Almeida^{1,2} · Desirée Tamara Scheidt^{1,2} · Paulo A. Raymundo-Pereira³ · Osvaldo N. Oliveira Jr³ · Bruno Campos Janegitz⁴ · Sergio Antonio Spinola Machado¹ · Emanuel Carrilho^{1,2}

Received: 21 December 2021 / Revised: 29 January 2022 / Accepted: 1 February 2022
© Springer-Verlag GmbH Germany, part of Springer Nature 2022

Abstract

This paper reports the development of a low-cost (< US\$ 0.03 per device) immunosensor based on gold-modified screen-printed carbon electrodes (SPCEs). As a proof of concept, the immunosensor was tested for a fast and sensitive determination of S proteins from both SARS-CoV and SARS-CoV-2, by a single disposable device. Gold nanoparticles were electrochemically deposited via direct reduction of gold ions on the electrode using amperometry. Capture antibodies from spike (S) protein were covalently immobilized on carboxylic groups of self-assembled monolayers (SAM) of mercaptoacetic acid (MAA) attached to the gold nanoparticles. Label-free detection of S proteins from both SARS-CoV and SARS-CoV-2 was performed with electrochemical impedance spectroscopy (EIS). The immunosensor fabricated with 9 s gold deposition had a high performance in terms of selectivity, sensitivity, and low limit of detection (LOD) (3.16 pmol L^{-1}), thus permitting the direct determination of the target proteins in spiked saliva samples. The complete analysis can be carried out within 35 min using a simple one-step assay protocol with small sample volumes (10 μL). With such features, the immunoplatform presented here can be deployed for mass testing in point-of-care settings.

Keywords SARS-CoV · SARS-CoV-2 · S protein · Diagnosis · Immunosensor · Gold nanoparticles

Introduction

The crisis with COVID-19 has highlighted the need for analytical devices to monitor and detect high-incident diseases caused by viruses and other pathogens with rapid propagation and mutations. Low-cost, portable analytical sensors [1–3] are perhaps the only alternative for the diagnosis of such infections as the one caused by the coronavirus (SARS-CoV-2) [4, 5]. Indeed, the lack of such sensors explains why developing countries could not test their population to the extent recommended by the World Health Organization, which would have been essential for the monitoring to prevent the person-to-person transmission chain [6, 7]. Mass testing has been almost entirely based on molecular techniques, especially real-time polymerase chain reaction (RT-PCR), which is not amenable to use outside specialized laboratories. At the research level, various methods have been used to diagnose SARS-CoV-2 infection via the detection of S or N proteins in different biological matrices [8–10]. A summary of the sensors developed in recent

SP 13600-970, Brazil

ão Carlos, Araras,

Published online: 15 February 2022

Springer

months is presented in the Supplementary Material (Section S1 and Table S2). Of particular relevance to our work are the electrochemical immunoassays. For example, carbon black-based screen-printed electrodes (SPE) and magnetic beads (MBs) were used to immobilize antibodies and detect S and N proteins with limits of detection (LOD) of 19 ng mL^{-1} and 8 ng mL^{-1} , respectively [8]. A working electrode (WE) coated with graphene oxide (GO) was modified with 8-hydroxyquinoline (8H), 1-ethyl-3-(3-dimethylamino-propyl)carbodiimide (EDC), and N-hydroxysuccinimide (NHS) coupled with gold nanostars (AuNS), generating an ultrasensitive sensor that could detect the trace of viruses in aquatic biological media [6].

Electrochemical sensors with a set of electrodes, viz. working (WE), reference (RE), and counter (CE) electrodes, allow for multi-target detection, simple arrays, portability, and fast responses, being ideal for applications in situ [2, 11, 12]. Analytes can be detected and quantified through redox reactions when binding occurs between the target and the biorecognition element [13], and, therefore, the sensing performance depends strongly on the WE material [14, 15]. SPEs are suitable for mass production and miniaturization at low prices, being advantageous compared with typical solid electrodes [16–18]. They may be produced on almost any type of substrate, either rigid or flexible, and on stretchable surfaces, using different materials [19], including paper [20], ceramic [21], and polymers [22]. When used in conjunction with nanomaterials, SPEs may lead to highly sensitive electrochemical sensors [2, 23]. In this context, electrodeposited gold on SPEs enhances electrochemical activity [24] owing to a facilitated electron transfer and catalytic activity for oxidation and reduction reactions [2, 23, 25, 26]. Gold deposition as a film ensures high conductivity and large surface-area-to-volume ratios, and enables modification with biomolecules. The properties of the gold layer may be tuned by varying the deposition potential (E_d) and deposition time (t_d), thus permitting the optimization of sensing performance [24, 27, 28].

In this study, we developed an immunosensor based on gold-carbon composite material, which detected the S proteins of SARS-CoV and SARS-CoV-2 as a proof of concept. To the best of our knowledge, this is the first time a single biosensor is used to detect both pathogens.

Materials and methods

Chemicals

Hydrogen tetrachloroaurate (III), mercaptoacetic acid (MAA), EDC, NHS, bovine serum albumin (BSA), potassium hexacyanoferrate (II) trihydrate, potassium

hexacyanoferrate (III), fluorescein 5(6)-isothiocyanate (FITC), and sulfuric acid (H_2SO_4) were purchased from Sigma-Aldrich (USA). Carbon paste ink (ELETRODAG 423SS E&C) was obtained from LOCTITE® (Germany), and Ag/AgCl ink (90,701) was acquired from TICON (Brazil). Anti-SARS-CoV S protein antibodies (40,150-D006) and SARS-CoV S protein (40,150-V08B2) were purchased from Sino Biological (China), while SARS-CoV-2 glycoprotein S1 (ab273068) was obtained from Abcam (EUA). Polyethylene terephthalate (PET) sheets for electrode fabrication were obtained from local stationery shops and cleaned with isopropyl alcohol before use.

Fabrication of screen-printed electrodes

The screen-printing technique was used to produce carbon electrodes (Fig. 1a). First, a customized polyester screen (77 mesh) (Silk Center, Brazil) was designed using AutoCAD software and produced by Iasa Segmentos Industriais (Brazil). The carbon paste ink was then manually printed on a PET sheet with a polyurethane squeegee. The printed devices containing the three electrodes were then cured at $90 \text{ }^\circ\text{C}$ for 30 min. The reference electrodes were manually painted with Ag/AgCl ink and dried at $90 \text{ }^\circ\text{C}$ for 45 min. An insulator adhesive tape was used to delimit the geometric area of the working electrode at 12.56 mm^2 .

Electrodeposition of gold

All electrodes received an electrochemical pretreatment with sulfuric acid (0.5 mol L^{-1}) within a potential range between -2.5 and $+2.5 \text{ V}$ at a scan rate of 100 mV s^{-1} [29]. Two voltammetry cycles were performed, and the sulfuric acid was completely replaced after each cycle. Gold nanoparticles were electrogenerated on screen-printed electrodes by applying a constant potential of -4.0 V in an electrochemical cell containing $20 \text{ mL } 5.0 \text{ mmol L}^{-1}$ hydrogen tetrachloroaurate (III) solution with 0.5 mol L^{-1} sulfuric acid under vigorous stirring for 9 s (or 30 s or 90 s) (Fig. 1b) [30].

Optical characterization of the modified electrodes

Images of the gold nanostructures were obtained with a scanning electron microscope (SEM) (ZEISS, LE0 440, model 7060) equipped with an OXFORD® system detector. A Thermo Scientific Prisma E Scanning Electron Microscope (SEM) with ColorSEM Technology and integrated energy-dispersive X-ray spectroscopy (EDS) was used to assess the chemical composition of the modified electrodes. The antigen–antibody interaction was studied using a confocal fluorescence microscope Zeiss LSM 780 with an argon laser. SARS-CoV

Electrochemical immunosensors using electrodeposited gold nanostructures for detecting...

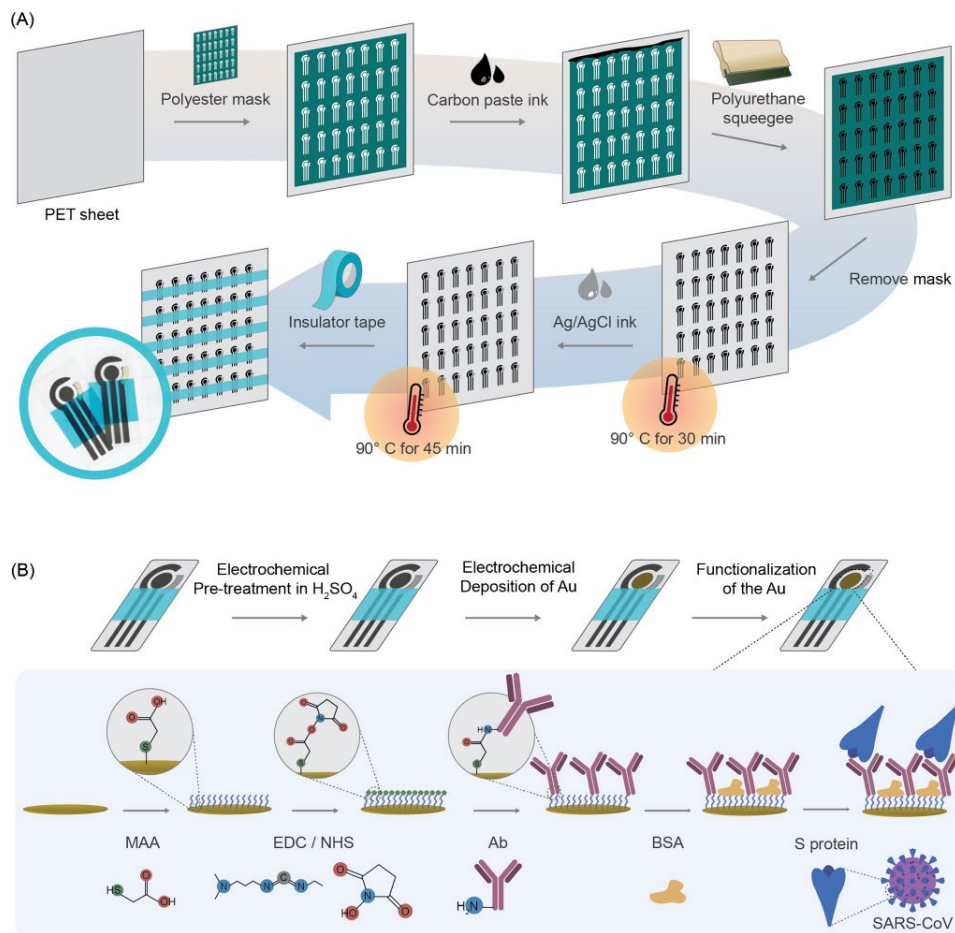


Fig. 1 Step-by-step immunosensor fabrication. **a** Fabrication steps of the screen-printed electrodes. **b** Electrochemical treatments, Au deposition, and modification of working electrodes with antibodies

S protein was labeled with fluorescein isothiocyanate (FITC) by mixing the two molecules in a 1:20 ratio for 1 h at room temperature (25 °C). Dialysis was then used to remove unbound FITC. The fluorescence of the modified electrodes was measured in the absence and presence of labeled S proteins, validating its binding to the biosensor surface.

Electrochemical characterization of the modified electrodes

Modified electrodes using different gold electrodeposition conditions were characterized using cyclic voltammetry (CV). Bare carbon electrodes and devices submitted to 9, 30, and 90 s of gold deposition protocol were evaluated. First, CV was performed in a potassium hexacyanoferrate (II)/(III) solution (4 mmol L⁻¹ each, 0.1 mol L⁻¹ PBS, pH

7.0) (2 cycles, 100 mV s⁻¹, from -0.3 to 0.7 V). The electrodes were also submitted to CV in 0.1 mol L⁻¹ sulfuric acid to assess the amount of gold present on the electrode (2 cycles, 100 mV s⁻¹, from 0.0 to 1.5 V).

Functionalization of the gold surface with antibodies

Modified-gold electrodes were pretreated with cyclic voltammetry (CV) (0.0–1.5 V, 100 mV s⁻¹, 10 cycles) in sulfuric acid (0.1 mol L⁻¹, ultrapure water). Then, 20 µL of an MAA solution (10 mmol L⁻¹, ultrapure water) was incubated on the gold working electrode. After 2 h, electrodes were washed with ultrapure water and dried using a low N₂ stream. Next, 20 µL of a mixture of EDC and NHS (10 mmol L⁻¹ and 20 mmol L⁻¹ respectively) in MES buffer 100 mmol L⁻¹ (pH 6.0) was incubated on the modified electrode for 1 h to promote the antibody attachment on the carboxylic groups [12, 31–34]. The electrodes were then rinsed using MES buffer (100 mmol L⁻¹, pH 6.0) and dried using N₂. Twenty microliters of 1 µg mL⁻¹ anti-protein S antibodies (PBS, 0.1 mol L⁻¹, pH 7.0) was added to the electrode for 1 h. The antibody's concentration applied is within the concentration range reported in the literature for the manufacture of immunosensors used for SARS-CoV-2 detection, which range from 1 ng L⁻¹ to 100 µg L⁻¹ [31, 32, 35–40]. Electrodes were washed using PBS (0.1 mol L⁻¹, pH 7.0) and dried with an N₂ gas stream. Finally, a BSA solution (1% w/v, 30 min, 0.1 mol L⁻¹ PBS, pH 7.0) was incubated on the electrode for 30 min for blocking the bioreceptor layer [33, 35–37]. After washing the modified electrode with PBS (0.1 mol L⁻¹, pH 7.0) and drying it with N₂, the biosensor was ready for use. A similar protocol for building the immunosensor was recently described by Stefano et al. [40]. The samples were added to the working electrode and incubated for 30 min (0.1 mol L⁻¹ PBS, pH 7.0). After this period, electrodes were carefully washed using PBS (0.1 mol L⁻¹, pH 7.0), and electrochemical measurements were performed (Fig. 1b). Unless indicated otherwise, positive samples were composed of SARS-CoV S protein, while negative samples were composed of BSA. To reduce the evaporation of the droplets, all the solutions for incubation were performed in a closed container with wet wipes. All procedures were performed at room temperature (25 °C).

Electrochemical immunosensing

The charge transfer resistance (R_{ct}) of the immunosensors was determined using electrochemical impedance spectroscopy (EIS) in a potassium hexacyanoferrate (II)/(III) solution (4 mmol L⁻¹ each, 0.1 mol L⁻¹ PBS, pH 7.0). First, to activate the double layer of the biosensor, a CV was performed (2 cycles, from -0.3 to 0.7 V, 100 mV s⁻¹). Then,

EIS measurements were performed in open circuit conditions (OCP) (10 kHz to 100 mHz, E_{oc} 10 mV). The reproducibility of the immunosensor was investigated by analyzing the signal of three parallel assemblies after the interaction with 10⁻⁹ mol L⁻¹ protein S. The variability is quantified in terms of relative standard deviation (RSD) in the signals. Repeatability was assessed using RSD of ten successive measurements in a single immunosensor after interaction with 10⁻⁹ mol L⁻¹ S protein. The LOD was estimated as the analyte concentration corresponding to an $R_{ct} = b_m + 3s_b$, where b_m is the mean value for blank samples, and s_b is the standard deviation of the blank measurements ($n = 6$) [41].

Biological samples

Saliva was used as a biological sample to test the practical application of the device. A pooled human saliva was obtained from Innovative Research (IRHUSL5ML) and centrifuged at 8000 rcf for 10 min prior to use. Then, the supernatant was spiked with SARS-CoV S protein to reach concentrations from 10⁻¹¹ to 10⁻⁷ mol L⁻¹ and one sample was prepared with inactivated SARS-CoV-2 viruses at 10⁶ PFU mL⁻¹. For the electrochemical analysis of fortified biological samples, SDS 0.05% (w/v in PBS) was used as the washing solution between incubations.

Results and discussion

Characterization of Au-modified SPCEs

The photographs of Au-modified SPEs in Fig. 2a indicate an increased deposition of Au as the electrodeposition time increases. The chemical composition of the films was confirmed through elemental mapping and EDS measurements in Fig. 2b, Figure S1, and Figure S2. While bare SPE has a carbon-based surface, Au features appear with increasing Au deposition. A homogeneous thin film was noted for bare SPE, coated with Au structures with regular size and morphology. Different Au structures are shown in the SEM images of Fig. 2c–f, with no significant defects for bare SPE and Au-coated SPEs. The bright spots on the images can be attributed to Au, while other features in Fig. 2c are graphite flakes and carbon nanoparticles from SPE ink. According to ImageJ processing, the Au nanoparticles increased with electrodeposition time, reaching diameters 143 ± 31, 425 ± 161, and 752 ± 207 nm ($n = 10$), for 9, 30, and 90 s, respectively. The Au deposition was characterized using cyclic voltammetry in 0.1 mol L⁻¹ sulfuric acid. Figure 2g shows no redox peaks for bare SPE (black), as expected. The CVs for SPE/Au are typical of surfaces containing Au in 0.1 mol L⁻¹ H₂SO₄, with anodic and cathodic peaks at +1.15 V (E_{pa}) and +0.4 V (E_{pc}) due to oxidation (formation) and reduction

Electrochemical immunosensors using electrodeposited gold nanostructures for detecting...

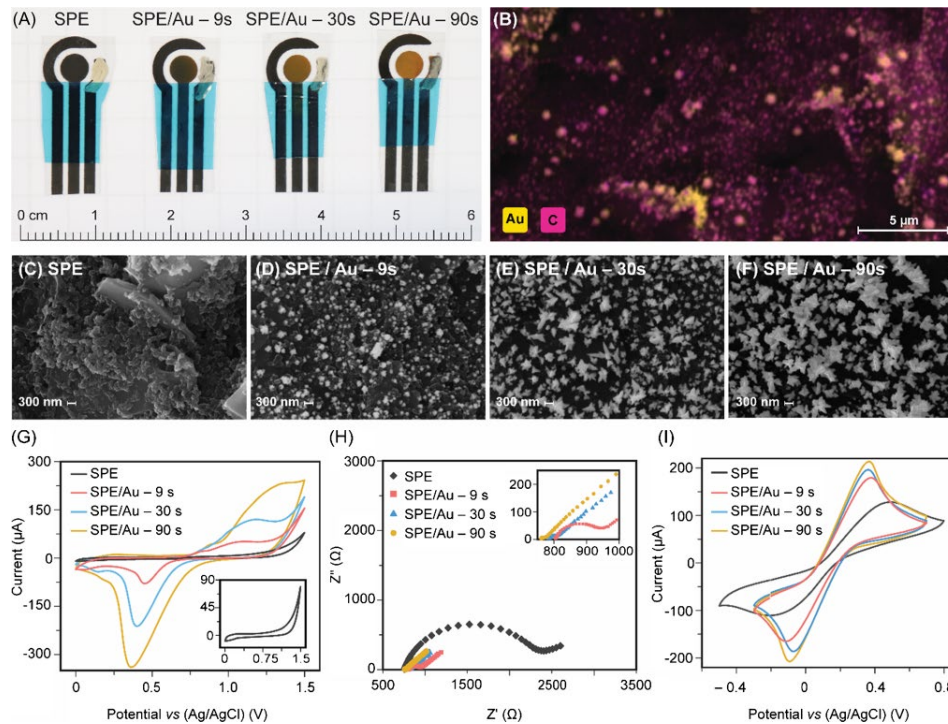


Fig. 2 **a** SPE before and after electrodeposition of gold for 9, 30, and 90 s. **b** Elemental mapping of an SPE after electrodeposition of gold for 9 s. Pink and yellow shades, respectively, represent carbon and gold. **c** Bare SPE. SPE modified with gold nanostructures electrodeposited during **d** 9 s, **e** 30 s, and **f** 90 s. **g** Cyclic voltammograms in 0.1 mol L⁻¹ H₂SO₄ for bare SPE (black), SPE modified with gold nanostructures electrodeposited during 9 s (red), 30 s (blue), and 90 s (yellow) at -4.0 V in a 5.0 mmol L⁻¹ hydrogen tetrachloroaurate (III) solution containing 0.5 mol L⁻¹ sulfuric acid. Scan rate 100 mV s⁻¹.

The insert shows a zoomed view of the CV of SPE. **h** Nyquist plots for bare SPE (black), SPE modified with gold nanostructures electrodeposited during 9 s (red), 30 s (blue), and 90 s (yellow) in 0.1 mol L⁻¹ PBS containing 4.0 mmol L⁻¹ [Fe(CN)₆]⁴⁻³⁻ from 10 kHz to 100 mHz. **i** CVs for bare SPE (black), SPE modified with gold nanostructures electrodeposited during 9 s (red), 30 s (blue), and 90 s (yellow). CV conditions: 0.1 mol L⁻¹ PBS containing 4.0 mmol L⁻¹ [Fe(CN)₆]⁴⁻³⁻ at a scan rate of 100 mV s⁻¹.

of Au oxides, respectively [42]. The concentration of electroactive species ($\Gamma/\text{mol cm}^{-2}$) of AuNPs on the sensor was estimated with $\Gamma = Q/nFA$, where Q (C) is the background-corrected electric charge calculated by integrating the cathodic peak, n is the number of electrons, F is the Faraday constant (96,485.34C mol⁻¹), and A is the geometric surface area (0.012 cm²). The estimated charges (Q) were 111, 392, and 966 μC , and the concentrations of electroactive species were 9.6, 34, and 83×10^{-8} mol cm⁻² for AuNP_{9s}, AuNP_{30s}, and AuNP_{90s}, respectively (Figure S3). The values of Γ increased in the order: AuNP_{9s} < AuNP_{30s} < AuNP_{90s}, as expected with the increase in AuNPs with longer deposition times already observed with SEM and EDS. The increase in

AuNPs on the electrode leads to an increased reduction peak from Au⁺ to Au⁰, corroborating the cyclic voltammograms in Fig. 2g.

The shape and morphology of the nanoparticles affect the electrochemical properties of modified electrodes, primarily due to the electroactive areas [43, 44]. Thus, the electrodeposition time is a crucial factor, as observed in Fig. 2d-f, with peak current increasing with time due to increased surface area. Thicker films preclude electron transfer and induce a large capacitive current, while the small capacitance prevailing with thin films enhances sensitivity [24]. The importance of patterning SPE with Au structures became apparent in the increased electron transfer compared to bare SPE

electrodes, as inferred from CV and EIS measurements. Figure 2h shows the Nyquist diagrams for the four electrodes consisting of semicircles and diffusion straight lines. These were analyzed using a modified Randles equivalent circuit $[R_s(CPE[R_{ct}Z_w])]$, where R_s is the solution resistance, R_{ct} is the charge transfer resistance, Z_w is the Warburg impedance, and CPE is a constant phase element. The apparent heterogeneous electron rate constant was determined using $k_{app} = RT/F^2 R_{ct} CA$, in which F is the Faraday constant, C is the probe redox concentration in solution (4.0 mmol L^{-1}), R is the gas constant ($8.3145 \text{ J K}^{-1} \text{ mol}^{-1}$), T is the temperature (298 K), A is the geometric area (0.1256 cm^2), and R_{ct} is the charge transfer resistance obtained by fitting the data. k_{app} values calculated for bare SPE and SPE/Au are listed in Table S1. R_{ct} for SPE/Au ($< 88 \Omega$) is smaller than for bare SPE (1335Ω) due to the synergy in having SPE and Au sites for electron transfer. The significant increase in k_{app} (from 15 to 5×10^4 times, depending on the gold amount) for the SPE/Au electrode confirms the increased electron transfer during the redox process [45]. The same effect can be observed in the CV in $[\text{Fe}(\text{CN})_6]^{4-/3-}$ (Fig. 2i), in which the peak current of the oxidation/reduction of the redox pair increased with longer electrodeposition times. This observation has important implications for the performance of electroanalytical devices. The electrochemical behavior of gold-modified electrodes was also assessed in mechanical flexion tests. Even after 50 successive manual bending cycles, no significant changes in current or potential of $[\text{Fe}(\text{CN})_6]^{4-/3-}$ oxidation peaks were observed (deviations of 6.0% and 5.3% for current and potential, respectively, $n = 3$) (Figure S4).

Assembling the immunosensor

An immunosensor was assembled with a modified SPE with a gold deposition time of 9 s and monitored through the Nyquist diagrams in Fig. 3a. The use of a 9-s deposition time is justified by the increased sensitivity of these devices, as shown in “Analytical performance of the immunosensor.” The immobilization of MAA as a self-assembled monolayer (SAM) on the electrode caused R_{ct} to increase to 212.9Ω (curve: diamond, red) from 144.5Ω for the bare electrode (curve: inverted triangle, black). A significant decrease to 76.8Ω occurred with the immobilization with EDC/NHS, probably due to the pH used in the reaction (6.0). Antibody immobilization on the SPCE/AuNP/MAA/EDC-NHS surface increased R_{ct} slightly to 92.4Ω . With BSA immobilization for blocking active carboxylic acids, R_{ct} increased to 259.3Ω . The incubation of $10^{-6} \text{ mol L}^{-1}$ antigen (SARS-CoV S protein) on the SPCE/AuNP/MAA/EDC-NHS/Ab immunosensor led to a further increase in R_{ct} to 362.4Ω due to hindered electron mobility with the formation of the antigen–antibody complex. This complex represents an additional barrier between the electrode and $[\text{Fe}(\text{CN})_6]^{3-/4-}$ redox probes. Similar behavior was observed by Brazaca et al. [34] and Huang and co-workers [46], who considered the results to indicate biosensor assembling, decreasing the chances of a false positive response during impedimetric assays. The antibody-antigen interaction was also investigated using confocal fluorescence microscopy. The images taken before and after the interaction between MAA/EDC-NHS/Ab functionalized electrode and a fluorescein-labeled

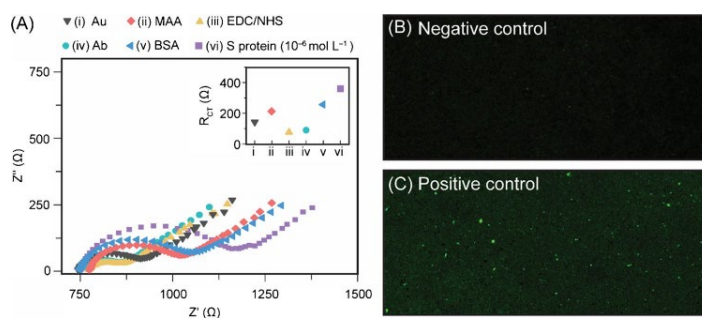


Fig. 3 a Nyquist plots in 0.1 mol L^{-1} phosphate buffer containing $5.0 \text{ mmol L}^{-1} [\text{Fe}(\text{CN})_6]^{3-/4-}$ using: (i) bare SPCE/AuNP (inverted triangle, black), (ii) SPCE/AuNP/MAA (diamond, red), (iii) SPCE/AuNP/MAA/EDC-NHS (triangle, yellow), (iv) SPCE/AuNP/MAA/EDC-NHS/antibody (circle, green), (v) SPCE/AuNP/MAA/EDC-NHS/antibody/BSA (left-pointing triangle, blue), (vi) and SPCE/AuNP/MAA/EDC-NHS/antibody/BSA/antigen (square, purple).

Conditions: $0.1\text{--}100,000 \text{ Hz}$ frequency range with pulse amplitude 10 mV . Inset: equivalent circuit to fit the experimental data. The insert brings R_{ct} values (Ω) after each functionalization step calculated using $[R_s(CPE[R_{ct}Z_w])]$ as an equivalent circuit. Fluorescence images of **b** MAA/EDC-NHS/Ab functionalized electrode, and **c** functionalized electrode after detection of fluorescein-labeled protein S from SARS-CoV. Amplification $20\times$

Electrochemical immunosensors using electrodeposited gold nanostructures for detecting...

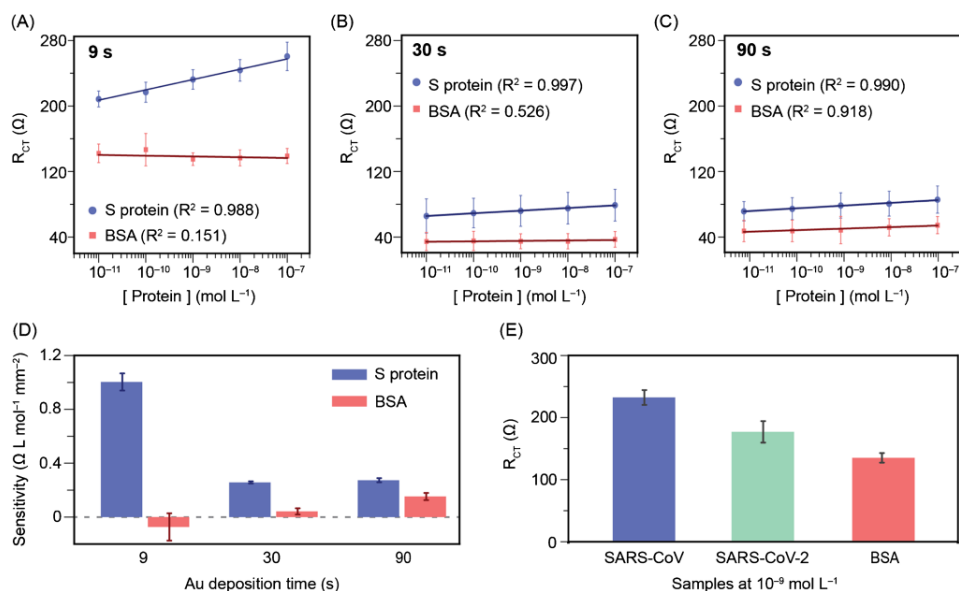


Fig. 4 Calibration curves of S protein and BSA for different Au deposition times: 9 (a), 30 (b), and 90 s (c). **d** Sensitivities for S protein and BSA for each Au deposition condition. EIS conditions: 0.1 mol

L⁻¹ PBS containing 4.0 mmol L⁻¹ [Fe(CN)₆]^{4-/3-} at OCP. **e** R_{ct} signals from SARS-CoV, SARS-CoV-2, and BSA at 10⁻⁹ mol L⁻¹ in PBS

SARS-CoV S protein in Fig. 3b and c confirm the effective biological recognition.

Analytical performance of the immunosensor

Calibration curves obtained from R_{ct} for devices constructed with three gold electrodeposition times (9, 30, and 90 s) are shown in Fig. 4. All the immunosensors could differentiate SARS-CoV S protein from BSA, with R^2 and/or sensitivity values being significantly decreased for the BSA control assays. The highest sensitivity and selectivity were observed for the immunosensor containing fewer AuNPs (9 s electrodeposition), as indicated in Fig. 4D with $R^2=0.988$ and sensitivity 1.00 Ω L mol⁻¹ mm⁻². With 9 s electrodeposition time, homogeneous spherical AuNPs are generated, thus confirming that the shape and morphology affect the electroanalytical performance [47]. For longer deposition times (30 and 90 s)—or larger gold nanostructures—the sensitivity is lower (0.258 and 0.274 Ω L mol⁻¹ mm⁻² for 30 and 90 s, respectively), with poor reproducibility (>25%, $n=3$) which might be due to gold leaching. Although the longer deposition time led to increased electrochemical currents (“Characterization of Au-modified SPCEs”), electrodes with 9 s electrodeposition exhibited better analytical parameters for

detecting the S protein since the resistance to charge transfer was the parameter of interest rather than the electrochemical current. Furthermore, the cost of the sensing units is decreased with less gold being deposited, and therefore the 9 s electrodeposition time was used in subsequent studies.

All the sensing results reported so far were obtained with SARS-CoV protein as the target analyte. We now report on the use of the same immunosensor to detect SARS-CoV-2 S protein. Figure 4e shows that SPEs modified with 9 s gold deposition time could distinguish 10⁻⁹ mol L⁻¹ S protein from SARS-CoV, S protein from SARS-CoV-2, and BSA (control) with a statistically significant difference using the ANOVA-Tukey test ($p \leq 0.05$). To confirm this statistical significance, we plotted the data for BSA, SARS-CoV, and SARS-CoV-2 at the same concentration of S protein (10⁻⁹ mol L⁻¹ in PBS) using principal component analysis (PCA). Figure S5 indicates excellent distinction of the samples, with more than 94% of data explained by PCA. We emphasize that all measurements were performed with the proteins separately and at the same concentration (BSA, SARS-CoV, and SARS-CoV-2).

As expected, R_{ct} after interaction with S protein from SARS-CoV-2 had an intermediate value due to its lower interaction rate with the antibodies than the S protein from

SARS-CoV. R_{ct} differs in each case which means that the immunosensor platform may be used to differentiate SARS-CoV viruses. The reason the immunosensor could be used to detect both S proteins, from SARS-CoV and SARS-CoV-2, is associated with their similar features. Indeed, SARS-CoV and SARS-CoV-2 are closely related, and their S proteins have an overall protein sequence identity of 76%. The S1 receptor-binding domain is less conserved than the S2 fusion domain (76 and 90% identity, respectively) [48]. According to the producer of anti-S protein antibodies used in this study, there is cross-reactivity with SARS-CoV-2 S protein [49]. The same was observed by Bates [50], who measured cross-reactivity for most SARS-CoV structural protein-targeted antibodies evaluated against SARS-CoV-2 S protein.

The reproducibility in device fabrication was tested with three immunosensors obtained with 9 s gold deposition, which were made to interact with 10^{-9} mol L $^{-1}$ S protein. The immunosensor reproducibility was good, with an RSD of 5.12% ($n=3$). Although the immunosensor was designed to be disposable, the repeatability of the sensor was evaluated to ensure signal stability. This was done with ten successive measurements in a single device, and the response to 10^{-9} mol L $^{-1}$ SARS-CoV S protein varied with a 4.51% RSD ($n=10$). The LOD of the immunosensors was 3.16 pmol L $^{-1}$ or 83.7 pg mL $^{-1}$.

It is worth mentioning that the values used for quantifying S protein throughout this paper correspond to the total R_{ct} value from EIS measurements. Therefore, it corresponds to the biosensor itself (MAA, EDC/NHS, antibody, BSA blocking layer) plus the analyte. We have decided to use the total R_{ct} value instead of ΔR_{ct} (before and after sample interaction) due to two main reasons. The first one is the simplification of the test for the user, requiring a single measurement. Furthermore, since using ΔR_{ct} involves two measurements rather than one, the reproducibility of the

tests may be affected [41]. Indeed, the RSD% values ($n=3$) for R_{ct} are 5.37% before and 5.12% after sample interaction, while RSD% was 9.64% for the difference.

Application of the immunosensor in biological samples

Since saliva is a common means of transmission of infectious diseases [51], human saliva samples were applied to evaluate the analytical performance of the immunosensor produced with 9 s gold electrodeposition. As with other coronaviruses, the spike protein is abundantly expressed during virus infection and is most effective at inducing antibody responses in the host. Then, early diagnosis can be made by detecting antibodies against the SARS-CoV spike protein [52, 53]. SARS-CoV S protein concentrations (from 10^{-11} to 10^{-7} mol L $^{-1}$) were added to commercial human saliva supernatant obtained after centrifugation of the biological fluid. To assure that the changes in R_{ct} are due to antigen–antibody interactions, a control was conducted with saliva samples spiked with BSA in the same concentration range. To reduce nonspecific interactions between saliva components and the immunosensor, the latter was washed after sample incubation using PBS with the addition of a surfactant (SDS). Figure 5 shows the Nyquist plot (Fig. 5a) and the calibration curves (Fig. 5b) for human saliva spiked with SARS-CoV S protein (blue) and BSA (red). The curves are similar to those where PBS was used, with R_{ct} increasing linearly ($R^2=0.996$) with the analyte addition (in log scale). As expected, a higher sensitivity was observed for S protein ($5.935 \Omega \text{ L mol}^{-1} \text{ mm}^{-2}$) compared to BSA ($1.725 \Omega \text{ L mol}^{-1} \text{ mm}^{-2}$). However, R_{ct} is significantly higher than in the curves with PBS, probably due to nonspecific interactions with other saliva components. The increase of R^2 ($R^2=0.929$) and sensitivity related to BSA curves

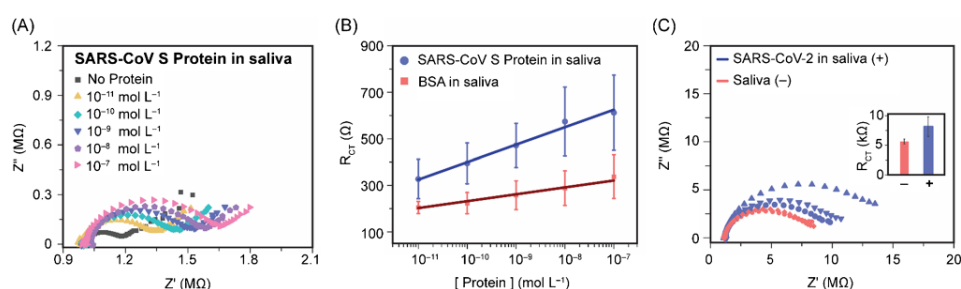


Fig. 5 Application of the proposed immunosensor in biological samples. **a** Nyquist plots after incubation of S protein from SARS-CoV from 10^{-11} to 10^{-7} mol L $^{-1}$ in saliva samples. **b** Calibration curves for S protein from SARS-CoV and BSA in saliva. **c** Nyquist plot for

detection of inactivated SARS-CoV-2 viruses in saliva. The inset shows the R_{ct} obtained for negative (in the absence of the virus) and positive (in the presence of 10^6 PFU mL $^{-1}$ of the virus) samples

corroborates this hypothesis. This behavior is probably due to the successive incubations in saliva and not due to the concentration of BSA itself. Therefore, considering a single incubation (30 min), the immunosensor can differentiate control and positive samples. It can distinguish S protein and BSA in concentrations ranging from 10^{-11} to 10^{-7} mol L^{-1} ($n=3$) even in a complex environment, indicating its potential applicability in biological samples.

Last, the biosensors were tested regarding their ability to detect inactivated SARS-CoV-2 viruses in saliva samples. As expected, the measured R_{ct} was significantly increased in the presence of the virus (10^6 PFU mL^{-1}) due to interaction with the immunosensor (Fig. 5c). As the typical range of positive cases of patients infected with SARS-CoV-2 is from 10^5 to 10^7 PFU mL^{-1} , the proposed method exhibited excellent performance at a fortified sample at 10^6 PFU mL^{-1} , showing potential applicability to clinical samples. It is also interesting to note that biosensors with similar or higher LODs than the one presented here were tested in real saliva clinical samples and showed great agreement with RT-PCR [8].

A list of immunosensing platforms for SARS-CoV and SARS-CoV-2 is shown in Tables S2 and S3, in the supplementary material. It is worth mentioning that none of the devices from the literature have been tested for the detection of both SARS-CoV and SARS-CoV-2, which is the case here. The immunosensor that we reported is competitive with other platforms. Even though its LOD is higher than more sophisticated immunosensors, its low cost (US\$ 0.03) and potential direct applicability to biological samples represent considerable advantages. The immunosensor is also advantageous due to the ease of preparation and manipulation, as it is label-free.

Conclusions

The fabrication of SPCEs decorated with electroformed gold nanoparticles was optimized and characterized. As a proof of concept, the electrodes were functionalized with a SAM and a layer of anti-S protein antibodies for a sensitive determination of S proteins from SARS-CoV and SARS-CoV-2. The label-free immunosensing platform had a LOD of 3.16 pmol L^{-1} and provided quantitative results in fortified human saliva using only 10 μL in a 30 min single incubation step. The high analytical performance exhibited by the disposable immunosensor and its simple operation—with no need for signal amplification strategies—make the method a potential alternative to identify SARS-CoV and SARS-CoV-2 in point-of-care settings. The immunosensor for S protein is competitive with other affinity electrochemical biosensors in terms of simplicity, test time, and sensitivity. Moreover, if necessary, the antibodies used in its construction can be

updated to detect new variants of the disease. The features of the simple immunosensor are promising for the deployment of mass testing in any country. For the commercialization, efforts are still needed for a complete validation with a more significant number of samples and of different nature, in addition to a comparison with gold-standard techniques such as ELISA immunoassays and RT-PCR. Regardless, the gold-based immunosensor demonstrated good analytical performance and can be explored as an alternative for a faster and cheaper diagnosis of COVID-19.

Supplementary Information The online version contains supplementary material available at <https://doi.org/10.1007/s00216-022-03956-1>.

Acknowledgements The authors are grateful to Dr. Flavio Protásio Veras and Bruna Manuella Souza e Silva from the Center for Research in Inflammatory Diseases (FMRP/USP) for providing inactivated virus samples.

Funding The authors are grateful to São Paulo Research Foundation (FAPESP) (Grant #2018/19750–3, 2016/01919–6, 2017/05362–9, 2018/22214–6, 2020/09587–8, 2017/21097–3, and 2019/01777–5); Conselho Nacional de Desenvolvimento Científico e Tecnológico (CNPq) (Grants 164569/2020–0, 303338/2019–9, and 423952/2018–8); and Coordenação de Aperfeiçoamento de Pessoal de Nível Superior – Brasil (CAPES) (Finance Code 001; grant #3007/2014 – PROCAD; and Epidemias grant# 88887.504861/2020–00) for financial support. We would like to thank the INCTBio grants (FAPESP #2014/40867–3 and CNPq #465389/2014–7, #315824/2020–4).

Data availability The data associated with this manuscript is available and has been deposited in: Canniatti Brazaca, Lais; Imamura, Amanda Hikari; Oezau Gomes, Nathalia; Bortholazzi Almeida, Mariana; Tamara Scheidt, Desirée; Raymundo-Pereira, Paulo Augusto; Novais de Oliveira Jr, Osvaldo; Campos Janegitz, Bruno; Spinola Machado, Sergio Antonio; Carrilho, Emanuel (2021), "Electrochemical immunosensors using electrodeposited gold nanostructures for detecting the S proteins from SARS-CoV and SARS-CoV-2," Mendeley Data, V1, <https://doi.org/10.17632/vzb9sn7cc2.1>

Declarations

Conflict of interest The authors declare no competing interests.

References

1. Feng W, Newbigging AM, Le C, Pang B, Peng H, Cao Y, Wu J, Abbas G, Song J, Wang D-B, Cui M, Tao J, Tyrrell DL, Zhang X-E, Zhang H, Le XC. Molecular diagnosis of COVID-19: challenges and research needs. *Anal Chem*. 2020;92:10196–209. <https://doi.org/10.1021/acs.analchem.0c02060>.
2. Hernández-Rodríguez JF, Rojas D, Escarpa A. Electrochemical sensing directions for next-generation healthcare: trends, challenges, and frontiers. *Anal Chem*. 2021;93:167–83. <https://doi.org/10.1021/acs.analchem.0c04378>.
3. Raziq A, Kidakova A, Boroznjak R, Reut J, Öpik A, Syritysk V. Development of a portable MIP-based electrochemical sensor for detection of SARS-CoV-2 antigen. *Biosens Bioelectron*. 2021;178:113029. <https://doi.org/10.1016/j.bios.2021.113029>.

4. Brazaca LC, dos Santos PL, de Oliveira PR, Rocha DP, Stefano JS, Kalinke C, Abarza Muñoz RA, Bonacin JA, Janegitz BC, Carrilho E. Biosensing strategies for the electrochemical detection of viruses and viral diseases – a review. *Anal Chim Acta*. 2021;1159:338384. <https://doi.org/10.1016/j.aca.2021.338384>.
5. World Health Organization (2020) Coronavirus disease 2019 (COVID-19): situation report, 52. <https://apps.who.int/iris/handle/10665/331476>. Accessed 12 Mar 2021
6. Hashemi SA, GolabBehbahan NG, Bahrani S, Mousavi SM, Gholami A, Ramakrishna S, Firoozsani M, Moghadami M, Lankarani KB, Omidifar N. Ultra-sensitive viral glycoprotein detection NanoSystem toward accurate tracing SARS-CoV-2 in biological/non-biological media. *Biosens Bioelectron*. 2021;171:112731. <https://doi.org/10.1016/j.bios.2020.112731>.
7. Ji T, Liu Z, Wang G, Guo X, Akbar khan S, Lai C, Chen H, Huang S, Xia S, Chen B, Jia H, Chen Y, Zhou Q. Detection of COVID-19: a review of the current literature and future perspectives. *Biosens Bioelectron*. 2020;166:112455. <https://doi.org/10.1016/j.bios.2020.112455>.
8. Fabiani L, Saroglia M, Galatà G, De Santis R, Fillo S, Luca V, Faggioni G, D'Amore N, Regalbuto E, Salvatori P, Terova G, Moscone D, Lista F, Arduini F. Magnetic beads combined with carbon black-based screen-printed electrodes for COVID-19: a reliable and miniaturized electrochemical immunosensor for SARS-CoV-2 detection in saliva. *Biosens Bioelectron*. 2021;171:112686. <https://doi.org/10.1016/j.bios.2020.112686>.
9. Yakoh A, Pimpitak U, Rengpipat S, Hirankarn N, Chailapakul O, Chaiyo S. Paper-based electrochemical biosensor for diagnosing COVID-19: detection of SARS-CoV-2 antibodies and antigen. *Biosens Bioelectron*. 2021;176:112912. <https://doi.org/10.1016/j.bios.2020.112912>.
10. Seo G, Lee G, Kim MJ, Baek S-H, Choi M, Ku KB, Lee C-S, Jun S, Park D, Kim HG, Kim S-J, Lee J-O, Kim BT, Park EC, Il KS. Rapid detection of COVID-19 causative virus (SARS-CoV-2) in human nasopharyngeal swab specimens using field-effect transistor-based biosensor. *ACS Nano*. 2020;14:5135–42. <https://doi.org/10.1021/acsnano.0c02823>.
11. Alanazi K, Garcia Cruz A, Di Masi S, Voorhaar A, Ahmad OS, Cowen T, Piletska E, Langford N, Coats TJ, Sims MR, Piletsky SA. Disposable paracetamol sensor based on electroactive molecularly imprinted polymer nanoparticles for plasma monitoring. *Sensors Actuators B Chem*. 2021;329:129128. <https://doi.org/10.1016/j.snb.2020.129128>.
12. Martins G, Gogola JL, Budni LH, Janegitz BC, Marcolino-Junior LH, Bergamini MF. 3D-printed electrode as a new platform for electrochemical immunosensors for virus detection. *Anal Chim Acta*. 2021;1147:30–7. <https://doi.org/10.1016/j.aca.2020.12.014>.
13. Cesewski E, Johnson BN. Electrochemical biosensors for pathogen detection. *Biosens Bioelectron*. 2020;159:112214. <https://doi.org/10.1016/j.bios.2020.112214>.
14. García-Miranda Ferrari A, Rowley-Neale SJ, Banks CE. Screen-printed electrodes: transitioning the laboratory in-to-the field. *Talanta Open*. 2021;3:100032. <https://doi.org/10.1016/j.talo.2021.100032>.
15. Paschoalino WJ, Kogikoski S Jr, Barragan JTC, Giarola JF, Cantelli L, Rabelo TM, Pessanha TM, Kubota LT. Emerging considerations for the future development of electrochemical paper-based analytical devices. *ChemElectroChem*. 2019;6:10–30. <https://doi.org/10.1002/celec.201800677>.
16. Du CX, Han L, Dong SL, Li LH, Wei Y. A novel procedure for fabricating flexible screen-printed electrodes with improved electrochemical performance. *IOP Conf Ser Mater Sci Eng*. 2016;137:12060. <https://doi.org/10.1088/1757-899x/137/1/012060>.
17. Dungchai W, Chailapakul O, Henry CS. Electrochemical detection for paper-based microfluidics. *Anal Chem*. 2009;81:5821–6.
18. Ibáñez-Redín G, Wilson D, Gonçalves D, Oliveira ON. Low-cost screen-printed electrodes based on electrochemically reduced graphene oxide-carbon black nanocomposites for dopamine, epinephrine and paracetamol detection. *J Colloid Interface Sci*. 2018;515:101–8. <https://doi.org/10.1016/j.jcis.2017.12.085>.
19. Wang S, Liu N, Yang C, Liu W, Su J, Li L, Yang C, Gao Y. Fully screen printed highly conductive electrodes on various flexible substrates for asymmetric supercapacitors. *RSC Adv*. 2015;5:85799–805. <https://doi.org/10.1039/C5RA16724H>.
20. Martins TS, Bott-Neto JL, Oliveira ON Jr, Machado SAS. Paper-based electrochemical sensors with reduced graphene nanoribbons for simultaneous detection of sulfamethoxazole and trimethoprim in water samples. *J Electroanal Chem*. 2021;882:114985. <https://doi.org/10.1016/j.jelechem.2021.114985>.
21. Escamilla-Gómez V, Hernández-Santos D, González-García MB, Pingarrón-Carrazón JM, Costa-García A. Simultaneous detection of free and total prostate specific antigen on a screen-printed electrochemical dual sensor. *Biosens Bioelectron*. 2009;24:2678–83. <https://doi.org/10.1016/j.bios.2009.01.043>.
22. Narakathu BB, Devadas MS, Reddy ASG, Eshkeiti A, Moorthi A, Fernando IR, Miller BP, Ramakrishna G, Sinn E, Joyce M, Rebros M, Rebrosova E, Mezei G, Atashbar MZ. Novel fully screen printed flexible electrochemical sensor for the investigation of electron transfer between thiol functionalized viologen and gold clusters. *Sensors Actuators B Chem*. 2013;176:768–74. <https://doi.org/10.1016/j.snb.2012.10.069>.
23. Qian L, Durairaj S, Prins S, Chen A. Nanomaterial-based electrochemical sensors and biosensors for the detection of pharmaceutical compounds. *Biosens Bioelectron*. 2021;175:112836. <https://doi.org/10.1016/j.bios.2020.112836>.
24. Kumar A, Gonçalves JM, Sukeri A, Araki K, Bertotti M. Correlating surface growth of nanoporous gold with electrodeposition parameters to optimize amperometric sensing of nitrite. *Sensors Actuators B Chem*. 2018;263:237–47. <https://doi.org/10.1016/j.snb.2018.02.125>.
25. Gupta P, Goyal RN, Shim Y-B. Simultaneous analysis of dopamine and 5-hydroxyindoleacetic acid at nanogold modified screen printed carbon electrodes. *Sensors Actuators B Chem*. 2015;213:72–81. <https://doi.org/10.1016/j.snb.2015.02.066>.
26. Satyanarayana M, Goud KY, Reddy KK, Gobi KV. Biopolymer stabilized nanogold particles on carbon nanotube support as sensing platform for electrochemical detection of 5-fluorouracil in-vitro. *Electrochim Acta*. 2015;178:608–16. <https://doi.org/10.1016/j.electacta.2015.08.036>.
27. Cherevko S, Chung C-H. Direct electrodeposition of nanoporous gold with controlled multimodal pore size distribution. *Electrochim Commun*. 2011;13:16–9. <https://doi.org/10.1016/j.elecom.2010.11.001>.
28. Kumar A, Furtado VL, Gonçalves JM, Bannitz-Fernandes R, Netto LES, Araki K, Bertotti M. Amperometric microsensor based on nanoporous gold for ascorbic acid detection in highly acidic biological extracts. *Anal Chim Acta*. 2020;1095:61–70. <https://doi.org/10.1016/j.aca.2019.10.022>.
29. Raymundo-Pereira PA, Gomes NO, Machado SAS, Oliveira ON. Simultaneous, ultrasensitive detection of hydroquinone, paracetamol and estradiol for quality control of tap water with a simple electrochemical method. *J Electroanal Chem*. 2019;848:113319. <https://doi.org/10.1016/j.jelechem.2019.113319>.
30. Hernández-Saravia LP, Sukeri A, Bertotti M. Fabrication of nanoporous gold-islands via hydrogen bubble template: an efficient electrocatalyst for oxygen reduction and hydrogen evolution reactions. *Int J Hydrogen Energy*. 2019;44:15001–8. <https://doi.org/10.1016/j.ijhydene.2019.04.186>.
31. Soares JC, Soares AC, Angelim MKSC, Proença-Modena JL, Moraes-Vieira PM, Mattoso LHC, Oliveira ON Jr. Diagnostics of SARS-CoV-2 infection using electrical impedance spectroscopy

- with an immunosensor to detect the spike protein. *Talanta*. 2022;239:123076. <https://doi.org/10.1016/j.talanta.2021.123076>.
32. Zaccariotto GC, Silva MKL, Rocha GS, Cesarino I (2021) A novel method for the detection of SARS-CoV-2 based on graphene-impedimetric immunosensor. *Materials* 14
 33. Brazaca LC, Bramorski CB, Cancino-Bernardi J, da Silveira C-M, Markus RP, Janegitz BC, Zucolotto V. An antibody-based platform for melatonin quantification. *Colloids Surfaces B Biointerfaces*. 2018;171:94–100. <https://doi.org/10.1016/j.colsurfb.2018.07.006>.
 34. Brazaca LC, Janegitz BC, Cancino-Bernardi J, Zucolotto V. Transmembrane protein-based electrochemical biosensor for adiponectin hormone quantification. *ChemElectroChem*. 2016;3:1006–11. <https://doi.org/10.1002/celec.201600099>.
 35. Mehmandoust M, Gumus ZP, Soyлак M, Erk N. Electrochemical immunosensor for rapid and highly sensitive detection of SARS-CoV-2 antigen in the nasal sample. *Talanta*. 2022;240:123211. <https://doi.org/10.1016/j.talanta.2022.123211>.
 36. Mojsoska B, Larsen S, Olsen DA, Madsen JS, Brandslund I, Alatrakchi FA (2021) Rapid SARS-CoV-2 detection using electrochemical immunosensor. *Sensors* 21
 37. Zamzami MA, Rabbani G, Ahmad A, Basalah AA, Al-Sabban WH, Nate Ahn S, Choudhry H. Carbon nanotube field-effect transistor (CNT-FET)-based biosensor for rapid detection of SARS-CoV-2 (COVID-19) surface spike protein S1. *Bioelectrochemistry*. 2022;143:107982. <https://doi.org/10.1016/j.bioelechem.2021.107982>.
 38. Zhang M, Li X, Pan J, Zhang Y, Zhang L, Wang C, Yan X, Liu X, Lu G. Ultrasensitive detection of SARS-CoV-2 spike protein in untreated saliva using SERS-based biosensor. *Biosens Bioelectron*. 2021;190:113421. <https://doi.org/10.1016/j.bios.2021.113421>.
 39. Zhao J, Fu Z, Li H, Xiong Y, Cai S, Wang C, Chen Y, Han N, Yang R. Magnet-assisted electrochemical immunosensor based on surface-clean Pd-Au nanosheets for sensitive detection of SARS-CoV-2 spike protein. *Electrochim Acta*. 2022;404:139766. <https://doi.org/10.1016/j.electacta.2021.139766>.
 40. Stefano JS, Guterres e Silva LR, Rocha RG, Brazaca LC, Richter EM, Abarza Muñoz RA, Janegitz BC. New conductive filament ready-to-use for 3D-printing electrochemical (bio)sensors: towards the detection of SARS-CoV-2. *Anal Chim Acta*. 2022;1191:339372. <https://doi.org/10.1016/j.aca.2021.339372>.
 41. Anderson DJ. Determination of the lower limit of detection. *Clin Chem*. 1989;35:2152–3. <https://doi.org/10.1093/clinchem/35.10.2152>.
 42. Raymundo-Pereira PA, Shimizu FM, Coelho D, Piazzeta MHO, Gobbi AL, Machado SAS, Oliveira ON. A nanostructured bifunctional platform for sensing of glucose biomarker in artificial saliva: synergy in hybrid Pt/Au surfaces. *Biosens Bioelectron*. 2016;86:369–76. <https://doi.org/10.1016/j.bios.2016.06.053>.
 43. Carbone M, Nesticò A, Bellucci N, Micheli L, Pallechi G. Enhanced performances of sensors based on screen printed electrodes modified with nanosized NiO particles. *Electrochim Acta*. 2017;246:580–7. <https://doi.org/10.1016/j.electacta.2017.06.074>.
 44. Karra S, Wooten M, Griffith W, Gorski W. Morphology of gold nanoparticles and electrocatalysis of glucose oxidation. *Electrochim Acta*. 2016;218:8–14. <https://doi.org/10.1016/j.electacta.2016.09.097>.
 45. Varodi C, Pogacean F, Coros M, Rosu M-C, Stefan-van Staden R-I, Gal E, Tudoran L-B, Pruneanu S, Mirel S (2019) Detection of 8-hydroxy-2'-deoxyguanosine biomarker with a screen-printed electrode modified with graphene. *Sensors* 19
 46. Huang M, Li H, He H, Zhang X, Wang S. An electrochemical impedance sensor for simple and specific recognition of G-G mismatches in DNA. *Anal Methods*. 2016;8:7413–9. <https://doi.org/10.1039/C6AY01705C>.
 47. Xu J, Zhao S, Teng T, Abdalla AE, Zhu W, Xie L, Wang Y, Guo X. Systematic comparison of two animal-to-human transmitted human coronaviruses: SARS-CoV-2 and SARS-CoV. *Viruses*. 2020;12:244.
 48. Jaimes JA, André NM, Chappie JS, Millet JK, Whittaker GR. Phylogenetic analysis and structural modeling of SARS-CoV-2 spike protein reveals an evolutionary distinct and proteolytically sensitive activation loop. *J Mol Biol*. 2020;432:3309–25. <https://doi.org/10.1016/j.jmb.2020.04.009>.
 49. Sino Biological (2021) SARS-CoV/SARS-CoV-2 spike antibody, chimeric MAb. <https://www.sinobiological.com/antibodies/cov-spike-40150-d006>. Accessed 17 May 2021
 50. Bates TA, Weinstein JB, Farley S, Leier HC, Messer WB, Tafesse FG. Cross-reactivity of SARS-CoV structural protein antibodies against SARS-CoV-2. *Cell Rep*. 2021;34. <https://doi.org/10.1016/j.celrep.2021.108737>.
 51. Dave PK, Rojas-Cessa R, Dong Z, Umpaichitra V (2021) Survey of saliva components and virus sensors for prevention of COVID-19 and infectious diseases. *Biosensors* 11
 52. Chang M-S, Lu Y-T, Ho S-T, Wu C-C, Wei T-Y, Chen C-J, Hsu Y-T, Chu P-C, Chen C-H, Chu J-M, Jan Y-L, Hung C-C, Fan C-C, Yang Y-C. Antibody detection of SARS-CoV spike and nucleocapsid protein. *Biochem Biophys Res Commun*. 2004;314:931–6. <https://doi.org/10.1016/j.bbrc.2003.12.195>.
 53. Haynes LM, Miao C, Harcourt JL, Montgomery JM, Le MQ, Dryga SA, Kamrud KI, Rivers B, Babcock GJ, Oliver JB, Comer JA, Reynolds M, Uyeki TM, Bausch D, Ksiazek T, Thomas W, Alterson H, Smith J, Ambrosino DM, Anderson LJ. Recombinant protein-based assays for detection of antibodies to severe acute respiratory syndrome coronavirus spike and nucleocapsid proteins. *Clin Vaccine Immunol*. 2007;14:331–3. <https://doi.org/10.1128/CVI.00351-06>.

Publisher's note Springer Nature remains neutral with regard to jurisdictional claims in published maps and institutional affiliations.